Synthesis and Characterisation of Nanoscale Oxides for Energy Applications

Thesis submitted in accordance with the requirements of the University of Liverpool for the degree of Doctor in Philosophy by Joseph William Roberts

September 2014

Table of Contents

Notation

Symbol	Units	Description	Symbol	Units	Description
α	---	Porosity	E_v	eV	Valance band edge
α	m^{-1}	Absorption coefficient	F	N	Force
α	K^{-1}	Coefficient of thermal expansion	FF	---	Fill Factor
Δ	°	Phase difference	HV	Pa	Vickers Hardness
Δl	m	Length change	h	m	Pore height
Δm	kg	Mass change	I	A	Current
ΔV	V	Voltage	I	$W.m^{-2}$	Transmitted light intensity
ε	---	Integrated coverage	I_m	A	Current at maximum power
ε_{inner}	---	Inner surface strain	I_{sh}	A	Short circuit current
ε_{outer}	---	Outer surface strain	I_{td}	$A.m^{-2}$	True current density
η	---	Conversion efficiency	I_0	A	Diode saturation current
θ	°	Spherical angle	i	A	Anodic current
λ	m	Wavelength	J	$s^{-1}m^{-2}$	Molecular flux
μ_e	$m^2V^{-1}s^{-1}$	Electron mobility	k	$m.V^{-1}$	Interpore spacing proportionality
μ_p	$m^2V^{-1}s^{-1}$	Hole mobility	k	---	Extinction coefficient
ρ	$kg.m^{-3}$	Density	k	$J.K^{-1}$	Boltzmann's constant
ρ_{metal}	$kg.m^{-3}$	Metal density	k_1	$kgm^{-2}s^{-1}$	Constant
ρ_{oxide}	$kg.m^{-3}$	Oxide density	k_2	$kg.m^{-2}$	Constant
σ	$S.m^{-1}$	Conductivity	L	m	Cone edge wall length
τ	m^{-2}	Density of reactive states	l	m	Original length
τ	s	Average time between collisions	l	m	Pore depth
$\emptyset$	eV	Electron detector work function	M	kg	Mass
Φ_m	eV	Metal work function	m	kg	Molecular mass
φ_B	eV	Metal-semiconductor junction barrier height	m_e^*	kg	Effective electron mass
φ_i	eV	Built-in potential	m_{film}	kg	Deposited film mass
Ψ	---	Amplitude Ratio	N_e	m^{-3}	Electron density
A	m^2	Area	N_p	m^{-3}	Hole density
A	---	Temperature dependant constant	n	---	Number of pores
A_b	m^{-2}	Base area	n	---	Metal atoms/oxide molecule
A_{pore}	m^{-2}	Cross section pore area	P	$N.m^{-2}$	Partial pressure
$A_{sputtered}$	m^{-2}	Sputtered surface area	P_{light}	$W.m^{-2}$	Incident light power
A_t	m^{-2}	Tip area	q	C	Electron charge
$A_{template}$	m^{-2}	Template upper surface area	R	m	Template radius
A_{total}	m^{-2}	Total area	R_s	Ω/□	Sheet resistance
A_{upper}	m^{-2}	Upper surface area	$r_c(x)$	m	Radius of curvature at x
A_w	m^{-2}	Wall area	S	m^{-2}	Saturation dose
a	---	Aspect ratio	S_c	---	Sticking coefficient
amu	$g.mol^{-1}$	Atomic mass unit	s_d	m	Sputtering penetration depth
B	---	Temperature dependant constant	T	K	Temperature
b_t	m	Barrier layer thickness	t	s	Time
C_{inner}	m	Inner surface circumference	t	m	Deposition thickness
$C_{neutral}$	m	Circumference at neutral axis	t	m	Sample thickness
C_{outer}	m	Outer surface circumference	U	V	Self-ordering Voltage
D_p	m^{-2}	Pore density	V	m^{-3}	Volume
d	m	Radius of curvature at $x = 0$	V_A	V	Applied voltage
d	m	Diagonal length	V_m	V	Voltage at maximum power
d	m	TCO thickness	V_{metal}	m^3	Metal volume
d_b	m	Diameter at NW base	V_{oc}	V	Open circuit voltage
d_i	m	Interpore distance	V_{oxide}	m^3	Oxide volume
d_p	m	Pore diameter	V_T	V	Thermal voltage
d_t	m	Diameter at NW tip	w	m	Width
E	$V.m^{-1}$	Electric field	w	$kg.m^{-2}$	Weight gain per unit area
$E_{binding}$	eV	Photoelectron binding energy	w_t	m	Wall thickness
E_c	eV	Conduction band edge	X	eV	Electron affinity
E_F	eV	Fermi energy	x	m	Film thickness
$E_{kinetic}$	eV	Emitted photoelectron energy	x	m	Distance from max deformation
E_{photon}	eV	Incident photon energy			

Acronyms

Acronym	Description	Acronym	Description
AAO	*Anodised Aluminium Oxide*	MFC	*Mass Flow Controller*
AC	*Alternating Current*	MFP	*Mean Free Path*
AFM	*Atomic Force Microscope*	MIM	*Metal Insulator Metal*
ALD	*Atomic Layer Deposition*	MOCVD	*Metal Organic Chemical Vapour Deposition*
ALE	*Atomic Layer Epitaxy*	MOSFET	*Metal Oxide Semiconductor Field Effect Transistor*
AM	*Air Mass*	MRAM	*Magnetoresistive Random Access Memory*
APA	*Anodic Porous Alumina*	NTs	*Nanotubes*
ASM	*American Society for Metals*	NWs	*Nanowires*
ATO	*Anodised Titanium Oxide*	OAO	*Oxide Alumina Oxide*
AZO	*Aluminium-doped Zinc Oxide*	ONO	*Oxide Nitride Oxide*
BJT	*Bipolar Junction Transistor*	PAA	*Porous Anodised Alumina*
CCD	*Charge Coupled Device*	PAM	*Porous Alumina Membranes*
CIGS	*Copper Indium Gallium Selenide*	PAO	*Porous Aluminium Oxide*
CMOS	*Complementary Metal Oxide Semiconductor*	PBR	*Pilling-Bedworth Ratio*
CTO	*Cadmium Stannate*	PL	*Photoluminescence*
CVD	*Chemical Vapour Deposition*	PLD	*Pulsed Laser Deposition*
DC	*Direct Current*	PV	*Photovoltaic*
DEZ	*Diethyl Zinc*	PVD	*Physical Vapour Deposition*
DIC	*Differential Interference Contrast*	QCM	*Quartz Crystal Microbalance*
DRAM	*Dynamic Random Access Memory*	RAM	*Random Access Memory*
EDS	*Energy Dispersive X-ray Spectroscopy*	RF	*Radio Frequency*
EP	*Electrophoretic*	RSF	*Relative Sensitivity Factor*
FEGSEM	*Field Emission Gun Scanning Electron Microscope*	RT	*Room Temperature*
FF	*Fill Factor*	SAED	*Selected Area Electron Diffraction*
FTO	*Fluorine-doped Tin Oxide*	SEM	*Scanning Electron Microscope*
FWHM	*Full Width Half Maximum*	SPV	*Surface Photovoltage*
GB	*Grain Boundary*	SQUID	*Superconducting Quantum Interference Device*
GZO	*Gallium-doped Zinc Oxide*	TA	*Transitional Anodisation*
HA	*Hard Anodisation*	TCO	*Transparent Conductive Oxide*
HDHC	*Hard Drawn High Conductivity*	TEM	*Transmission Electron Microscope*
HDs	*Hexagonal Domains*	TFT	*Thin-Film Transistor*
HV	*Vickers Hardness*	TiP	*Titanium Isopropoxide*
IEA	*International Energy Agency*	TMA	*Trimethyl Aluminium*
ITO	*Indium Tin Oxide*	TMP	*Trimethyl Phosphate*
IZO	*Indium Zinc Oxide*	UV	*Ultra Violet*
LCD	*Liquid Crystal Display*	VLS	*Vapour Liquid Solid*
LED	*Light Emitting Diode*	VS	*Vapour Solid*
LPCVD	*Low Pressure Chemical Vapour Deposition*	XPS	*X-ray Photoelectron Spectroscopy*
MA	*Mild Anodisation*	XRD	*X-ray Diffraction*
MBE	*Molecular Beam Epitaxy*	XRR	*X-ray Reflectivity*

Acknowledgements

This PhD thesis would not have been possible without the guidance and support of my supervisors, colleagues, friends and family. I would like to thank Paul Chalker and Richard Potter for providing guidance and direction for my work. My colleagues Dave Atkinson, Matt Werner, Paul Marshall, Karl Dawson, Pete King, Paul Williams, Thomas Boegelein, Stephanie Herodotou and Zahra Golraki all deserve appreciation for advising on experimental planning, execution and trouble shooting, as well as taking their time to train me on various pieces of equipment. I would also like to thank my friends and family, Teresa Partida, Ken, Anne and Julia Roberts, Daniel McKinnon, David and George Perry, Phil Jenn, Rich Hurst, David Surridge, Robert and Andrew Wilkinson, Jocelyn Hughes, Phil Jones and George Hitchmouth for helping me get through all the work and keeping my spirits high by providing timely and necessary distractions and for letting me bounce ideas off them without them appearing too disinterested.

Abstract

The motivation for this research is the synthesis and characterisation of nanostructured oxide materials for potential applications in renewable energy generation or storage. In particular, the research in this thesis addresses the development of nanostructured oxide materials which could be exploited as photovoltaics and transparent conductive oxides.

The exploitation of anodised aluminium oxide (AAO) to fabricate nanostructured semiconductor pn-junctions as the basis photovoltaic devices is investigated. Various microstructures are modelled with the aim of identifying ones with high interface area and consequently high energy conversion efficiencies. Experiments reveal that AAO prepared using an oxalic acid electrolyte could be achieved with a growth rate of 5.7μm/h. The uniformity and size of the hexagonal cross-section pores is influenced by the first-step anodisation time. Atomic layer deposition (ALD) was used to coat commercially available AAO, to synthesise conformal nanotubes or wires. It was observed that the uniformity of the nanostructures breaks down towards the bulk of the AAO, without high exposures, due to the lack of precursor penetration. However, the proposed geometric mass-gain model to understand the process is supported by experimental mass gain measurements and how deposition occurs within the templates.

A second materials system based on copper / copper oxide is also explored as a method of synthesising and controlling the formation of nanostructured oxide materials. The surface preparation of the starting copper sheet material was investigated and it was found to be pivotal in the nanoscale morphology achievable with subsequent heat treatment to grow nanowires and porous layers. Thermal growth of CuO and Cu_2O on pre- treated copper foils at 500°C exhibited growth of high aspect ratio CuO nanowires. Further studies on the growth process disproved the vapour-liquid-solid and vapour-solid growth mechanisms for

the nanowires and showed that tensile strain within the Cu substrate was the driving force behind the nanowire growth. The use of nanometre-scale ALD alumina barrier layers was employed to suppress spallation and preserve the nanowire surfaces. It was found that for samples with alumina layers between ~3 and 15nm the oxide spallation was significantly reduced and that for samples with ~20nm of alumina the diffusion of Cu atoms to the surface was hindered. Photovoltaic measurements were made on electrolytically synthesised Cu_2O surfaces coated with ALD TiO_2, ZnO and Ga-doped ZnO to form pn-junctions. The samples showed only weakly rectifying behaviour which was attributed to short-circuits between the n-type layers and the back contact. Several of the samples did show some difference in electrical response when under illumination indicating that, at least in some parts of the device, the pn-junction had formed.

Lastly the growth and characterisation of ALD Ga-doped ZnO was investigated to determine the optimal doping levels for the growth of highly conductive and transparent oxides, to be used as a front contact for photovoltaic devices. It was found that Ga doping at around 1at% in ZnO produced film with the lowest resistivity. CdTe films were then grown onto substrates coated in 1at% Ga-doped ZnO and subjected to AM1.5 photovoltaic IV testing, yielding photovoltaic cells with conversion efficiencies ~10.8% and fill-factors of ~65%.

1 Introduction

Research and funding for renewable energy sources has increased worldwide in the past few decades. With around $5.5x10^8$ TWh/year available from the sun at the Earth's surface, and current world energy use at around 40,000 TWh/year [(1)], solar power alone can theoretically provide for all of the world's energy needs. The International Energy Agency (IEA) gives values for electricity production of around 21,000 TWh for 2010. Renewable resources, i.e. geothermal, solar, wind and biofuels account for just 3.7% of this total or ~780 TWh. This figure has been increasing year upon year. The data for 1973 shows 0.6% or 36TWh renewable electricity production from a total of ~6,000 TWh [(2)].

A major part of this thesis was the synthesis and characterization of nanostructures and nanostructured surfaces which would be used for the production of thin film and nanostructured photovoltaic devices. Two materials were studied extensively, aluminium and copper.

Aluminium oxide is a wide band-gap insulator which can be grown from aluminium metal by many different techniques. In this case, electrolysis was used to produce highly uniform, porous nanotube arrays within thick (relatively speaking) aluminium oxide plates. In terms of photovoltaic devices, these were to be used as a scaffold material onto which functional oxides could be grown, as the aluminium oxide itself was far too insulating and thick to be used as one of the functional layers.

Copper was also of interest as its oxides, primarily cuprite and tenorite, could be processed into a wide variety of different types of nanostructure through various different types of oxide growth. Both of these oxides also exhibit naturally occurring p-type conduction, making them potential candidates for one of the functional layers in p-n solar devices.

The following literature review covers the growth of nanostructures and nanostructured surfaces in both aluminium oxide (p. 7) and copper oxide (p. 32) including current theories governing the growth mechanisms, current and future uses of these materials and state of the art research around the world. Theory and practice of Atomic Layer Deposition (ALD) is covered along with comparisons with other thin film growth techniques (p. 44). The final section in the literature review looks at semiconductor materials theory, relating to n and p type materials and junctions, Transparent Conductive Oxides (TCOs) and photovoltaic devices (p. 54).

Section 3 in this thesis covers the experimental techniques and equipment that were used in the experimental sections (p. 77).

Sections 4 - 6 cover experimental work conducted for this thesis. The first of the experimental sections covers the growth and characterisation of porous anodised aluminium oxide, beginning with two possible uses for the material as a scaffold structure for a high p-n junction area photovoltaic device (p. 87). In the first experiment (p. 92) the growth rate of Anodised Aluminium Oxide (AAO) in oxalic acid is determined following work by other research groups. Following this, the effect on the hexagonal pore arrangement from changing the duration of the primary anodisation as part of a two-step anodisation process is investigated (p. 98).

The production of AAO templates was found to be fairly labour intensive, especially when using the two-step process. Because of this pre-made through-hole AAO templates were purchased and used as scaffold material for the deposition of titanium dioxide via ALD. The next experiment (p. 108) used standard ALD deposition parameters to deposit material onto AAO templates and planar Si wafers. EDX and SEM imaging were used to assess the success of the deposition. Very little growth of TiO_2 was observed within the AAO structure which led to the next experiment (p. 124). In this experiment, increased exposure times of

precursor gases were used to allow more material to deposit on the AAO pore walls deep with the templates. This approach was found to be successful but with the drawback of vastly increased growth times. Because of this, an alternative approach, using p-type copper oxides as the starting substrate material was investigated. The initial experiment with this material looked at methods of producing a repeatable, uniform surface from the copper sheet by the application of various cleaning treatments (p. 131). In the next experiment, cleaned Cu foil was anodised to produce a porous oxide surface which could be potentially used as a substrate for ALD of n-type layers forming an active p-n junction (p. 138). Due to probable stagnation effects in the electrolyte caused by the particular experimental set up used, the oxides grown were determined to be of insufficient uniformity and porosity for further growth work without a major redesign of the anodisation equipment. Focus was switched to the thermal oxidation of copper as a method for the production a uniform p-type oxide layer. In the next experiment (p. 149) Cu sheet was thermally oxidised at different temperatures and durations to determine a suitable growth regime and growth rate for future deposition work. It was found that under certain growth conditions copper oxide nanowires could be grown. As this was in keeping with the nanostructured theme of this thesis, the mechanism behind the growth of these structures was investigated further (p. 163). Some problems were encountered due to the fragility of the thermally grown oxides leading to additional experiments to see if it was possible to cleanly remove large sections of oxide from the substrate by the introduction of a thin alumina barrier layer prior to oxidation (p. 186). It was found that the barrier layer actually improved the stability of the oxide allowing larger sections to be retained on the copper substrate. Due to the relatively high electrical resistance of the CuO nanowires, an experiment was carried out to see if it was possible to thermally reduce the nanowires into the more useful Cu_2O, whilst still retaining the nanostructured surface (p. 200). The next experiment returned to using the anodised copper nanostructured substrates in

conjunction with ALD of TiO_2 (p. 206) to produce an active p-n junction which would be used for photovoltaic testing. This study also tested methods of electronically isolating each of the active layers to avoid short circuit paths and enhance the efficiency of any subsequent photovoltaic devices. These devices were then tested using bespoke photovoltaic testing apparatus (p. 216). Additional development work was carried out regarding ALD grown transparent conductive oxides for use in CdTe-based photovoltaic devices as these would be an important part of any solar power cell (p. 232). Because these films were produced with ALD, they could then be used in future work in combination with the nanostructured surfaces developed earlier in this thesis. Finally, in section 7 (p. 243), possible directions for further experiments are outlined.

2 Literature Review

2.1 Nanostructures and Nanostructured Surfaces

2.1.1 Anodised Aluminium Oxide

Anodised under the correct conditions, aluminium and several other metals form a thick porous oxide layer comprised of a very high density of nanometre diameter pores perpendicular to the original material surface. Through careful control of the anodisation, these pores can form a hexagonally close-packed arrangement with near identical geometries. The choice of anodisation parameters allows templates to be grown with tunable pore diameters (from 6nm to 500nm [3, 4, 5, 6]), porosities (from 1% to >15% [7, 8]) and aspect ratios (>1000 [9]). Additional chemical treatments can then be used to further tune the parameters of the templates. This facile and well understood control, as well as their inherent temperature and chemical stability, makes them ideally suited for the production of nano-structured devices. A wide variety of materials can be deposited via a range of deposition processes to build up electronically active layers for use in functional devices.

Anodised aluminium oxide (AAO) templates, also referred to by various researchers as porous anodic alumina (PAA), porous alumina membranes (PAM), porous aluminium oxide (PAO), anodic porous alumina (APA) and Alumite, have been studied extensively since their discovery in 1941 by J.D. Edwards and F. Keller[10]. A second paper in 1953 was devoted to characterising the nature of the porous oxide and the parameters affecting its growth[11]. This is regarded by many as the start of this field of research.

AAO templates are characterised by a high density of up to $10^{12}/cm^2$ of near parallel, nanometre scale pores perpendicular to the oxide surface[12]. The oxide itself can be several hundred microns thick[13], leading to structures with the potential for extremely high aspect ratios of over 10^3 [9]. One of the main benefits of using these templates/membranes is that

the geometrical parameters of the oxide can be easily tuned through the appropriate choice of electrolyte and anodisation voltage[9], with pore diameters ranging from 6nm[14] to 500nm[9] reported in the literature to date. Another advantage of this oxide, especially when utilised as a template for the deposition of other materials, is that due to the particular nature of the growth of the oxide, under certain conditions pores can arrange themselves into a regular hexagonal array with a tightly defined spacing[15]. This feature makes them ideally suited to the production of high density vertically aligned nanowires (NWs) and nanotubes (NTs).

2.1.1.1 Barrier layer oxide and nano-porous oxide

Anodisation has been used for many decades as a method of improving the corrosion properties, wear resistance and aesthetic appearance[16] of aluminium. While investigating the effect of different electrolytes used during the anodisation process, Keller *et al*. (1941) discovered a low current efficiency regime that occurs when using sulphuric, oxalic and phosphoric acids[10,11]. When anodised in near-neutral electrolytes and at current efficiencies above 60%, (for example boric or malonic acids[17]), barrier layer oxide is formed. Prior to anodisation, the aluminium surface has a native oxide several nm thick[18] that is formed rapidly upon contact with atmospheric oxygen. During anodisation, electrons from the cathode cause the disassociation of the acidic species making up the electrolyte, forming O^{2-} and OH^{-} anions. These travel to the anode, i.e. the oxide/electrolyte interface under the influence of the electric field in the cell. At this interface, the electric field causes the dissolution of Al^{3+} ions, which migrate towards the cathode. O^{2-} and OH^{-} ions pass through the oxide layer interacting with Al^{3+} ions throughout the oxide, producing new Al_2O_3.

A study by Thompson using inert xenon markers showed that normal, barrier type alumina films grow by the simultaneous ingress of O^{2-} and OH^{-} from the electrolyte and the egress of

Al^{3+}. As the xenon markers moved little relative to each other, it was taken that growth occurs at both the film/electrolyte interface and the film/substrate interface, as opposed to within the bulk of the alumina. The driving force for this type of oxide growth was found to be high field ionic conduction, which obeyed the equation $i = A\exp^{(BE)}$; i = anodic current density, A and B = temperature dependant constants, E = field strength ($E = \Delta V/x$; ΔV = potential drop across oxide film, x = film thickness) [19]. The major difference between barrier layer and porous growth is that for the former Al^{3+} ions reaching the electrolyte/oxide interface contribute to oxide growth, whereas in the case of porous growth Al^{3+} ions are dissolved into the electrolyte[15].

2.1.1.2 AAO Growth Mechanisms

The proposed mechanism for the formation of AAO is that a critical current density exists for each pH of electrolyte below which oxide formation at the oxide/electrolyte interface does not occur, meaning that the voids resulting from the loss of Al^{3+} ions to the electrolyte are not filled by new oxide (Figure 1). The changes in geometry caused by these embryonic pores increase the local electric field strength and also locally decrease the resistance of the oxide directly underneath the embryonic pores, allowing current and hence ionic species to transverse the oxide barrier layer with greater ease at these locations. The result of this is that Al^{3+} ions are ejected from the oxide surface at preferential sites, i.e. the embryonic pores, so a self-reinforcing system is set up with areas that have lost Al^{3+} ions concentrating the local field strength and reducing the localised resistance as anions from the electrolyte have less far to travel. The penetration paths develop and continue to penetrate deeper into the oxide layer. To begin with, even for a well polished aluminium surface, pores initiate at any geometrical irregularity that is capable of producing an above average local electric field. This gives rise to an irregular pore arrangement[19].

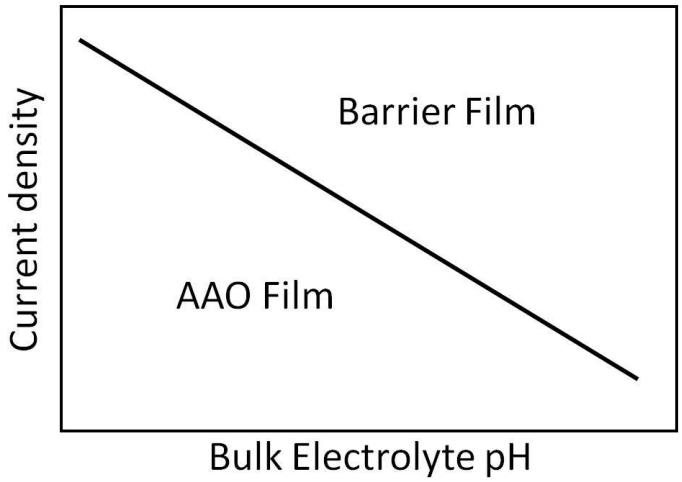

Figure 1: Relationship between electrolyte pH and current density for barrier or porous-type anodic alumina formation[19].

After the initial few seconds of anodisation the embryonic pores approach the metal/oxide interface. A barrier layer of oxide separates the electrolyte from the metal. All new oxide growth occurs within this barrier oxide with positive ions dissolving from its surface, i.e. at the pore-base/electrolyte interface. Because the Pilling-Bedworth ratio of alumina on aluminium is around 1.28[20], a compressive strain field exists within the oxide as it is produced. Where the strain fields underneath adjacent pores meet, oxide is pushed upwards causing the average oxide thickness to increase whilst the barrier layer at the base of the pores remains at a steady thickness. This theory is backed up by results from Houser and Hebert[21] in an experiment in which tungsten tracers were implanted into the barrier layer oxide prior to anodisation. Oxides that were cross-sectioned after differing lengths of anodisation showed the W markers travelling from the base of the barrier layer and up the centres of the pore walls. A viscous flow model was proposed by the group was found to fit well with experimental data. The driving force for the flow was thought to be localised joule heating in the barrier layer which would decrease the viscosity, along with the strains produced from the volumetric mismatch between the oxide and the metal.

Jessensky *et al*.[15] proposed a model by which the pores are able to move relative to one another during the anodisation due to mechanical strain caused by the volumetric

expansion of the oxide. Repulsive forces in the barrier layer oxide between pores caused by oxide formation across the entire oxide/metal interface result in the vertical growth of oxide where the strain fields meet. This model was used to explain the observed regular scalloped appearance of the metal/oxide interface that can be seen when the oxide is removed from the metal substrate.

Another model based on the interaction of electric fields between neighbouring pores was also proposed by Su and Zhou to explain the motion of the pores[22]. Cross sectional images of the porous oxide at the oxide/metal interface show that the barrier layer of oxide at the pore bases is slightly larger than half the minimum wall thickness between adjacent pores. The wall thickness can be related to the barrier layer thickness and the spherical angle by the equation:

$$w_t = 2b_t sin(\theta)$$

Where b_t = barrier layer thickness (m) and 2θ is the spherical angle of lines joining the peaks of the metal/oxide interface and passing through the intersection of the pore base and the pore walls at the oxide/electrolyte interface (Figure 2).

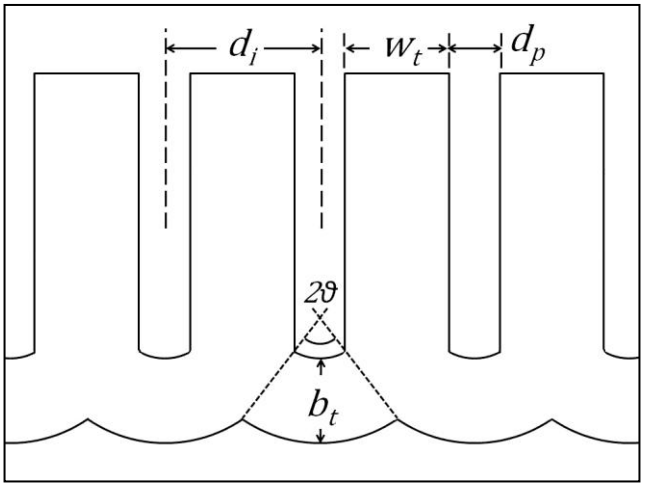

Figure 2: Cross section of ideal structure for a completely ordered porous oxide

Where two pores are separated by a larger than average distance, i.e. when the thickness of the oxide between the two pores is greater than $2b_t sin(\theta)$, dissolution of the oxide

from the pore walls is increased on neighbouring surfaces. In this way, the pores migrate towards each other as the anodisation progresses. Similarly, when the thickness of the oxide between two adjacent pores is less than $2b_t sin(\theta)$, dissolution of the oxide on the neighbouring surfaces is reduced allowing a higher proportion of the vertically ejected oxide to be retained, effectively increasing the distance between the pore centres. When the thickness of oxide between two adjacent pores is equal to $2b_t sin(\theta)$ then an equilibrium exists between the pores and the two will remain separated by this distance.

M. Curioni *et al.* conducted a study investigating the nature of the barrier layer formed in AAO via *in situ* electrochemical impedance spectroscopy[17]. Several important conclusions of the study were given; the barrier layer oxide formed at the base of each pore could be represented by a metal-p-i-n junction (where p means p-type, i means intrinsic type and n means n-type semiconductor behaviour), transport of Al^{3+} and O^{2-} ions across the oxide determines the growth rate of the barrier layer, the composition of the electrolyte controls the ejection of barrier layer oxide that goes on to form the pore walls via modification of its mechanical properties, and that the rate of ejection of oxide modulates ionic conduction by determining the current flow and hence the barrier layer growth rate (Figure 3).

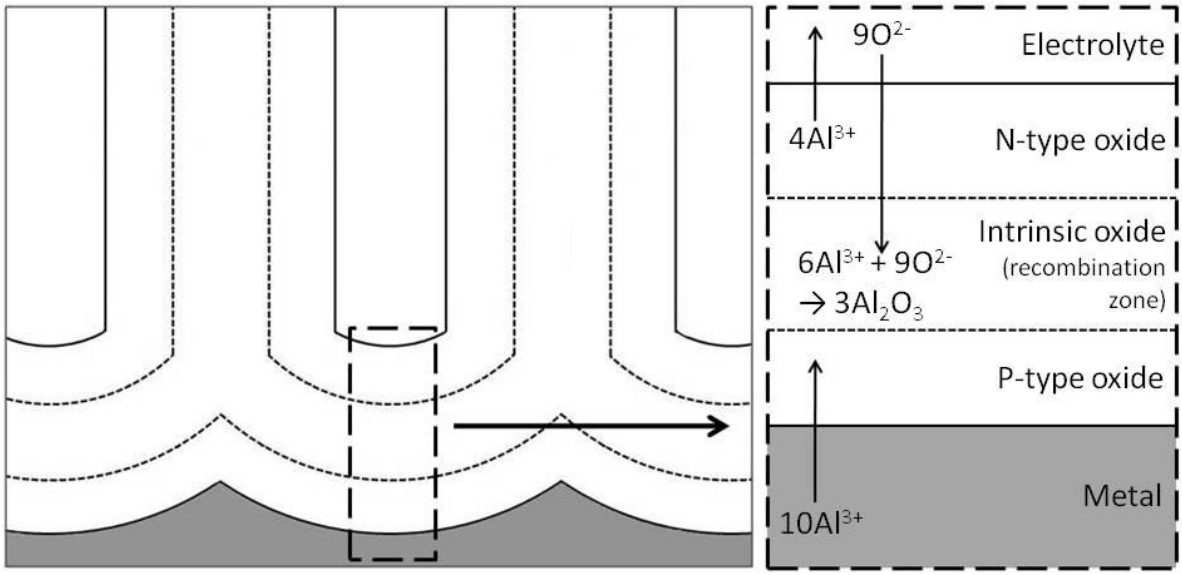

Figure 3: Schematic view of the m-p-i-n junction structure of the barrier layer in AAO[17].

2.1.1.3 AAO Current Profiles

The current profiles seen for the potentiostatic anodisation of aluminium show a pattern that can be used to assess whether a porous layer has been produced or not. The profile can be divided into three distinct stages, each reflecting a change in the processes occurring (Figure 4).

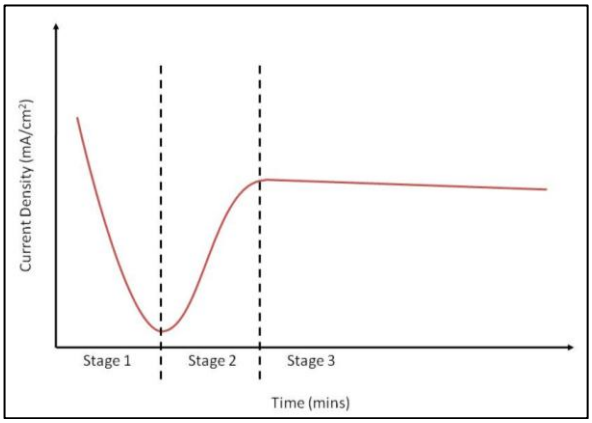

Figure 4: Schematic current profile for potentiostatic anodisation of aluminium

In the initial stage the current starts out at a maximum value and decreases. This occurs due to an overall increase in the resistance of the cell caused by a thickening of the native oxide layer. At the same time penetration paths begin to form at the oxide/electrolyte interface. These develop through the oxide layer quicker than the oxide is thickening. The reduced resistance of the oxide directly underneath each embryonic pore begins to alter the flow of charged species from passing through the oxide relatively uniformly to preferentially passing through the oxide at the base of each pore. The current density moving through the cell therefore appears to reduce, when in fact it is increasing at the base of each pore. The localised current density at the base of each pore can be approximated by:

$$I_{td} = I/(D_p \alpha).$$

Where I_{td} = True current density, summed across all pore bases (mA/cm^2), I = current (mA), D_p = pore density ($number/cm^2$) and $\alpha = \frac{\pi}{2\sqrt{3}}\left(\frac{d_p}{d_i}\right)^2$ = Keller porosity[11].

Before the penetration paths have reached an equilibrium distance from the aluminium substrate most, if not all of the current is passed through the pores concentrating the formation of oxide at the pore bases. As the penetration paths approach an equilibrium distance from the underlying metal, the resistance of the cell starts to decrease. The second stage seen in the current profile is an increase in the current density which reaches a maximum when the pore bases are at the equilibrium distance from the metal. At this point all oxide growth occurs beneath the base of each pore.

The third and final stage of the current profile is a near steady-state regime. Oxide is formed underneath each pore and ejected upwards where the strain and electrical fields of adjacent pores meet. Current is passed down the length of each pore via the electrolyte. As the pores deepen over the remaining duration of the anodisation the current drops slightly from its initial value. This could be a result of an increase on the relative viscosity of the electrolyte molecules as they are forced to travel further down the lengths of the narrow pores. Should this be the case it would manifest itself as a larger drop in current for narrower (higher aspect ratio) pores compared to wider ones.

2.1.1.4 Standard AAO Production Parameters

For use in a particular application, e.g. membrane filters with specific pore size or as a scaffold template for the growth of specific diameter NWs, a wide range of pore sizes can be achieved by choosing an appropriate electrolyte and voltage system. To begin with, samples are degreased and electropolished using a perchloric acid solution. For a small-medium interpore spacing, 0.3M (1.7wt%) sulphuric acid can be used with voltages ranging from 19-70V, giving interpore spacings of 50-140nm. Within this range 0.3M (2.7wt%) oxalic acid can also be used at 40V to give pore spacings of around 100nm. For larger pore spacings and pore diameters 1.1M (10wt%) phosphoric acid is used at between 160-195V. This gives pores with spacings of 405-500nm[(9)]. The electrolyte temperature is usually kept

static via a cooling circuit between 0°C and room temperature. A pore widening treatment can be used after the anodisation to increase the porosity of the sample; This is usually achieved by immersion of the sample in 5wt% phosphoric acid at room temperature for 10-30 minutes[23, 24], with the duration of the reaction controlling the degree of pore widening. Over-exposure to the acid can be used to produce ordered arrays of vertically aligned alumina nanowires as the acid etches away the walls between adjacent pores and leaves the thicker oxide found at the intersection of three neighbouring pores[25, 26]. The porous oxide grows linearly with time with typical growth rates of between 1 and 8µm/hour[8,14, 27, 28, 29,30].

2.1.1.5 Self-ordering of pores in AAO

For each electrolyte there exists an ideal voltage range in which a single anodisation of several hours will produce a porous structure with long range hexagonal ordering[31]. Using sulphuric acid it has been found that this self-ordering occurs at 25-27V, corresponding to an interpore spacing of around 60-70nm [32]. Aluminium anodised in oxalic acid at 40V showed self-ordering with an interpore spacing of roughly 100nm [33]. Aluminium anodised in phosphoric acid at 195V also showed this effect, producing a regular porous structure with an interpore spacing of approximately 500nm [6]. For both self-ordered and amorphous regimes it has been shown that a linear relationship exists between the interpore spacing and the applied voltage with a constant value of around 2.5nm/V [32], regardless of the electrolyte used.

Nielsch et al observed that the value of d_p/d_i remained constant for each electrolyte within the self-ordering regime, and that this value gave a porosity of around 10%. Both the barrier layer thickness at the pore bases and the interpore spacing are a function of the anodisation voltage used, and with the constant value of d_p/d_i required for self ordering, the group proposed the equation:

$U = \sqrt{\frac{2\pi}{\sqrt{3}\alpha}\frac{d_p}{2k}}$, where k = the interpore spacing proportionality constant of 2.5nm/V, α = 10% porosity, and U = the voltage required to achieve self-ordering. In other words, by knowing the pore diameter (d_p) that a specific pH of electrolyte will produce, this equation yields the correct anodisation voltage to observe self-ordering [34].

2.1.1.6 Alternative growth methods for AAO

2.1.1.6.1 Two-step Anodisation

For certain applications it is necessary to produce AAO templates with long range ordered pores. Several methods exist to enable this. One way of doing this is to perform a two-step anodisation. This involves performing a primary anodisation step to produce a sacrificial porous oxide layer. The oxide is then dissolved using an appropriate acid. Due to the effects mentioned previously, i.e. the motion of the pore bases due to increased oxide viscosity, interaction of neighbouring strain fields and the interaction of neighbouring electrical fields, the aluminium surface is left with partial spherical indents, with each individual indent corresponding to the barrier layer base of each pore. For a sufficiently long single step anodisation, the majority of indents will have been able to reach an equilibrium spacing relative to their neighbours. The aluminium is then anodised a second time, using the same voltage and electrolyte to ensure that the pore spacing is kept constant. A single penetration path is initiated in each indent left after the first anodisation, the raised edges of which act to concentrate the local electric field. As the spacing of the indents has already reached near-equilibrium for the particular voltage-electrolyte combination there is very little driving force to cause further horizontal motion of the pore bases. This gives rise to very straight pores with uniform spacing (Figure 5).

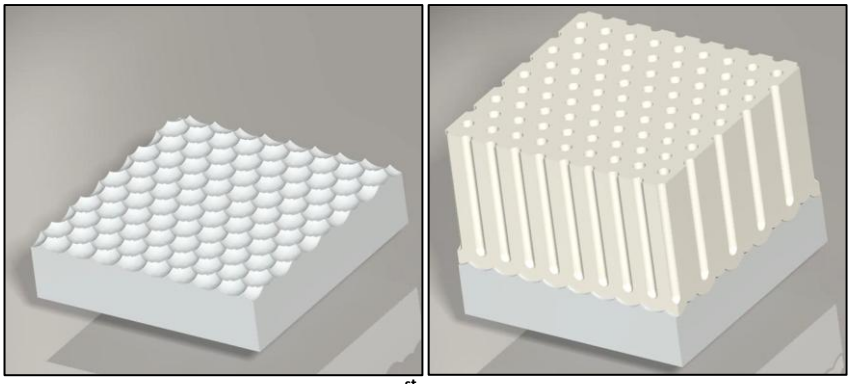

Figure 5: Left – Aluminium surface after removal of 1st-step oxide. Right – Ordered AAO grown during 2nd-step anodisation.

One drawback with this method is that it can be difficult to create ordered pore domains larger than a few microns in diameter. During the 1st-step, pores initiate at the substrate surface near simultaneously. As the growth commences and the pore bases start to move relative to each other areas of hexagonally arranged pore bases appear, with the neighbouring hexagonal domains (HDs) either changing smoothly from one orientation to another or changing abruptly. Boundaries between HDs show an increased number of 7, 5 and 4 coordinated pores which in turn gives an interpore spacing which deviates from the average. The orientation of the underlying aluminium crystals has only a minor effect on the orientation of the HDs produced. Beck and Petrikowski found that the regularity of the hexagonal pores was related to the fraction of (100) oriented planes[35]. If this is the case for a particular HD, then its boundaries will correspond to some degree with the grain boundaries of the underlying crystal. Another implication of this is that any treatment, such as an annealing step, which could increase the area of (100) oriented planes at the surface prior to anodisation will produce larger HDs.

As the anodisation proceeds, it has been shown that the average HD area increases[33]. This happens via a process akin to grain growth in annealed crystals, with larger domains consuming their smaller neighbour. The major difference between the two processes is that the growth of HDs proceeds much more slowly[32], and as such using long 1st-step anodisation times is not regarded as an effective method for obtaining long range ordered

templates. Li et al proposed that a linear relationship exists between the average domain size and the anodisation time and the temperature of the anodisation [36]. However, Nielsch et al. applied the addendum that this only holds up to a critical time, whereby further anodisation goes on to increase the disorder of the pore arrangement. This was found to be because for long anodisation durations the increasing aspect ratio of the pores as they lengthen begins to limit diffusion of fresh acidic species to the pore bases, altering the pH and thus changing the growth conditions [34].

To increase the pore ordering and reduce the process duration the two-step anodisation process outlined above was developed by Masuda and Satoh in 1996[37]. After a 10h primary anodisation in 0.3M oxalic acid at 40V and 17°C the resultant porous oxide was removed by immersion in a mixture of 6wt% phosphoric acid and 1.8wt% chromic acid for 14h at 60°C. The second anodisation was conducted using the same parameters as the first for 5mins yielding a highly ordered porous oxide structure.

Nasirpouri *et al.* recently investigated the effect that 3-step anodisations have on the ordered structure of AAO[12]. It was found that larger HDs could be produced for a 3-step anodisation of the same total duration as a 2-step anodisation. Also, the size distribution of pore diameters and pore spacings was found to be narrower for 3-step anodisations. The drawbacks to using such a technique are increased handling of samples between steps (to remove the oxide layer) and higher consumable material use.

2.1.1.6.2 **Through-hole AAO**

In recent years AAO templates have been increasingly used as nano-porous filters for solvent cleaning, biological filtration, and metallic/semiconductor NW production applications. Several companies now supply pre-made through-hole AAO of various pore diameters and thicknesses. Yuan *et al.* described a simple process for the production of through-hole AAO[38]. High purity Al foil was degreased using acetone in conjunction with

ultrasonic cleaning. The sample surface was then etched using 0.3M/l NaOH. A two step anodisation was conducted in 0.5M/l oxalic acid at voltages between 20-80V using the standard phosphoric and chromic acid solution to remove the oxide after the first step. To remove the resultant porous oxide the sample was set as the anode in a 1:1 (by volume) solution of $HClO_4$ (72% w/w) and $(CH_3CO)_2$ (98%). A 3 second anodisation at 5V above the two-step anodisation voltage caused the immediate detachment of the porous oxide from the Al_2O_3 barrier layer hemispheres and the Al substrate. One of the main advantages of this technique over other methods of creating through-hole AAO, i.e. dissolving the Al substrate and chemically etching away the barrier layer with phosphoric acid, is that the solution used does not attack the pore walls causing them to widen, thus introducing additional uncertainty into the actual pore width or the possibility of over exposing the template causing the pore walls to breakdown.

2.1.1.6.3 **Pre-patterned AAO**

Pre-patterning of the aluminium prior to anodisation can remove the requirement for a second anodisation step whilst giving additional levels of control over the resultant pore morphology[32]. A high-hardness material, usually SiC[39] or SiN[40], is prepared using standard lithography techniques to produce a surface of regularly spaced nanometre-scale convexes. A mechanical press is then used to indent the convex pattern onto the aluminium sample using high pressures of around 100kg/cm^2 or more[39, 40]. The resulting concave structures act as initiation points for embryonic pores by virtue of the electrical field concentration caused by their geometry. By tailoring the spacing of the convexes with regard to the selected anodisation parameters and sought after pore arrangement, once the anodisation is started there is little driving force to cause the rearrangement of the pores through the interaction of neighbouring strain/electrical fields. Several advantages can be gained by using this technique; highly ordered pore structures with pore diameters and spacings outside of the normal range of self-organisation can be produced, alternative

pore structures can also be produced other than the hexagonal structure favoured by standard anodisation. Using this method, square and triangular arrays have been produced by Masuda and co-workers[39].

2.1.1.6.4 **Enhanced Growth Rate AAO**

Whether using standard single-step anodisation, two-step anodisation or pre-patterning, one major drawback limiting the commercial uptake of ordered AAO for the production of usable devices is the slow oxide growth rate. Several groups have attempted to address this issue by modifying the normal parameters used. One such improvement is the use of hard anodisation (HA) parameters. As well as significantly improving the growth rate of the oxide, pore spacings of 220-300nm can be achieved. These values are between the ranges of pore spacings obtainable using normal parameters outlined previously. By using 0.3M oxalic acid with much higher voltages than normal (120-150V compared to ~40V), a new self-ordering regime was found with oxide growth rates of between 50-70μm/hour[9]. To prevent dielectric breakdown of the oxide layer under the influence of the increased potential drop, the group grew a layer of oxide at least 400nm thick in the same electrolyte under mild anodisation (MA) conditions (40V for 5-10mins). Once this protective layer was in place the voltage was slowly increased to the HA conditions.

As an alternative to HA, the growth rate of the oxide can be improved by increasing the conductance of the electrolyte. Salerno *et al.* used oxalic acid under MA conditions to achieve growth rates of around 60μm/hour by using either 1-Butyl-3-methylimidazolium 2-(2-methoxyethoxy) ethyl sulphate or 1-Butyl-3-methylimidazolium tetrafluoborate in a 1:1 ratio with the acid. The oxides produced showed partial ordering after a single anodisation with the potential for increased ordering after a two-step anodisation process[41].

2.1.1.6.5 **AAO with Modified Pore Structures**

Several microelectronic devices can be fabricated from arrays of nanowires produced by the deposition of various materials into AAO templates. Since the properties of the devices come partly from the materials used and partly from the geometry of the nanowire arrays, methods of precisely controlling the NW geometry allow a much wider range of devices and device properties to be engineered. Other possible applications such as molecular filtration devices can be made directly from the AAO templates themselves, providing that the structure of the pores is well controlled. In recent years, several research groups have reported methods that allow for the precise control of the AAO pore geometries.

W. Lee *et al.* described a method of producing diameter modulated AAO pores using a mixture of mild and hard anodisation parameters. Using a pre-patterned aluminium substrate with 275nm interpore spacing, MA was applied in 4wt% phosphoric acid for several minutes to initiate pore growth. The anodisation was conducted at 110V. For mild anodisation in H_3PO_4 this voltage corresponds to the interpore spacing of ~275nm, although it is well outside the normal self-ordering range for this acid, hence the use of an imprinting stamp. Following this, HA was carried out at 137V in 0.015M oxalic acid, again corresponding to an interpore spacing of ~275nm. These two anodisation steps were repeated several times. Because of the difference in oxide porosity produced by MA and HA in acids of these concentrations (~3% and ~10%, respectively) this yielded highly ordered pores showing clear segments with alternating pore diameters[(9)].

Using the previous method required a time consuming changeover of electrolyte to enable the pore morphology to be controlled. Further work by W. Lee *et al.* resulted in the discovery that pulsed current anodisation of aluminium in an H_2SO_4 electrolyte could be used to produce similar structures without the requirement of different electrolytes for the MA and HA parts of the anodisation. MA was carried out at 25V for 180s followed by HA at

35V for 0.1s. Both processes were carried out at 1°C. The same process was also found to work with oxalic acid, but only at higher electrolyte temperatures. In this case, MA was conducted at 40V and HA was conducted at 53V. By performing several of these anodisation cycles, AAO templates with multiple pore diameter modulations could be built up. The alumina formed during the two different anodisation types showed different mechanical properties. Oxide formed by MA is denser and contains fewer defects than that formed by HA. One result of this is that the group were able to preferentially etch away the HA sections of the oxide whilst leaving the MA oxide forming very thin, porous lamina structures. This was done with 5wt% phosphoric acid at 45°C [(42)].

Further development in the control of AAO pore structure was demonstrated by Losic *et al.* to address a limitation of previous approaches which only controlled the diameter of the pores and not the geometry of the pore structures[(43)]. By introducing a Transitional Anodisation (TA) step between the MA and HA steps during an anodisation, the rate of change from one pore diameter to the other could be affected, effectively giving control of the vertical curvature of the structure. This was done by a gradual increase in voltage and current across a single cycle (Figure 6). This approach was tested in phosphoric, oxalic and sulphuric acid electrolytes. It was found that the method worked for all three electrolyte systems. The group postulated that the structures were formed due to a change in curvature of the barrier layer base of each pore between MA and HA conditions, with the curvature decreasing as the current approached HA conditions.

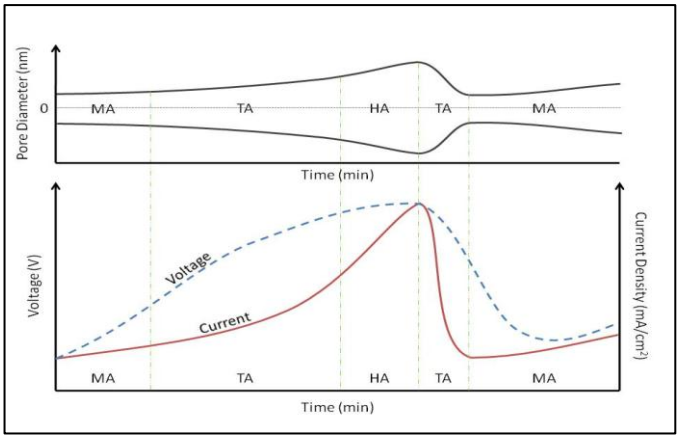

Figure 6: Top: Profile of the structural modification of one pore during a single anodisation cycle. Bottom: Schematic representation of a single cycle used in cyclic anodisation. Adapted from ref 43.

2.1.1.7 Metrology of AAO Templates

Methods of quantifying the quality of AAO templates, particularly the degree to which the pore arrangement deviates from a perfect hexagonally close packed structure, are necessary to assess the success of different template production techniques. This is especially important for macro-scale devices that require the nano-scale structure to exist over large distances, such as magnetic recording media. Furthermore, any deviation from the regular structure is likely to result in an increase in the average pore spacing. For applications that require high surface area, such as catalysis, this deviation could result in a reduction in surface area. The quality of the pores themselves is also an important factor. Techniques to quantify the level of defects in the bulk of the AAO such as misalignment of individual pores, number and size of voids, impurity levels and the number of branched structures are also necessary to gauge how well a particular device application will function.

Mátéfi-Tempfli *et al.* proposed a method to quantify the degree of pore ordering for AAO templates. Following SEM imaging of the template surface, image analysis software such as ImageJ[44] or IgorPro is used to isolate the coordinates of the pore centres. Delauney tessellation is then carried out on the coordinates, either within the image analysis program or using a program such as MatLab. This gives a triangular grid with the vertices centred on each pore. The distance between vertices can then be measured for each edge. Averaging

these distances gives the average interpore spacing. A histogram plot of the frequency of lengths was used to quantify the distribution of interpore distances. For their analysis, the group excluded triangles with edge lengths and internal angles that fell outside 10% of the average values. To assess the total ordering of the template the ratio of [area of triangles – excluded triangular area]/[total triangle area] was calculated. Values approaching unity indicated a highly ordered triangular, and hence hexagonal, array[45].

2.1.1.8 Porous Oxide Growth in Other Metal-Electrolyte Systems

Porous oxide growth under anodising conditions has been shown to occur in several other metal-oxide systems. There are several prerequisites for porous oxide growth to enable the production of similar structures to those seen in AAO.

- Oxide growth should occur at or just above the metal-oxide interface and not at the oxide-electrolyte interface.
- Ionic species from the electrolyte should be capable of diffusing through the formed oxide.
- The PBR of the oxide should be above 1, providing a compressive strain field to allow self ordering of the metal-oxide interface. The electrolyte should be capable of electric-field enhanced dissolution of the oxide, and dissolution should occur at a high enough rate to ensure that the nascent pores formed by the vertical ejection of oxide are not filled[22].

Other metals that have shown porous oxide growth include Hf, Zr, Nb, Ta, W and Ti[22]. With all of these other systems, fluorine anions are a required part of the electrolyte as they increase the oxide dissolution rate and the current flow to levels that avoid barrier layer oxide growth[22, 46, 47, 48, 49]. For the anodisation of Ti, Su and Zhou used an ethylene glycol based electrolyte containing 0.3wt% NH_4F and 2wt% H_2O. The anodisation was carried out at 60V and 15°C for 20-1200 minutes[22]. Noticeable differences exist between AAO and

anodised titanium oxide (ATO): With ATO, the oxide is produced as close packed, hexagonally arranged titanium dioxide nanotubes. This has been attributed to the formation of titanium oxide hydroxide ($H_2Ti_3O_7$) at the oxide-metal interface which is then ejected vertically between adjacent pores. The hydroxide becomes dehydrated forming lower volume β-TiO_2. This process separates adjoining pores forming nanotubes[22].

For the other metal oxide systems mentioned above, research seen so far has not shown evidence of self-ordering of the pore structures. Hafnium anodised in 1M H_2SO_4 with 0.2wt% NaF at voltages between 10 and 60V showed fairly disordered pore arrangement, similar to that seen for AAO after a single anodisation outside of the self-ordering regime. It was found that the pore diameters increased with increasing voltage at roughly 1.5nm/V [46]. Sieber *et al*. formed Nb_2O_5 with pore diameters of 20-30nm via anodisation in 1M H_2SO_4 with varying low levels of HF (0.5-2wt%) at 20V [48]. Again, this technique formed a porous oxide layer with little pore ordering. Similar results have been seen in the anodic anodisation of tungsten[49] and alloyed TiAl[47].

2.1.1.9 Applications of AAO Templates

AAO templates can be used for many diverse applications due to the ease at which the porous structure can be controlled. Several current and future applications are listed below:

2.1.1.9.1 Photonic Crystals

Photonic crystals are able to interact with electromagnetic waves in ways dictated by the specific periodic nature of features that make up the bulk or surface material. One key aspect of these devices is that the period of the structures is of the same magnitude as half the wavelength of light with which it interacts[50]. By assembling repeating structures made from different materials with a sufficiently large difference in dielectric constants it is possible to engineer photonic band gaps into the device which display unique light

propagation properties[32]. Since the periodicity of AAO pores can be tuned to almost any value between 4nm and 500nm, the structures can interact with electromagnetic wavelengths of around 8nm to 1µm (low energy x-rays through to infrared, including visible light). Additionally, by depositing multiple layers of alternating, different dielectric materials, structures with much smaller features can be produced (i.e. composite NWs). These give the potential to manipulate even higher energy electromagnetic waves.

2.1.1.9.2 **Nano-composite Structures**

It is possible to produce multi-material nanowire and nanotube arrays using a wide variety of deposition/plating technologies for a wide range of device applications[32].

Wu *et al.* fabricated Zn, Co and Fe oxide nano-composite structures by immersion in an aqueous solution of 1:2:1 molar ratio $Zn(NO_3)_2$, $Co(NO_3)_2$ and $Fe(NO_3)_3$. The templates were then dried and annealed in a muffle furnace at 500°C. TEM, SEM, SAED, EDS and XRD were used to analyse the resultant structures. The results indicated that zinc oxide and iron oxide formed a solid solution with Co^{2+} and Co^{3+} ions present. Suggested applications of these devices were in microwave absorbing devices or as catalysts for synthesising carbon NTs[51].

Han *et al.* used electrophoretic (EP) deposition to coat the upper surface of an AAO structure with Ga-doped ZnO, giving an Al-AAO-ZnO composite device. Conflict between the requirements for a conductive material for EP-deposition and an insulator substrate for the gas sensing application mean that AAO is one of the few substrates that can be used in this approach. The electric field from the Al base permeating through the oxide allowed the Ga-doped ZnO suspension to be deposited, while using a thick enough AAO layer (>80µm) stopped any potential short-circuiting of the gas sensing layer when in use. The sensor showed a significant change of resistance when exposed to change in the concentration of formaldehyde gas. Compared to other gas sensors prepared using EP deposition, this device showed higher sensitivity. This was attributed to the removal of a high temperature anneal

required for previous devices which caused the Ga-doped ZnO to increase in grain size, reducing the effectiveness of the devices[52].

2.1.1.9.3 **Two-step Replication**

Several down-sides exist that limit the use of AAO as a functional material. These include low conductivity, high brittleness and low chemical stability in certain environments. One way of avoiding these drawbacks whilst retaining the highly ordered structure is to use the template as a starting point for a two-step replication process. Typically, a polymer negative of the AAO is created and is used as a scaffold for the electrochemical or electroless deposition of pure metals or semiconductors. By this route a wide variety of materials can be manufactured to display the same periodic nano-structure as the original AAO template[32].

2.1.1.9.4 **Nano-dot Arrays**

Through hole AAO can be used as a mask for the deposition of nano-dot arrays[32]. A line-of-sight deposition process is used with a piece of AAO attached to a substrate. Masuda and Satoh used vacuum evaporation of gold to deposit orderly 40nm diameter Au nano-dots on a Si substrate[37]. This was done to reduce the high equipment cost associated with the production of nano-dot arrays made by electron beam lithography. Short anodisation times to create the AAO were used as it was important to limit the thickness of the template due to an increased chance of defects (y-junctions, non-parallel pores, etc.). High density ordered arrays of Au dots, approximately 1.2 x 10^{10} cm^{-2} were produced over several cm^2. By tailoring the AAO growth regime the diameter, density and spacing of the nano-dots can be controlled with relative ease. The nano-dot height was controlled by the duration of the vacuum evaporation.

Bennett *et al.* recently demonstrated the use of through-hole AAO as an etch mask in the creation of GaMnAs semiconductor nano-dots[53]. MBE was used to grow a 10nm buffer

layer of GaAs on an oxide-desorbed, semi-insulating GaAs substrate at 580°C. A 15nm epitaxial layer of $Ga_{0.93}Mn_{0.07}As$ was then grown over the buffer layer and annealed in air at 230°C. 35-40nm of Cr was deposited by thermal vacuum evaporation. The Cr nano-dots left after the dissolution of the AAO template served as a mask during a subsequent plasma etch step. The semiconductor material remaining was then tested for its magnetic properties using a Superconducting Quantum Interference Device (SQUID). It was found that the array showed an easy magnetisation axis across the surface (radially to the nano-dots) and a hard axis perpendicular to the surface. In the radial direction (easy axis) super-paramagnetism was observed with a blocking temperature of 30 K.

2.1.1.9.5 **LCD Displays**

Hong *et al.* recently demonstrated the use of AAO as an alignment layer in Liquid Crystal Displays (LCD). Using a two-step fabrication process, AAO was grown onto a pair of glass substrates coated in ITO, Ti and Al. By the end of the second anodisation the AAO layer had become highly transparent. Mylar spacers on top of the AAO created a cavity when the two substrates were sandwiched together which was filled with the liquid crystal. Optical measurements using visible light (300-800nm) revealed that the device had a transmittance of around 40%. The threshold voltage of the LCD was found to be around 2.2 V_{rms}, and the typical response time of the LCD was 62.5 ms, as driven with a square waveform and an amplitude 3 V_{rms} [(54)].

2.1.1.9.6 **Magnetic Memory**

Several groups have recently been investigating the application of AAO to the next generation of magnetic and flash memory devices[(32)]. Materials and structures that display magnetic anisotropy allow devices to be built with a higher density of bits. Another advantage is that mistakes in reading and writing can be reduced by limiting the influence of surrounding magnetic domains when performing read/write operations[(55)].

Huang *et al.* fabricated an Si-SiO_2-Al_2O_3-SiO_2 (OAO) triple layer stack to compare performance against a conventional Si-SiO_2-Si_3N_4-SiO_2 (ONO). It was found that OAO stack showed a better charge trapping ability, a larger shift of threshold voltage and decreased effective charge density[56].

Zhao *et al.* report using atmospheric CVD over AAO templates to produce dense arrays of CrO_2 NWs. The group found marked anisotropy in the magnetic properties of the NW arrays, with the coercivity of the array parallel to the wires (320 Oe) greater than 6 times that of the perpendicular direction. It was also found that when using CVD the depth of penetration of the CrO_2 NWs was inversely proportional to the pore diameter with 40nm, 75nm and 100nm diameter pores having CrO_2 deposition depths of 6µm, 1.5µm and ~200nm respectively. This effect was attributed to sublimed CrO_3 depositing on the pore openings and quickly sealing them off. At the template temperatures used this formed a mixed oxide liquid phase which was able to penetrate deeper into the pores under capillary action until the pressure within the base of the pore was high enough to resist further ingress of the liquid[57].

Metzger *et al.*[27] and Bao *et al.*[58] used AC electrodeposition to create 65-750nm long polycrystalline Fe and Co NWs in disordered and ordered AAO templates. The group found that the squareness of the hysteresis loops was dependent on the wire length; shorter wires showed less anisotropy and a lower squareness in the direction parallel to the wires. In the direction perpendicular to the NWs there was a slight difference in the coercivity with shorter NWs having a larger coercivity, and only slightly below that of the parallel direction. The deposited wires also showed a large variation in length between pores, with the Fe NWs ranged from 160nm to 520nm while the Co NWs ranged from around 700nm to 1.65µm.

2.1.1.9.7 **Catalysis**

For a given size of AAO, a significant increase in surface area can be achieved by the introduction of the porous structure. Coating this in an appropriate material using thin film deposition processes can yield a rigid membrane structure able to facilitate liquid and gas phase reactions that require a catalyst to lower the activation energy of the reaction. Although the surface area to weight ratio is not as high as that of nanometre diameter powder catalysts, the rigidity offered by the supporting AAO template could increase the range of devices that can be produced. Other advantages of thin film coated AAO templates over fine powder catalysts include no agglomeration of catalyst material, reducing the available surface area and no loss of catalyst material due to flow of the chemical reactants and products.

Using Atomic Layer Deposition, Pellin *et al.* deposited several different thin film materials on to highly ordered through-hole AAO templates. Deposited oxides included Al_2O_3, TiO_2, ZnO, V_2O_5, and Pd. To test the catalytic behaviour of the coated membranes compared to conventional high surface area γ-Al_2O_3 powder catalysts, AAO templates with 40nm diameter pores were fabricated and coated with 1 and 15nm of Al_2O_3 by ALD. This left the templates with 38nm and 10nm diameter pores, respectively. A monolayer of vanadium oxide was then impregnated onto the surface of the AAO. The γ-Al_2O_3 powder was impregnated with 20 wt% V_2O_5/Al_2O_3. The oxidative dehydrogenation of cyclohexane (C_6H_{12}) was studied to determine the selectivity of the catalysts, determined by the relative production of cyclohexene (C_6H_{10}), cyclohexadiene (C_6H_8) and the unwanted by-product benzene (C_6H_6). It was found that the selectivity of both AAO templates was much higher than that of the γ-Al_2O_3 powder, with the larger pore template showing the best selectivity, producing higher proportions of C_6H_{10} and C_6H_8. At increased reaction temperatures the yield of products increased but at a cost of reduced selectivity for all samples tested[(59)].

Tacchini *et al.* produced TiO_2 nanotubes in an AAO template using a variety of titanium precursors. Each precursor was cooled until solid when an AAO template was placed on its surface. The chamber was then evacuated and the precursor allowed to warm past the solid-liquid transition temperature. Once this temperature had been reached, the pressure drop encouraged the precursor liquid to enter and fill the porous structure of the templates. After removal from the vacuum chamber the upper and lower surfaces of the templates were wiped clean and the templates were baked in an O_2 atmosphere to oxidise and solidify the nanostructures. The Alumina templates were then dissolved in phosphoric and chromic acid leaving an array of TiO_2 nanostructures. The resultant structures were tested for their photocatalytic ability to breakdown methylene blue dye, compared to commercially available high surface area anatase powder. This work was conducted to address known problems with recovery of the powder catalysts for reuse in further catalysis reactions. It was found that anatase nanotubes created from Ti-isopropoxide precursor had higher photocatalytic activity than those produced from other precursors (Ti-propoxide, Ti-butoxide and $TiCl_4$) but lower activity than the commercial anatase powder. The disadvantages due to lower activity, i.e. reduced degradation of the methylene blue dye, were offset by the ease of recovery of the templates compared to the powders for their use in further catalytic reactions[60].

2.1.2 Copper Oxide Nanostructures

The properties of copper oxides have been studied extensively by the scientific community and a wealth of data is available regarding the growth of the different oxides and their properties (electrical, mechanical, thermal, etc.). Several oxides of copper exist; CuO (Tenorite), Cu_2O (Cuprite) and $Cu^{1+}{}_2Cu^{2+}{}_2O_3$ (Paramelaconite). Of these oxides, the ones of interest for the production and manufacture of functional devices are cuprite and tenorite.

2.1.2.1 Cuprite (Cu_2O)

Cuprite is well known in the scientific literature as a p-type oxide with a direct band gap of around 2.17eV and a cubic crystal structure with a space group of O_h^4 = pn3m [61, 62]. Visually speaking, this form of copper oxide has a red appearance. The p-type nature of this oxide is thought to derive from a departure from the stoichiometric oxide structure [63], due to a naturally occurring metal deficiency (or possibly a surplus of interstitial oxygen ions) providing holes in the valence band. Using calculations from first principles, Raebiger et al. found that the p-type nature of Cu_2O was majoritively due to Cu ion vacancies and that stable concentrations of Cu vacancies can reach up to 10^{20} cm^{-3}, yielding hole concentrations of around 10^{18} cm^{-3} [64].

2.1.2.1.1 Applications of Cu_2O

Cu_2O is used in a wide range of electronic and photochemical devices because of its band-gap, intrinsic p-type nature, ease of fabrication and low cost. Described below are a few examples of current uses of Cu_2O.

Li et al. fabricated $Cu_2O/Cu/TiO_2$ nanotube heterojunction arrays from Cu/Cu_2O nanoparticles and anodised TiO_2 nanowires. These were used to promote the photocatalysis of water at the liquid/device interface to produce H_2 gas under illumination of visible light. The group found that in comparison with previously made Cu_2O/TiO_2

photocatalytic structures the H_2 production rate was increased due to an increased light absorption range induced by the surface plasmon response of the Cu/Cu_2O interface [65].

Using similar techniques, many other groups have used Cu_2O for the production of hydrogen via photocatalysis of water under UV irradiation. Depositing the p-type Cu_2O onto n-type nanostructured materials such as TiO_2 [66], ZnO [67] and Si [68], typically by wet deposition methods, these groups were able to optimise the photocatalytic activity of the devices by tuning the geometrical properties of the substrate nanostructures.

Liu et al. deposited graphene sheets onto nanocubes of Cu_2O producing electrochemical sensors to detect glucose and hydrogen peroxide. Cu_2O nanocube powder was synthesised via the reduction of aqueous $Cu(OH)_4$. The addition of graphene oxide in the solution resulted in a coating of graphene over the Cu_2O nanocubes which in turn increased the sensitivity of the devices and prolonged their lifetime[69].

Jiang et al. produced a Cu_2O homojunction structure and using two electrodeposition steps deposited both n-type and p-type copper oxide onto FTO. This device was tested for its ability to sense acetaldehyde and other gases at different concentrations in air. Surface Photovoltage (SPV) measurements using a chopped light source at 532nm and 405nm and a lock-in amplifier showed that these devices could achieve high sensitivity for the detection of acetaldehyde at room temperature [70].

Lv et al. produced magnetron sputtered n-ZnO/i-ZnO/p-Cu_2O heterojunction PV devices using the insulating ZnO layer to attempt to reduce leakage current. The group investigated the effect of different thicknesses of i-ZnO and what effects this had on the resulting device characteristics measured without illumination. The active layers were deposited onto indium-zinc oxide (IZO)/glass substrates and electrical contacts were made using metallic indium. It was found that for increasing the i-ZnO thickness from 0nm to 200nm in 50nm

increments, the leakage current improved significantly. The I-V characteristics for the 0nm i-ZnO device showed very high leakage and did not display the expected rectifying behaviour. For higher thicknesses rectifying behaviour was observed along with increasing threshold voltage, from around 0.5V to 0.9V for 100nm and 200nm i-ZnO layers. The Ideallity factor for the dark curves was found to increase from 3.6 to 8.9 with increasing thickness, where and ideallity factor of 1-2 is considered optimal [71,72].

Nam et al. constructed Cu_2O based thin-film transistors using RF sputtering to deposit varying thicknesses of Cu_2O on to p-type Si substrates. The Cu_2O layer formed the active channel, the Si substrate and SiO_2 dielectric acted as the gate whilst the source and drain were formed from Ni top contacts. The group found that an optimal Cu_2O layer thickness of 45nm resulted in the best transfer function. For thinner layers it was found that the on current was quite low whilst for thicker layers the turn-on voltage increased and a subthreshold slope hump appeared [73].

2.1.2.1.2 **Electronic Properties of Cu_2O**

Cu_2O has several advantageous properties when considering applications such as photovoltaics or photocatalysis. Various values within a relatively large range have been measured for the bandgap of Cu_2O, produced by numerous different methods, usually between 1.7eV and 2.6eV [72,73]. Most commonly the bandgap is quoted as around 2.1eV. This corresponds to a wavelength of ~590nm, allowing the material to absorb radiation at this or higher energies, and to use this energy to promote electrons to a useable state in the conduction band. Essentially this means that the material is well suited to absorption of a large portion of the visible light spectrum (from green down to UV). Several other electronic properties play an important role in the application of this material in energy generation settings, the resistivity (comprised of the minority carrier diffusion length, mobility and concentration), and the optical absorption properties. Gupta et al. give the

absorption coefficient as ~10^5cm^{-1} [72], but a more detailed analysis by Malerba et al. gives the extinction coefficients (related to the absorption coefficient by $\alpha = (4\pi k)/\lambda$, where α = absorption coefficient, k = extinction coefficient and λ = wavelength[74]) for bulk and thin film Cu_2O at different wavelengths and substrate temperatures [75]. In their paper they list the extinction coefficients of the material for light with wavelengths of 250nm to 2.5µm, part of which is shown below in Figure 7.

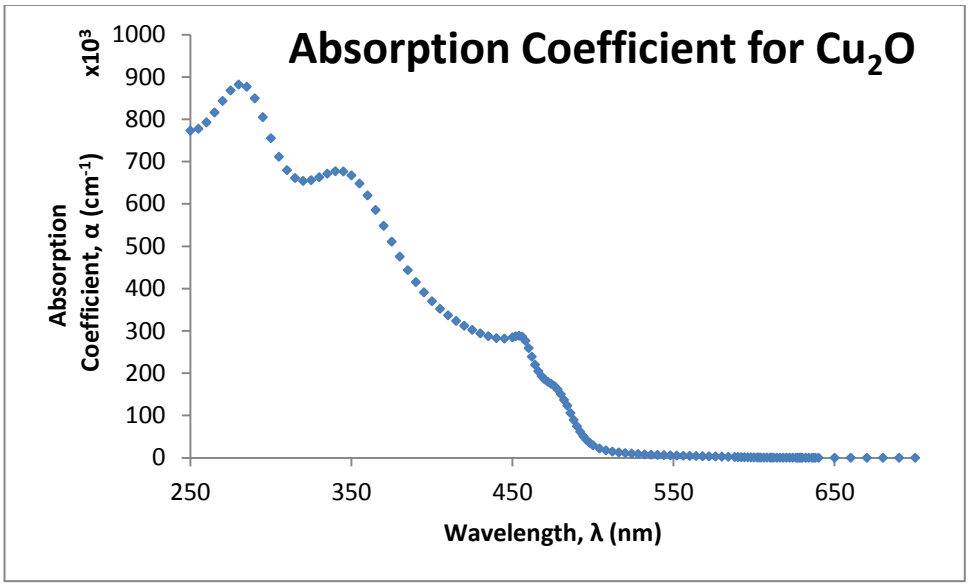

Figure 7: Absorption Coefficient for Cu_2O, calculated from ref 75.

The mobilities, carrier concentrations and diffusion lengths for Cu_2O vary quite significantly depending on the growth method and particular growth parameters. Typical values for the mobility are around 1-10 cm^2/Vs [76], although some growth methods can yield higher values in the 50-90 cm^2/Vs range [72,73]. Carrier concentrations can also vary significantly, 10^{16} cm^{-3}was reported by Munos-Rojas et al. for thin films grown by fast atmospheric ALD [76], while for Cu_2O grown by electrodeposition Jiang et al. reported values of between 6.7x10^{15}cm^{-3} and 7.9x10^{17}cm^{-3} depending on the pH of the deposition process [77]. The minority carrier lifetime (related to the minority carrier diffusion length, the diffusivity and the recombination rate) also plays an important role in assessing the performance of this material in energy generation applications. Bhattacharyya et al. give the lifetimes of carrier in sputtered Cu_2O at ~250ns [78]. Values for the minority carrier diffusion length also vary

significantly, with Gupta et al. reporting ~3.5µm [72], Dimitriadis reporting between 1µm and 4µm [79], and Sculfort et al. reporting lengths of 0.5µm [80]. As these widely varying values indicate, the electrical properties of Cu_2O are highly dependent on the methods and growth conditions used to produce the oxide.

2.1.2.2 Tenorite (CuO)

Tenorite is a black/grey p-type semiconducting oxide with a direct band gap of around 1.2eV to 1.4eV. In a similar manner to Cuprite, it has been reported that the origin of p-type conduction in this oxide is due to the presence of negatively charged copper vacancies [81]. The crystallographic form of the oxide is monoclinic with a space group of C2/c.

2.1.2.2.1 Applications of CuO

Recently, Lee et al. used CuO to modify electrospun TiO_2 nanofibres and investigated their use in the photocatalytic splitting of H_2 from H_2O. By modifying the ratio of Cu to Ti in the initial electrospinning setup and also changing the post-growth calcination temperatures, the group were able to optimise the catalysis of H_2O. They found that the CuO modified fibres showed an increase in the amount of H_2 produced from a H_2O-ethanol mixture compared to TiO_2 fibres and that the samples made with 6mol% Cu and calcinated at 450°C produced the most H_2 [82].

Gao et al. produced p-CuO/n-Si photovoltaic devices by reactive magnetron sputtering. ~100nm of CuO was sputtered on to cleaned Si<100> wafers from a Cu target while the O_2:Ar flow ratio was varied. The group found that the hole concentration and the mobility changed from ~$9x10^{15}cm^{-3}$ and $0.05cm^2Vs^{-1}$ to <$1x10^{15}cm^{-3}$ and ~$0.4cm^2Vs^{-1}$ with increasing partial pressure of O_2. In analysing the PV devices produced the group found that an O_2:Ar ratio of 1:1 produced the best devices giving a power conversion efficiency of 0.41% and a fill factor of 0.2 [83].

Nagaraju et al. produced p-n junctions utilising CuO and ZnO as the p- and n-type materials, respectively, on cellulose paper fibre bundles by hydrothermal synthesis. These simple devices showed rectifying behaviour with a turn-on voltage of 0.93V. Devices such as these could lead to cheap, flexible and disposable paper/fibre based electronics [84].

Additional uses include solar energy conversion [83,85], gas sensing [86], cold field emission devices [87,88] and batteries [89].

2.1.2.2.2 **Electronic Properties of CuO**

As with Cu_2O, the electronic and opto-electronic properties of CuO vary over quite a wide range in the literature due to variations in production and processing parameters. While investigating the growth of different types of CuO nanostructures for their properties as bacteriacides, Karunakaran et al. found that the conductivity of CuO grown by various means ranged from 0.0021μSm^{-1} to 0.4μSm^{-1} (0.3GΩm to 2.3MΩm). The authors proposed that this variation was due to crystalline defects away from the stoichiometric ideal increasing the conductivity of the samples. A decrease in the presence of these defects led to an increase in the resistivity [90]. Gopalakrishna et al. used spray pyrolysis to deposit CuO films on to glass substrates. The grown films showed resistivities ranging from 0.05Ωcm to 4.0Ωcm, mobilities between 3$cm^2V^{-1}s^{-1}$ down to ~0$cm^2V^{-1}s^{-1}$ and carrier concentrations greater than $10^{18}cm^{-3}$. Interestingly, for the films grown, it seemed as though treatments to increase the carrier concentration also served to reduce the mobility [91]. CuO films grown by Jundale et al by a sol-gel method from cupric acetate powder unusually showed n-type properties (indicative of oxygen vacancies), with resistivities around 1MΩcm, carrier concentrations ~$10^{19}cm^{-3}$ and mobilities ~$10^{-5}cm^2V^{-1}s^{-1}$ [92].

Bandgap energies (indirect) for CuO range from ~1eV up to 1.9eV depending on growth conditions [93,94]. CuO films grown by anodic electrodeposition and analysed at Toyohashi University of Technology showed p-type conductivity, resistivity of 2.2x10^5Ωcm, bandgap of

1.46eV and an absorption coefficient of $1.3x10^{4}cm^{-1}$. After annealing in air at 500°C the resistivity reduced significantly to 3.3Ωcm, the absorption coefficient increased to $2.2x10^{4}cm^{-1}$ and the bandgap shifted to 1.35eV. Carrier concentrations and mobilities of the films were found to be $4.4x10^{13}cm^{-3}$ and $1.1cm^{2}V^{-1}s^{-1}$.

2.1.2.3 Thermal Growth of Copper Oxides

Examination of the copper-oxygen phase diagram shows the Cu oxides formed as molten copper solidifies for different weight percentages of oxygen (Figure 8). For oxygen levels of around 1.4%, the melt solidifies at around 1200°C, forming Cu_2O. At 1080°C α-Cu begins to form down to 375°C at which point the Cu_2O transforms to CuO [95]. This diagram indicates that CuO forms preferentially at low temperatures, while the formation of Cu_2O requires higher temperatures.

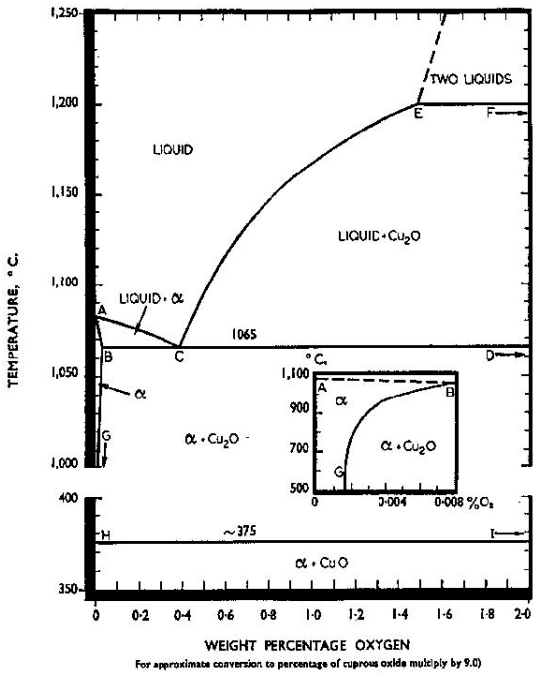

Figure 8: Copper-Oxygen equilibrium phase diagram [95].

2.1.2.3.1 Planar Growth

Xu et al. studied the effect of temperature on the oxidation of 99.9% Cu foil in humid, flowing air at 1 atmosphere pressure. It was found that the oxidation rate of the foil increased with increasing temperature. Three separate oxidation regimes were proposed

for low, medium and high temperature oxidation reactions. At low temperatures (up to 300°C) the oxidation occurred by a grain boundary diffusion process, resulting in sub-micron thickness Cu_2O and CuO layers. Between 300°C and 700°C sub-boundary diffusion (via lattice dislocations) was thought to be the dominant diffusion process and at 800°C and above, lattice (bulk) diffusion was taken to be dominant [96].

Experiments performed by Adegboyega et al. explored the electrical properties of Cu oxides fabricated at high temperatures. Samples were air annealed at between 750°C and 1020°C. Only the sample oxidised at 1020°C showed p-type behaviour under thermoelectric probe measurements. The absence of p-type conductivity for the other samples tested was attributed to the formation of CuO within and at the surface of the Cu_2O layer [97]. Further evidence of the p-type nature of Cu_2O was given by the production of a working Cu/Cu_2O photovoltaic cell with an open circuit voltage of 0.25-0.30V and a short circuit current density of 2.5-3.0 $mA.cm^{-2}$.

2.1.2.3.2 **CuO Nanowire Growth**

CuO nanowires can be grown on a copper substrate by a simple thermal oxidation treatment. Cu samples are heated in a normal atmosphere or a controlled oxygen environment to between 400°C and 600°C for a period of a few hours then allowed to furnace cool to room temperature. A multi-layered structure is formed consisting of the Cu substrate, a polycrystalline layer of columnar Cu_2O, a layer of polycrystalline columnar CuO and a final layer of closely packed vertically aligned CuO nanowires on the upper surface.

One theory for the growth of these nanowires is that strains build up in the planar oxide layers, firstly due to the volumetric change as the base metal oxidises to Cu_2O, and as the Cu_2O oxidises to CuO, then secondly due to the different coefficients of thermal expansion for each of the layers as the structure is cooled. These strains, along with the thermal

energy in the sample provide the activation energy to allow grain boundary diffusion of Cu ions to occur throughout each layer.

Several mechanisms have been proposed to explain the growth of these CuO nanowires, the most notable of which are stress induced formation, vapour-solid diffusion and short-circuit grain boundary diffusion. Recently work by Hansen et al. [98] and Mema et al. [99] have provided evidence supporting the case for growth by short-circuit grain boundary diffusion. As the sample is exposed to temperatures between 400°C and 700°C in an oxygen containing atmosphere, the exposed surfaces are oxidised to polycrystalline Cu_2O. Providing that the partial pressure of oxygen is high enough a second layer of CuO grows on the surface of the oxide. For a given O_2 partial pressure this layer remains at a constant thickness until the Cu substrate is consumed, at which point the Cu_2O is further oxidised to CuO. Cu ions migrate through the Cu_2O via grain boundary diffusion and react at the Cu_2O/CuO interface consuming oxygen ions and increasing the thickness of the Cu_2O layer. Simultaneously at the sample surface, migration of oxygen ions down through the oxide allows further oxidation, keeping the CuO layer at a near constant thickness.

If the Cu/Cu_2O and Cu_2O/CuO interfaces remain in good contact with one another throughout the oxidation, Cu ions can diffuse along the grain boundaries of both oxide layers to the surface. Here they react with atmospheric O_2 where the grain boundaries meet the upper surface of the sample, providing nucleation points for nanowire growth.

Once nucleated, the nanowires grow from the tip in a bi-crystal structure [98]. The grain boundary between the two crystals facilitates the transport of Cu ions from the substrate to the nanowire tip and allows the growth of the nanowire to continue.

Detailed parameters showing how to grow CuO nanowires are given by B. Hansen et al. [100]. In their paper the oxidation method is described as follows:

Samples were brought up to 500°C in either a pure O_2 or O_2-Ar mixed atmosphere with a heating rate of around 50°C/min. Samples were then held at this temperature for 150 minutes. Samples were then cooled (no cooling rate given) to room temperature in an inert atmosphere to prevent further oxidation.

Mema et al. describe a slightly different process:

Samples were heated to a temperature of 450°C in a pure O_2 atmosphere at 10°C/min and held for 30 minutes. The samples were then cooled to room temperature at the same rate under the same atmospheric conditions.

The growth mechanisms of CuO nanowires are explored in more detail in this document.

2.1.2.4 Anodic Oxidation of Copper Metal

Several groups worldwide have studied the electrochemical response of Cu foils when anodised in different electrolytes. Allam et al. performed experiments on the anodisation of Cu foil in aqueous and ethylene glycol electrolytes containing hydroxide, chloride and fluoride ions at room temperature. The resultant films were found to be dependent on the pH of the electrolyte, with electrolytes with pH<10 showing no growth at 10V. By increasing the pH of the electrolyte to above this value it was observed that a light blue precipitate was produced from the Cu surface which did not adhere to the Cu. SEM analysis of the precipitates retrieved from the solution showed that nanoribbons and nanoneedles of oxide had been produced. Further tests were conducted using NH_4Cl as an additive to the original H_2O + KOH electrolyte. SEM analysis of the anodised surface showed that the grown oxide was retained on the surface and that the morphology had changed to producing highly dense square section pillars of oxide across the surface, several hundred nanometres high and around 1µm across each side. In the presence of Cl^- ions the growth of the oxide film was found to be independent of the electrolyte pH. It was also noted that

when the KOH concentration was increased to 0.2M, the uniformity of the oxide across the surface changed, producing dendritic structures in localised regions of the surface. Further work was carried out on the anodisation process with NH_4Cl replaced with NH_4F. It was found than in H_2O + KOH + NH_4F electrolytes the grown oxide morphology was altered again, this time producing porous spheres of oxide approximately 1μm in diameter uniformly across the surface. The pores within each sphere appeared as sub-micron crescent shapes. Altering the composition of the electrolyte to ethylene glycol + KOH + NH_4F and increasing the anodisation voltage to 30V changed the surface structure to one comprised of a leaf-like surface. The pores of this surface bared a similarity to those seen in the aqueous electrolyte, with crescent-like pores produced [(101)].

Caballero-Briones et al. studied the anodisation of Cu foil in 0.1M NaOH aqueous electrolyte. After anodisation it was found that a Cu_2O film had been produced on the surface of the samples. AFM imaging showed that the grown films were dense, polycrystalline and had a difference in height between the highest and lowest points of around 140nm [(102)].

Another group studied the anodisation of Cu foil in H_2O. Singh et al. showed that during the anodisation two different processes occurred dependent on the duration of the anodisation. In the earlier stages of the anodisation (up to 30 minutes) the SEM results showed that nanothreads had formed on the surface and been lost as precipitates to the electrolyte. These threads were around 0.6 – 1.0μm in length and around 10 – 25nm in diameter. For longer durations (>30 minutes) it was found that the oxide lost to the electrolyte had changed to the production of nanowire structures. For all anodisations analysis of the Cu foil surface showed that oxide was being grown in the form of small, sub-micron cube-like structures of Cu_2O. The group also measured the band gap of the produced structures. It was found that the nanowires and nanothreads had higher band

gaps than seen for bulk Cu_2O (2.6eV c.f. 2.17eV for bulk Cu_2O). This was attributed to quantum size effects due to the restriction imposed by the near one-dimensional aspect of the structures [103].

2.2 Atomic layer deposition

Atomic layer deposition (ALD) is widely recognised to have been first developed by Suntola in the 1980s under the name Atomic Layer Epitaxy (ALE) to allow the controlled deposition of III-V and II-VI compounds for thin-film transistor (TFTs) device displays[104]. Compared to other deposition processes available at the time, ALE provided the ability to deposit conformal mono-layers of material at relatively low temperatures over non-planar surfaces without relying on line-of-sight deposition. Because of the inherently low deposition rate, ALE was not taken up for use in other applications. Recently however, due to the ever-continuing miniaturisation of microprocessors and digital memory in the semiconductor industry, ALD is finding multiple applications in the production of MOSFETs, CMOS, interconnects, MRAM, etc[105]. A report by BCC Research put the worldwide market for ALD in 2014 at around $978 million with an expected compound annual 5 year growth rate of over 35% [106].

2.2.1 ALD Theory

Atomic layer deposition uses a binary sequence of precursor gases to deposit thin layers of material on to a surface. The process utilises the surface chemistry reactions between the sample surface and the reactant species to limit the reaction in such a way that the precursors are only able to react with each other and the sample surface and not in the atmosphere above the sample. By repeating the sequence of precursor pulses conformal layers of solid material can be built up with thicknesses controlled by the number of cycles and not by the exposure time[104], as is characteristic of other deposition processes such as CVD and PVD. By using this method a high level of control can be achieved over the thickness of the deposit to sub-nanometre precision.

To begin with the reactor is heated to the required temperature and the first precursor is brought into the reactor chamber. For highly volatile precursors this can be achieved by

vapour draw; for lower volatility substances an inert carrier gas such as argon can be used via a bubbling or boost mechanism. The precursor molecules collide with all surfaces within the chamber as the gas passes through. Within a certain ranges of temperatures for the particular precursors and substrates used, the molecules will adsorb as a monolayer onto the exposed surfaces. If the surface temperature is too low, it is possible for condensation of the precursor to occur onto the exposed surfaces, giving a thickness of greater than one monolayer. Low temperature may also mean that the activation energy of a required reaction is not achieved. This would result in less than monolayer growth per cycle. For temperatures above the desired range for ALD, the activation energy required to sever the surface bonds may be reached, causing desorption of the molecules and leaving the surface with less than one monolayer thickness, i.e. patchy island-type growth. A second consequence of having an excessive reactor temperature is that the gas molecules in the reactor chamber might breakdown, depositing material onto all surfaces in a PVD reaction, increasing the growth rate to more than one monolayer per cycle (Figure 9).

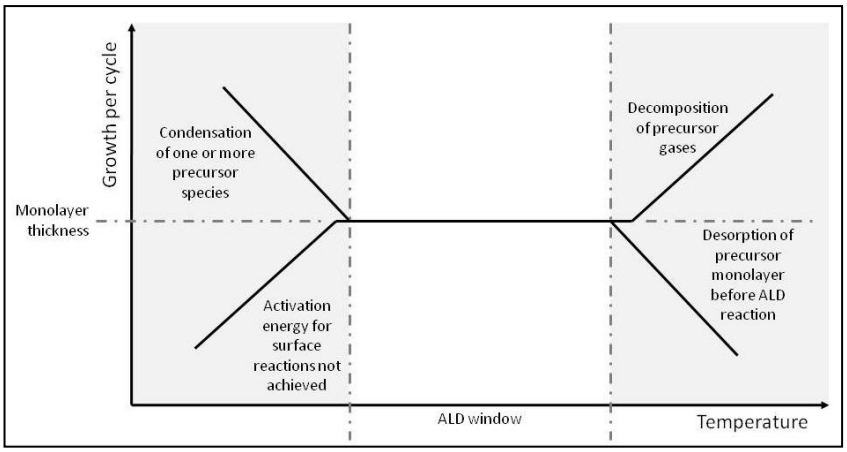

Figure 9: Temperature dependant growth window for ALD. Adapted from Ref 104.

Figure 10 shows a schematic diagram outlining the ALD process using the deposition of TiO2 from $TiCl_4$ and H_2O as an example. Once sufficient time for surface saturation to occur has been reached, flow of the first precursor is stopped and an inert purge gas is flowed through the reactor chamber. The purge gas clears the chamber of all precursor molecules

that have not adsorbed to any surfaces, leaving just a saturated monolayer of adsorbates. The second precursor gas is then introduced. As with the first precursor, the molecules of the second collide with all exposed surfaces. The precursors and reactor temperatures are chosen so that the necessary energies are available for a specific chemical reaction to take place when the second precursor comes into contact with the first. The unwanted products of the reaction, i.e. the chemical groups attached to the central atoms in the precursor molecules are returned to the gas phase and leave the chamber with the introduction of another purge gas step. With a sufficiently high number of precursor molecules and a high enough exposure for each precursor a monolayer of the desired material can be built up. Once the purge gas has removed the remaining second precursor along with all gas phase by-products the cycle is repeated. The newly deposited layer of material acts as a new solid surface for the adsorption of the first precursor molecules in the next cycle.

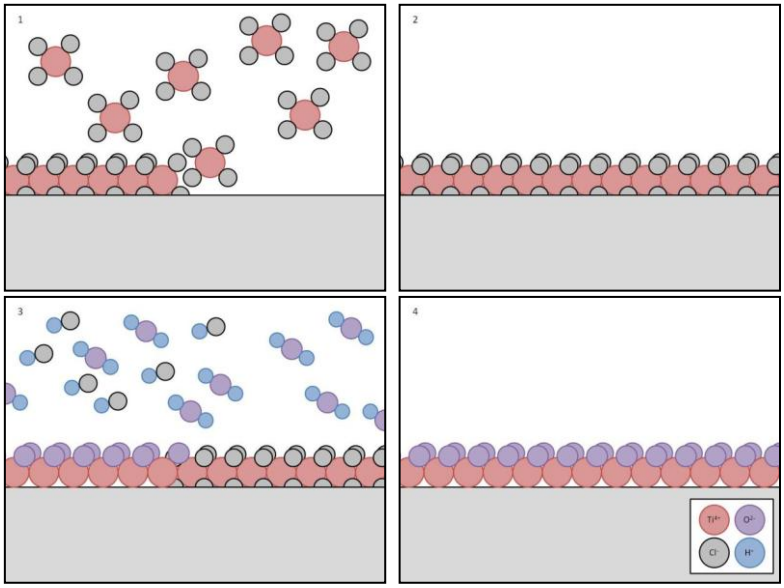

Figure 10: ALD of TiO_2 using $TiCl_4$ and H_2O precursors. 1) $TiCl_4$ gas is introduced into the reactor and adsorbs onto the sample surface. 2) The chamber is purged with Ar. 3) H_2O vapour is introduced into the chamber and reacts with the $TiCl_4$ to form TiO_2 on the sample surface. 4) HCl by products and unreacted H_2O are removed by a second Ar purge. The cycle is then repeated.

2.2.1.1 Requirements for successful ALD of Planar and Non-Planar Surfaces

One of the major advantages of ALD over other deposition techniques is that line-of-sight deposition is not required. This gives the ability to deposit conformal coatings over very

complex substrate geometries. To fully and evenly coat high aspect ratio structures, Gordon *et al.* proposed that several criteria must be met[107]:

1. Chemistry
2. Stoichiometry
3. Kinetics

2.2.1.1.1 ALD Surface Chemistry and Precursor Stiochiometry

For chemistry and stoichiometry a difference in surface geometries would have very little effect in governing the success of an ALD coating reaction. In terms of the chemistry requirement, the chemistry of the precursor materials and the surface chemistry of the substrate must be compatible with each other to produce self-limiting monolayer per cycle growth via alternating surface saturation of the precursor species[107]. For stoichiometry the number of precursor molecules introduced into the chamber with each step must exceed the number of available surface reaction sites. This includes all exposed surfaces that are at the required temperature within the reactor chamber as deposition will occur on all exposed surfaces[107]. For high surface area structures such as powders, trench or pore substrates, it is possible for relatively small samples to have a surface area equal to or larger than that of the rest of the reactor. The total combined surface area can in some cases exceed several m^2, requiring large precursor doses.

2.2.1.1.2 ALD Kinetics (Planar Surfaces)

For planar surfaces, monolayer coating of the substrate can be achieved with very short exposure times. This can be shown using kinetic gas theory. The flux of molecules on to a surface (number of molecules passing through a plane from one side) can be shown as[107]:

$$J = \frac{P}{\sqrt{2\pi mkT}}$$

Where J = flux ($s^{-1}m^{-2}$), P = partial pressure of precursor near the surface (Pa), m = molecular mass (kg), k = Boltzmann's constant ($1.38 \times 10^{-23}JK^{-1}$) and T = temperature (K).

The time required to achieve a saturation dose on a surface is given by:

$$t = \frac{S}{J} = \frac{S\sqrt{2\pi mkT}}{P}$$

Where t = time (s) and S = saturation dose (m^{-2}).

This can be rearranged to give the exposure required to coat a planar surface.

$$Pt = S\sqrt{2\pi mkT}$$

Where Pt = exposure ($Pa.s$). A more convenient unit of exposure is the non-S.I. unit the Langmuir (L), which is 10^{-6} $torr.s$ or 7500.6 $Pa.s$.

The above equation assumes a unity sticking coefficient of the precursor molecules on the substrate. The sticking coefficient for a particular precursor-substrate combination is determined by several parameters; the geometry of the surface site, the effect of neighbouring adsorbates, the velocity, angle and orientation of the incoming precursor molecule, the surface temperature and the reaction energetics of the contacting atoms. The sticking coefficient can be measured by carrying out a test deposition on the planar surface of a quartz crystal microbalance (QCM) within the ALD reactor, or by measuring the thickness profile of a multi-cycle deposition using a high surface area porous template with pore diameters smaller than the mean free path of the gas molecules at a particular temperature and pressure [108]. The exposure equation can be modified to include the effects of a non-unity sticking coefficient:

$$Pt = S_c S\sqrt{2\pi mkT}$$

Where S_c = sticking coefficient (no units).

2.2.1.1.3 **ALD Kinetics (Non-Planar Surfaces)**

For substrates with structural features much larger than the mean free path of the gas phase precursor molecules no modification of the above equation is required. For porous, trench or powder depositions in which the structural features are equal to or smaller than the mean free path, the exposure required for conformal coating is increased. For the porous structures that are the subject of this thesis, the pore diameters can be between 10 to 10^3 times smaller than the mean free path of the precursor molecules above the sample at typical reactor temperatures and pressures. The result of this is that within the pores, the number of collisions with the sample surface greatly outnumbers collisions between gas molecules. As pressure is simply a reflection of the number of collisions with a unit surface area per unit time, this effectively means that the pressure within the pores is much higher than the pressure within the rest of the chamber. As a consequence, models that assume Knudsen-type flow within the pores can be employed to accurately model the exposure times required for conformal coating [109].

Gordon *et al.* derived an equation for predicting the required minimum precursor exposure[107]:

$$Pt = S\sqrt{2\pi mkT}\left(1 + \frac{19a}{4} + \frac{3a^2}{2}\right)$$

Where a = aspect ratio of the pores = l/d_p. As before, this equation assumes that S_c = 1. Multiplying the right hand side by S_c would allow the equation to be used with different precursor/substrate combinations. For deposition thicknesses that are of a similar scale to the diameter of the pores, for example d_p < 20nm, it is likely that the deposition can noticeably alter the aspect ratio. To account for this, the authors suggested that the

minimum exposure should be calculated from the predicted aspect ratio at the end of the deposition cycle.

An alternative set of equations was developed by Elam *et al.*[109]. Monte Carlo simulations were found to agree well with experimental ALD of Al_2O_3, ZnO and SiO_2 onto through-hole AAO templates with pore diameters of 19, 47 and 65nm, and template thicknesses of 50µm. It should be noted that due to the use of through-hole templates deposition occurred from both sides of the template simultaneously, effectively meaning that the template thickness used in the calculation of minimum exposure times was 25µm.

$$\varepsilon = K\sqrt{t}$$

Where ε = integrated coverage (1 = full, conformal coating), t = time (s)

$$K = 2.1 \times 10^3 \frac{d_p\sqrt{P}}{lamu^{1/4}\sqrt{\tau}}$$

Where d_p = pore diameter (m), P = pressure ($torr$), l = pore depth (m), amu = mass of reactant molecule (amu) and τ = density of reactive sites ($10^{15} cm^{-2}$). Setting ε = 1 and converting to S.I. units gives:

$$Pt = 7.524 \times 10^{-11}\sqrt{m}\, S\left(\frac{h}{d_p}\right)^2$$

Elam *et al.* found that the sticking coefficient between the precursor molecules and the AAO substrate and the aspect ratio of the AAO template determined whether the deposition was diffusion limited or reaction limited[109]. For their analysis the diffusion coefficient was quantified by calculating the hopping coefficient based on a random-walk analysis. Via the Monte Carlo simulations it was found that if the sticking coefficient is much larger than the hopping coefficient then the deposition was diffusion limited, with reactive sites filling up in order starting with those at the pore entrance. This type of deposition

showed distinct boundaries between coated and uncoated areas within the pores. For this type of deposition regime it was found that ε was proportional to $\sqrt{t}$. Conversely, if the hopping coefficient was much larger than the sticking coefficient then the deposition was found to be reaction limited. For this type of deposition the reactive sites filled up randomly, giving even coverage throughout the length of the pores. For reaction limited deposition it was found that ε was proportional to t.

2.2.1.2 ALD Compared to Other Thin Film Deposition Techniques

ALD offers many unique benefits for thin film growth compared to other deposition processes. Pakkala and Putkonen list several of these[110]:

- High surface conformality: For the production of nano-structured materials the conformality offered by ALD is unsurpassed by any other deposition process.
- Pinhole free films: Due to the self-limiting, conformal nature of ALD films, the bottom-up growth method allows for uniform growth without pinhole defects, given sufficient exposure of precursors in each cycle. This makes it an ideal process for the growth of passivation barriers and insulators.
- Repeatability and Scalability: Self-limiting growth of the films, along with robust and well defined precursor chemistries allows growth to be achieved without the need for in-situ monitoring or prolonged operator supervision. Once the growth curves for a particular precursor combination have been obtained, scaling-up the process to an industrial level is relatively straightforward; a larger reactor space will undergo the same deposition as a smaller one, given the same process temperatures, exposure and precursor chemicals.
- Ultrathin films: Once surface saturation of the precursors has been achieved in a single cycle, no further growth can take place within normal ALD operating parameters. In this way dense, smooth, single atomic layers of material can be

deposited for use in semiconductor devices with nanometre-scale and possibly sub-nanometre scale features.

For the creation of nano-structured materials, deposition onto high aspect ratio or non-planar substrates, ALD is often the process of choice due to the extremely high level of control over the thickness of the deposited film and the unmatched conformality that can be achieved (Figure 11). An additional benefit of using ALD is the generally low temperature required for the deposition, enabling the process to be carried out on heat-sensitive devices.

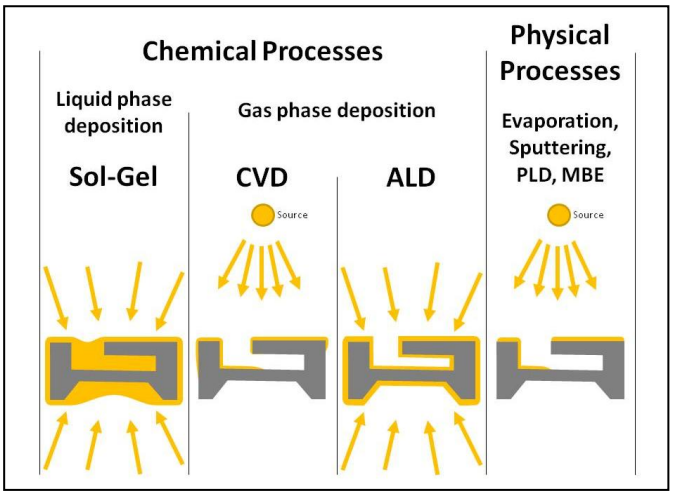

Figure 11: Comparison of different thin film deposition techniques (Adapted from ref 110)

2.2.1.3 Delta Doping in ALD films

Because of the self-limiting and cyclic nature of atomic layer deposition, controlled doping of thin films can be easily achieved by the inclusion of additional precursor gases within the ALD recipe. For example, the opto-electronic properties of ALD ZnO can be adapted to produce transparent conductive oxide (TCO) films by the addition of atoms such as P, Al, Ga, etc. For an undoped film, the growth recipe would typically follow an $(A\text{-}B)_n$ pattern, with A and B representing the first and second precursor pulses respectively, and n being the number of complete cycles. To introduce the dopant into the film this cycle could

become something along the lines of $((A\text{-}B)_n\text{-}C\text{-}B)_m$ or $((A\text{-}B)_n\text{-}C\text{-}D)_m$ where C and D represent different precursors.

The reason that doping of ALD films is desirable is that precise control of the electronic or optical properties of the films can be finely tuned to meet specific targets if the undoped films fail to meet either or both criteria. For example, Tynell et al. used Al and P substitutional doping of ZnO films to increase the n-type carrier concentration of the resultant films whilst leaving the optical transparency unaffected in the visible range. DEZ, TMA, TMP and H_2O precursors were used at deposition temperatures ranging from 160°C to 220°C. Films with dopant atomic percents from 0-5% were grown on glass substrates and measured by XRD, XRR, four-point probe and Seebeck coefficient measurements. The group found that the carrier concentration increased from ~$0.75x10^{18}cm^{-3}$ to ~$2.75x10^{18}cm^{-3}$ with increasing dopant concentration and that the results for both the P and the Al dopants were approximately the same [111]. As another example, Weinreich et al. created ZrO_2 thin films doped with Si and Al to inhibit the crystallisation of the ZrO_2 from the amorphous phase. The ZrO_2 was being proposed as the thin films insulator (around 10nm) in a metal-insulator-metal (MIMs) capacitor system for future DRAM applications. For this application, the structural properties and the surface roughness of the insulating film play a crucial part in the performance of any such devices, and in this case the addition of the dopant atoms in the centre of the films allowed the crystallisation temperature of the ZrO_2 to be increased. This meant that the films stayed in the amorphous or monoclinic phases even after subsequent annealing, these phases showing the most suitable properties for this application [112].

2.3 Semiconductor Materials Theory

2.3.1 Introduction

Semiconductors are a special type of material between the classification of conductors and insulators. In a conducting material, for example most pure metals at standard conditions, one or more of the valence electrons associated with each atomic nucleus are free to move from atom to atom. When the material is under no external influence these electrons move about randomly. With enough atoms, the movement of each electron is effectively neutralised by the movement of another electron within the material giving an overall net current across the material of zero. When an external influence is applied, for example the positive and negative terminals of a battery, these delocalised electrons allow current to flow. Electrons enter the material from the negative terminal, pass from atom to atom and exit the material at the positive terminal. Conductive materials are characterised by a very low resistivity of below 10^{-8} Ωm. At normal, everyday temperatures this resistivity is primarily caused by thermal vibrations in the positive ionic lattice (the ordered crystalline or polycrystalline structure comprised of the positively charged nuclei of the metal atoms).

Insulators are dielectric materials characterised by a high resistivity, beyond the order of around 10^{10} Ωm. This behaviour arises from the nature of chemical bonding in the material. In a solid insulator the valence electrons are tightly bonded to each atomic nucleus requiring a very high energy input to liberate them and allow even a limited amount of conduction. If these high energies are achieved it can result in permanent damage to the material as the chemical bonds that contained the now mobile electrons may break irreversibly in the process.

Between these two extremes are semiconductors, with resistivity's ranging from around 10^{6} to 10^{-5} Ωm. For current to flow in a semiconductor, charge carriers (either electrons,

holes or both) must be given enough energy to break free from the original host nucleus via promotion to an empty, energetically possible energy level [113].

2.3.2 Electronic Band Gaps

The Pauli exclusion principle states that no two identical fermions (electrons, protons, etc., i.e. any subatomic particle with half integer spin) can exist with the same quantum state simultaneously. Electrons orbiting a single atom can be described by four quantum numbers which describe the electron's quantum state; n, l, m_l, m_s. Each electron must have a discrete set of quantum numbers (Table 1). In the case of a single isolated atom, each pair of electrons (one spin up and one spin down) can only exist at specific allowable energy levels, separated from the other allowable energy levels by forbidden energies.

Table 1: Quantum Numbers

Name	Symbol	Description	Allowed Values
Principle Quantum Number	n	Shell	$1 \leq n$
Azimuthal Quantum Number	l	Subshell	$0 \leq l \leq n-1$
Magnetic Quantum Number	m_l	Energy Shift	$-l \leq m_l \leq l$
Spin Number	m_s	Electron Spin	-½,½

If an identical atom (of the same element and with the same number of electrons) is brought into proximity with the first, they will both have the same allowable electron energies. To adhere to the Pauli exclusion principle, electrons cannot exist in close proximity with the same set of quantum numbers. As the atoms are brought closer and closer together, the exclusion principle forces the highest allowable energy levels for both atoms to split in two (the highest energy electrons are the ones located in the "valence" orbitals, furthest away from the nucleus, and hence the first to interact with each other). As the atoms move closer, each interacting orbital splits further, essentially forming a continuous band of allowed electron energies. This band is referred to as the conduction band. When the atoms are close enough together so that the distances are nearly equal to the separation between chemically bound atoms (~0.01 – 0.1Å), this same bifurcation

process effects the electrons closer to the nucleus causing neighbouring orbitals to form a second continuous band called the valence band (Figure 12).

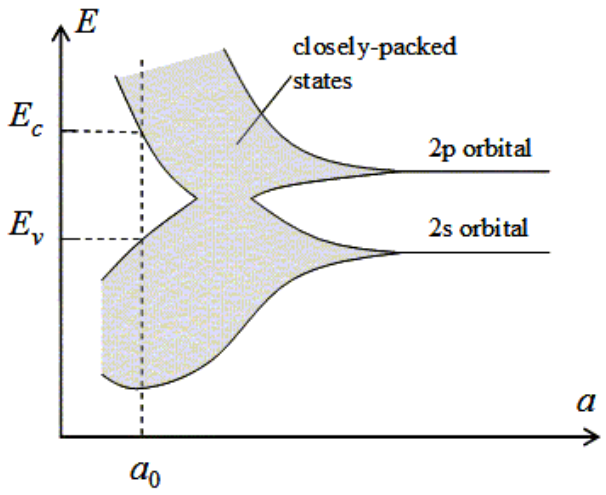

Figure 12: Allowable energy levels against interatomic spacing (a_0 = atomic spacing in crystal lattice, E_c = electron energy at bottom of the conduction band, E_v = electron energy at the top of the valence band) [114]

In semiconductors and insulators the conduction and valence bands are separated by a band gap containing zero allowable electron energies. Electrons in the valence band require an energy input equal to or greater than the band gap energy (E_g) to be promoted into the conduction band (Figure 13). Above absolute zero, this energy can be provided by several different mechanisms. Thermal energy (phonons) can provide this energy as can interactions with electromagnetic waves (photons).

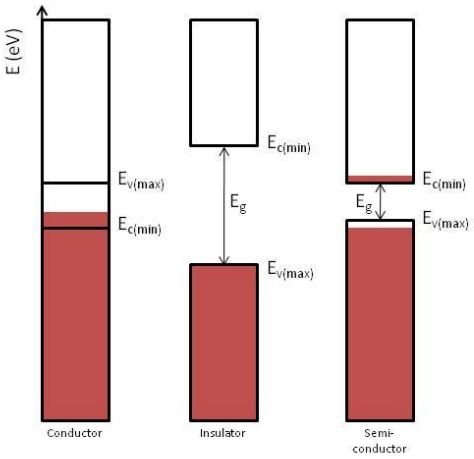

Figure 13: Example electronic band structures for conductors, insulators and semiconductors above 0K. Red represents energy levels occupied by electrons.

2.3.3 Fermi Energy and Fermi Level

In a semiconductor or insulator at absolute zero (0K) all the electrons within the material will be at their lowest energy state. Referring to the band structures in Figure 13, the valence band will be completely filled with electrons and the conduction band will be completely empty of charges. At 0K the Fermi energy (E_F) and Fermi level (a.k.a. the chemical potential (μ)) of the highest energy electrons are all equal. For temperatures above absolute zero the Fermi function describes probability of finding a fermion (in this case an electron) with a particular energy (E) associated with it for a given temperature (T) and Fermi energy. It should be noted that at temperatures above 0K the Fermi level refers to the highest occupied electron state and that the Fermi energy can be thought of as the average of the summed electron and hole energies.

$$f(E) = \frac{1}{1 + e^{(E-E_F)/kT}}$$

Only electrons with energies greater than the Fermi energy participate in the conduction process, the rest remain bound to their associated atomic nuclei. This also applies to conduction via holes, i.e. only holes with energies lower than the Fermi energy take part in conduction [113].

2.3.4 N and P-type Semiconductors

The conduction mechanism in a semiconductor material can be thought of as due to either electrons, holes or both. In intrinsic (or undoped) semiconductor materials conduction occurs by equal numbers of holes and electrons. The conductivity of the material can be expressed as:

$$\sigma = q(N_e\mu_e + N_p\mu_p)$$

Where σ = conductivity (S.m^{-1}), q = the charge of an electron (-1.602x10^{-19}C), N_e and N_p = the density of electrons and holes respectively (m^{-3}) and μ_e and μ_p = the electron and hole mobilities (m^2/V.s).

For pure intrinsic semiconductors, every electron promoted to the conduction band leaves a hole in the valence band, $N_e = N_p$ giving:

$$\sigma = Nq(\mu_e + \mu_p)$$

Semiconductors can be doped with additional atomic species to alter this conduction mechanism. Impurities with a different valence orbital structure introduced into an intrinsic semiconductor will have a large effect on the conduction mechanism. This process is called doping. For example, if an intrinsic semiconductor such as Si (group IV in the periodic table) is doped with a group V element such as As, the As atoms can substitute for Si within the crystal structure. In crystalline Si, the Si atoms have four outer electrons atoms each of which is covalently bonded to its four nearest neighbours. If an Si atom is replaced with an As atom with five electrons in its outer shell, then four of these electrons will covalently bond with the four nearest Si atoms leaving the fifth as a free charge carrier. In terms of the energy band structure this extra electron, only loosely bonded to its host As atom by weak electrostatic attraction (~0.01eV), is located within the forbidden energy band, in this case at an energy close to the conduction band minimum. A slight input of energy (thermal energy, electromagnetic energy, etc.) promotes this electron into the conduction band allowing it to participate in the conduction process. Since the electron has come from the forbidden energy gap, it leaves no hole in the valence band and the conduction mechanism is said to be n-type. Because of the low energy input required to liberate these free electrons, the conductivity of the sample can be increased dramatically by even very low impurity concentrations. This type of doping produces what are termed donor states [(113)]. Because this process leaves no associated hole once the donor electron is promoted to the

conduction band, the number of electrons involved in conduction is greater than the number of holes; $N_e \gg N_p$, thus the equation above for intrinsic semiconductors when applied to n-type materials becomes:

$$\sigma \cong N_e q \mu_e$$

Conversely, if Si is substitutionally doped with group III atoms such as Ga, which has three outer electrons available for bonding, only three of the four nearest neighbour Si atoms can form covalent bonds with it. This process can be viewed as a hole loosely bonded to the impurity atom. The effect of this is that an acceptor state is introduced into the forbidden band gap, at an energy just above that of the valence band maximum. With a slight input of energy, an electron from a nearby atom can be persuaded to occupy the hole associated with the impurity. This leaves an electron hole around the donating Si atom, and in such a way the hole can be thought of as moving though the material. Referring back to the band gap analogy, for conduction to occur in a material of this type an electron is promoted from the valence band into a slightly higher energy state than that found at the top of the valence band. This leaves behind a hole in the valence band without producing an additional electron in the conduction band. Semiconductors of this kind are said to be p-type, where $N_p \gg N_e$. The conductivity in p-type materials is expressed as:

$$\sigma \cong N_p q \mu_p$$

In both p and n type semiconductors, above 0K some conduction will occur due to the activity of electrons in p-type materials and holes in n-type materials. These are termed minority carriers. It should also be noted that doping to produce n and p-type materials shifts the Fermi level from its original, intrinsic energy. In n-type materials the Fermi energy is raised towards the bottom of the conduction band and in p-type materials it is lowered towards the valence band.

2.3.5 Carrier Recombination

When travelling through a semiconductor material electrons and holes can recombine, effectively removing themselves from the conduction process. The energy associated with the pair, in particular the difference in energy of the electron before and after recombination, is lost via one of several mechanisms. In radiative recombination the energy difference is large enough that a photon can be produced. This photon will have the same energy as that lost by the electron. Due to this, the wavelength (i.e. the energy) of emitted photons from a semiconductor can be tuned to that which is desired by careful materials selection and doping. This process forms the basis of light emitting diode devices and solid state lasers. Another mechanism by which carriers within the material can be lost is non-radiative recombination. In this process any excess energy that was carried by the electron is lost in the form of phonons (vibrations within the crystal structure) causing localised heating of the material. The final recombination process is Auger recombination where the electron loses its energy to another electron in the form of kinetic energy. This can either happen by an already mobile electron increasing its kinetic energy, or by a loosely bound electron being promoted into a higher energy state, thus making it available for conduction [(114)]. Each of these recombination processes are reversible, and can be utilised to generate free carriers within a semiconductor.

2.3.6 Semiconductor Junctions

When an interface is formed between materials with dissimilar band structures and electrical properties the interaction between them can cause short-scale movement of electronic charges across the interface as the Fermi levels attempt to reach thermal equilibrium. This process can be utilised to produce semiconductor devices with electronic properties not found in any of the materials if used individually. These junctions form the basis of numerous electronic components such as MOSFETs, Schottky diodes, LEDs, etc.. Multiple devices can be printed onto single integrated circuits to exhibit more complicated

device behaviours such as those seen in microprocessors, RAM, charge-coupled devices, etc..

2.3.6.1 Metal-Semiconductor (M-S) Junctions

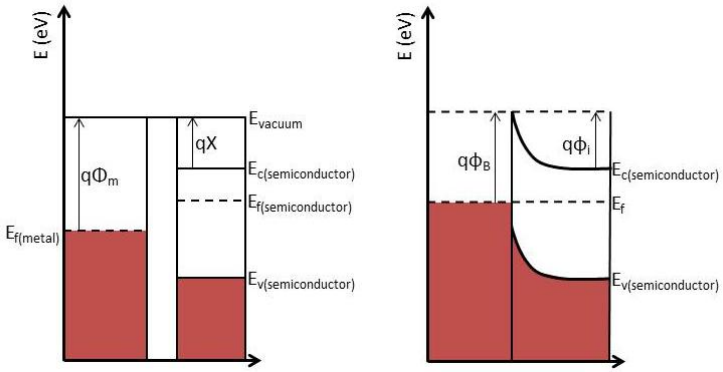

Figure 14: Left: band structures of a metal (with work function = $q\Phi_m$) and an n-type semiconductor (electron affinity = qX) before electrical contact is made between them. Right: After contact is made and the layers reach thermal equilibrium by electrons from the semiconductor travelling into the metal to lower their energy. This leaves a sea of positive ions which in turn creates a negative electric field, lowering the band edges of the semiconductor. Electrons continue to flow across the barrier until the Fermi energies of the two materials are equal.

Figure 14 shows the band structure representation of a metal and an n-type semiconductor before and after they have been brought into contact. Once contact between the two is made and they have reached thermal equilibrium a potential barrier exists that electrons can tunnel through or otherwise be given enough energy to pass over before conduction can occur. Under positive bias, whereby the positive terminal of a current source is connected to the metal, the Fermi energy of the metal is lowered with respect to the semiconductor resulting in a smaller potential drop. This allows a positive current to pass through the circuit from the metal to the semiconductor. When subjected to a negative bias, the Fermi energy of the metal raises with respect to the semiconductor. This has the effect of increasing the barrier potential and increasing the size of the depletion region, effectively stopping the flow of current and behaving as a rectifying junction.

For an n-type semiconductor this barrier height can be calculated:

$$\varphi_B = \Phi_m - X$$

For a p-type semiconductor the barrier height is:

$$\varphi_B = \frac{E_c - E_v}{q} + X - \Phi_m$$

The built-in potential (φ_i), i.e. the difference between the Fermi energies of the metal and semiconductor can also be calculated [(114)]:

For n-type junctions:

$$\varphi_i = \Phi_m - X - \frac{E_c - E_{f(n-type)}}{q}$$

And for p-type junctions:

$$\varphi_i = X + \frac{E_c - E_{f(p-type)}}{q} - \Phi_m$$

From these results the potential across the semiconductor can be calculated as the built-in potential (φ_i) minus the applied voltage:

$$V = \varphi_i - V_a$$

2.3.6.2 P-N Junctions

When two semiconductors with different majority carriers are brought into contact, or when adjacent regions of a semiconductor are doped n and p-type the resultant device can show rectifying characteristics. This device property forms the basis of MOSFETs, BJTs, solar cells, LEDs, and many other types of widely used devices.

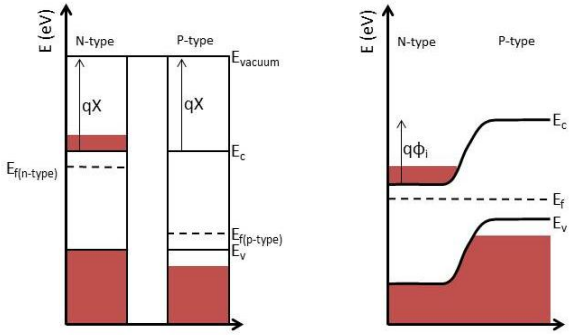

Figure 15: Left: P and n-type semiconductors before electrical contact is made between them. Right: An abrupt p-n junction in thermal equilibrium.

Figure 15 shows the electronic band structures for p-type and n-type semiconductors before and after thermal equilibrium is achieved. To reach thermal equilibrium, electrons from the n-type region diffuse across the boundary into the p-type region while holes from the p-type transfer into the n-type material. With no externally applied potential, over a short distance on either side of the interface both semiconductors lose their majority carriers. The area is known as the depletion region (Figure 16).

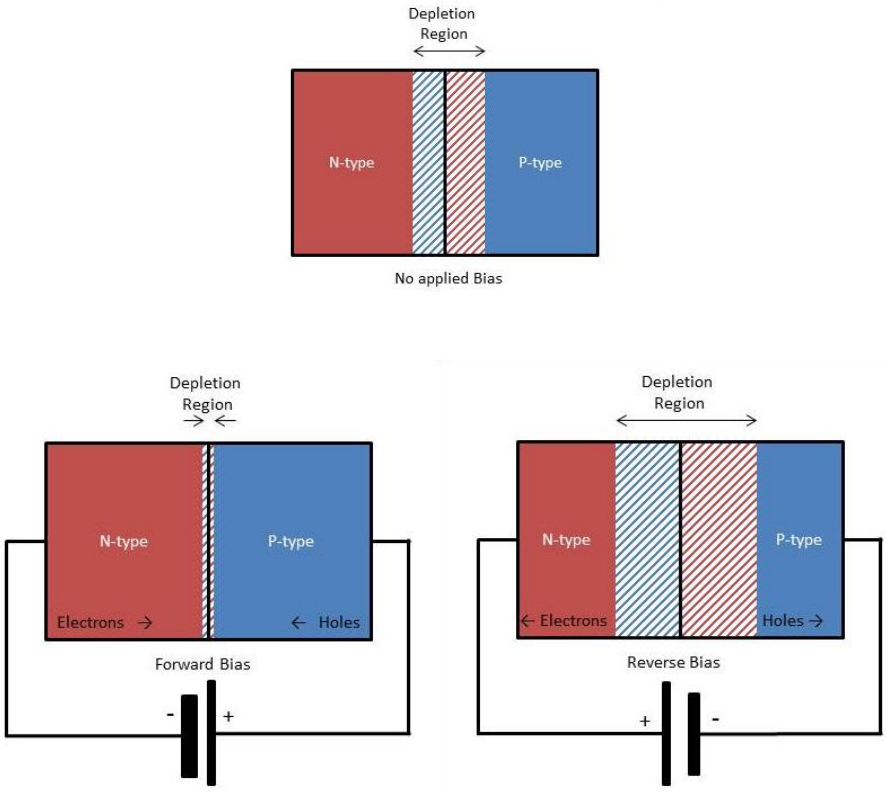

Figure 16: P-n junction devices with a) no bias applied. b) forward bias and c) reverse bias.

Figure 16 shows schematically the effect of applying forward and reverse biases to a p-n junction structure. In the first image no bias is applied and a depletion region is formed across the interface. The size of this zone is proportional to the built-in potential of the device. The bottom left image shows the device under forward bias. Electrons from the negative terminal are able to fill the empty spaces formed at the n-type side of the depletion region, while holes from the positive terminal fill up the holes on the p-type side. The size of the depletion region is reduced allowing current to flow across the junction. Referring back to the equilibrium band structure in Figure 15, an applied forward bias will have the effect of reducing the energy difference between the conduction and valences bands at both sides, i.e. raising both band edges on the n-type side and lowering both band edges on the p-type side. Majority carriers on either side of the interface are then able to cross the much reduced depletion zone via quantum tunnelling. The bottom right image shows the effect of reverse bias on the p-n junction. In this case no current is able to flow across the junction as the size of the depletion region is increased by the applied electric field.

It is possible to increase the minimum width of the depletion region by placing a third layer of intrinsic semiconductor material between the n and p-type materials. This is a useful technique when constructing solar cells or photodiodes as it enables absorption of electromagnetic radiation to be maximised within the depletion zone, yielding a higher photocurrent [2,114,115,116,117,118].

2.3.7 Transparent Conductive Oxides (TCOs)

Once two suitable materials have been grown together to form an opto-electronic junction, a method is required to extract any photo-generated current produced. A common method to achieve this uses a large area conductive back contact (generally opaque/reflective) and thin, closely spaced metallic strips on the top surface. These are required to be thin so that

they don't cause excessive shadowing of the p-n junction and thus a reduction in the photo-current. The spacing is dictated by the minority carrier diffusion length, the recombination rate of charge carriers within the material, the mobility of the carriers and other related parameters such as the resistivity. For materials with less than ideal conductivity, short minority carrier diffusion length and high recombination rates, this top contact setup would require a high number of closely spaced strips, reducing the efficiency of the device. Alternatively, a transparent conductive layer can be used, which allows the photo-generated current to be collected from all across the upper layer's surface. If this material is highly transparent to the required wavelength of light, then shadowing of the p-n junction can be eliminated. Transparent Conductive Oxides (TCOs) are a class of materials in which the properties of conductivity and transparency have been decoupled via degenerative doping of medium/wide band gap semiconductors [119]. Currently, the market for TCOs is dominated by Indium Tin Oxide (ITO), for both PV and LED technologies. Due to the expected scarcity of Indium in the coming years and a predicted increase in cost for the raw material, a concerted effort has been made to move away from these materials to cheaper, more readily available ones such as ZnO heavily doped with Ga or Al, for example, which in some cases can match or outperform ITO in terms of conductivity and transparency [120].

2.3.7.1 TCO deposition techniques

A variety of techniques have been employed in the manufacture and development of TCOs since the discovery, around a century ago, that partially oxidised sputtered cadmium displayed both high transparency and reasonable conductivity. It was found that the conductivity of the material was due to a resident oxygen deficiency giving rise to free carriers associated with metal defect levels at the bottom of the conduction band. Many different TCOs have been produced by a variety of techniques (RF and DC magnetron sputtering, PLD, CVD, Spray Pyrolysis, and ALD [121]) including CdSnO [122], B doped ZnO [123], Al doped ZnO (AZO) [63,124,125,126], Ga doped ZnO (GZO) [127,128], Sn doped ZnO [129], Sb_2O_5

doped SnO_2 [130], cadmium stannate (CTO) [131], ITO [132], F doped ITO [133], ITO doped with MoO_3 [134], CdTe [135], to name just a few. Table 2 shows some figures of merit for several experimental TCOs.

Table 2: A selection of transmittance and resistivity values for TCOs grown by different techniques

Material	Growth Method	Transmittance (%)	Resistivity (Ωcm)	Reference number
AZO	RF Sputtering	90.2	5.344×10^{-4}	124
CdSnO	RF Sputtering	~80	10^{-4}	122
GZO	RF Sputtering	99.5 (@550nm)	6.95×10^{-4}	127
CTO	RF Sputtering	>90	R_s = 15Ω/□	131
GZO	DC Sputtering	>80	4.89×10^{-4}	128
AZO	RF Sputtering	~90	$\sim 7 \times 10^{-4}$	63
AZO	PLD	~90	6.6×10^{-4}	125
SnO_2:Sb	PLD	>82	7.8×10^{-4}	130
AZO	PLD	68	2.23×10^{-4}	126
ITO:Mo	PLD	~90	4.86×10^{-6}	134
CdTe	PLD	>60	----	135
ZnO:B	LPCVD	----	1×10^{-3}	123
ZnO	MOCVD	>80	$\sim 2 \times 10^{-1}$	132
ITO	MOCVD	>80	3.5×10^{-4}	132
FTO	LPCVD	>80	R_s = 3Ω/□	133
AZO	Spray Pyrolysis	>85	8.1×10^{-3}	136
ZnO:Sn	Spray Pyrolysis	80	1.2×10^{2}	129

2.3.7.2 Conduction Mechanisms in TCOs

There are several important factors to be considered when selecting or developing materials for TCO applications. These are resistivity (ρ) or conductivity (σ), sheet resistance (R_s), free carrier mobility (μ), free carrier density (N), the extinction coefficient (κ) and the absorption coefficient (α) at the particular wavelengths of interest (λ). The transmitted intensity of the light through the film (I) is related to these values and the incident light intensity on a material of a certain thickness (d) by:

$$I = I_0 e^{-\alpha d} \text{ where } \alpha = \frac{4\pi\kappa}{\lambda}$$

When assessing TCO performance, the ratio of conductivity to the absorption coefficient can be used:

$\sigma/\alpha = 1[R_s \ln(T+R)]^{-1}$ where T is equal to the total transmittance of the material and R is equal to the total reflectance.

Another useful equation relates the conductivity of the material (σ_e^0) to the mobility through the average time between carrier collisions (τ) and to the number of charge carriers (n_e):

$\sigma_e^0 = n_e e^2 \tau / m_e^*$ where e is the charge of an electron and m_e^* is the electron effective mass in this particular material.

A thorough derivation of the above equations can be found in Exarhos and Zhou (2007) [121].

Transparent wide bandgap oxides can be doped to produce defect energy levels close to either just below the conduction band minimum (for n-type donors) or just above the valence band maximum (for p-type donors). In either of these materials only a small input of energy is then required to promote an electron to make conduction possible (Figure 17).

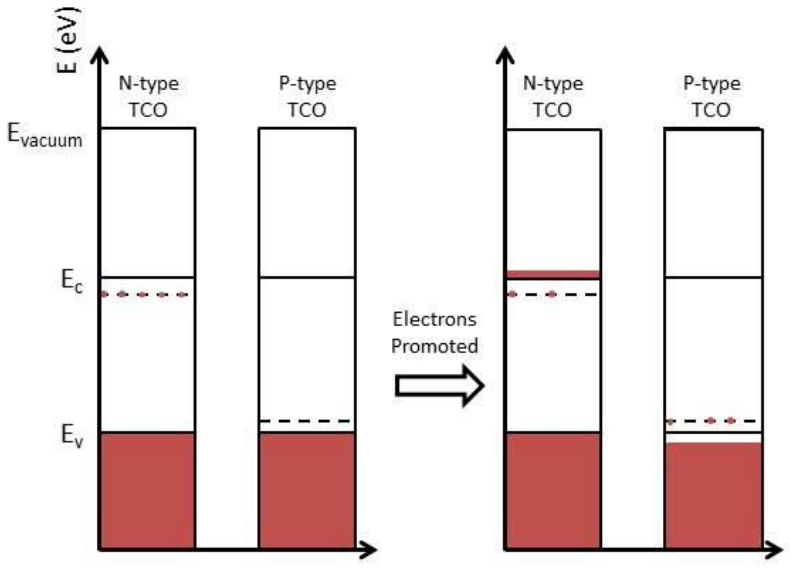

Figure 17: Doping and Conduction mechanism in wide bandgap TCOs

2.3.8 PV Devices

One application of p-n junctions, p-i-n junctions and m-s junctions is in the manufacture and design of photovoltaic (PV) devices such as solar cells, light activated diodes, etc.

Electrons within the depletion zone of a p-n junction can be promoted from the valence band up to the conduction band by the absorption of a photon producing an electron-hole pair which is available for conduction. For this to occur in a direct band gap semiconductor, the photon has to have energy greater than or equal to the band gap energy of the semiconductor in which it is absorbed. For indirect band gap materials, the promotion of an electron also involves a change in momentum. Since the photons themselves do not carry much momentum, for this to occur a phonon (lattice vibration) must also be absorbed or emitted by the electron. Once an electron hole pair has been produced, one of several different processes can occur. The electron can drop back into the valence band, annihilating the electron-hole pair and emitting energy, either via electromagnetic waves and/or phonons. To do this there has to be a viable method for it to shed the extra energy it previously absorbed. Defects within the crystal structure such as dislocations and impurities can provide this opportunity, as can larger structural inhomogeneities such as grain boundaries and precipitates. Each of these defects is able to provide additional allowable energy levels within the forbidden band gap by which the electron can lose energy. If this occurs then no usable current is produced by the event. Another possibility, if the electron-hole pair is produced within the depletion zone of the p-n structure, is that the built-in electric field is able to pull the pair apart. This results in an electron travelling towards the positive terminal and a hole travelling towards the negative terminal, and provided that there are no more recombination events along its path, a usable current is produced.

2.3.8.1 Characterisation of PV Devices

Shown below (Figure 18) is the expected IV (current-voltage) curve for a functional photovoltaic device. Without illumination, the device shows rectifying behaviour, inhibiting current flow through the junction when under reverse bias (at potentials lower than the breakdown voltage) and allowing current through under forward bias. When illuminated, the generation of additional charge carriers within the depletion region on either side of the p-n junction along with the electron-hole separation facilitated by the built-in electric field causes a current to flow. At 0V, the current produced is termed the short circuit current (I_{sh}). When under forward bias, the point where 0A current occurs is termed the open circuit voltage (V_{oc}). The points marked I_m, V_m and P_m correspond to the maximum power output that the device can achieve.

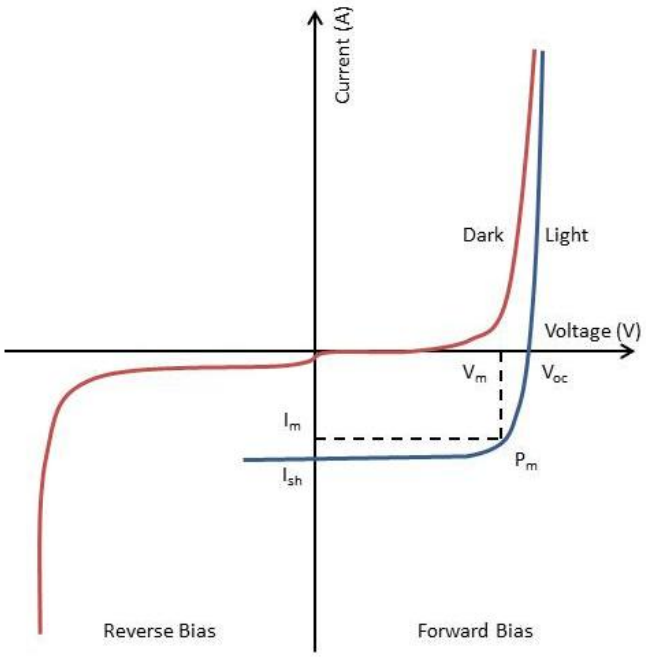

Figure 18: IV curve for a photovoltaic device under dark (red line) and illuminated (blue line) conditions (not to scale).

The dark curve can be characterised by a diode curve:

$$I = I_o(exp(V_A/V_T) - 1)$$

Where I = current (A), I_0 = diode saturation current (A), V_A = applied voltage (V) and V_T = the thermal voltage (V).

Once illuminated, an additional term for the light generated current is added:

$$I = I_o(exp(V_A/V_T) - 1) - I_{sh}$$

Where I_{sh} = the light generated current (A), i.e. the short circuit current.

The maximum power that can be obtained (P_m) can be found when the product of I and V is at its maximum. This yields the values for I_m and V_m. Since the power is found from the rectangular area enclosed by the points (0, 0), (V_m, 0), (0, I_m) and (V_m, I_m), it is apparent that a perfect illuminated IV curve should be approaching a rectangular shape. The fill factor (FF) is used to determine how close to a rectangle this area is and is calculated by:

$FF = \frac{I_m V_m}{I_{sc} V_{oc}}$ where $FF = 1$ represents an ideal device.

The conversion efficiency (η) of the device is another widely used parameter when characterising photovoltaic devices and represents the ratio of photovoltaic power output to the power of the illumination falling on it and can be calculated from [137]:

$$\eta = \frac{I_m V_m}{P_{light}} = \frac{FF.I_{sc}V_{oc}}{P_{light}}$$

2.3.8.2 Current Trends in PV

Photovoltaic devices have been undergoing research and development since their discovery in the late 1800's. Up until the 1940's and the development of the first solid state PV devices, progress in this field was relatively slow and more involved in understanding the physics behind the process of light induced chemical reactions rather than developing the devices for practical use in energy generation. With the advent of solid state electronics and the production of a 6% efficient silicon based solar cell in 1954 by Charpin et al.,

research and development into the devices accelerated and by the end of the 1950's PV devices were being utilised for energy production in space based technologies, where they offered significant advantages over other methods of energy generation (i.e. high power to weight ratios). At this time, with the abundance and low cost of fossil fuels, nuclear power, hydroelectric power, etc., PV found little application for terrestrial energy generation. More recently, with the understanding that fossil fuels are a finite resource and contribute significant pollution to the atmosphere, safety concerns with nuclear power and disposal of spent radioactive material, environmental and social issues with the construction of large hydroelectric projects, photovoltaics have started to become a cost effective and environmentally friendly alternative to more traditional methods of large and small scale energy production.

2.3.8.2.1 Types of photovoltaic and current materials systems

El Chaar et al. produced a comprehensive review of photovoltaic technologies in 2011 [138]. In this article they classify photovoltaic technologies into four separate types: Crystalline Si PV, Thin Film PV, Compound Semiconductor PV and Nanostructured PV. These classes are further broken down as shown in Figure 19.

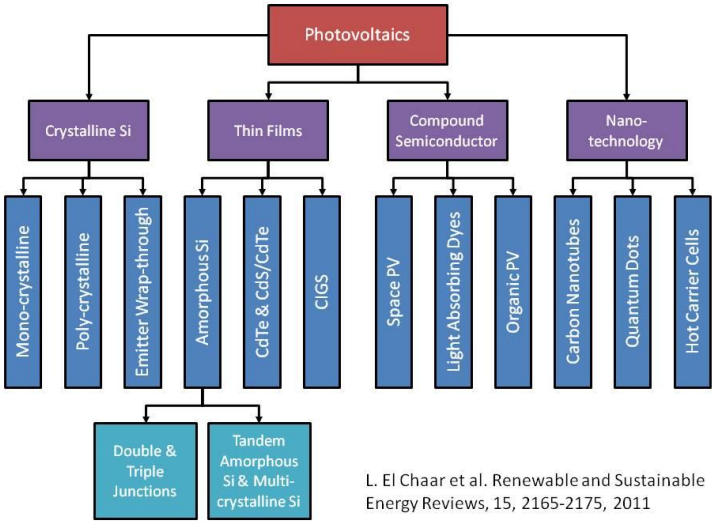

Figure 19: Types of photovoltaic technology

Crystalline Si:

This material saw the first mass produced photovoltaic modules and was a direct result of advances in the Si-based computer industry. As such it is the longest running and most well developed of the photovoltaic technologies. Mono-crystalline Si PV utilises Si p-n junctions for the generation of photocurrent and is grown via the same methods (Czochralski growth) used for the growth of Si wafers in the computer industry. Typical currents and efficiencies for mono-crystalline Si PV are ~35mA/cm^2 and ~25%. The problems associated with this technology stem from the relatively small bandgap (~1.1eV) and the fact that it is indirect. This leads to excess heat generation from the absorption of radiation (the difference in eV can be converted into heat) and the production of phonons in the device from the change in momentum of charge carriers. Another problem with this material is that the cost of the Si substrates is inherently coupled to the price of Si used in the microelectronics industry. When surplus Si wafers are produced, the cost of these cells is very favourable giving devices with a high output per unit cost, however, some years the electronics industry uses a significantly higher fraction of the Si wafer produced, driving the price of the raw material up. Consequently, this led to the development of poly-crystalline silicon PV, which uses a different and cheaper growth process to produce wafers of more-or-less uniformly oriented poly-crystals. Polycrystalline PVs tend to be lower in efficiency (~15%) but still perform well in terms of output per unit cost. Further efficiency improvements have been made with the design of the collectors used to retrieve the generated current. In standard cells, part of the upper surface of the device is shaded by the thin metal contacts. Emitter wrap-through cells have both contacts situated on the back of the cell allowing much incident light onto the front of the device. This can produce an increase in efficiency of around 10-20% compared to normal front contacts.

Thin Film PV:

Thin film photovoltaics use much less active material than Si-based PV because the wafer sawing process used for mono and poly-crystalline Si requires that the produced wafers have a thickness of several hundred microns. In thin film PV the active materials are deposited onto glass or metal substrates via sputtering, CVD, electrolysis or other thin film deposition techniques. This means that the material requirements are much lower than those of Si-based approaches. Additionally, high manufacturing throughput can be achieved further lowering production costs. Amorphous silicon is produced from a vapour deposition process depositing around 1 micron of material with a bandgap of around 1.7eV, much more suited to absorption of visible light than crystalline Si. Other advantages over crystalline Si include easier large scale production due to better uniformity and lower materials costs. The efficiency of a-Si is lower than that of crystalline Si and further degrades to around 4-10% once exposed to sunlight due to the Staebler-Wronski effect [(139)]. Several different strategies exist for architecture of a-Si cells. These can be either single, double or triple junction a-Si cells or tandem cells that utilise both amorphous and crystalline Si. These type of architectures use different layers of the material to absorb specific parts of the solar spectrum, effectively protecting the materials against degradation when exposed to sunlight and increasing the cell efficiencies to nearer 10%. The drawback of these compared to the cells discussed previously is that they require higher levels of processing so manufacturing costs are increased. Another popular type of thin film cell uses CdTe as the absorber layer, which has an ideal bandgap of around 1.45eV. These devices can yield efficiencies of around 15% and are relatively cheap to manufacture on a large scale, and as such are a popular choice for MW solar power plants. The toxicity of cadmium raises some concerns, however, as disposal and recycling of the modules adds considerably to the full lifecycle costs. The final major thin film PV currently in use is based on a solid solution of Cu-In-Se and Cu-Ga-Se (CIGS). By tuning the ratio of In:Ga in the semiconductor

($CuIn_xGa_{(1-x)}Se_2$) the bandgap can be shifted from around 1eV to 1.7eV and are generally used in a heterojunction structure along with n-type Al-doped ZnO (a TCO). Efficiencies with CIGS devices can reach up to 20%. Due to the reliance on the relatively rare material indium in these devices, future production costs are expected to rise as the raw materials become scarcer.

Compound Semiconductor PV

This class of photovoltaics include complex multi-junction cells for both terrestrial and extraterrestrial applications, light absorbing dye cells and organic and polymer based PV cells. Multi-junction devices based on GaAs/InGaP, which use several p-n heterojunctions to maximise the absorption of the solar spectrum, have recently reported the highest efficiencies for PV at just over 40%. PV devices used by the satellite industry are subject to different constraints than those used elsewhere. Because of the absence of atmospheric gases which filter out certain frequencies of light, space based PV is able to utilise a higher proportion of the electromagnetic spectrum. Further design constraints require the cells to be able to withstand high levels of potentially damaging radiation, micrometeor impacts and harsh temperature swings. Another difference between terrestrial and spaced based PV is that the electrical output per unit mass takes greater precedent than the output per unit cost, as high launch costs tend to dominate the overall cost of satellite production. Light absorbing dyes use high surface area semiconductor materials such as Si or TiO_2 coated in a dye (typically iodide) which produces electron-hole pairs when irradiated by light. A liquid electrolyte in contact with the dye transports the generated current to the anode. Highest efficiencies for dye-sensitized cells are around 11% and in general are between 5-10%. These cells are based on the action of chlorophyll used by plants in photosynthesis, however, due to their use of liquid electrolytes, problems are encountered in sealing the cells and using them in outdoor conditions. A major benefit of this type of cell

is the low production cost compared to more traditional approaches. Organic solar cells use semiconducting composite polymers as the active layer, sandwiched between a transparent thin film electrode and a conductive back contact. These cells tend to have maximum efficiencies around 4%, but benefit from low processing and manufacturing costs as well as being inherently flexible and easier to dispose of at the end of their life.

Nanotechnology PV

The use of nano-sized components such as nanotubes, nanowires, monolayer sheets, quantum dots, etc. allows materials properties otherwise unobtainable to be designed and manufactured. For example, carbon nanotubes can be either metallic or semiconducting depending on whether the sheet of hexagonally arranged carbon atoms is rolled up in an "armchair", "zigzag" or chiral manner. Further modification by the attachment of additional functional groups to the inside, outside or ends of the tubes is also possible and can enable further tuning of materials properties. Another advantage of using nanomaterials is that the effective area of a p-n junction (for example) can be increased enormously compared to that of a standard planar interface, whilst also reducing material usage. By reducing the length which charges generated in the absorber layers of nanostructured solar cells travel before being collected, it is possible to produce very high efficiency PV cells (theoretically >60%) by prohibiting electron hole pairs from shedding their heat in the absorber layer. PV devices utilising nanostructured materials and hot-carriers are relatively new and are still undergoing research and development.

2.3.8.2.2 **CuO and Cu_2O PV**

Cu_2O offers many potential benefits for PV due to the abundance of the material (Cu), its low toxicity and its band gap of around 2eV, which enables it to absorb photons with wavelengths above ~600nm. Research into Cu_2O based photovoltaics began in the early 1900s when Wilhelm Hallwachs produced a Schottky-type cell from Cu and Cu_2O. After its

initial discovery, however, further work stalled partly due to the low efficiencies of produced devices and partly from competition with emerging devices based on Si hetero and homostructures. As the knowledge base around the manufacture and use of Si increased rapidly, little further work was done on Cu_2O PV until the 1970s. During this time several groups worked to produce PV devices based on this material which had a potential theoretical efficiency of close to 20%, but to this date the highest efficiencies have only reached around 3.8%. Adbu et al. attributed the difficulty in realising the theoretical efficiency to several factors, namely the high resistivity of Cu_2O produced by various different processes (i.e. a low carrier concentration and mobility, along with a high chance of carrier recombination), problems with producing Cu_2O homojunctions due to difficulty in fabricating n-type Cu_2O, and most significantly, a Cu rich layer present in nearly all devices caused by the depletion of oxygen from the interface. This causes a Schottky-type barrier between the Cu and Cu_2O which then dictates the device performance, regardless of any other materials used [(115)]. In recent years, it has been shown that it is possible to fabricate n-type Cu_2O through electrochemical deposition, and that by controlling the pH of the electrolyte Cu_2O p-n homojunctions can be produced. Wei et al succeeded in producing Cu_2O homojunctions PV cells on FTO glass with conversion efficiencies of ~0.1% [(140)]. Cu_2O heterojunction and Schottky barrier photovoltaics have also received increased attention in recent years, with a lot of work centred around n-ZnO(doped)/p-Cu_2O devices. Nishi et al made Cu_2O based Schottky barrier photovoltaic devices using aluminium doped Zinc oxide (AZO) as the n-type layer. Conversion efficiencies of ~2.2% were achieved using this technique [(141)]. Leading on from this work, Minami et al. produced AZO/ZnO/Cu_2O cells with a conversion efficiency of 3.8% via thermal oxidation of Cu metal followed by a thin sputtered film of ZnO (~50nm) then AZO sputtering. The addition of the thin ZnO layer stopped the device acting as a Schottky barrier, thus increasing the conversion efficiency [(142)].

3 Experimental Techniques

3.1 Optical Microscopy

Optical microscopy is widely used in many fields of research including biology, entomology geology, metallography and materials science, to name just a few. In general, a series of high precision lenses are used to magnify and focus transmitted or reflected light on to an eye piece, a pair of eye pieces or a digital CCD chip, from where observations can be made or images recorded.

In this work, several different optical microscopes were employed to assess Al and Cu samples after electropolishing and after oxidation. For standard microscopy, a white light source was reflected from the surface of mounted and polished samples and recorded using a digital camera and a PC. Samples were mounted in conductive epoxy resin (allowing further analysis via electron microscopy if required) and polished using standard metallography procedures, i.e. coarse polishing with P120 paper then using successively finer grade paper until a surface finish with a roughness of less than ~1μm was achieved using cloth discs impregnated with diamond paste or an emulsion of <100nm silica particles.

To assess electropolished Al and Cu samples DIC microscopy was employed. This technique was also used for the measurement of grain size in heat-treated Cu samples. DIC uses a standard optical microscope with the addition of a birefringent Nomarski prism and two polarising filters. White light is passed through a polarising filter and then the Nomarski prism prior to the objective lens where it is split into polarized orthogonal components. Slight differences in the topography of the sample surface mean that when the light reflects from the sample, it experiences slight differences in optical path length. After passing back through the objective lens the orthogonal components are focused onto the interference

plane of the Nomarski prism which recombines them. Leaving the prism, the light then passes through a second polarising filter oriented at 90° to the first polariser. This allows only light that is now polarised to the orientation of the second filter to pass through where it then travels on to the eye piece. At the eye piece, the slight differences in optical path length cause the light to interfere with itself, producing an image where the intensity is directly related to the optical path length and hence the variation in topography of the surface under examination. The benefit of this technique is that variations in the surface topography much smaller than those visible by normal optical microscopy techniques can be resolved.

In the following reports all optical microscopy was performed using Nikon Epiphot microscopes with Infinity 2 digital cameras and processed using Infinity Analyse software (section 4.2 - AAO Growth Rate, p. 92). Nomarski lenses and prisms were also used for additional optical microscopy (section 5.1 - Cu Surface Cleaning Tests, p. 131 and section 5.3 - Thermal Growth of Planar CuO/Cu_2O and Quench Tests, p. 149).

3.2 Electron Microscopy

A Scanning Electron Microscope (SEM) uses an electron gun to produce a beam of narrow energy electrons which can be focussed and scanned across a sample surface. The SEMs used during this work used two different types of electron emission. In the first case, electronic heating of a tungsten filament inside a high vacuum chamber causes thermionic emission of electrons which are then passed through a series of apertures and magnetic lenses further down the vacuum column. The second type of emission is field effect emission, whereby a large potential difference between a sharp tungsten cathode and torus shaped anode provides a high electric field gradient at the cathode tip and allows electrons within the material to tunnel out towards the anode. The hole in the centre of the anode allows some of the electrons to pass through, were they move on to be focussed in

the vacuum column. Once focussed, a final set of magnetic lenses scan the electron beam across the surface of the sample in a raster pattern.

Several different processes can be used to detect the surface of the sample under examination. When the focussed electron beam hits the surface, an interaction volume is formed in which the incoming electrons repeatedly lose energy from absorption and scattering. This interaction volume is a teardrop shape and extends from the surface to a depth of between <1µm and ~5µm, depending on the beam energy and the atomic weight and density of the sample. These electrons lose energy by elastic and inelastic scattering in the material. If an incoming electron inelastically scatters from an electron within the sample, two processes can occur. The electron in the material can be given enough energy to escape its host nucleus and, if close enough to the sample surface, can leave the sample where it is picked up by a secondary electron detector. Alternatively the impinged upon electron can be given enough energy to promote it to an unoccupied orbital state, after which it collapses back to its original state either directly or via intermediate energy orbitals, in which case electromagnetic energy is released in the form of X-rays. These X-rays show a characteristic energy depending on which element they originated from. The X-rays are generated throughout the entire depth of the interaction volume and due to their small wavelength can pass relatively unhindered through the sample material where they can be picked up by an X-ray detector. If an incoming electron is elastically scattered it will have the same energy as it did when it was emitted, allowing a backscatter electron detector to differentiate between reflected electrons and inelastically scattered electrons.

Each of the different detection mechanisms provides complementary information about the sample under analysis. The most common imaging mode, secondary electron imaging, provides a high resolution image of the sample surface. As the secondary electrons have a large cross section relative to the substance of the material that they are travelling through,

electrons generated deep within the tear-drop volume are unlikely to escape directly to be picked up by the secondary electron detector. This means that the majority of the electrons registering at the detector originate from within the top few nanometres of the surface of the sample. As the electron beam is scanned across the sample, height changes on the surface alter the angle of incidence of the beam with the surface; any deviation from the normal registers as an increase of the number of secondary electrons reaching the detector and hence a brighter pixel in the resulting image. Using this technique can yield resolutions finer than 0.5nm coupled with a large depth of field.

Back-scattered electron imaging also gives information about the top few nanometres of a surface. In this case, the number of reflected electrons is closely tied to the atomic number of the atoms present in the surface. Atoms with a higher atomic number have a larger cross section with which to reflect the incoming electrons and as such appear brighter on the resulting image. This technique can be used to show a distribution of the atomic species across the surface of the sample and give information about compositional variation.

For experiments shown later in this document two electron microscopes with EDX were used: A JEOL 7001F with Oxford EDS (EDX) system with processing by INCA EDX software (4.3 - Effect of 1st Step Anodisation Duration on AAO Pore Arrangement, p. 98, 4.4 - Deposition of TiO_2 into Anopore AAO Templates Using ALD, p. 108, 5.2 - Anodisation of Cu Foil to Produce High Aspect Ratio Cu_2O Surfaces, p. 138 and 5.6 - Growth of High Surface Area Cu_2O Nanostructures, p. 200). Additional electron microscopy was performed using a JEOL 6610 (W filament) with Oxford EDS (EDX) system and processing by INCA EDX software (sections 4.4 - Deposition of TiO_2 into Anopore AAO Templates Using ALD, p. 108, 5.3 - Thermal Growth of Planar CuO/Cu_2O and Quench Tests, p. 149, 5.4 - Effect of Initial Strain on Thermally Grown CuO Nanowires, p. 163, 5.5 - Growth of CuO Nanowires Through an

ALD Al_2O_3 Barrier Layer, p. 186 and 6.1 - PV Testing of Anodised Cu substrates Coated with TiO_2 via ALD, p. 216).

3.3 X-Ray Diffraction

X-ray diffraction is used to study crystalline solids. A Cu Kα x-ray beam with a wavelength of 1.5418Å is fired at the sample while it is rotated in the x-y plane with optional rotation about the z axis. An x-ray scintillator detector is geared to rotate with the sample, progressing through twice the angle moved by the sample in a Bragg-Brentano θ-2θ setup. As the x-rays are of a similar magnitude to the bond lengths of crystalline solids (~1-3Å) the beam is able to penetrate several microns to hundreds of microns into the surface. At the surface the beam can be effectively thought of as many parallel x-rays coming into the surface at the same angle. An x-ray scattering of a lattice plane near to the surface will travel a shorter distance than one scattering of the same index plane deeper in the sample (Figure 20).

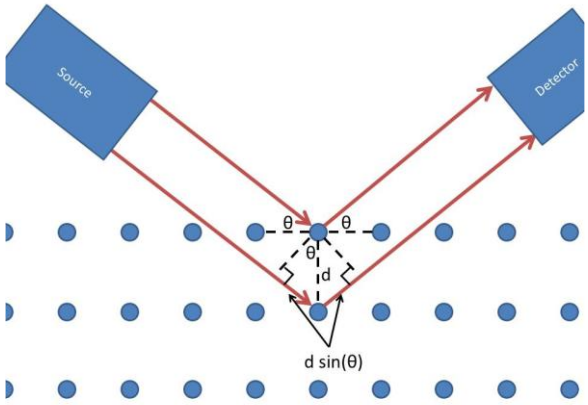

Figure 20: Bragg-Brentano θ-2θ setup

For a given wavelength of radiation, at certain angles the equation nλ =2dsin(θ) will be satisfied (where n is an integer, λ is the wavelength of radiation, d is the spacing between lattices planes and θ is the angle of incidence of the beam and the surface) and the reflected radiation will be in phase resulting in constructive interference and an increase in

counts at the detector. At angles where the Bragg equation is not satisfied destructive interference takes place giving a low count number and background noise.

Typically, this type of X-ray diffraction is used for poly crystalline solids or powders. For powdered samples, or polycrystalline samples with little or no preferential crystallographic orientation, the high number of crystals means that there are many crystals presenting every possible orientation to the source and detector as the sample is scanned through a range of angles. The resultant scan can then be checked against reference scans either manually or using software with the peak locations and relative intensities allowing for identification of particular materials and crystallographic phases. For samples preferred orientation (such as epitaxial films) or for samples with few crystal orientations present identification may prove more challenging as the relative intensities may differ from their reference patterns and some peaks may be entirely missing. Other effects that may be seen include a broadening of peaks (FWHM) which indicates a reduction in the size of individual crystals (this effect begins when the average crystal diameter is below ~200nm) or a deviation from the expected peak location which indicates either tensile or compressive strain in the lattice (for example, strain induced by substitutional dopant atoms).

XRD carried out for the work shown here was conducted using a Rigaku-Miniflex θ/2θ setup, Cu Kα X-ray source with a wavelength of 1.54Å (sections 5.2 - Anodisation of Cu Foil to Produce High Aspect Ratio Cu_2O Surfaces, p. 138, 5.6 - Growth of High Surface Area Cu_2O Nanostructures, p. 200, 5.7 - ALD of TiO_2 on to Anodised Cu_2O Nanostructured Surfaces, p. 206 and 6.1 - PV Testing of Anodised Cu substrates Coated with TiO_2 via ALD, p. 216).

3.4 Raman and Photoluminescence

Raman spectroscopy uses a monochromatic laser to excite electrons from their resting states up to virtual energy states. When they relax back to a different stable state they emit radiation of a wavelength characteristic of the transition. Holographic filters, notch filters or

edge filters are used to screen and reject the emitted and reflected light at the excitation wavelength used leaving only emitted light that has undergone either an increase or decrease in energy. Using this technique can give information about the vibrational state of electron clouds and bond around atoms in the material. If a molecule has a higher vibrational/rotational energy following the transition then the emitted photon will have lower energy than the incident light (Stokes shift). If the molecule ends up with a lower vibrational/rotational energy then the emitted light will be a higher energy than the incident light (Anti-Stokes shift). This technique can be used to characterise materials as each material has a characteristic Raman pattern. It can also be used to observe changes in bonding so that closely related materials can be distinguished (e.g. SiO, SiO_2, etc.).

Photoluminescence (PL) can be used to study the electrical characteristics of a material (as opposed to the chemical bond characteristics studied with Raman spectroscopy). Under optical excitation with a monochromatic laser of sufficient energy photons are absorbed creating electrical excitations. These excitations will eventually relax back to their ground state through the creation of heat or through radiative decay. If radiative decay occurs the energy of the emitted light can provide information about the electronic structure of the sample, such as the size of the bandgap in semiconductors and the presence of electron/hole traps within the bandgap. This makes it particularly suitable for studying interfaces and surfaces which are normally associated with different electrical properties to that of the bulk materials. In the following pages all Raman spectroscopy and photoluminescence measurements were performed using a LabRam spectrometer and a 514nm laser source.

3.5 X-Ray Photoelectron Spectroscopy

X-ray Photoelectron Spectroscopy (XPS) uses a monochromatic x-ray beam to excite and liberate electrons within the top few nanometres (up to ~10nm) which are then collected

by an electron energy analyser and an electron detector. Each electron near the surface of the material is bound to it's host atom with a particular strength (Binding Energy). By measuring the kinetic energy and number of the emitted electrons, and also with knowledge of the energy of the incident x-rays (typically 1486.6eV from a Al Kα source), the binding energy of the electrons can be determined using the Rutherford equation: $E_{binding} = E_{photon} - (E_{kinetic} + \emptyset)$ where $E_{binding}$ is the binding energy, E_{photon} the energy of the incident x-ray, $E_{kinetic}$ the measured energy of the detected electron and $\emptyset$ the work function of the detector (all in eV). The resultant scan shows peaks at characteristic energies corresponding to the atomic composition present within the top ~10nm of the surface. As the incident beam is of a relatively high energy (c.f. the binding energies of electrons around the nucleus) it is able to liberate electrons from different shells around each atom. This gives several distinctive peaks at specific energies for each element above lithium in atomic weight. Using Relative Sensitivity Factors (RSFs) for each element present allows the composition to be determined (At%) to an accuracy of around 0.1%. Additionally, since the shape and strength of any electron clouds around a host atom are affected by the type of bonding the host atom is involved in, the binding energy of liberated electrons is also affected. Close scans covering a few tens of eV along with Gaussian/Lorentzian peak fitting can be used to examine the nature of the bonds in the surface of the sample. In section 5.5 - Growth of CuO Nanowires Through an ALD Al_2O_3 Barrier Layer, p. 186, a VG Scientific Escalab mk II XPS system using an Al xray anode was used.

3.6 Ellipsometry

Ellipsometry is an extremely useful technique for the measurement of thin films. Many techniques that would normally be employed to measure the thickness of a material, such as cross sectioning followed by optical microscopy/SEM/etc. can struggle to provide

accurate measurement of very thin films (<~100nm) or else have high running costs associated with them. Ellipsometry works by illuminating a sample with elliptically polarised light and measures the change in amplitude (amplitude ratio = Ψ) and phase (phase difference = Δ) of any reflected or transmitted light. As even sub-nanometre films will modify both of these parameters ellipsometry can provide very accurate thickness measurements (as well as being able to measure other optical properties). Typically, once the Ψ and Δ values have been measured, a model based upon known or best-guess optical parameters (i.e. the complex refractive index comprised of the refractive index and the extinction coefficient) for the film under observation is used to determine the films thickness. However, many different things can affect the optical properties of a material such as crystallographic phase, surface roughness, adsorbates, impurities and dopants (even at very low concentrations) and voids so care should be taken when using text-book values. All ellipsometry measurements in the following experiments were done using a Rudolf Research Auto EL single wavelength (632.8nm) ellipsometer.

3.7 Hardness Testing

The hardness of a material is a combination of several bulk material properties (such as ductility, yield strength, elasticity, viscosity, etc.). Several standard measurement techniques have been developed to measure indentation hardness including Rockwell, Brinell and Vickers hardness. All hardness testing in the following pages was carried out using a Matsuzawa Seiki Co. Vickers micro-hardness tester (section 5.4 - Effect of Initial Strain on Thermally Grown CuO Nanowires, p. 163). A standardised indenter head is applied to the surface of a material with a known force and for a known duration. In this case a Vickers diamond pyramid was used. After the indenter was withdrawn an optical microscope was used to measure the length of the diagonals from the square impression left in the surface. For this particular indenter the Vickers equation was used to determine

the Vickers Hardness of the materials tested: $HV = F/A \approx 1.8544F/d^2$ where HV = Vickers Hardness (Pa), F = applied force (kgf) and d = average diagonal length (mm).

4 Nanostructured Surfaces - Anodised Aluminium Oxide

4.1 Introduction

Anodised Aluminium Oxide (AAO) [1,50,143] can be used to create highly regular arrays of nanowires and nanotubes via the deposition of materials onto its surface. Many different materials can be deposited by a variety of deposition techniques [144], allowing this method to produce structures with many different functionalities and a wide range of technological applications. One of the advantages of this technique over other methods of nanowire/tube manufacture is the high degree of control it is possible to achieve over the pore size, interpore spacing (both controlled by a combination of electrolyte pH and anodisation voltage) and the length of the pores (controlled by the anodisation duration).

A possible method to use this material in a PV device is shown below in Figure 21.

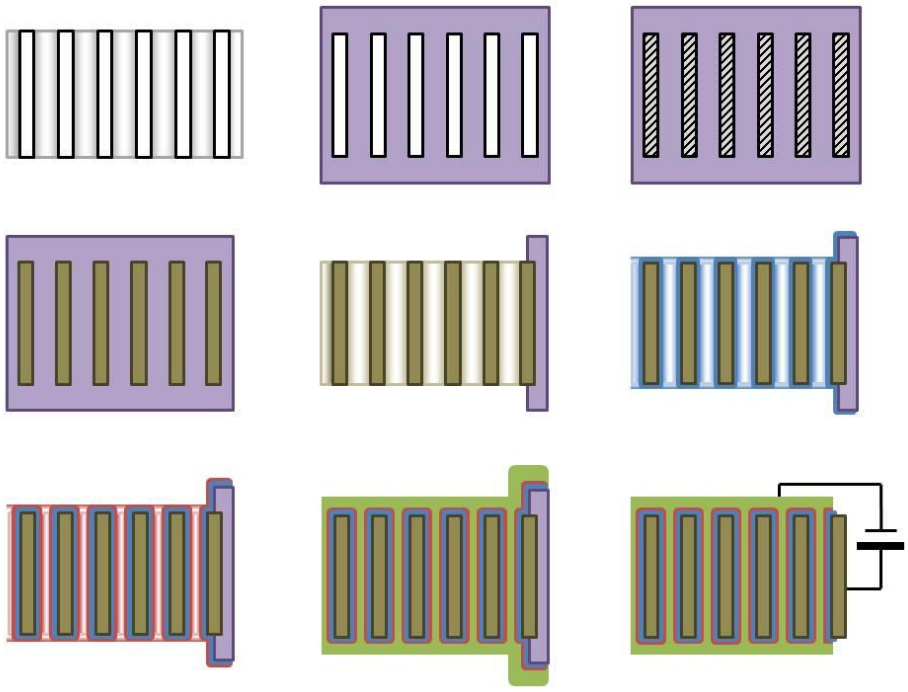

Figure 21: Through-hole AAO template PV device design

An AAO template, produced so that the pores are open at both surfaces, is filled with a chemically resistant material (purple) to form a 3D negative mask of the AAO. The

aluminium oxide is chemically etched away using a suitable etchant. Once the AAO has been removed metal is deposited into the mask. When the mask has been sufficiently filled the mask material is removed leaving the edges still covered. This covered area will be where electrical connection is made to the back contact. Alternatively, a thin metallic layer could be deposited directly and conformally over the AAO template, negating the need to use the described masking steps. Next, ALD is used to deposit the n-type, p type and TCO thin film semiconductors (blue, red and green, respectively) forming the pn-junction and the transparent top contact. The remaining mask material is removed leaving part of the back contact exposed. Electrical connection is made between any part of the growth surface (TCO) and the back contact. This layout of device would offer several advantages: the absorption length of the incident radiation could be matched by the depth of the pores rather than by using a thick absorber layer, reducing material usage. Additionally, as both the back contact and the transparent conductive oxide essentially run all the way through the body of the device, all parts of the active p and n materials would be a very short distance from their respective contacts.

The premise behind this device is to maximise the available pn-junction area whilst utilising as small an amount of space as possible. For example, a normal circular template with radius (R) = 10cm and height (h) = 60μm would have a total surface area of around 0.06m^2. An AAO template comprising of a regular hexagonal arrangement of pores with pore diameters (d_p) = 200nm and an interpore distance (d_i) = 300nm would contain ~4x10^{11} pores, have a porosity of ~0.4 and a total surface area available for deposition of ~15.23m^2. Depositing 50nm of n-type material onto this structure followed by deposition of a p-type material would give a junction area of ~7.57m^2, a 120x increase in area compared to deposition on a similar sized planar structure.

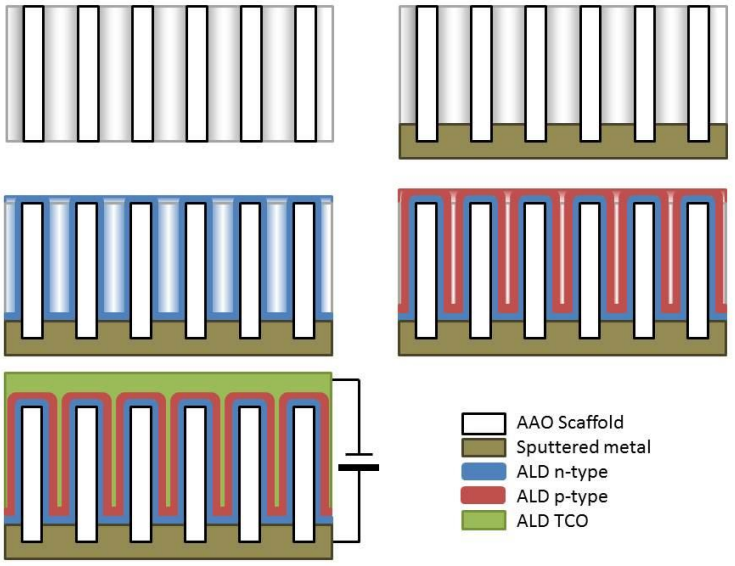

Figure 22: Through-hole AAO PV device design

In this second design (Figure 22) metal is deposited on the rear surface of the through pore AAO template using a line of sight deposition technique such as sputtering or evaporation. This would serve as the back contact. Because of their high aspect ratio and shadowing effects of line of sight deposition techniques, the material would only be deposited a small depth into the pores. Using ALD, a thin layer of n-type semiconductor material would be deposited over the remainder of the exposed AAO template and also at the base of each pore in contact with the metal. Next a p-type material would be deposited over the n-type material forming the pn-junction. Finally a thicker layer of p-type TCO would be deposited which would serve as the top contact and allow light through to the active layers beneath.

Using the same values as in the example for the previous device (R = 10cm, h = 60µm, d_p = 200nm, d_i = 300nm, t = 50nm and the sputter depth, s_d = 2µm) gives an uncoated template area after the back contact application of 14.72m^2 (a comparative loss of around ~0.5m^2) and a pn-junction area of ~7.50m^2 (reduced by ~ 0.07m^2 c.f. the first design). Models describing the derivation of these values can be found in Appendix sections 9.2 and 9.3.

As can be seen from Figure 21 and Figure 22, the area of the pn-junction interfaces for these designs is much larger than that which could be achieved through a more conventional thin-film deposition approach using a planar surface, and is controlled primarily by the height of the template. Another advantage with this design is that the n and p-type films can still be very thin and yet have a large absorption path length for incoming radiation (i.e. the full length of the pores). This would have the potential to save material costs compared to planar devices, where the absorbing layers have to be as thick as the penetration depth of the light (determined by the attenuation coefficient of the material using the Beer-Lambert law) which can be up to hundreds of microns. To achieve the same absorption with this design would simply be a case of using an AAO template of that thickness, while the active layers could be kept in the tens to hundreds of nanometres range. Another possible benefit is that the back contact (depending on the quality and the material of the metal deposited) could act as a reflector, returning any unabsorbed light back up the length of the pore and helping to increase the efficiency of the device or reduce material usage.

There are two significant challenges with these device designs. The first is that as material is deposited and the pores fill up, the diameter of each pore reduces by twice the deposited thickness. This means that it would become more and more difficult for precursor molecules to enter the pores and continue conformal deposition during ALD. In turn this would increase the need for longer exposure and purge times as the deposition progressed. At some critical pore diameter, one would imagine that as it got more difficult for precursor molecules to enter the pores, this conformality would break down, and deposition would only occur near the pore mouth and at the upper surface, blocking further deposition within the pores and leaving long tear-drop shaped voids. In the second design another challenge to overcome is that although any current generated within the p-type layer has a very short distance to travel to the TCO contact, i.e. the thickness of the p-type layer,

current generated near the top surface in the n-type layer would have to travel the full length of the pores to reach the back contact. This would require that the n-type material had a high number of charge carriers and high carrier mobility. This problem could be avoided by depositing a thin layer of conformal metal over the AAO template before the deposition of the n-type layer using ALD or possibly a liquid based approach. Of course, this would also reduce the diameter of the pores and reduce the space available for the active layers.

Ideally for a PV device, a minimum amount of scaffold material should be used leaving the remaining space available for the active layers. With AAO this means a pore diameter as large as possible, approaching the same size as the interpore distance ($d_p \approx d_i$) and giving a porosity (α) close to 1. For perfectly ordered hexagonal pores the maximum value of α is ≈ 0.907 whilst still retaining material at the closest approach between neighbouring pores. Additionally, space is required for ohmic contacts to both the p and n layers to extract usable power.

4.2 AAO Growth Rate

An important consideration in the production of AAO templates is the oxide growth rate. Higher growth rates, without adverse effects such as oxide cracking or the formation of excess barrier layer oxide could allow the cost of production to be reduced and also enable a higher through-put during manufacturing. A literature search revealed that growth rates for various different methods of AAO production range from 0.2µm/hour to 70µm/hour, depending on the electrolyte composition, the temperature of the electrolyte/aluminium and the voltage of the anodisation[27,28,29,30]. Of those that used similar techniques and experimental parameters to those described in this paper, growth rates of 1.59µm/h (at 25V in oxalic acid) to 30µm/h (for ultra small nanopores initiated at 1-10V, followed by prolonged anodisation at 60-70V in oxalic acid) have been reported.

Aluminium samples were anodised in 0.5M oxalic acid at 5°C and 50V. The duration of the anodisations was varied for each sample from 3 hours to 46.5 hours. The thickness of the produced oxide was measured by optical microscopy. A growth rate of 5.7µm/h (1.58nm/s) was determined for these experimental parameters.

The electrolytic cell was set up as shown in Figure 23. High purity aluminium sheet was cut into squares approximately 8mm x 8mm, and each was cleaned in distilled water, acetone and ethanol. The sample dimensions were measured and the samples were attached to the anodes and electropolished in 5% perchloric acid, 61% methanol and 34% propan-1,2-diol at -15°C, 48V and 0.58A for 20 seconds. After cleaning again, the anodes were placed in the electrolytic cell and connected up to the power supply and the data logger. The electrolyte used was either 0.3M or 0.5M oxalic acid cooled to 5°C.

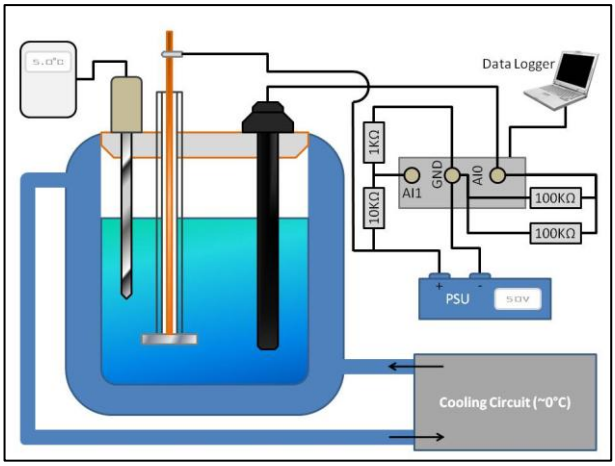

Figure 23: Anodisation cell setup

For the 0.3M electrolyte a constant voltage of 30V was used during the anodisations whilst the duration was varied; 3h, 4.5h and 6h. It should be noted that during the 4.5h anodisation, the cooling on the electrolytic cell failed and the electrolyte had reached a temperature of 26°C by the end of the experiment. For the 0.5M electrolyte a constant voltage of 50V was used following parameters laid out by Zhao *et al.*[13]. The durations of the anodisations were 3h, 6h, 18.75, 19h, 24h and 46.5h. All samples were then cleaned and detached from the anode assemblies. Taking care to orientate the samples so that the oxide layer faced away from the direction of rotation of the polishing discs (to avoid pulling the oxide layer away from the aluminium substrate), the samples were polished in cross section on P600 paper then P1200 for 30s each. The angle of the polished edge relative to the surface of the samples was kept as close as possible to 90° so that measurements of the oxide thickness would not be exaggerated. As they were polished manually, it is estimated that the actual angle is 90°±3°, any more would be easily observable with the naked eye. It is estimated that an error of this magnitude would only increase the measured oxide thickness by around 0.14%. After polishing, the averages of ten measurements of oxide thickness were recorded for each sample using ImageJ software [44].

4.2.1 Results and Discussion

Growth rates of 6µm/hour [27], 1.3-5µm/hour (calculated)[28], 50-66µm/hour (with the addition of an ionic liquid to increase ionic transport in the electrolyte)[41], 0.5-3µm/hour (3V to 10V in oxalic acid), 0.2-1µm/hour (in phosphoric acid) and up to 30µm/hour (70V in oxalic acid)[14], 7.5µm/hour (26V at -3°C in sulphuric acid)[29], 2.27µm/hour (in sulphuric acid at 25V), 3.95µm/hour (in sulphuric acid at 40V), 1.59µm/hour (in oxalic acid at 25V) and 2.20µm/hour (in oxalic acid at 40V)[8], 50-70µm/hour (for hard anodisation parameters in oxalic acid)[9] and 2.4µm/hour (in oxalic acid at 40V)[30] have been reported in the literature to date. Clearly those performed under hard anodisation or in the presence of an additional ionic conductor in the electrolyte would be the most suitable for industrial production as they give growth rates roughly 10 times higher than other methods.

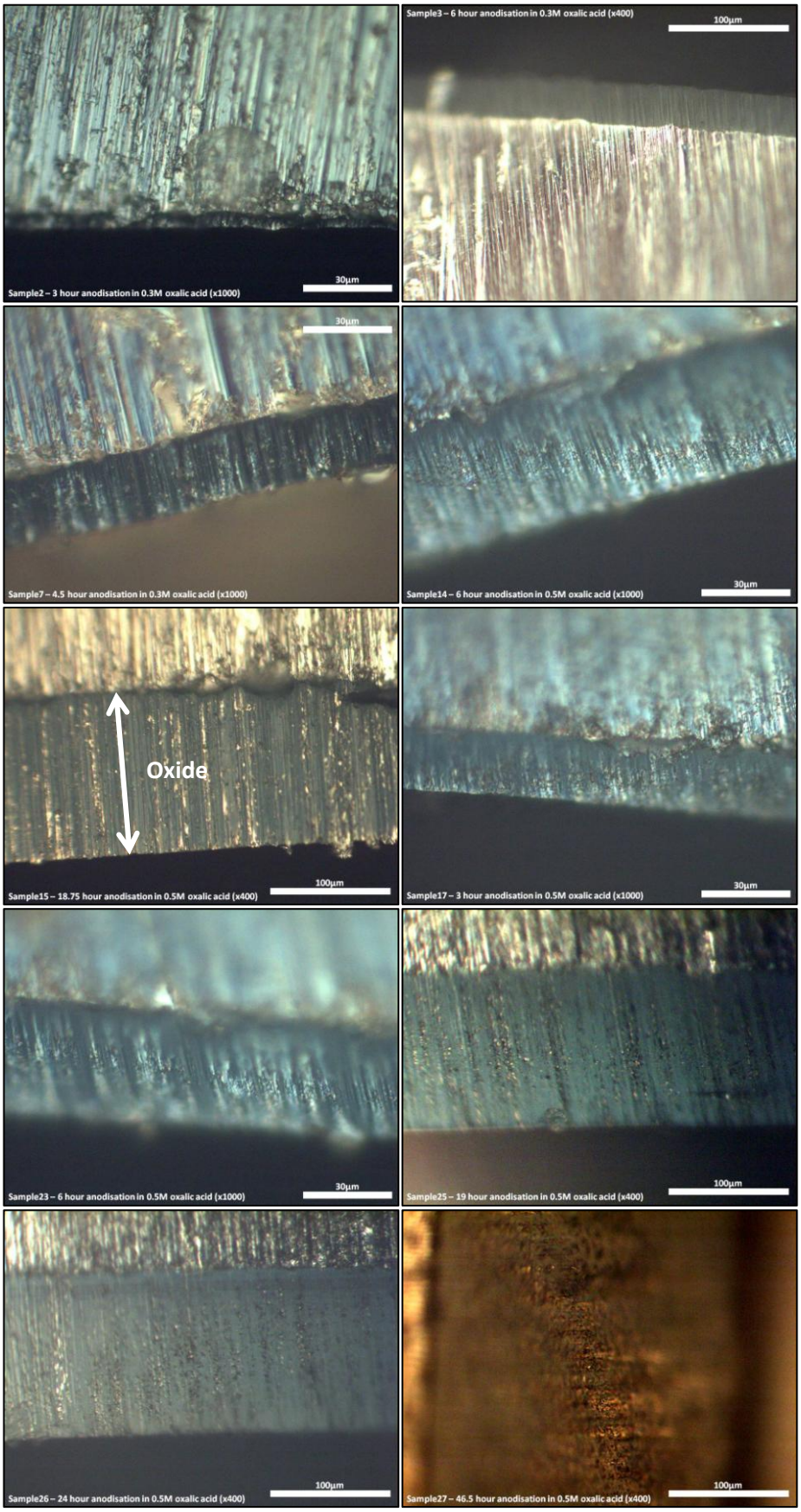

Figure 24: Images used for oxide thickness measurements

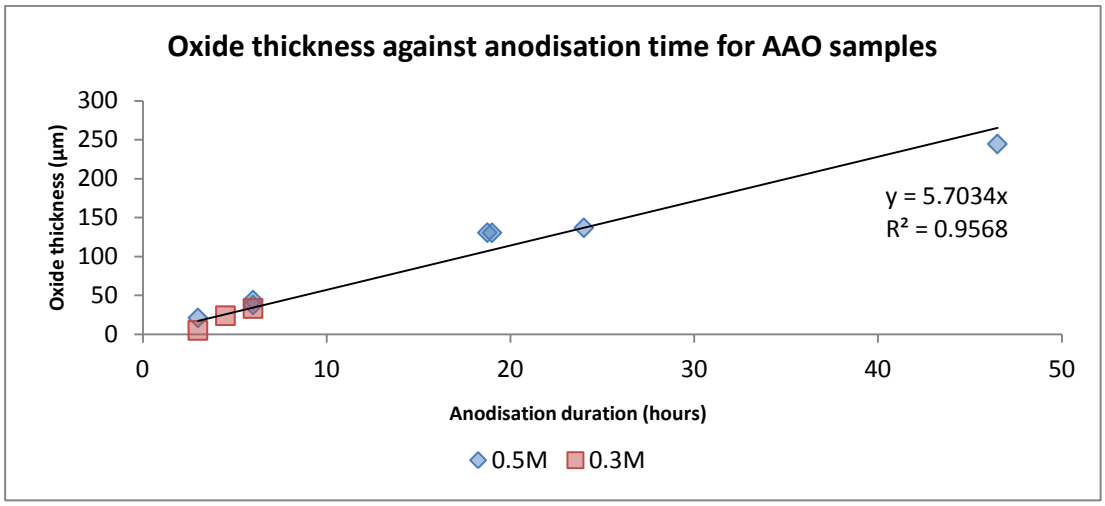

Figure 25: Oxide thickness against anodisation time for all samples

Table 3: Anodisation parameters, oxide thickness and oxide growth rates

Sample	Peak Current Density (mA/cm^2)	Average Steady Current Density (mA/cm^2)	Duration (hours)	Oxide thickness (µm)	Final Electrolyte Temperature (°C)	Oxide growth rate (µm/h)
2	10.9	2.1	3	5.07	5.5	1.69
3	07.9	4.8	6	33.21	5	5.54
7	09.9	7.1	4.5	23.95	26	5.32
14	23.9	7.0	6	44.04	6	7.34
15	10.1	4.7	18.75	130.65	6	6.97
17	19.6	6.6	3	21.15	5	7.05
23	29.7	7.2	6	37.72	5	6.29
25	36.8	6.6	19	130.47	5.4	6.87
26	88.8	6.8	24	136.92	6.1	5.71
27	62.7	4.8	46.5	244.61	4.5	5.26

Table 3 shows experimental details and oxide thicknesses measured from Figure 24. Figure 25 shows that the average growth rate for this set of experiments was found to be 5.70µm/h, which is towards the higher end of the range normally quoted for anodisations performed under similar conditions. This could be due to differences in the anodisation cell setup. In some cell arrangements, the cooling system is in direct contact with the aluminium, and the electrolyte is cooled via contact with the aluminium. The aluminium sample is also orientated differently, with the anodised surface facing upwards and with current to the sample being delivered from above. Presumably the temperature of the

anodised sample is then fairly close to that of the coolant. In the setup used for these experiments, the temperature reported is that of the electrolyte, 1-3cm away from the aluminium sample. The sample is also orientated “upside-down”, with current passing upwards into the sample from the carbon cathode. It is plausible that with this upside-down setup, heat evolved at the metal/oxide interface is less likely to dissipate into the electrolyte via convection currents as it would do for the alternative setup. It has been implied in other papers that the temperature of the interface is a controlling parameter of the rate of oxide growth, along with the anodisation current.

4.2.2 Conclusions

A growth rate of 5.7µm/h was found when anodizing aluminium metal in 0.5M and 0.3M oxalic acid at 50V. This is marginally higher than the figure reported by other researchers using similar conditions, although none that explicitly reported the oxide growth rate used exactly the same parameters as this experiment.

4.3 Effect of 1st Step Anodisation Duration on AAO Pore Arrangement

Since their discovery in 1941[10] and further research in 1953[11], AAO templates have shown excellent potential for the production of high aspect ratio nano-structures. The high uniformity of the pore arrangement that can be achieved mean that these templates offer a highly controllable method of producing precision geometry nanostructures made from a nearly endless variety of materials. This can be done via several processes such as CVD[145], PVD[146], sol-gel deposition[147], ALD[148], liquid ALD[149], electrochemical deposition[5], and several other methods, each with its own benefits and drawbacks[144].

Producing an amorphous pore arrangement, in which the interpore spacing and the pore diameters vary from pore to pore is a relatively simple process, and is done by a single anodisation in a mildly acidic electrolyte at controlled voltages and temperatures. Producing uniformly ordered pores is a more involved process requiring a primary anodisation step, dissolution of the formed oxide and then a secondary anodisation. Alternatively, the second step can be negated if the aluminium surface is mechanically indented with appropriately sized nano-scale concaves prior to the first anodisation.

Previous results suggested that the grain size and orientation of the underlying aluminium has only a minor effect on the hexagonal domain (HD) size and orientation. It was initially expected that the domain boundaries would be highly coincident with the aluminium grain boundaries, as the crystallographic orientation of each grain would affect the resultant angles that the HDs formed at. One would also expect that grains of a certain size would produce HDs of a similar size. This was shown not to be the case, at least for samples prepared without a pre-annealing step.

High purity aluminium samples were anodised in 0.5M oxalic acid, 50V at 5°C using the same anodisation parameters as used in section 4.2. The anodisation time varied between samples from 6 hour to 46.5 hours. The oxide was removed by immersion in 6wt% phosphoric acid and 1.8wt% chromic acid at room temperature for 16 hours. FEGSEM imaging in conjunction with Heyn analysis was used to determine the average diameter of hexagonally arranged indentations at the interface between the oxide and the substrate for each sample. A possible correlation between anodisation time and domain size was found, with the average domain diameter increasing at a rate of 34nm/h.

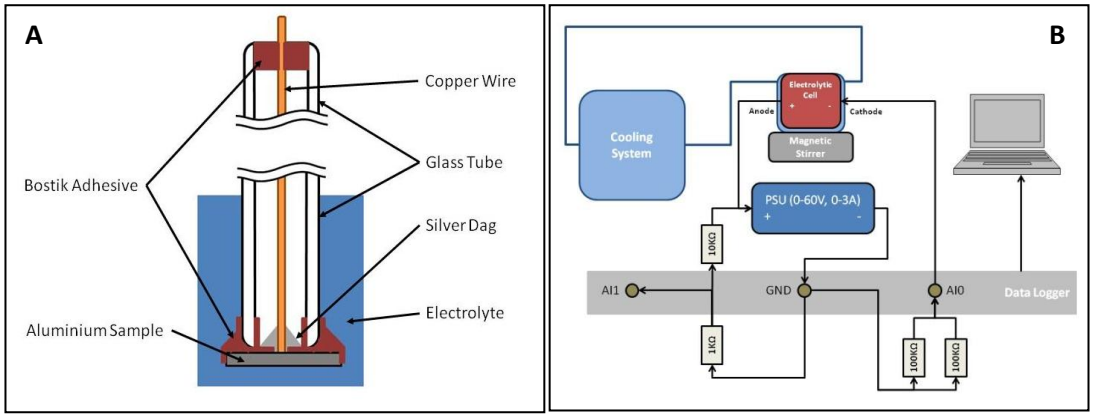

Figure 26: Anode construction (A) and Electrolytic cell set up (B).

High purity aluminium sheet, approximately 0.5mm thick, was cut into squares roughly 8mm by 8mm. The samples were rinsed in distilled water, acetone and ethanol then dried in hot air, to reduce the number of contaminants on the surface. Each sample was then attached to a glass and copper electrode using silver dag and Bostik "All purpose" adhesive (Figure 26, A). The samples were then electropolished to a mirrored finish in 61% methanol, 34% propane-1,2-diol and 5% perchloric acid at -10°C (±5°C), 48V (±0.1V), 0.6A (±0.1A) for 20s. The samples were cleaned again using the same process as outlined above, whilst remaining attached to the electrodes. After electropolishing, the electrodes (anodes) were set up within the anodisation cell with 0.5M oxalic acid as the electrolyte and a carbon rod as the cathode (Figure 26, B). The electrolyte was cooled to 5°C (±2°C). Samples were anodised for 6, 19, 24 and 46.5 hours during which the current, voltage and electrolyte

temperature were measured every 5 seconds. Following each anodisation, samples were cleaned and dried. The samples were then placed in a solution of 6wt% phosphoric acid and 1.8wt% chromic acid at room temperature for 16 hours to dissolve the oxide layer followed by rinsing in the usual manner. This left each sample with a surface covered in a very thin layer of barrier oxide and a series of HDs of various average diameters.

The samples were imaged using FEGSEM. For their analysis, hexagonal domains were manually outlined (Using "ImageJ"[44]) to allow easy identification of neighbouring domains. For the outlining process, regions that clearly switched from "arm-chair" to "zig-zag" orientation or vice-versa, were highlighted first. The ends of these lines were then connected by following apparent paths denoted by lines of raised areas at the intersection of four, five or seven lines of pores. In some cases it was more difficult to determine where the lines should lie as the change between differently oriented domains was gradual. In these instances the line was drawn through pores where it was thought that the change in angle of the lines was greatest. The size of the aluminium grains and the size of the HDs were then recorded using the Heyn intercept method[150]. Multiple images were used for each sample. The average grain size for each sample was recorded by drawing 10 lines at random across each image, determining the line lengths from comparison with the scale bars and counting the number of HDs intersected by the lines. The average HD size for each sample was calculated by summing the average HD size for each image and dividing by the number of images used. As the HD size for each line drawn was calculated, the maximum and minimum values for each image were recorded. These were then averaged by summing the maximum sizes for each sample and dividing by the number of images. This gave the average maximum HD size and the average minimum HD size for each sample.

4.3.1 Results and Discussion

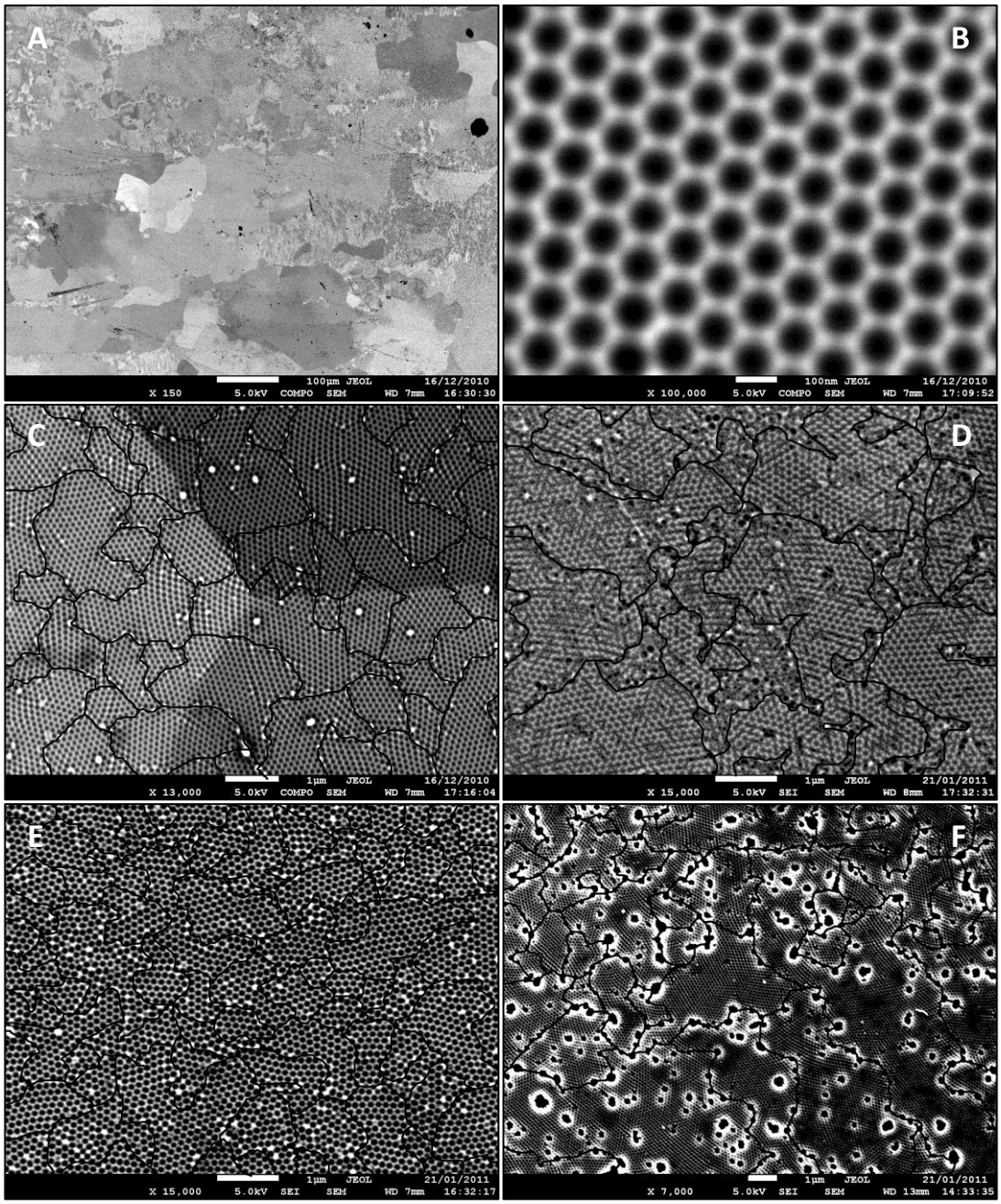

Figure 27: (A) Aluminium surface after anodisation for 6h in 0.5M oxalic acid at 5°C and 50V followed by oxide dissolution in 6wt% phosphoric acid and 1.8wt% chromic acid for 17h at RT. Differently orientated grains are clearly visible (average grain diameter approximately 70µm). (B) Close up of hexagonal domain (HD). (C) HDs outlined [6h run]. (D) HDs outlined [19h run]. (E) HDs outlined [24h run]. (F) HDs outlined [46.5h run].

Micrographs shown in Figure 27 are representative of the majority of the sample surfaces. For the analysis of grain size and hexagonal domain size, multiple images were taken of each sample at varying magnifications and subjected to the Hayn analysis method. This was done to reduce the chance of misleading results due to imaging of unrepresentative sample areas.

FEGSEM analysis of the sample anodized for 6 hours showed that the individual grains were clearly visible (Figure 27 (A)). Using the Hayn intercept method for measuring grain sizes it was determined that the average grain size of the aluminium substrate was approximately 70μm, although there was a great deal of variation between the smallest and largest with some clusters comprised of grains <<1μm. Figure 27 (B) and (C) show the same sample in higher magnifications. (C) shows a meeting point of three aluminium grains. Most of the outlined HDs can be seen crossing over the grain boundaries with little or no alteration to their orientation. This was in agreement with work by other institutions[35], where it was found that the only microstructural component that noticeably influenced the size of HDs was the fraction of aluminium grains showing (100) crystallographic orientation.

For images (D) and (F), i.e. 19h and 46.5h, the process had introduced defects. For the 19h sample, it appeared that the oxide dissolution had not fully completed as the pores seem relatively small compared to the interpore spacing, although this could just be an artefact of the relative contrast compared to the other images. There are also small areas of completely amorphous structure. For the sample anodised for 46.5h, a different problem presented itself. Large holes appeared between and amongst the hexagonal domains. These could have been a result of the unusually long anodisation duration, or a result of the oxide dissolution step being too aggressive. Since the oxide was dissolved using the same parameters as used for the other samples, it is implied that the oxide dissolution was not the sole cause of the pits seen.

It should also be noted that the oxide dissolution step did not complete as expected, with significant amounts of alumina remaining on parts of the surface of two of the samples. For example, the 19h sample still retained the 1st step alumina at its centre, while at the edges dissolution had progressed further and completely removed the oxide leaving the expected indentations. Between the two extremes, partial dissolution of the oxide had occurred,

resulting in a mat-like structure of Al_2O_3 nanowires and tubes (Figure 28, (A) and (B)). In the 46.5h sample the oxide had dissolved from most of the surface, and only a small amount remained covering one corner of the sample in the form of Al_2O_3 nanowires and nanotubes (Figure 28, (C) and (D)).

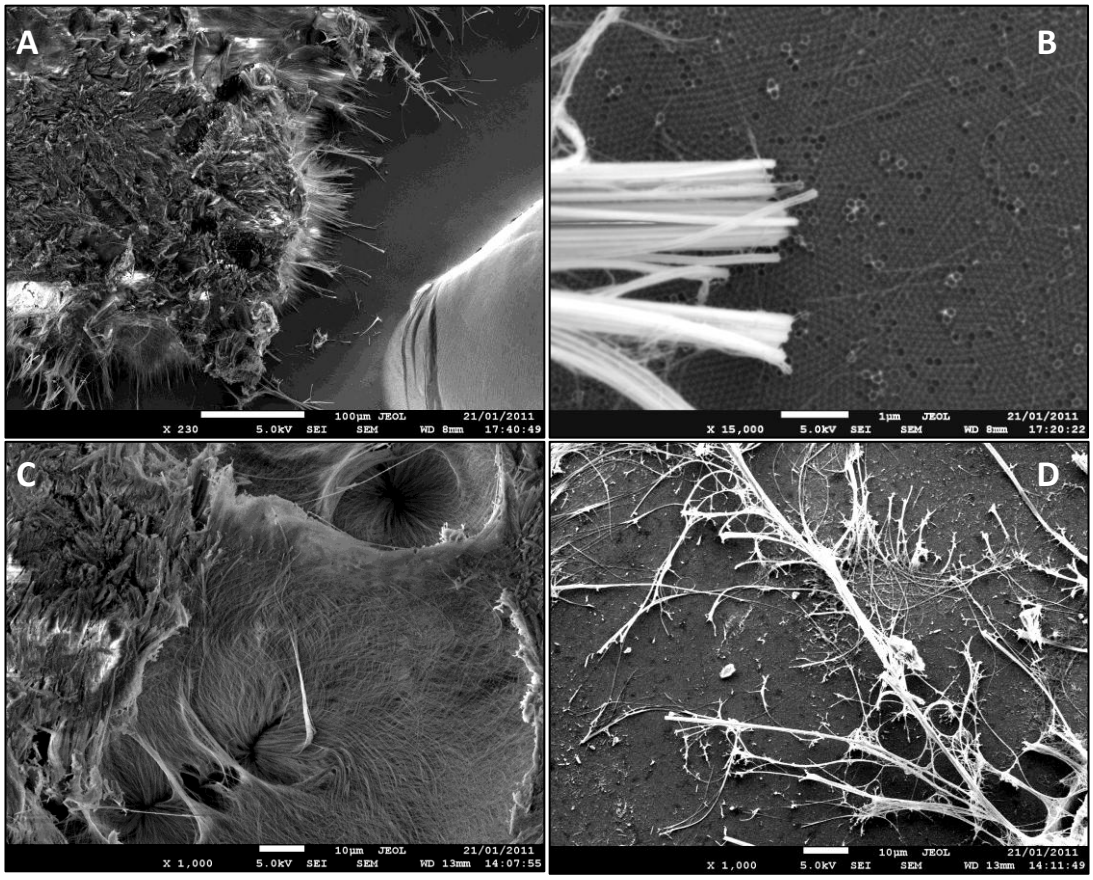

Figure 28: Unexpected structures seen in samples anodised for 19h (A), (B) and 46.5h (C), (D).

From these images it seems as though the dissolution of the oxide does not occur equally across all exposed surfaces of the oxide, as one might expect for a uniformly crystallographically amorphous oxide, but instead seems to preferentially attack either the mid-point of the pore walls between neighbouring pores (which would produce hexagonal nanotubes with outer diameters equal to the interpore spacing) or the entirety of the pore walls (which would leave nanowires of much smaller diameters, i.e. similar magnitude to the point of intersection between three adjacent pore walls). From Figure 28 (B), it seems that both of these processes had taken place, as both structures were visible. Could this process be controlled it might offer a route to the production of high aspect ratio hexagonal

alumina nanotubes. As the oxide is produced at the base of each pore and ejected vertically, it is plausible that the oxide between pore walls is of a different nature to the oxide that makes up the bulk of the pore walls, and hence is attacked preferentially, separating the individual tubes. The nanotubes grown here are similar in appearance to TiO_2 nanotubes grown by via a similar anodisation process in electrolytes containing water and fluorine [151]. It was found by Li et al. that the density of the produced oxide between pores was lower than for that making up the "bulk" material due to the incorporation of additional OH groups. This lower density leads to a splitting of adjacent pores forming the nanotubes as the growth of the oxide proceeds. It is plausible that a similar process has occurred here, with molecules from the electrolyte becoming incorporated into the pore walls and further concentrated where adjacent strain fields meet. Once exposed to the phosphoric acid used to dissolve the 1st step oxide, these areas could preferentially dissolve leaving the structures seen.

Table 4: Results from Heyn analysis of FEGSEM images

Run duration (hours)	Average Electrolyte Temp (°C)	Overall Average HD size (nm)	Max Average HD size (nm)	Min Average HD size (nm)	Standard deviation (nm)	Number of Lines Sampled
6	5.5	1226	3037	764	424	50
19	6.3	1623	3617	695	761	40
24	6.5	832	1865	505	246	40
46.5	4.1	2593	5856	819	1119	40

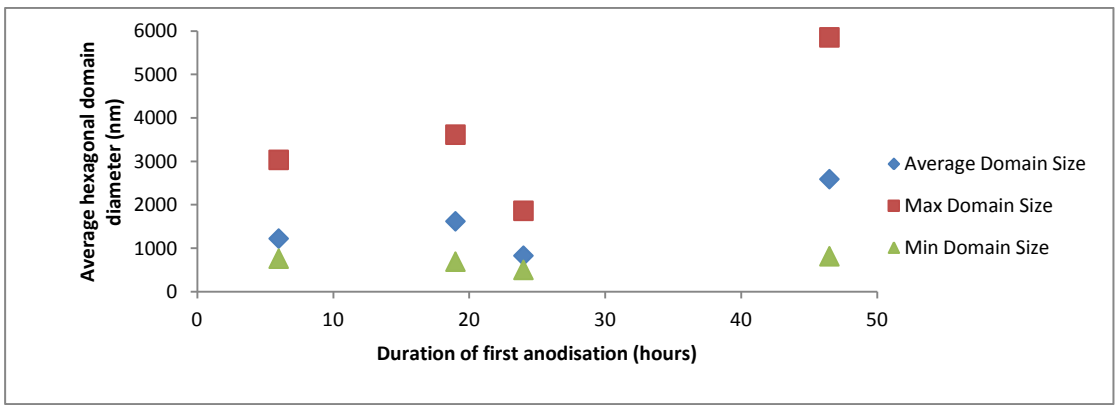

Figure 29: Average domain diameter against anodisation duration

Table 4 and Figure 29 show the results of the Hayn intercept analysis. Moving from shorter to longer anodisation durations, there appeared to be a trend whereby the average HD size increased in a linear manner along with the maximum average HD size. Ignoring for the moment the sample anodised for 24h, the average HD size increases linearly following the equation:

$Average\ HD\ diameter = 34t + 1004$ where t = time in hours and $HD\ diameter$ is in nm (Coefficient of determination (R^2) = 0.998).

The maximum and minimum average HD sizes were also recorded for each sample. It was thought that the process might follow a similar pattern to that exhibited by grain growth, i.e. the larger grains grow by consuming neighbouring smaller grains. For these three samples, the maximum average grain size was found to follow the equation:

$Maximium\ average\ HD\ diameter = 71.4t + 2467$ with a coefficient of determination of 0.984.

The minimum average HD diameter did not change much between experiments, remaining around 700nm (±100nm). This does not necessarily mean that the process did not follow grain growth, as there was some difficulty in assessing the smaller HDs. Obviously, the smallest possible HD would be the same size as one pore diameter, but determining how disorderly areas should be split up presented its own difficulties and was thought to be of little benefit. It was decided that disordered areas should simply be counted as 1 domain for this analysis. In further experiments examining this process, this should be addressed. The best way would be to automate the process, possibly utilizing a similar method as shown in Mátéfi-Tempfli S., 2008[45], i.e. particle analysis of the FEGSEM images followed by Delauney and Voronoi tessellation.

Another factor to be considered is that the HD growth rate of 34nm/h was quite low, and may not be the most economically sound method of producing larger HDs when compared to other methods such as mechanically polishing, annealing and electropolishing[117] samples prior to the anodisations. If this effect is real, however, using it in conjunction with alternate anodisation techniques that significantly enhance the oxide growth rate and thus the relative motion of pores might be a viable option. One technique that should be considered would be to use an electrolyte additive to increase ionic conduction through the electrolyte[41]. Another could be to use hard anodisation parameters[9].

There is one significant outlier however; the sample anodised for 24h shows much smaller HDs than any of the other samples, even the one anodised for 6h. This could be the result of the sample having a rougher surface to begin with and therefore initiating more pores, or that the sample was in a more stressed state at the beginning of the anodisation. Both of these seem a little unlikely as all samples came from the same sheet of aluminium and were cut using the same methods. Including the data from this sample in the analysis significantly reduces the coefficient of determination for all of the remaining data and displaces the line of best fit to quite a large degree. Further tests at different anodisation durations would be required to categorically state whether this result was due to one or more uncontrolled anodisation parameters and whether the linear relationship between time and HD size is a real effect.

4.3.2 Conclusions

It appeared that the average hexagonal domain diameter increased at roughly 34nm per hour for samples anodised under the above conditions. As this was based on results from only three samples, further tests would be required to confirm that the observed effect is real, especially considering that one sample did not follow the same pattern. It is also questionable as to how useful this effect would be. At just 34nm/h, very long anodisation

times would be required to appreciably increase the diameter of HDs, whereas altering the other process steps might be a more effective way to increase domain sizes.

4.4 Deposition of TiO_2 into Anopore AAO Templates Using ALD

ALD of TiO_2 onto commercially purchased AAO templates was attempted to assess whether it was possible to use this technique to conformally coat the substrates including deep within the porous structure. AAO templates were used due to their extremely high aspect ratio (which would test the exposure theories proposed by other research groups), while ALD was chosen for its ability to uniformly coat the surfaces of structures unable to be coated by other deposition processes.

Experiments were carried out to test the effect of different purge, pulse and hold times for ALD precursors used to deposit on extremely high aspect ratio porous AAO templates. For the test parameters selected, partial deposition down the lengths of the AAO pores was found to occur but with preferential deposition at the upper and lower template surfaces and in the AAO pore mouths. Due to the extremely high aspect ratio of the pores, along with the sub-MFP pore diameters, it was thought that to achieve uniform coating, prohibitively long ALD run times would be required.

An OpAL ALD reactor was adapted to include a stop-flow valve and vacuum trap, in order to increase the residence time of precursor gases during each ALD cycle. Commercially available AAO templates of two different pore diameters and high aspect ratios of approximately 300 and 600 were subjected to various deposition parameters. By holding the $Ti(O^iPr)_4$ precursor gas within the reactor it was hypothesised that longer residence times would give the gas molecules a higher chance of adsorbing on all surfaces to the bottom of the pores, thus producing longer nanotubes. Secondly, a simple model of weight gain for a given thickness of deposited TiO_2 was proposed and tested.

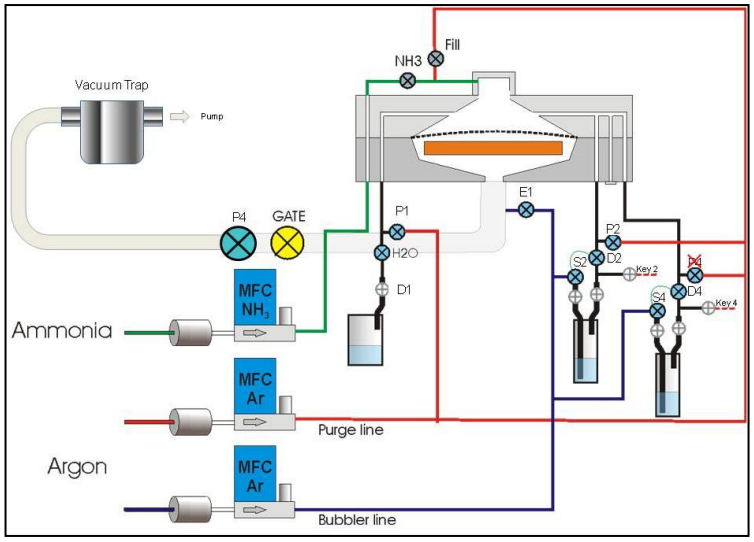

Figure 30: Schematic of modified OpAL ALD reactor

The ALD reactor was modified to allow precursor gases to be held within the reactor chamber for a controlled length of time. This was done by adding another ALD control valve between the vacuum pump and the reactor exhaust (Figure 30). To avoid damage to the vacuum pump due to unwanted precursor reactions that could occur while the gases were being held within the reactor, a vacuum trap consisting of several nested wire-mesh cages was installed between the new ALD valve and the vacuum pump. Due to software constraints, electronic control of the new valve could only be achieved by using the control for an existing valve; since the planned ALD runs required two precursors (H_2O and $Ti(O^iPr)_4$), the control system for the P4 valve on the second precursor bubbler was used. Unlike the other valves in the system, the P4 valve was set up to remain constantly open until a signal was received from the software, at which point the valve would close.

For safety reasons, the bubbler lines were not to be used during depositions utilising the stop-flow valve (P4). With the exhaust closed and the bubbler lines active it would be very likely that pressure could build to dangerous levels within the chamber, possibly causing damage and/or risk to any operators nearby. Because of this, both H_2O and $Ti(O^iPr)_4$ were delivered to the chamber by vapour-draw alone. To ensure that no additional pressure was

added by the bubbler lines, the manual valve on the gas inlet to the $Ti(O^iPr)_4$ bubbler was closed.

Table 5 shows the parameters and ALD sequence that were used for the deposition of TiO_2:

- Reactor bed temperature: 225°C
- $Ti(O^iPr)_4$ bubbler temperature: 60°C
- H_2O bubbler temperature: RT (~19°C)

Table 5: Process steps for deposition of TiO_2 varying Ti hold duration (Runs: STOPTest2[535], 536, 537, 538)

Step #	Title	Gas flow (sccm)	Open Valves	Duration (s)
1	Draw H_2O	200	D1, P4	0.05
2	Purge H_2O	200	P1, P4	10
3	Stabilise	0	P4	5
4	Ti vapour draw	0	D2, P4	3
5	Ti hold	0	None	x
6	Ti purge	200	P2, P4	4
7	H_2O draw	0	D1, P4	0.05
8	H_2O hold	0	None	1
9	H_2O purge	200	P1, P4	10
10	Stabilise	0	P4	1
11	Repeat steps 4-10 x300			

The duration of step 5 (Ti hold, x duration) was varied between experiments from 2 – 7 seconds as this was thought to be the limiting step due to hindered diffusion of $Ti(O^iPr)_4$ molecules down the AAO pores. Step 8 (H_2O hold) was not thought to be a limiting step (or at least not as limiting a step as step 5) due to the relative difference in size between the two; ~6Å for $Ti(O^iPr)_4$ [152] and ~1.5Å for H_2O.

Table 6: Deposition parameters testing variation of $Ti(O^iPr)_4$ purge times (Runs: 545, 546, 547)

Step #	Title	Gas flow (sccm)	Open Valves	Duration (s)
1	Draw H_2O	200	D1, P4	0.05
2	Purge H_2O	200	P1, P4	10
3	Stabilise	0	P4	5
4	Ti vapour draw	0	D2, P4	3
5	Ti hold	0	None	10
6	Ti purge	200	P2, P4	x
7	H_2O draw	0	D1, P4	0.05
8	H_2O hold	0	None	1
9	H_2O purge	200	P1, P4	10
10	Stabilise	0	P4	1
11	Repeat steps 4-10 x300			

The duration of step 6 ($Ti(O^iPr)_4$ purge, x duration) was varied between experiments from 2 – 6 seconds to attempt to limit any non-ALD deposition due to precursor overlap.

Table 7: Deposition parameters testing variation of H_2O purge times (Runs: 548, 549, 550, 552)

Step #	Title	Gas flow (sccm)	Open Valves	Duration (s)
1	Draw H_2O	200	D1, P4	0.05
2	Purge H_2O	200	P1, P4	10
3	Stabilise	0	P4	5
4	Ti vapour draw	0	D2, P4	3
5	Ti hold	0	None	10
6	Ti purge	200	P2, P4	4
7	H_2O draw	0	D1, P4	0.05
8	H_2O hold	0	None	1
9	H_2O purge	200	P1, P4	x
10	Stabilise	0	P4	1
11	Repeat steps 4-10 x300			

The duration of step 9 (H_2O purge, x duration) was varied between experiments from 6 – 14 seconds in an attempt to limit any CVD-like deposition due to precursor overlap.

Table 8: Deposition parameters testing variation of H_2O hold times (Runs: 551, 553, 554, 555)

Step #	Title	Gas flow (sccm)	Open Valves	Duration (s)
1	Draw H_2O	200	D1, P4	0.05
2	Purge H_2O	200	P1, P4	10
3	Stabilise	0	P4	5
4	Ti vapour draw	0	D2, P4	3
5	Ti hold	0	None	3
6	Ti purge	200	P2, P4	4
7	H_2O draw	0	D1, P4	0.05
8	H_2O hold	0	None	x
9	H_2O purge	200	P1, P4	10
10	Stabilise	0	P4	1
11	Repeat steps 4-10 x300			

A silicon wafer was included in each ALD run for the purpose of ellipsometric measurements after the deposition. The Si wafer was measured at a minimum of two locations to check for deposition homogeneity. Anopore AAO templates were also placed within the reactor for each run, one with average pore diameters of 200nm and one with average pore diameters of 100nm. Each sample was weighed before and after the ALD run to determine the weight gain.

Due to the disordered arrangement of pores in each sample (having only undergone a single anodisation step with no pre-patterning) there was thought to be some variation in both the pore diameters and the interpore spacings. For the purposes of the mass gain predictions, average values were used: 100nm and 200nm average pore diameters (as quoted by the manufacturers) and 152nm and 330nm average interpore spacing, respectively. These two values were found by taking the mass of the templates, calculating the expected mass for a solid alumina disc of the same dimensions using the lower quoted value for the density of the oxide (3.95g/cm^3) and dividing one by the other to find the porosity (0.3967 and 0.3322 respectively). By rearranging the Keller porosity equation, average values for d_i could be found.

A simple model of the surface area of the pores was constructed. The surface area was found to be:

$$A = \frac{2\pi^2 d_p h R^2}{\sqrt{3}{d_i}^2}$$

Where R = AAO template radius, d_p = average pore diameter, d_i = average distance between the pore centres, h = AAO template thickness.

This equation gave values of 0.125m^2 and 0.053m^2 for the 100nm and 200nm pore diameter templates respectively.

An equation for the maximum expected mass gain was also proposed:

$$M = \rho n \pi h\left(d_p t - t^2\right)$$

Where ρ = deposition density, $n = \frac{2\pi R^2}{\sqrt{3}{d_i}^2}$ = number of pores and t = deposition thickness.

Given an ideal ALD coating, i.e. no deposition due to CVD or PVD like processes, the mass gain could be used to estimate the depth of penetration of the coating:

$$Penetration\ depth = \frac{M_{measured}}{2\rho n\pi\left(d_p t - t^2\right)}$$

This equation assumes equal deposition from both sides of the template and gives a maximum value of ½ of the template thickness.

SEM analysis and EDX depth profiling was conducted on several sample cross sections using a Jeol7001 electron microscope. Cross sections were prepared by mechanical fracture of the templates. EDX was performed at ten locations, 6µm apart, through the oxide with the first measurement taken at the upper surface and the last taken at the lower surface.

4.4.1 Results and Discussion

A series of experiments and simulations by J. W. Elam et al. were conducted into ALD of Al_2O_3, ZnO and SiO_2 onto through-hole AAO templates with d_p = 65nm and h = 60µm. It was found for Al_2O_3 ALD with a relatively high surface reaction probability (~10^{-3}) that the limiting step showed a $t^{1/2}$ time dependence indicative of diffusion limited behaviour, whereas SiO_2 ALD with a low surface reaction probability (~10^{-8}) showed a t^1 time dependence indicating reaction limited behaviour[109]. For the experiments conducted here it was presumed that the surface reaction probability for TiO_2 ALD was similar to that of Al_2O_3, hence the deposition would be diffusion limited. During the experiments concerning ZnO ALD, it was found that to achieve a uniform coating down the full 30µm (deposition occurred from both ends of each pore simultaneously) exposure times of around 30s were needed. One major difference that should be noted between the results found by Elam et al. and the results under discussion here are that the DEZ, TMA and $SiCl_4$ precursors have a significantly smaller effective molecular radii than $Ti(O^iPr)_4$; any diffusion limited processes

that occur would affect $Ti(O^iPr)_4$ to a larger degree, hence it is probable that longer exposure times would be necessary.

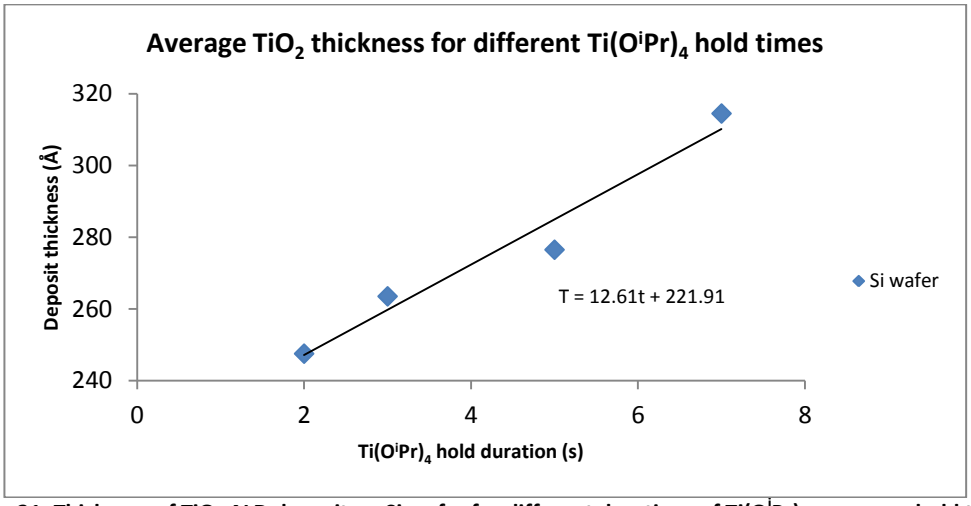

Figure 31: Thickness of TiO_2 ALD deposit on Si wafer for different durations of $Ti(O^iPr)_4$ precursor hold times

Figure 31 to Figure 34 show the average TiO_2 thickness deposited on each of the Si wafers used in this set of experiments, as measured by ellipsometry. Figure 31 shows a clear, near linear increase of thickness with increasing $Ti(O^iPr)_4$ hold time. This indicates that under these parameters ALD style growth was not occurring, as 300 precursor cycles were used for each run. For ALD growth, this graph should have shown a constant value of around 180Å, given an expected maximum growth rate of 0.5 - 0.6 Å/cycle [(143)]. These results could have been caused by either precursor decomposition within the reaction chamber as a result of the process temperature being too high or by residual precursor gases remaining within the chamber as the next precursor pulse enters, causing them to react in the atmosphere above the samples and deposited material in a continuous manner, akin to a CVD/PVD process. Since the deposition temperature of 225°C is well within the range for stable ALD of TiO_2 from a $Ti(O^iPr)_4$ precursor[(143)] (200°C - 275°C), it was thought that precursor overlap was more likely. The reason behind the long residence times for the remaining precursors during the purge step could be that the unreacted precursor that has managed to enter the pores of the AAO remains trapped within it for significant lengths of

time, requiring an increased purge duration to accompany the increased exposure of the precursor.

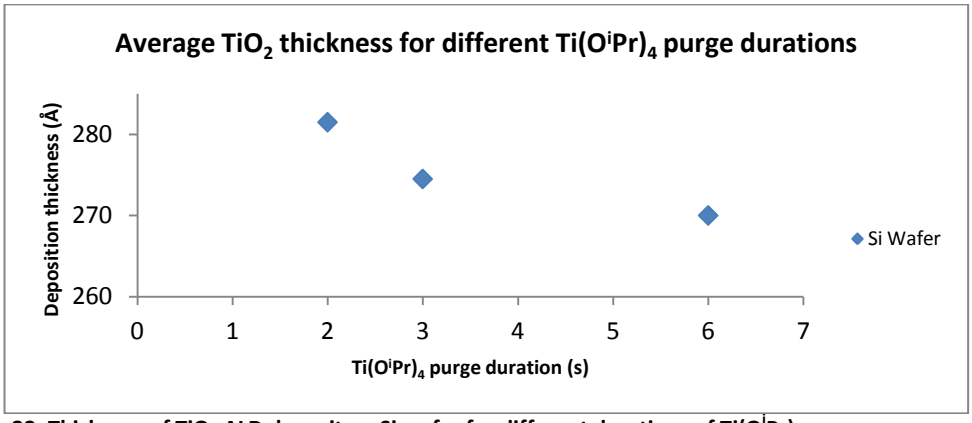

Figure 32: Thickness of TiO_2 ALD deposit on Si wafer for different durations of $Ti(O^iPr)_4$ precursor purge times

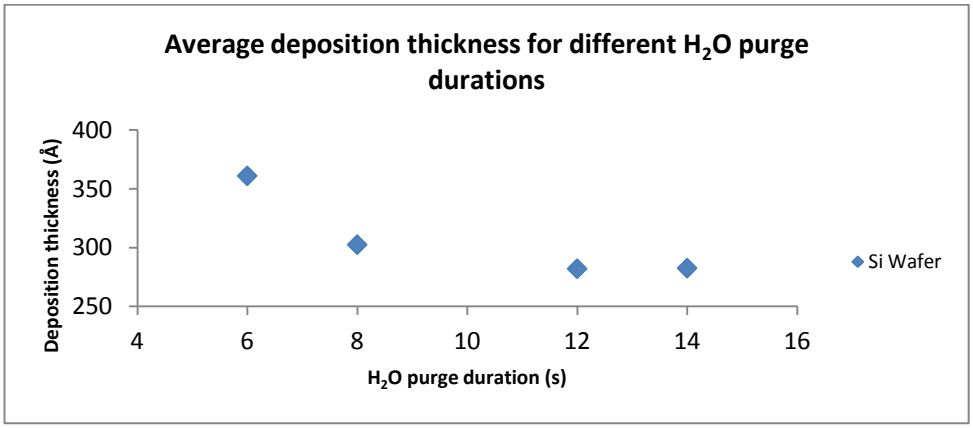

Figure 33: Thickness of TiO_2 ALD deposit on Si wafer for different durations of H_2O precursor purge times

Figure 32 and Figure 33 show the change in deposition thickness with increasing purge times for both $Ti(O^iPr)_4$ and H_2O precursors. In Figure 32, increasing the $Ti(O^iPr)_4$ purge duration from 1 to 6 seconds caused the deposition thickness to reduce by 11Å indicating that there could be some precursor overlap between the $Ti(O^iPr)_4$ pulse and the following H_2O pulse. In Figure 33 an increase in the H_2O purge time from 6 to 14 seconds caused a thickness reduction of 79Å, again indicating that there was some overlap between the H_2O pulse and the following $Ti(O^iPr)_4$ pulse. Both graphs show curves that look as if they may be "levelling off" at the higher purge durations, but further data points would be required to confirm this. Additionally, due to the relative difference in the deposition thickness decrease between both graphs it could be that the H_2O molecules are more likely to remain

in the reactor after a dosing pulse, subsequently reacting with the next $Ti(O^iPr)_4$ pulse. This could be due to higher adsorption/desorption of the molecules on the reactor walls compared to the $Ti(O^iPr)_4$ pulse, or it could be due to a higher number of H_2O molecules entering the reactor during a given pulse, thus a higher number of molecules remaining in the reactor after the H_2O purge. By increasing both purge durations simultaneously in future experiments it should be possible to bring the deposition thickness down to a level more indicative of ALD, i.e. ≤ 180Å over 300 cycles.

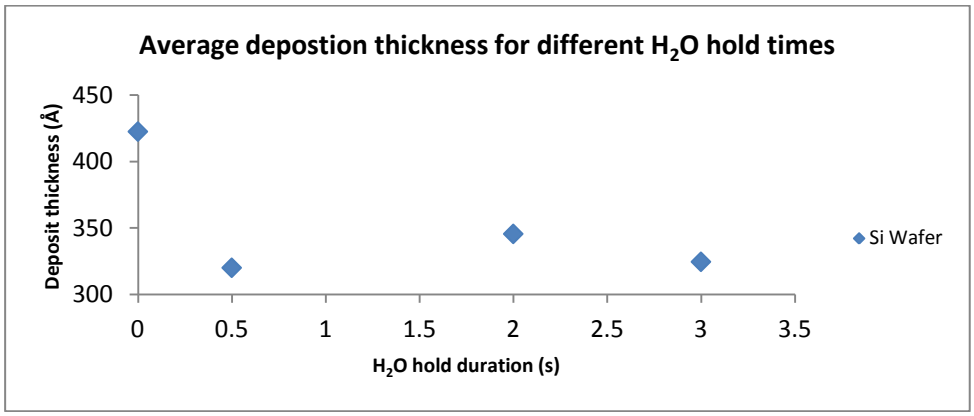

Figure 34: Thickness of TiO_2 ALD deposit on Si wafer for different durations of H_2O precursor hold times

Figure 34 shows the change in deposition thickness on a Si wafer for changing H_2O hold times. The first value (0 seconds hold time) give a deposition thickness of ~420Å or 1.4Å per cycle. A thickness of this magnitude is the result of a non-ALD style deposition. This seems a little counter-intuitive as for shorter hold times one would expect the deposition to be lower, especially considering that a non-ALD process could be occurring. It should be noted that during this run the Si wafer showed small yellowish dots of deposited material, visible with the naked eye; this indicated that there could have been a problem with the precursors used and that a completely unwanted and unexpected chemical reaction had taken place causing the high thickness seen in on the Si sample. The mass gain for each sample during the same run did not show a corresponding peak; it is possible that the growth was confined to specific locations on the samples, and although there was little variation in the ellipsometry data recorded from the Si wafer, this cannot be ruled out

without taking more readings. The following values (0.5, 2 and 3s hold times) show a reduced deposition rate compared to 0s, closer to the quoted value for the growth rate of TiO_2 from TiP and H_2O. These results imply that the full ALD surface reaction occurs in time scales shorter than 0.5s and that significant desorption of H_2O for hold times up to 3s does not occur.

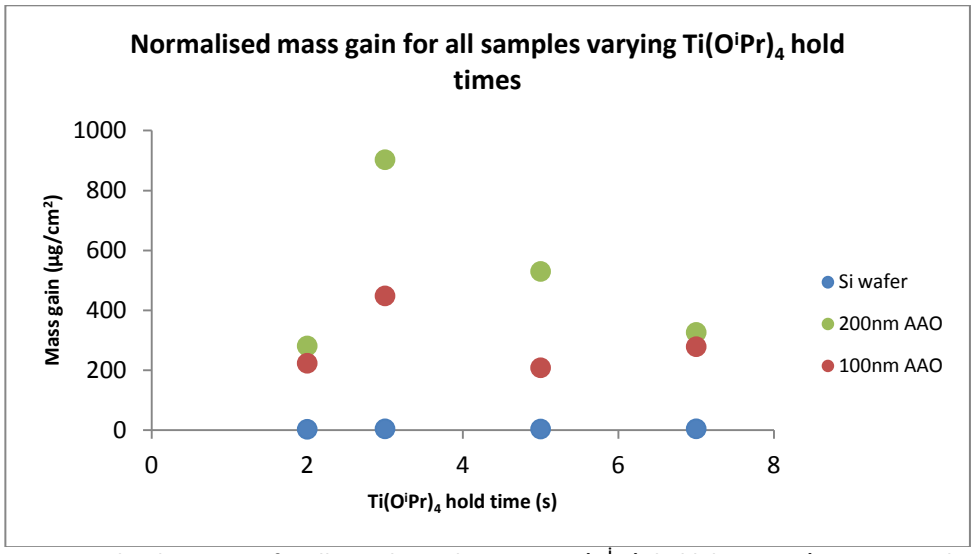

Figure 35: Normalised mass gain for all samples under varying $Ti(O^iPr)_4$ hold durations (using nominal surface area for AAO samples, i.e. discounting the additional surface area due to the porosity)

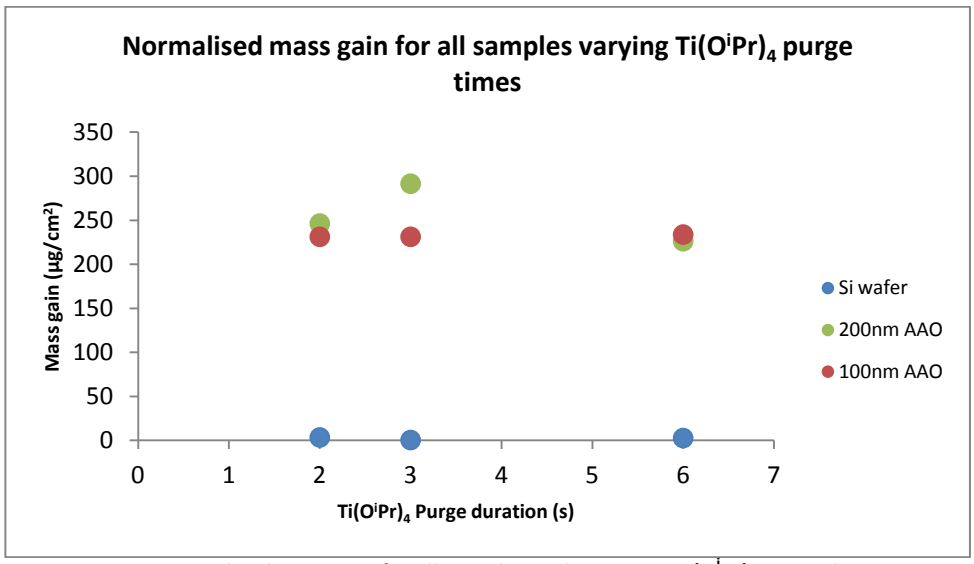

Figure 36: Normalised mass gain for all samples under varying $Ti(O^iPr)_4$ purge durations

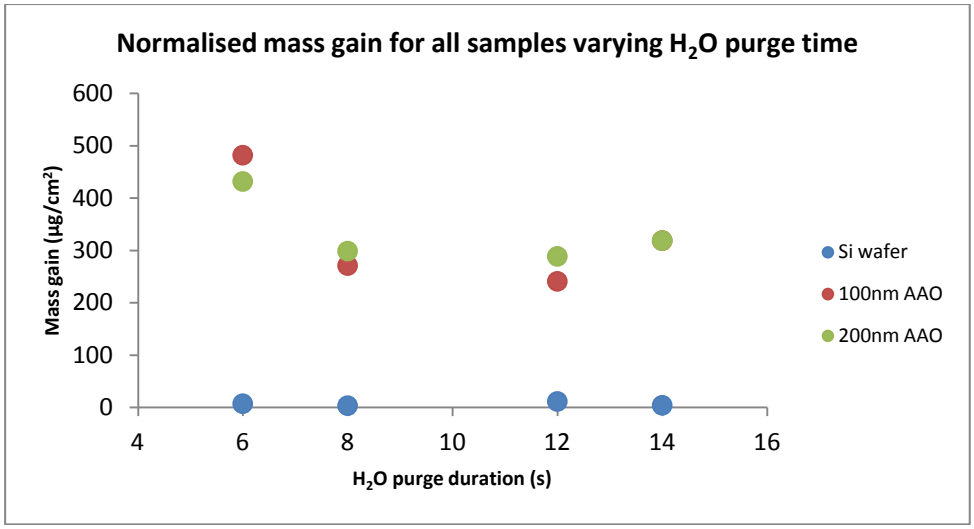

Figure 37: Normalised mass gain for all samples under varying H_2O purge durations

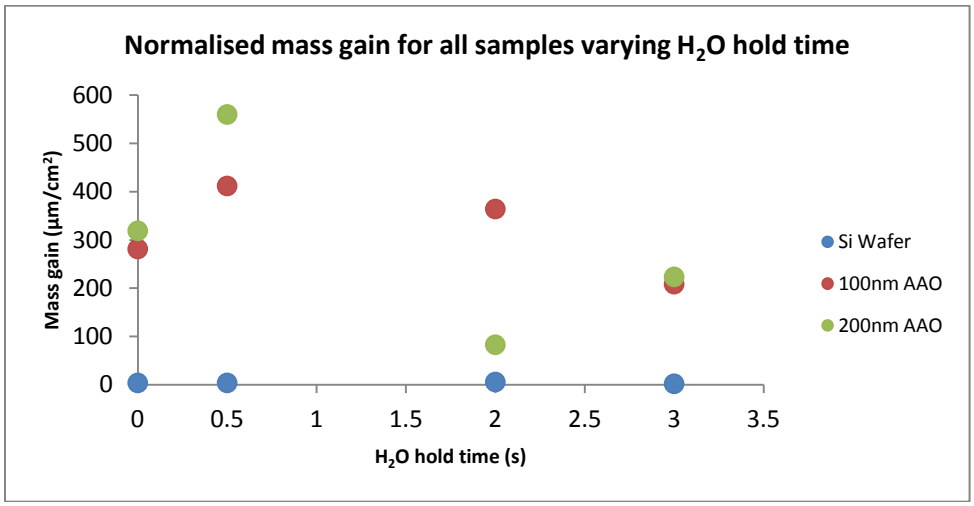

Figure 38: Normalised mass gain for all samples under varying H_2O hold durations

For Figure 35 to Figure 38, i.e. the normalised mass gain for each sample (normalised with respect to the calculated available surface area of each substrate. For a derivation of the surface area for AAO templates see Appendix 1), it is apparent that there is significant ingress of the ALD precursors, and also significant deposition taking place within the pores of the AAO templates when compared to the mass gain for the Si wafers. In the majority of cases, the mass gain for the 200nm pore diameter templates is larger than the mass gain for those with 100nm pore diameter, as would be expected due to much easier diffusion of precursors into and out of the larger pores. For both the 100nm and 200nm templates the mass gain is approximately 100-200 times greater than for the Si wafers.

Table 9: Comparison of maximum predicted mass increase against measured mass increase (±0.0005g)

$Ti(O^iPr)_4$ hold duration (s)	Deposition thickness on Si wafer (nm)	Predicted max mass gain - 100nm pores (g)	Actual mass gain - 100nm pores (g)	Predicted depth of deposit (µm - %)	Predicted max mass gain - 200nm pores (g)	Actual mass gain - 200nm pores (g)	Predicted depth of deposit (µm - %)	TiO_2 growth rate (Å/cycle)
2	24.75	0.00985	0.00030	0.9 – 1.5	0.00487	0.00037	2.3 – 3.8	0.825
3	26.35	0.01026	0.00060	1.8 – 2.9	0.00513	0.00120	7.0 – 11.7	0.878
5	27.65	0.01058	0.00028	0.8 – 1.3	0.00535	0.00070	3.9 – 6.5	0.922
7	31.45	0.01140	0.00037	1.0 – 1.6	0.00594	0.00043	2.2 – 3.6	1.048
$Ti(O^iPr)_4$ purge duration (s)								
2	28.15	0.01070	0.000307	0.9 – 1.4	0.00543	0.00033	1.8 – 3.0	0.938
3	27.45	0.01053	0.000307	0.9 – 1.5	0.00531	0.00039	2.2 – 3.7	0.915
6	27.00	0.01059	0.000310	0.9 – 1.5	0.00526	0.00030	1.7 – 2.9	0.900
H_2O purge duration (s)								
6	36.10	0.01220	0.00064	1.6 – 2.6	0.00664	0.00057	2.6 – 4.3	1.203
8	30.25	0.01116	0.00036	1.0 – 1.6	0.00576	0.00040	2.1 – 3.5	1.008
12	28.20	0.01071	0.00032	0.9 – 1.5	0.00544	0.00038	2.1 – 3.5	0.940
14	28.25	0.01072	0.00042	1.2 – 2.0	0.00544	0.00042	2.3 – 3.9	0.942
H_2O pulse duration (s)								
0	42.25	0.01291	0.00037	0.9 – 1.4	0.00748	0.00042	1.7 – 2.8	1.408
0.5	32.00	0.01151	0.00055	1.4 – 2.4	0.00603	0.00074	3.7 – 6.1	1.067
2	34.55	0.01196	0.00048	1.2 – 2.0	0.00641	0.00011	0.5 – 0.9	1.152
3	32.45	0.01178	0.00028	0.7 – 1.2	0.00613	0.00030	1.5 – 2.5	1.082

shows the results of each run along with comparisons of the recorded mass gain against the predicted maximum mass gain presuming complete conformal coating down each pore based on the recorded deposition. In all cases the recorded mass gain is much lower than the predicted mass gain and in most cases corresponds to a conformal deposition of between 0.9 and 6.7 percent of the pore depth (from both surfaces simultaneously). The one exception to this was the 200nm pore diameter AAO template used in the first set of experiments varying the $Ti(O^iPr)_4$ hold duration with a hold duration of 3 seconds. This showed an apparent deposition depth of over 11%. Again, due to the lack of true ALD growth, it is not possible to verify the validity of the model based on these results.

Another factor which may be influencing the use of the weight gain equations is that the samples may lose mass within the reactor when subjected to the reactor bed temperature and the low pressures of the atmosphere within the chamber. If this is happening during the deposition process then the measured weight gain will be higher than it appears. The manufacturers data on the Anopore discs used for this experiment states that “No additives

[are] used in the manufacturing process [which] ensures minimal extractables and no sample contamination" [116]. This implies that there should be little weight loss when placed under high temperature vacuum conditions. However, it is known that during the anodisation of Al in acid electrolytes a certain amount of the ions from the acid are incorporated into the Al_2O_3 layer that is in direct contact with the electrolyte. Typically, to produce templates with pore diameters of 100nm and 200nm, oxalic acid is used giving the possibility of the incorporation of oxalate anions [9]. It is possible that the temperatures and pressures used could cause the release of the anions into the reactor chamber. These might then go on to react with the ALD precursors as they are introduced, enabling unwanted gas phase reactions and possible deposition of unwanted material. The release of material could be tested by placing templates within the reactor at typical temperatures, pressures and durations, weighing the samples before and after. These templates could then be used for further ALD.

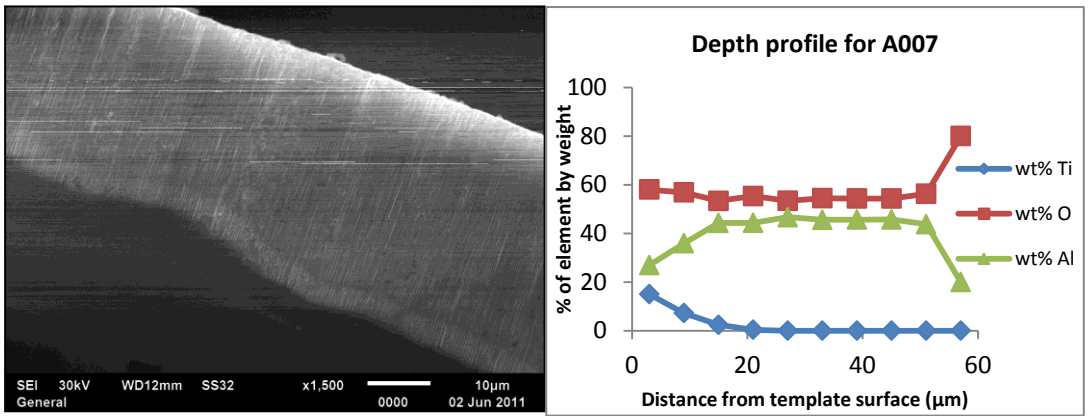

Figure 39: Left - SEM cross section of A007 (3s Ti dose, 5s Ti hold, 4s Ti purge, 0.05s H_2O draw, 1s H_2O hold, 10s H_2O purge, 300 cycles). Right – EDX depth profile

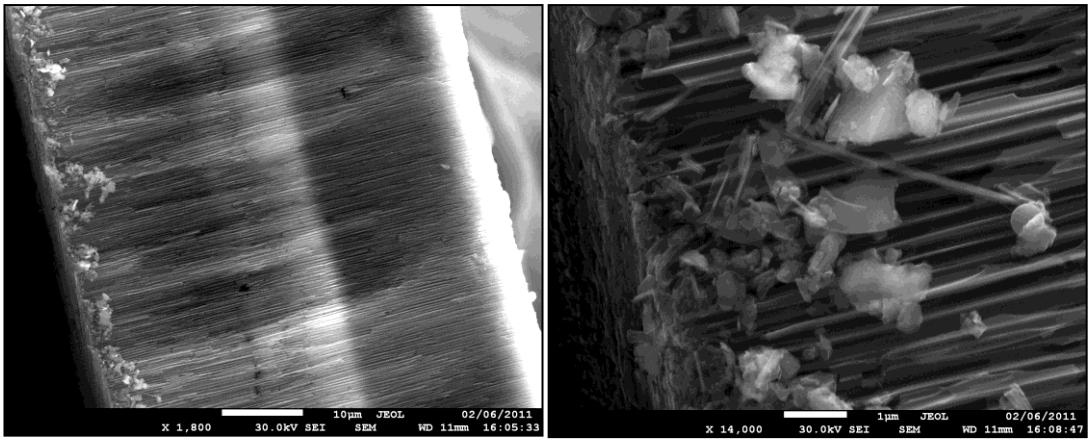

Figure 40: Left - SEM cross section of sample A016 (3s Ti dose, 7s Ti hold, 2s Ti purge, 0.05s H_2O dose, 1s H_2O hold, 6s H_2O purge, 300 cycles) showing charging effect at surface and unusual deposit on opposite surface. Right – Close up of unusual deposit at surface.

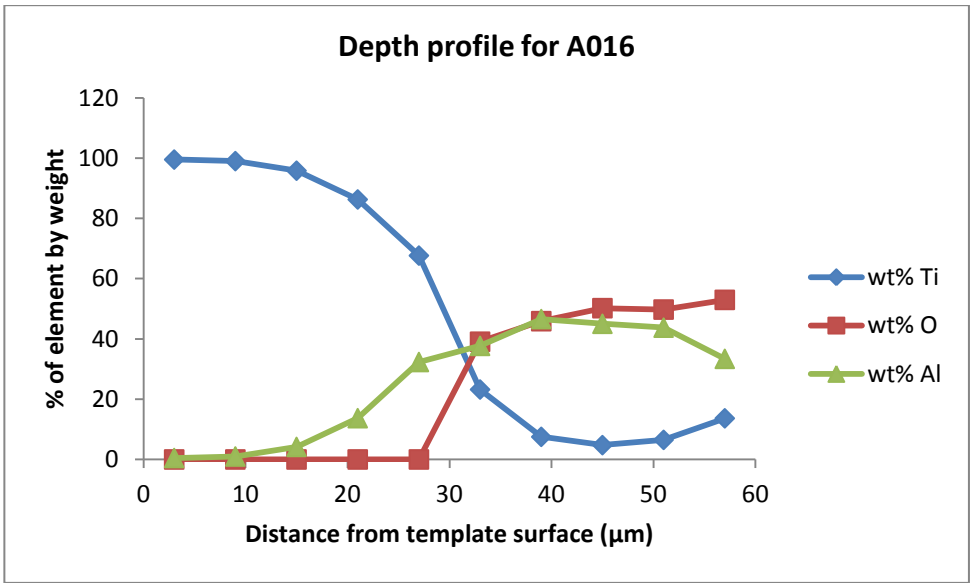

Figure 41: EDX depth profile for A016

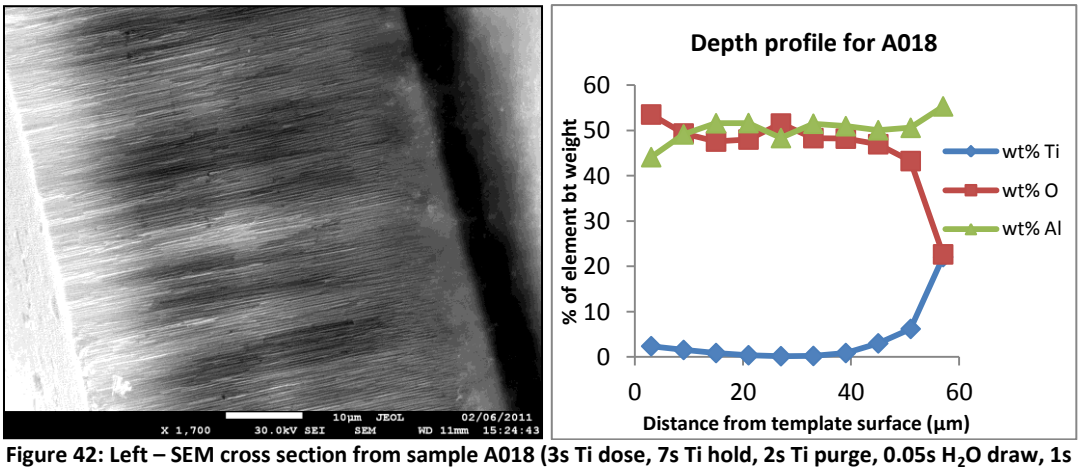

Figure 42: Left – SEM cross section from sample A018 (3s Ti dose, 7s Ti hold, 2s Ti purge, 0.05s H_2O draw, 1s H_2O hold, 14s H_2O purge, 300 cycles)

Figure 39 to Figure 42 show the SEM cross sections of the AAO templates and the results of the EDX line-scans. The SEM images show no clear evidence of NW structures within the

pores. All of the images show significant contrast difference between the bulk and the upper surface implying that there is some physical difference between the two manifesting as a difference in the electronic interaction with the electron beam, but whether this is due to the presence of nanostructures or just an effect of the AAO surface is unknown. Focussed Ion Beam (FIB) milling could be used in further work to produce vertical or lateral cross sections of the AAO tempates which could then be followed by high resolution SEM and EDX to image and quantify the distribution of TiO_2 within the pores.

From the EDX results it is clear that deposition of TiO_2 occurs preferentially on the upper surface. This is thought to be an effect of the pores tapering as they go deeper into the oxide, with the widest section being that which was anodised first. The wider pores allow gas molecules to diffuse into the structures more easily, giving higher levels of deposition. EDX for samples A018 (Figure 42) and A007 (Figure 39) show preferential deposition at one surface, with the ratio of Ti dropping to negligible levels at roughly 20µm depth. The profile for A016 (Figure 41) is rather odd as it shows that the cross section is nearly 100% Ti in the upper 20µm. This directly contradicts the SEM image of the same sample which shows that there is certainly Al and O there, i.e. the template material.

4.4.2 Conclusion

Depositions onto AAO templates showed significant normalised mass gain compared to planar Si wafers indicating that at least some deposition had occurred within the porous AAO structure.

Precursor overlap may be the cause of the failure of ALD to uniformly coat within the AAO structure as shown by the preferential deposition of material at the pore mouths. Longer purge times for both the H_2O and the $Ti(O^iPr)_4$ precursors are thought to be required in future experiments to reduce this effect.

The assumptions made in the mass gain model cannot be confirmed as either valid or invalid without further experimental results, and as such the error margins associated with these assumptions have not been quantified.

EDX Results suggested that deposition did not penetrate the full depth of the pores; much longer precursor hold times might be required to allow for diffusion liming effects of nano-scale pores. Additionally, higher partial pressures of reactants could be used to increase the precursor exposure, coupled with increased purge durations to allow the reactants to egress from the pores and reduce the chance of precursor overlap.

4.5 ALD of TiO_2 into AAO templates with Increased Precursor Exposure

Following on from the initial test depositions of TiO_2 onto high aspect ratio AAO templates, further experiments were carried out using higher precursor exposures (which, from the equations proposed by Gordon et al. and Elam et al., should increase the deposition of material within the porous structure). This was achieved by utilising a diffusion valve ALD system, increasing the residence time of the reactant gases over the substrate's surfaces.

TiO_2 was deposited onto 100nm pore diameter AAO templates using a modified Picosun ALD reactor. The diffusion valve modification was found to increase the exposure of precursors allowing an increased depth of deposition into the pores. SEM imaging and measured weight gain indicated that significant deposition had taken place in the templates, although no nanowires were visible.

100nm pore diameter AAO templates from Whatman [153] were placed inside a Picosun ALD reactor for the deposition of TiO_2. $Ti(O^iPr)_4$ and H_2O precursors were used. Temperatures for the precursor bubblers were 110°C and 19°C respectively. The chamber temperature was 225°C. Line flows for all experiments were kept constant (MFC10-40: 50sccm, MFC1: 100sccm). The following recipes were used:

Table 10: Sample PS4

Step #	Precursor	Flow (sccm)	Pulse time (s)	Purge time (s)	Stopflow duration (s)	Stopflow emptying (s)
1	$Ti(O^iPr)_4$	50	3	240	38	200
2	H_2O	50	3	240	38	200
3	Repeat x 150					

Table 11: Sample PS5

Step #	Precursor	Flow (sccm)	Pulse time (s)	Purge time (s)	Stopflow duration (s)	Stopflow emptying (s)
1	$Ti(O^iPr)_4$	50	5	240	38	200
2	H_2O	50	5	240	38	200
3	Repeat x 150					

Table 12: Sample PS6

Step #	Precursor	Flow (sccm)	Pulse time (s)	Purge time (s)	Stopflow duration (s)	Stopflow emptying (s)
1	$Ti(O^iPr)_4$	50	3	260	58	200
2	H_2O	50	3	260	58	200
3	Repeat x 150					

Table 13: Sample PS7

Step #	Precursor	Flow (sccm)	Pulse time (s)	Purge time (s)	Stopflow duration (s)	Stopflow emptying (s)
1	$Ti(O^iPr)_4$	50	3	190	38	150
2	H_2O	50	3	190	38	150
3	Repeat x 220					

Mass gain during ALD was recorded for all samples and compared with maximum expected mass gain calculations. Deposition thickness was recorded by inclusion of an Si wafer next to each template. The Si wafer was subjected to ellipsometric measurement after the ALD process. Templates were fractured in cross section and examined using a Jeol7001 FESEM with EDX analysis. It was noticed that when running the deposition on sample PS7, the ALD chamber pressure was much higher than for the other samples when the diffusion valve was active. This was attributed to the capillary tube used in the diffusion system becoming constricted, possibly from deposition of material in the tube during previous ALD runs. From the point of view of these experiments, this was viewed as a good occurrence as an increase in the pressure also increases the exposure (pressure multiplied by time) according to the equations devised by Elam *et al.* and Gordon *et al.*[107,109], and would result in an increased depth of NW:

$$Pt = 2.3 \times 10^{-7}\sqrt{m}\tau\left(\frac{l}{d_p}\right)^2$$ - J.W. Elam

$$Pt = S\sqrt{2\pi mkT}\left(1 + \frac{19a}{4} + \frac{3a^2}{2}\right)$$ - R.G. Gordon

4.5.1 Results and Discussion

Table 14: Deposition thickness, mass gain and predicted penetration depth for NW growth

Sample	Deposition thickness on Si wafer (nm)	Calculated max. possible mass gain (mg)	Measured mass gain (±0.05mg)	Predicted depth of Ti (μm)	Number of cycles	Growth rate (Å/cycle)
PS4	8.57	4.14	0.83	6.01	150	0.57
PS5	8.07	3.92	0.78	5.96	150	0.54
PS6	8.45	4.09	0.93	6.82	150	0.56
PS7	10.7	5.05	1.28	7.60	220	0.49

All porous samples showed weight gain significantly above that expected for a planar surface implying that considerable deposition of material into the pores of the template had occurred. All Si samples showed deposition rates consistent with ALD of $Ti(O^iPr)_4$ and H_2O, i.e. around 0.5-0.6 Å/cycle (). SEM imaging failed to show definitive evidence of NW growth as the contrast difference between Al_2O_3 and TiO_2 material was not apparent (Figure 43, Figure 45 and Figure 47). This could be due to the amorphous nature of both materials. It is possible that a post ALD annealing step may result in polycrystalline TiO_2 which may make imaging easier.

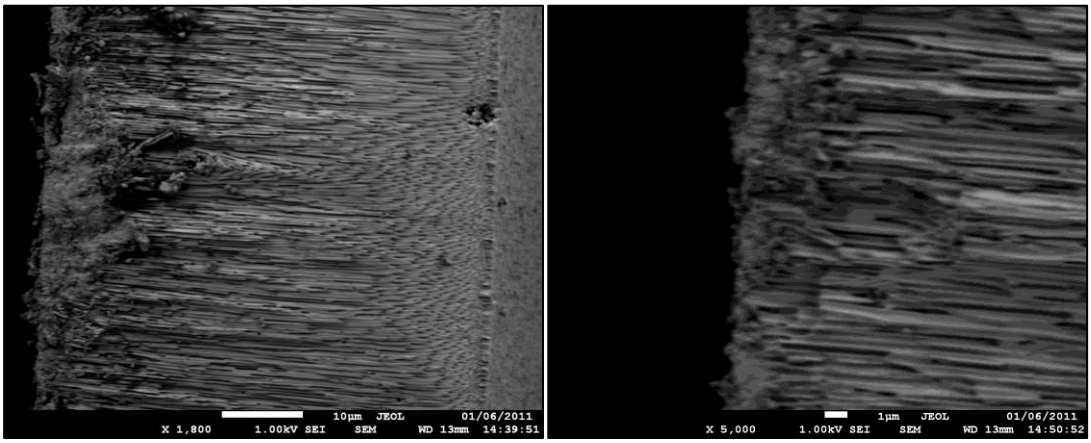

Figure 43: Left - Cross section of PS4, Right – Close up of deposit on upper surface

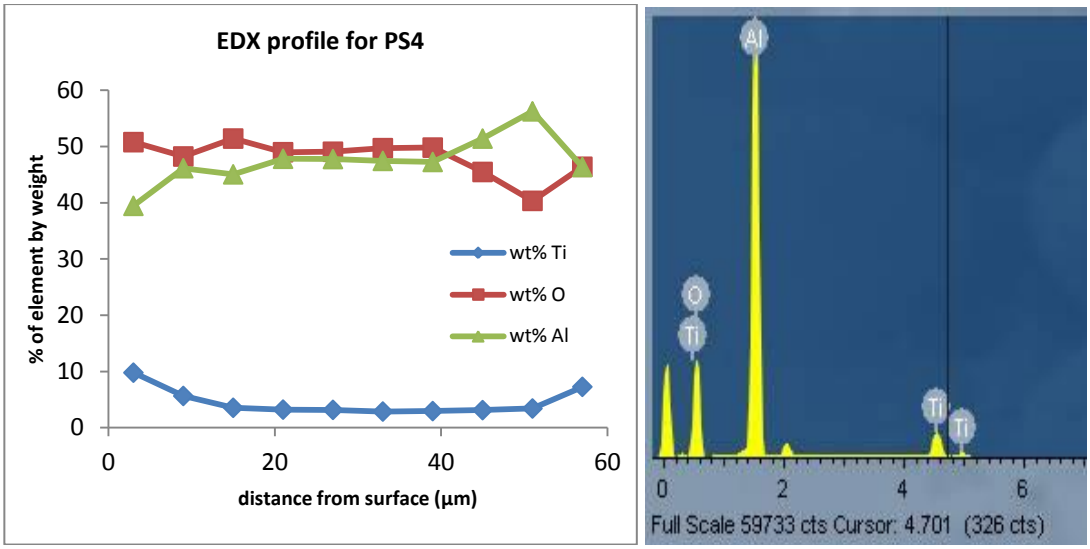

Figure 44: Left - EDX profile plot of sample PS4 (wt% Ti approx 10% at edges decreasing to 3% at middle), Right - Example EDX spectrum taken at ~21µm from sample surface.

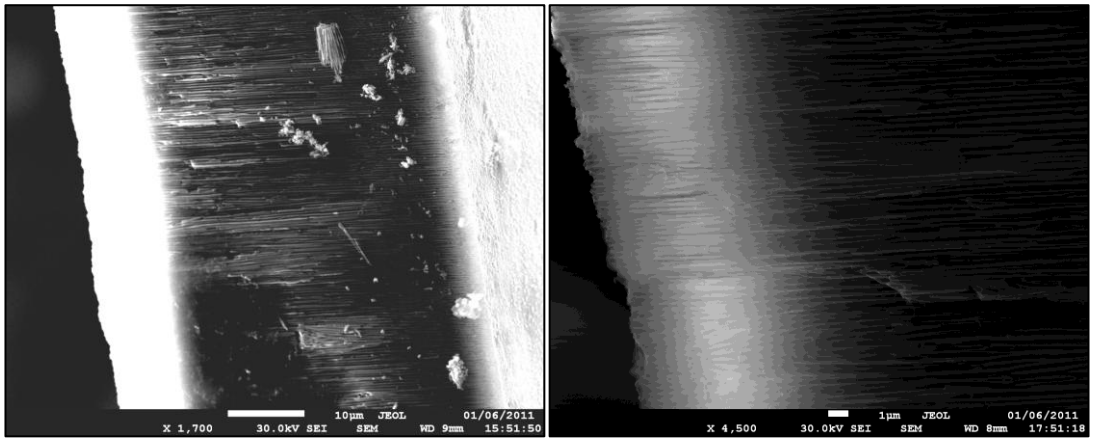

Figure 45: Left – SEM cross section of PS5 showing charging at upper surface. Right – Close up of charging area.

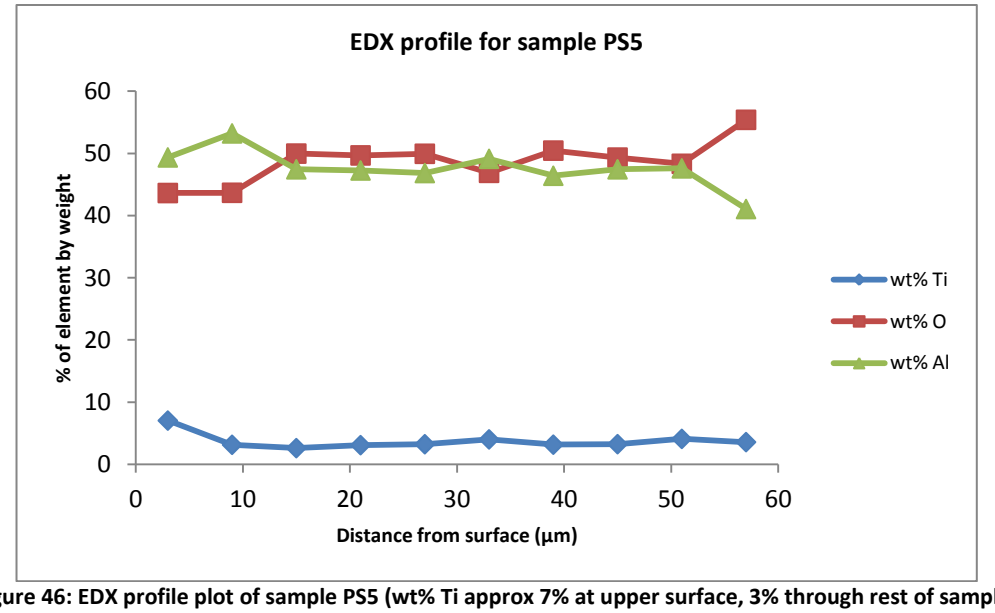

Figure 46: EDX profile plot of sample PS5 (wt% Ti approx 7% at upper surface, 3% through rest of sample)

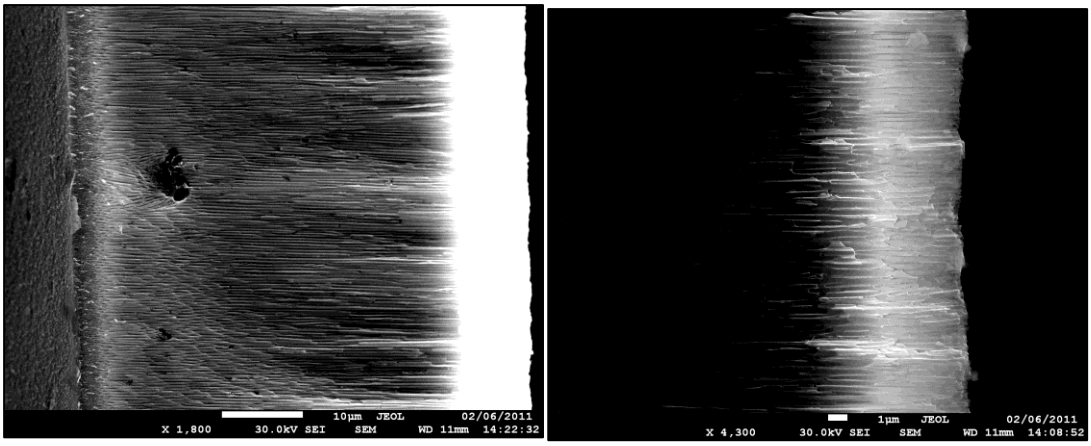

Figure 47: Left – SEM cross section of sample PS6, Right – Close up of charging area at surface.

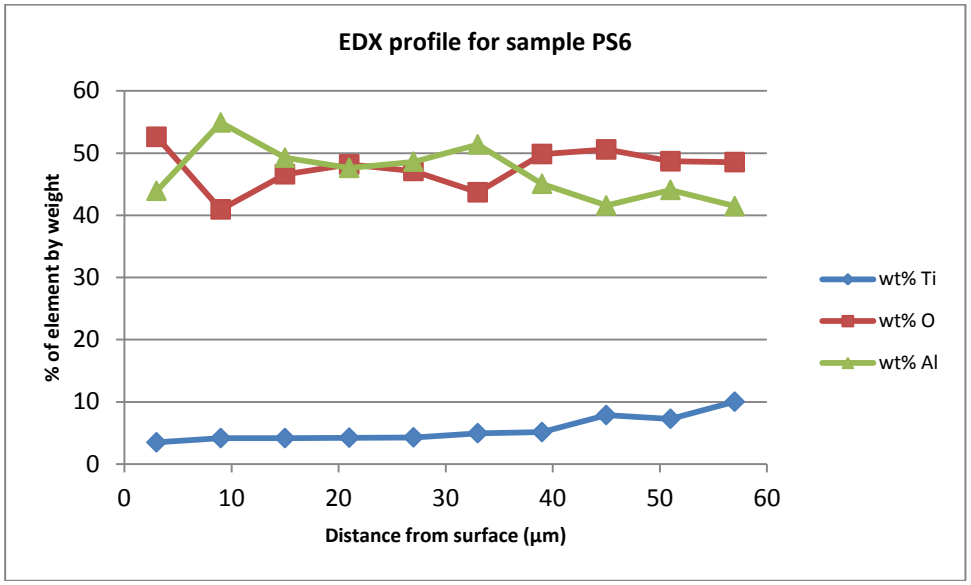

Figure 48: EDX profile plot for sample PS6 (wt% Ti approx 10% at upper surface, reducing to 3.5% at lower surface)

The EDX profiles (Figure 44, Figure 46 and Figure 48) show that Ti has succeeded to some degree in reaching right through to porous structure, although there is a significant difference in the amount of Ti present at the surfaces compared to the bulk of the template. Also, it appears as though deposition has not occurred equally from both sides for each template. This is thought to be because of a slight difference in pore sizes between the upper and lower surfaces. Previous SEM work found that for the majority of templates the pores on the upper surface were larger than those on the lower surface, except in a small percentage of the surface where they were roughly equal. The flow of gas molecules entering the smaller pores would be more restricted than those entering the larger pores from the other side leading to uneven deposition rates.

Both sample PS5 and PS6 show an interesting charging effect corresponding to the regions with the highest wt% Ti (Figure 45 and Figure 47). This could be due to the formation of high capacitance oxide NW structures which have charged under the influence of the electron beam. Close examination of the right-hand image in Figure 45 shows a reduced pore diameter in the first ~10µm from the sample surface compared to further down the pores. This roughly corresponds with the EDX plot, which shows the wt% Ti reducing to a minimum at around 9µm. It also roughly fits with the NW depth as predicted by the weight gain equation. Since the equation assumes equal deposition from both sides of the template, which the EDX shows has not happened here, the value should be doubled to account for deposition from one side. This gives a predicted depth of ~12µm, but assumes that the NW structures terminate abruptly at this depth. It is evident from the EDX that there has been some Ti ingress through the whole of the structure. Therefore the mass gain equation will yield an overestimate of the NW depth, as is seen here.

At the time of writing this document, SEM and EDX had not been performed on sample PS7, although the weight gain in comparison to the other samples indicates that the higher pressure seen in each ALD cycle may have resulted in deeper coating of the pores.

4.5.2 Conclusion

Using the diffusion valve modification on the Picosun ALD reactor resulted in increased weight gain in all samples.

Increasing the exposure (Pt), either by increasing the reactor pressure or increasing the precursor residence time seemed to increase depth of penetration of NWs, in line with predictions by Elam and Gordon. Further work is required to calculate or measure a true value for the precursor partial pressure.

TiO_2 NW structures did not show significant contrast difference compared to the Al_2O_3 matrix to allow SEM imaging. Future experiments could introduce a post ALD annealing step to attempt to produce crystalline TiO_2.

5 Nanostructured Surfaces – Copper Oxide

5.1 Cu Surface Cleaning Tests

It was noticed that the Cu sheet, as purchased, showed multiple blemishes and spots across its surface. These were thought to be a result of handling during the packaging process. The introduction of oils and/or moisture to the surface had resulted in the formation of patches Cu_2O, identified by its red appearance. It was conceivable that these could affect the results of any subsequent oxide growth experiments and as such should be removed by acid treatment leaving a bare Cu surface.

An oxide removal and surface cleaning process was determined for Cu sheet consisting of a 10 second dip in a solution of 20vol% HNO_3 and 80vol% H_2O at room temperature. Following the acid treatment samples were rinsed in distilled water and isopropanol before air drying.

High purity Cu sheet (99.9975%), purchased from Advent Research Materials, was cut into samples roughly 20mm x 20mm x 0.5mm. Several factors regarding the quality of the metal were noted upon delivery. Rolling marks were clearly visible across both surfaces as well as areas with a slightly red hue. This was known to be a result of partial oxidation at the sheet surfaces, resulting in the formation of a thin layer of Cu_2O. At low temperatures (<140°C) Cu is known to oxidise to Cu_2O. The oxidation follows a logarithmic relationship meaning that once a continuous layer has formed, the oxide provides a protective barrier against further oxidation.

A review of the literature reveals many different cleaning techniques that can be used to clean Cu. The ASM handbook recommends several cleaning procedures, although it does not specify the end application of the cleaned products [154]. It is probable that the cleaning methods described are used to give a clean “appearance”, i.e. an optically clean surface –

possibly not clean enough for semiconductor device purposes. The first recommended cleaning process is outlined below in Table 15.

Table 15: ASM recommended Cu cleaning process

Solution	Sulphuric Acid (vol%)	Nitric Acid (vol%)	Hydrochloric Acid (g/l)	Water (vol%)	Time (s)
Scale dip A	0	50	4	50	15 – 60
Scale dip B	25 – 35	35 – 50	4	35 – 40	15 – 60
Bright dip	50 – 60	15 – 25	4	bal	5 – 45

Another process recommended by the ASM handbook is a dichromate colour dip. This consists of a 30 second immersion of the Cu at room temperature in a solution of 30 – 90 g/l of sodium dichromate, 5 – 10 vol% sulphuric acid balanced with H_2O.

Other cleaning recipes described in various journal articles include acetone and dilute HNO_3 [(61)], ethanol rinse, de-ionised water rinse, air dried, 1.5M HCl dip, de-ionised water rinse and air dried [(155)], 30% HNO_3 and de-ionised water for 30 seconds [(156)], 37% HCl in an ultrasonic bath followed by a de-ionised water rinse [(157)] and aqueous HCl (1.5M) for 1 minute followed by a de-ionised water rinse [(96)].

For the first tests it was decided to use a HNO_3 dip followed by two consecutive de-ionised water dips, rinsing in ethanol and then drying in flowing air at room temperature.

Chemically, the reaction expected to take place would produce copper(II) nitrate, water and nitrogen dioxide:

$$Cu + 4HNO_3 \rightarrow Cu(NO_3)_2 + 2H_2O + 2NO_2$$

The reaction of the native oxide present on the Cu surface (presumed to be Cu_2O due to its low temperature of formation and reddish appearance) was expected to produce copper metal, copper(II) nitrate and water. The production of Cu metal would then proceed to react further with the nitric acid in accordance with the reaction described above.

$Cu_2O + 2HNO_3 \rightarrow Cu(NO_3)_2 + H_2O + Cu$

5.1.1 Results and Disccusion

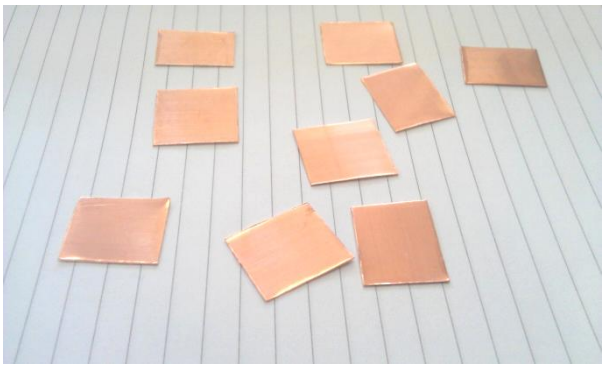

Figure 49: Cu samples cut from as received Cu sheet metal.

Figure 49 shows a selection of cut samples from the as received Cu sheet. Although not readily discernible, each of the samples pictured here had a slightly red tint across the surface indicating the presence of Cu_2O surface oxide. Also visible on the samples were darker areas, possibly due to localised thicker layer of oxides or surface contamination from the rolling/packaging or handling processes. Any further work in attempting to manufacture good quality semiconductor junctions from these samples could be detrimentally effected by these patches, as they could conceivably act as scattering/recombination traps when active devices are made. Because of this, a method to remove this oxide was sought.

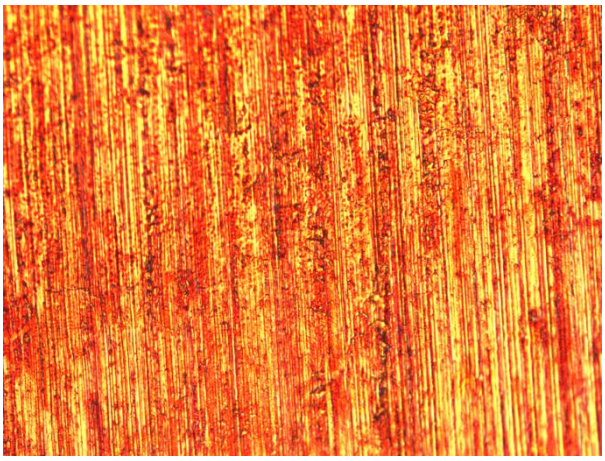

Figure 50: Optical microscopy image of as received Cu x600.

Figure 50 shows an optical microscopy image of the as received Cu at 600 times magnification. This image was included as is shows the red tint seen across the sample

surface, as well as some darker spots that may be indicative of CuO or Cu_3O_4 (both near black oxides). It was the aim of these experiments to find a process to remove these oxides leaving just the bare Cu underneath.

Figure 51: First sample after concentrated HNO_3 dip, rinsing in water and ethanol and several hours left in air.

The first experiment attempted used concentrated HNO_3 (70%). One Cu sample was dipped into the acid causing an immediate and vigorous reaction to occur. The previously clear acid turned a deep, translucent green colour within seconds and large amounts of gas were seen evolving at the surface of the Cu. The colour change of the solution signalled the presence of hydrated $Cu(NO_3)_2$. After the sample had been removed and subjected to rinsing in de-ionised water and ethanol the surface of the Cu had lost all of its reflectivity. Due to the high speed that the reaction progressed, it was thought that this loss of reflectivity was because of pitting on the Cu surface. Over the next few hours the surface oxidised (Figure 51) to a mixture of CuO, Cu_2O and possibly Cu_3O_4.

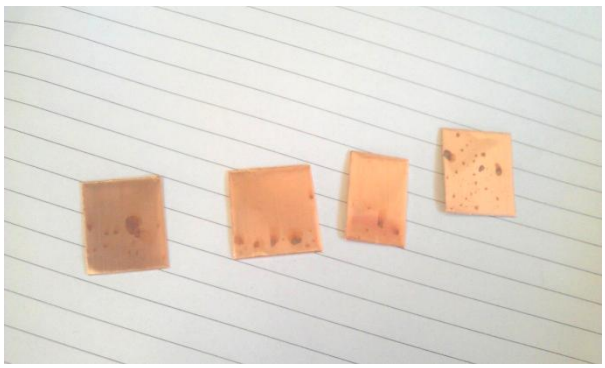

Figure 52: Samples after dip in 7vol% aqueous HNO_3, de-ionised water rinse, ethanol rinse and air dried.

After this experiment, for which it was concluded that the acid was too reactive for use, a new batch of HNO_3 was mixed with water. 25ml of HNO_3 (70%) was mixed with 75ml of de-ionised H_2O. The next four samples were dipped into this solution for 10, 20, 40 and 60 seconds. Figure 52 shows the samples (10s dip on the left, 60s dip on the right) after rinsing in water and ethanol followed by drying in air. Several observations were made while the dipping was being carried out. Firstly, once immersed in the nitric acid solution, the red surface layer was stripped away almost immediately exposing the underlying Cu on each of the samples. With this lower concentration of acid the reaction was much less vigorous, and no colour change was seen in the solution. For the samples dipped for 40 and 60 seconds, a further reaction was noticed. After around 30 seconds a broad line appeared along the base of the sample (i.e. the part of the sample immersed first). This line was noticeably darker than the exposed Cu and proceeded to move up the sample over the remainder of the dip. Once removed from the acid this line was no longer visible. After the dip treatment, the samples were rinsed in de-ionised water and ethanol and each sample appeared brighter than before the treatment. Under the influence of the air drier however, the last drops of ethanol to evaporate left dark marks on the sample surface. These can be seen in Figure 52. Closer examination of these spots using optical microscopy revealed the presence of localised oxide, much thicker and darker than the original surface oxide.

Figure 53: Edge of oxide spot after HNO_3 dip, water rinse, ethanol rinse and air drying, x100.

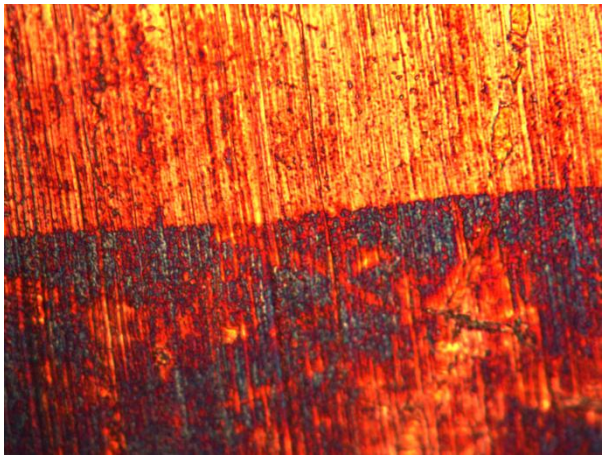

Figure 54: Edge of oxide spot after HNO_3 dip, water rinse, ethanol rinse and air drying, x1000.

Figure 53 and Figure 54 show the edges of one of these spots. From the colours visible, it seems as though the presence of evaporating ethanol has promoted the formation of Cu_2O (red) and CuO/Cu_3O_4 (black). Because of this a final test was necessary trying an alternative post-dip cleaning process.

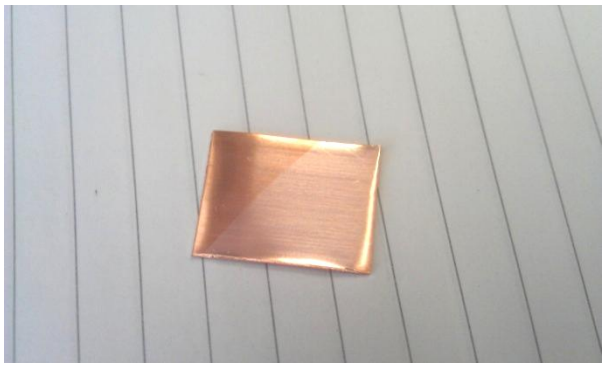

Figure 55: Cu sample after HNO_3 dip, water rinse, propanol rinse and air drying.

Figure 55 shows the result of a partial dip of the as received Cu into a solution of 20vol% HNO_3 and 80vol% H_2O for 10 seconds. Following the dip the sample was rinsed in de-ionised water and propanol then air dried. The lighter area of the sample corresponds to the part immersed in the acid solution.

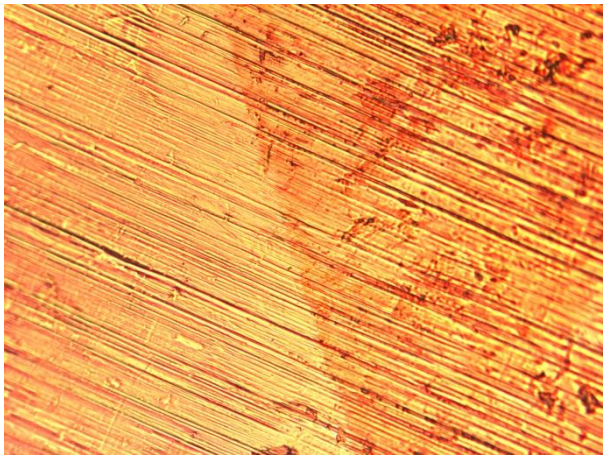

Figure 56: Dip edge after HNO_3 dip, water rinse, propanol rinse and air drying x600.

Figure 56 shows the sample surface at 600x magnification. From this image it is clear that this process has had the desired effect and that most, if not all, of the surface oxide has been removed. Further XRD/Raman analysis will confirm or disprove this.

One problem that presents itself is that Cu naturally forms a protective barrier of nano-scale Cu_2O at temperatures close to ambient in the presence of oxygen. Immediately after the dip any cleaned Cu samples for use in further work will start growing new oxide. The image shown in Figure 56 was taken roughly 2 hours after the acid dip giving an indication that the growth of new oxide is a slow process. To attempt to inhibit new oxide growth after cleaning, future samples should be stored in an air tight container or polyethylene bags along with a desiccating medium. An alternative to this would be to purge the containers with an inert gas such as argon or nitrogen.

5.1.2 Conclusion

Cleaning of high purity copper sheet can be achieved by a 10 second dip in a solution of 20vol% HNO_3 and 80vol% H_2O at room temperature. Cleaned samples should be rinsed in distilled water, isopropanol and then air dried.

Following cleaning samples should be stored in an air tight container along with a desiccant to limit re-oxidation of the surface.

5.2 Anodisation of Cu Foil to Produce High Aspect Ratio Cu_2O Surfaces

Several groups had produced high aspect ratio oxide nanostructures through a similar process to that used in the anodic oxidation of aluminium. Unlike AAO, Cu oxide anodised from Cu metal can act as more than just a scaffold structure due to its inherent p-type nature. This would give it possible uses as a functional layer in a heterojunction device structure.

High purity Cu sheet was anodised in KOH and NH_4F electrolytes in order to produce high aspect ratio nanostructured surfaces. The anodisations resulted in the formation of Cu_2O nanostructures showing a cubic geometry. These were dissimilar to the target structures produced by Allam et al., which were more leaf-like. A mechanism was proposed to account for the growth seen.

Following recent work by Allam *et al.*[101] at M.I.T., Cu foil (of unreported purity) was anodised in 0.15M KOH and 0.1M NH_4F electrolyte with H_2O as the solvent. A circular section of the foil (approximately 3.5cm diameter) was cut from the Cu sheet, mounted onto a blank epoxy mount of the same diameter using superglue and hand polished down to a 1µm finish. The sample was then auto polished for 3 hours using 50nm silica polishing paste. Following polishing, the Cu foil was scored into eight sections and placed face down on top a piece of filter paper inside a wide base dish. Acetone was then added to dissolve the superglue and free the foil sections from the epoxy mount.

Because ammonium fluoride was to be used as the electrolyte, a new anodisation cell had to be constructed that could withstand attack by fluorine ions for the ~5 minute duration of the anodisations. The cell consisted of a plastic beaker containing a plastic measuring cylinder which had been modified to act as a support for the anode and cathode. Several

5mm holes were drilled into the base and sides of the measuring cylinder to allow the electrolyte to circulate. A small rectangular section was cut from one side of the cylinder above the level of the electrolyte to act as a support for the top of the carbon cathode. Three 2mm holes were drilled several centimetres below the rectangular hole to allow the cathode to be firmly tied to the inside of cylinder using plastic cable ties. Opposite the cathode, two closely spaced 5mm holes were drilled. This was where the anode was to be attached, giving a constant separation and near constant anodisation area for successive experiments. To construct the anode, one end of a 1mm thick insulated copper wire was polished down to an angled, flat surface and glued to the back of the polished Cu foil using silver dag. To prevent anodisation of the Cu wire and the back of the Cu foil, Bostik™ all purpose adhesive was applied liberally over the back of one anode, ensuring that all metallic surfaces were covered. Once dry, the exposed Cu surface was positioned over the two closely spaced 5mm holes and secured in place using elastic bands. For the remaining three anodes used in this experiment, a solution of picien wax and toluene was used in place of the Bostik™ adhesive.

The anodisation was performed using a carbon cathode, which previous work by the same group had shown to be superior to more expensive Pt electrodes[158] and a HF resistant plastic beaker. A power supply operating in constant voltage mode was used to perform the anodisation. The 4 samples were anodised at 6V and ambient temperature with the anodisation duration varied to attempt to produce porous oxides of different thicknesses (100, 200, & 2x 300s).

After the anodisation the Cu anode which used Bostik adhesive was cleaned with distilled water and ethanol, then immersed in acetone and placed in an ultrasonic bath for 5 minutes. This resulted in the dissolution of the adhesive facilitating easy removal of the foil from the anode. The anodes which used picien wax backing were cleaned in the same

manner then immersed in toluene for 24h. The toluene dissolved most of the wax leaving the foils separated from the anode assembly.

Following from the anodisation, samples were characterised by FESEM imaging (Jeol7001 Field emission SEM, [10kV beam, ~16mm WD, ~200µA] and [25kV beam, ~10mm WD, ~100µA]), XRD (Rigaku-Miniflex, Cu X-ray source, λ=1.54Å) and Raman spectrometry (LabRam spectrometer, 514nm laser source, 100µm confocal aperture, 30s acquisition x2).

5.2.1 Results and Discussion

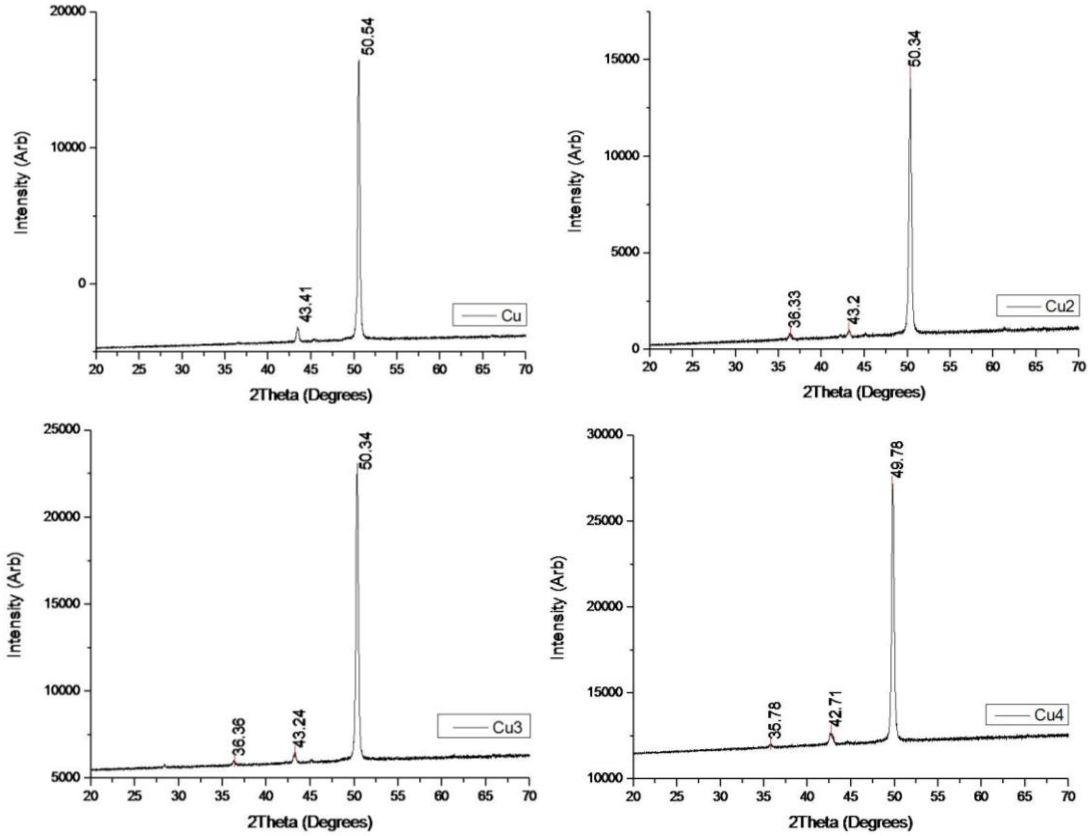

Figure 57: XRD profiles for samples A-D (1-4 respectively)

The XRD pattern for sample A (Figure 57) shows two peaks at 2θ values of 43.41° and 50.54°. Both of these peaks are a match for those seen in cubic Cu, (111) at 43.298° and Cu (200) at 50.434° [(159)]. These peaks are also seen in samples B-D, as one would expect due to the thin and porous nature of the formed oxide. Additionally, samples B-D show a further peak at around 36.3°. This could be from Cu_2O: (111) at 36.419° [(160)], from the CuO (111) peak at 36.637° [(161)] or possibly from the $Cu^{1+}{}_2Cu^{2+}{}_2O_3$ (004) peak at 36.343° [(162)].

The following table compares the anodisation results with the card file XRD patterns:

Table 16: Comparison of measured XRD peaks against reference oxides (Bold 2θ value indicates strongest peak)

Cu [159]	CuO (161)	Cu_2O (160)	Cu_3O_4 (162)	Sample A	Sample B	Sample C	Sample D
	36.637	29.555	28.494	43.41 (Cu + 0.112)	36.33 (CuO – 0.307), (Cu_2O – 0.089) or (Cu_3O_4 - 0.013)	36.36 (CuO – 0.277), (Cu_2O – 0.059) or (Cu_3O_4 +0.017)	35.78 (CuO – 0.857), (Cu_2O – 0.639) or (Cu_3O_4 – 0.112)
43.298	**42.559**	**36.419**	30.808	50.54 (Cu + 0.106)	43.20 (Cu + 0.098)	43.24 (Cu + 0.058)	42.71 (Cu – 0.588), (CuO +0.151) or (Cu_2O + 0.412)
50.434	61.791	42.298	**35.892**		50.34 (Cu + 0.094)	50.34 (Cu + 0.094)	49.78 (Cu – 0.654)
		52.455	36.343				
		61.345	44.142				
		69.571	48.376				
			58.357				
			64.179				
			65.186				

Table 17: XRD peak location data for samples A-D

Sample	Peak1	Peak2	Peak3
A	---	43.41	50.54
B	36.33	43.20	50.34
C	36.36	43.24	50.34
D	35.78	42.71	49.78

As can be seen in Table 16, the Cu peaks found in the anodised samples do not match perfectly with those found in the reference files. This could be because of several reasons, namely compressive/tensile stresses within the crystals (either as a result of the sheet rolling process, or from interstitial/substitutional impurities within each crystal) or sample misalignment relative to the sample holder edge. Assuming the two major peaks are from the Cu substrate, an estimation of the peak shift can be made to inform identification of the third peak. For the shift seen in the visible oxide peak, an additional mechanism may be

responsible; i.e. lattice mismatch between the Cu substrate and the grown oxide causing a tensile/compressive strain field at the substrate/oxide interface.

The average peak shifts for the Cu (111) and (200) peaks in samples A – D are approximately +0.1° for 1 and 2, +0.07° for 3 and -0.6° for sample 4. For each sample, the (200) peak is dominant (whereas in the reference files the (111) peak is more prominent than the (200)) indicating that the Cu substrate structure may be showing a preferential grain orientation.

If we assume that the peak shift seen is predominantly due to z-axis misalignment of the samples, then the shift in the additional peak in samples 2, 3 and 4 should be roughly the same size. For samples 2 and 3, this peak is shifted roughly 0.07° compared to the Cu_2O (111) and for sample 4 the shift is approximately 0.6°, which all match reasonably well with the shift seen in the Cu peaks. As the surface oxide is also red in appearance (not black or gray for the other oxide forms), it can be concluded that the anodisation has produced Cu_2O.

The SEM images taken of each sample (Figure 58 - Figure 61) show the morphology of the grown oxides at various points across the surface and at several different magnifications.

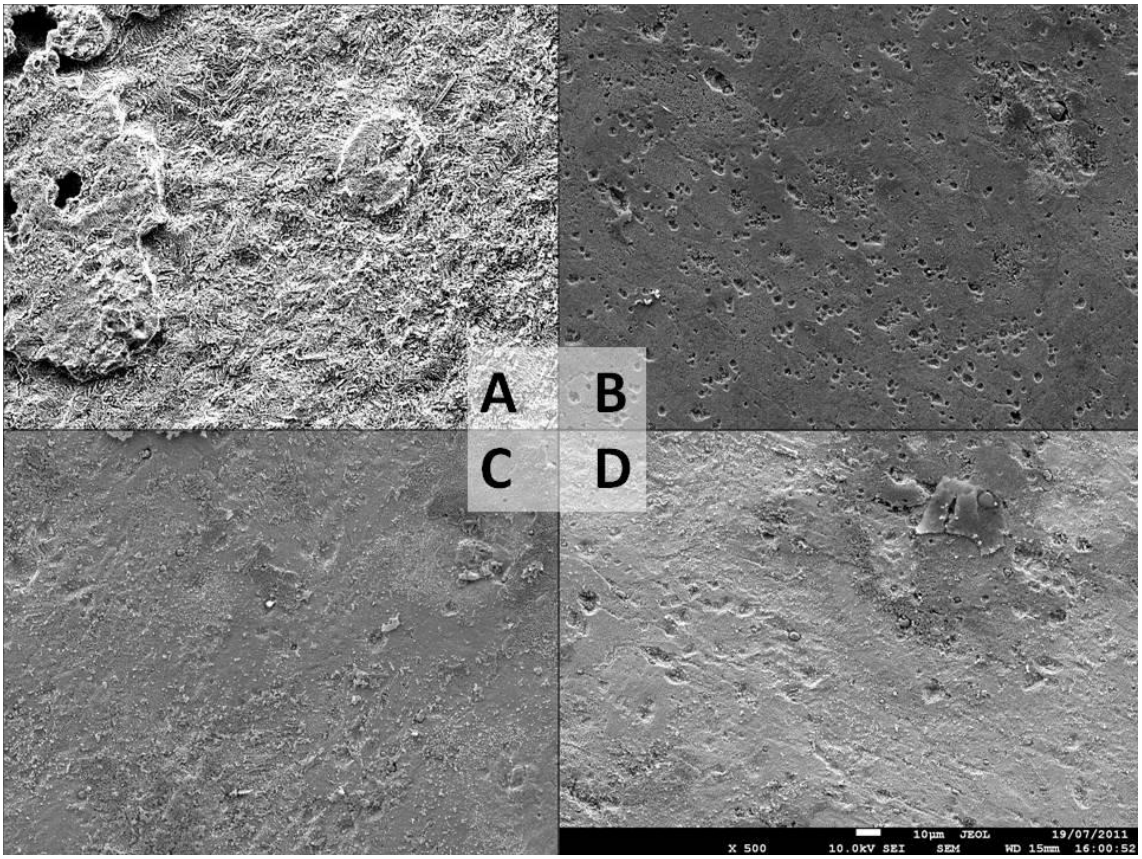

Figure 58: Low magnification (x500) FESEM images of samples A-D. (A) Sample anodised for 300s. Anode constructed using Bostik adhesive to electrically isolate back and sides of Cu foil. (B) Sample anodised for 300s. Electronic isolation achieved using picien wax. (C) Sample anodised for 200s. Anode constructed with picien wax. (D) Sample anodised for 100s. Anode constructed with picien wax.

Figure 58 shows the samples surfaces at low magnification (x500). The images shown are representative of the entire anodised surface for each sample. Images A and B show a distinct difference in the nature of the Cu_2O formed by the anodisation. The only appreciable difference between their experimental parameters was that the copper surface for sample A was isolated from the rest of the anodisation cell by Bostik™ adhesive. Electronic isolation was achieved for the remaining samples by the use of picien wax. Evidently, this has had some effect on the anodisation at the Cu surface with sample A showing a much more open and porous structure, as well as a greater surface roughness. Comparison of these samples at higher magnifications show that sample A formed a more ridged and leaf-like structure compared to the more isotropic structure seen in the other samples. The reasons for this could be that the growth of the oxide from the Cu substrate is enhanced along certain planes, increasing the growth rate in a particular direction, or that

the dissolution of surface oxide is orientation dependant, with the oxide volumes between leaves dissolving into the electrolyte at an enhanced rate.

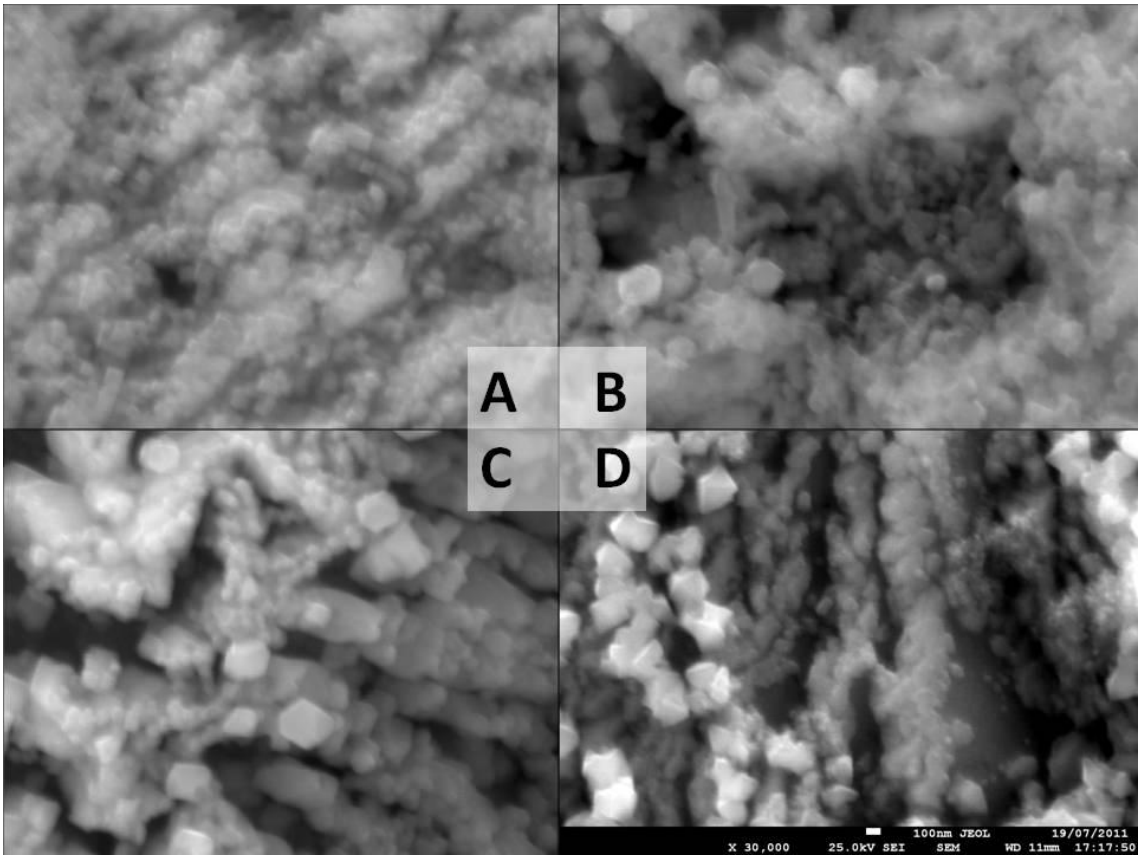

Figure 59: Samples A-D imaged at 30000x magnification

The leaf-like structure can be seen covering some areas in the other samples at higher magnifications, and at these magnifications the differences between the samples become less apparent. For example, at x30000 magnification (Figure 59), the cubic nature of the Cu_2O is obvious for each sample, with the porous structure made up of interconnected Cu_2O cuboids, with edge lengths of several hundred nanometres.

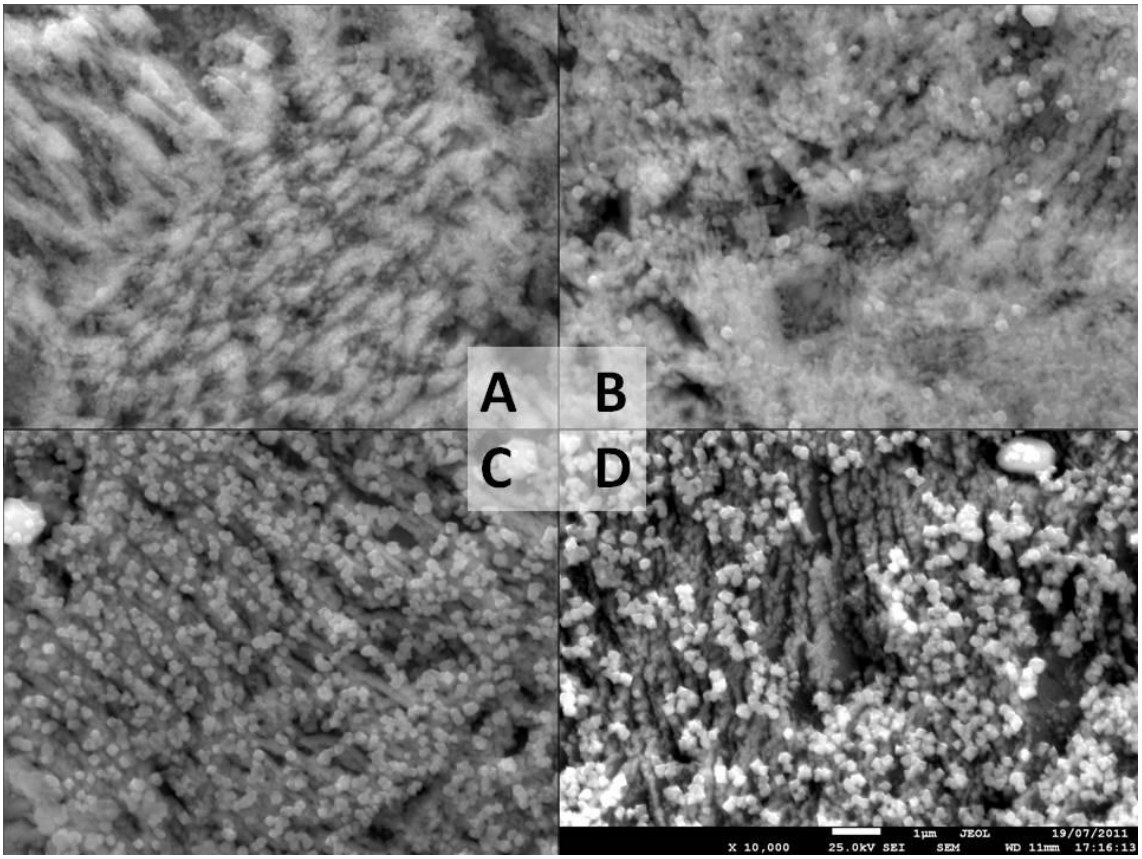

Figure 60: Samples A-D imaged at 10000x

Varying the duration of the anodisation had little effect on the structure of the oxide formed (samples B – D), although comparison of the SEM images at x10000 does seem to show more and deeper ridge features for the shortest anodisation (Sample D, Figure 60, 100s).

The aim of the experiment was to reproduce work by Allam et al. The surfaces produced here differ from the surfaces produced by the M.I.T. group in that their oxide had a much more open structure and an apparently higher uniformity across the sample surface. Reasons that could account for the differences seen include differences in the purity of the Cu substrate and influence of the adhesives used here in the anodisation cell, i.e. additional chemical reactions that seemed to hinder the dissolution of the oxide into the electrolyte. The cubic structures seen, however, could offer an explanation. These bear more similarity to structures seen when anodising Cu metal in more neutral electrolytes such as water [(103)]. It is possible that because of the layout of the anodisation cell, the circulation of the

electrolyte was insufficient, resulting in the acid species becoming depleted in the vicinity of the anode surface. As the depletion continued the local pH would increase changing the chemical reaction path.

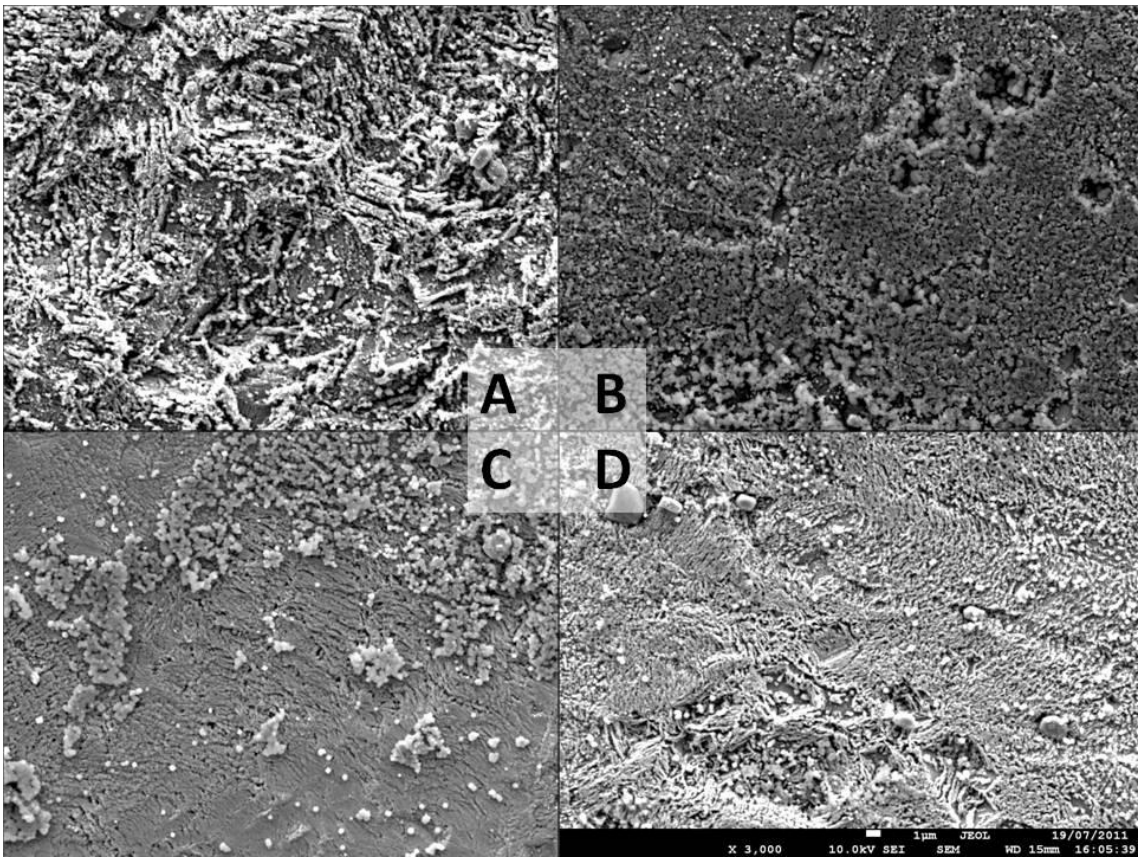

Figure 61: 3000x magnification FESEM images of samples A-D

In Figure 61, images A, B and D, the leaf-like structure seen on which the cubic structure was grown could be the beginning stages of the growth type seen by Allam et al.. Once the electrolyte was depleted, the growth type switched to that seen by Singh et al, producing the cubic structure. The deeper structures seen in sample D lend weight to this theory as the short (100s) anodisation had not depleted the electrolyte to the same extent and for samples A, B and C, reducing the prevalence of the cubic structures which closed up and covered the leaf-like surface.

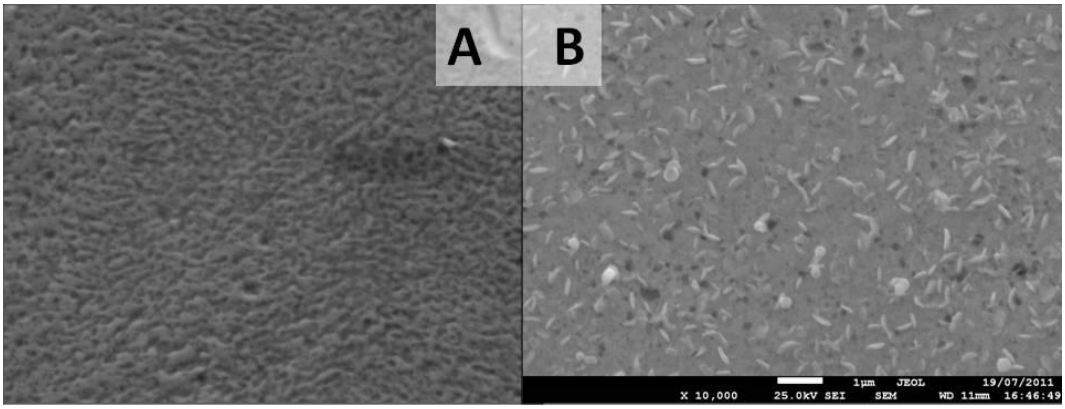

Figure 62: Representative images of unanodised sections of samples A and B. Imaged at 10000x magnification

Figure 62 shows SEM images from areas of samples A and B where the metal was covered up during the anodisation. From these images it is clear that the anodisation process was the cause of the structures observed, rather than solely immersion in the electrolyte or contact with any of the adhesives used.

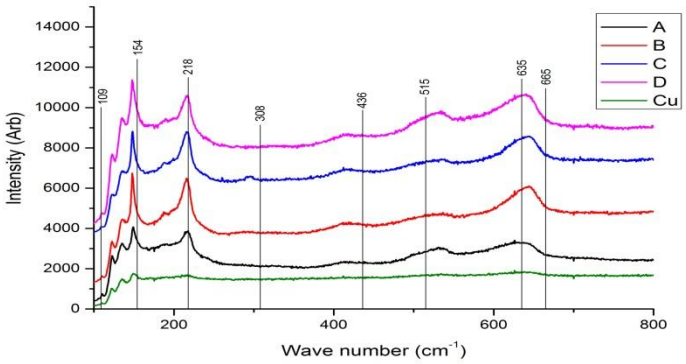

Figure 63: Raman spectra for as received Cu and anodised samples A – D. Peak locations are 123, 135, 148, 187, 216, 294, 415, 535 and 642 cm^{-1}.

H. Solache-Carranco et al. found Cu_2O raman peaks at 109, 154, 218, 308, 436, 515, 635, 665 and 820 wavenumbers (cm^{-1}) [62]. Comparing this to the Raman spectra in Figure 63 it can be seen that each of the anodised samples shows roughly the same features as each other, with peaks located at 123, 135, 148, 187, 216, 294, 415, 535 and 642 cm^{-1}. The as - received Cu sample also shows some of these peaks at much lower intensities, indicating the presence of a thin oxide film. Due to the particular set up of the Raman spectrometer used for this analysis it is possible that the first peak, located at 123cm^{-1}, could be part of the right-hand edge of the 109cm^{-1} peak. For the other peaks, there seems to be a

moderate deviation from the quoted values. This could partly be due to the broadness of some of the peaks, especially those at higher wavenumbers, where it was difficult to accurately locate the peak centres. Another factor that could help explain the deviation seen here is that this oxide has been produced anodically while the reference oxide was grown thermally. This may have had some effect on the crystal structure, and hence the nature of the bonding between atoms. Factors such as incorporated electrolyte species, deviation from the predicted stoichiometry, etc., could all have noticeable effects on the produced spectra.

5.2.2 Conclusion

Anodisation of 99.9% Cu sheet in KOH and NH_4F electrolyte was found to produce a non-planar Cu oxide at the sample surface. The oxide was identified as Cu_2O by Raman spectroscopy and X-ray diffraction.

The experiment durations tested here did not result in any variation of in the porosity of the grown oxides.

Significant differences were seen between the morphologies of the oxides grown at M.I.T. and those grown here, with the M.I.T. oxides showing higher porosity and uniformity. It was also undetermined whether the Cu oxide layer had completely covered the Cu substrate. Because of this, it was thought that any attempts to create a functioning device from this substrate may have been hindered by direct contact of additionally deposited material to the underlying Cu metal, resulting in short circuit paths which could render the device inoperable.

5.3 Thermal Growth of Planar CuO/Cu_2O and Quench Tests

The difficulties experienced in growing a nanostructured CuO/Cu_2O oxide surface via an anodisation route led to an exploration of other methods for producing Cu oxide from Cu metal. Arguably the simplest method was thermal oxidation in a normal air atmosphere.

Thermal oxidation of Cu metal was conducted at temperatures of 140°C, 500°C and 1000°C. Growth of the oxides at the two higher temperatures was found to follow a parabolic growth law, while the growth regime for the lower temperature was thought to follow a logarithmic law, in accordance with the literature. Due to the mismatch of coefficients of thermal expansion for the metal and both oxides in partially oxidised samples, significant spallation was seen. In an attempt to address this problem, quenching in different media of oxidised samples was undertaken to assess whether the spallation could be controlled. For each of the quenching media, the removal of the upper oxide layer was found to be too severe, removing large proportions of both oxide layers. Interestingly, several of the samples oxidised at 500°C showed growth of long CuO nanowires protruding from the upper CuO layer.

99.90% HDHC Cu sheet samples were oxidised in air at 1000°C, 500°C and 140°C for 1, 2 and 3 hours. Two more samples were also oxidised for 24h at 140°C. The samples were then slow cooled (approximately 1°C/min) overnight to reduce stresses in the upper oxide layer from differences in thermal contraction between the different oxides and the underlying Cu substrate. XRD and Raman spectroscopy were used to confirm the oxide types produced. A selection of samples were also cross-sectioned and imaged using optical microscopy to determine oxide thicknesses and growth rates. Additional samples were also oxidised at 500°C in air for 2 hours followed by quenching in air, hot water or cold water to see if this could be a suitable method for removing the upper CuO layer from the underlying Cu/Cu_2O.

5.3.1 Results and Discussion

Knowing the densities of Cu, CuO and Cu_2O it is possible to calculate expected maximum thicknesses, geometries and mass increases for a hypothetical sample. Starting with a square 1.5g, 0.45mm thick Cu sample with a density of 8.94g/cm^3 [163] the volume, the x and y dimensions of the sample and the approximate number of Cu atoms it contains can be calculated.

$$V = \frac{m}{\rho} = \frac{1.5}{8.94} = 0.1678\text{cm}^3$$

$V = xyz$ where $z = 0.045$cm. If $x = y$, then $x = \sqrt{\frac{V}{z}} = \sqrt{\frac{0.1678}{0.045}} = 1.9309$cm.

The molar mass of Cu is 63.546g/mol.

$N = \frac{m}{m_r} = \frac{1.5}{63.546} = 2.3605 \times 10^{-2}$ moles of Cu.

If this sample were to completely oxidise to CuO, with an m_r of 79.545g/mol and density of 6.31g/cm^3 [164] then the expected mass would be:

$$m_{CuO} = N.m_{r_{(CuO)}} = 2.3605 \times 10^{-2} \times 79.545 = 1.8777\text{g}.$$

This would give a maximum mass increase ratio of: $\frac{1.8777}{1.5} = 1.252$.

Presuming that the dimensional change in the x and y directions is negligible during the oxidation, the expected thickness can be calculated:

$$V = \frac{m_{CuO}}{\rho_{CuO}} = \frac{1.8777}{6.31} = 0.2976\text{cm}^3$$

$$z = \frac{V}{x^2} = \frac{0.2976}{1.9309^2} = 0.0798\text{cm}.$$

This shows that the maximum thickness of CuO grown from the upper and lower surfaces would be 0.399mm.

For the complete conversion of the metal to Cu_2O with an m_r of 143.09g/mol and density of 6.00g/cm^3 [164], the expected maximum mass would be:

$$m_{Cu_2O} = N.m_{r_{(Cu_2O)}} = \frac{2.3605\times10^{-2}}{2} \times 143.09 = 1.6888\text{g}$$

This would give a maximum mass increase ratio of $\frac{1.6888}{1.5} = 1.126$.

Table 18: Mass change results and thickness measurements for the oxidation of Cu sheet.

Sample number	Temp (°C)	Oxidation time (h)	Approximate surface area (cm^2)	Normalised mass increase (1=no change)	Weight gain per unit area (g/cm^2)	Oxide thickness (µm)
1	1000	3	7.09918	1.10687	2.256E-02	---
2	1000	3	7.10435	1.12589	2.692E-02	---
3	1000	3	7.10607	1.12655	2.717E-02	379.7
4	1000	3	7.09415	1.12688	2.645E-02	---
5	1000	2	7.10939	1.11145	2.413E-02	351.9
6	1000	2	7.10878	1.10640	2.300E-02	---
7	1000	1	7.10875	1.07619	1.647E-02	239.7
8	1000	1	7.11068	1.07514	1.632E-02	---
9	500	3	7.10543	1.00801	1.717E-03	25.0
10	500	3	7.12212	1.00774	1.727E-03	---
11	500	2	7.11863	1.00669	1.482E-03	19.8
12	500	2	7.10562	1.00638	1.369E-03	---
13	500	1	7.10430	1.00556	1.188E-03	---
14	500	1	7.12107	1.00421	9.367E-04	14.2
15	140	3	7.12432	1.00000	0.000E+00	---
16	140	3	7.12127	0.99999	-1.404E-06	---
17	140	2	7.11656	1.00001	2.342E-06	---
18	140	2	7.11646	1.00001	2.810E-06	---
19	140	1	7.13621	1.00002	4.671E-06	---
20	140	1	7.12660	1.00002	4.210E-06	---
21	140	0.5	7.10401	1.00006	1.267E-05	---
22	140	0.5	7.12819	1.00006	1.356E-05	---
23	140	24	7.12799	1.00002	5.144E-06	---
24	140	24	7.10044	1.00003	5.633E-06	---

Table 18 shows the experimental parameters, mass change and oxide thickness results for the first 22 planar oxide samples. For the first samples, 1-4, oxidized at 1000°C for 3 hours followed by furnace cooling, it can be seen that the mass of the samples has increased by around 12% indicating a significant absorption of oxygen from the atmosphere. The first image in Figure 64 shows a cross-section of sample 3. From this image it is apparent that

none of the original Cu metal has been retained. At the center of the sample the oxide appears less dense than the rest, this could be due to the intermediate conversion of the metal to a thin layer of Cu_2O before it fully oxidised to CuO. It can be seen from Table 18 and from the calculations above, that the sample shows a lower mass than predicted for a fully oxidised sample. This can be attributed to the loss of a small amount of the oxide to the crucible containers when removing the samples from the furnace. At the high temperatures used for this oxidation, diffusion of Cu and CuO was thought to be relatively high causing a small amount of bonding to occur between the samples and the crucible containers. This, coupled with the inherent brittleness of Cu oxides meant that when the samples were removed small portions of the surface at the lower corners broke away, reducing the mass increase. In future work this could be accounted for by measuring the mass of the sample before and after the oxidation including both the crucible and lid. Any spallation or mechanical damage to the samples would remain in the crucible after oxidation and would therefore be included in the second weight measurement.

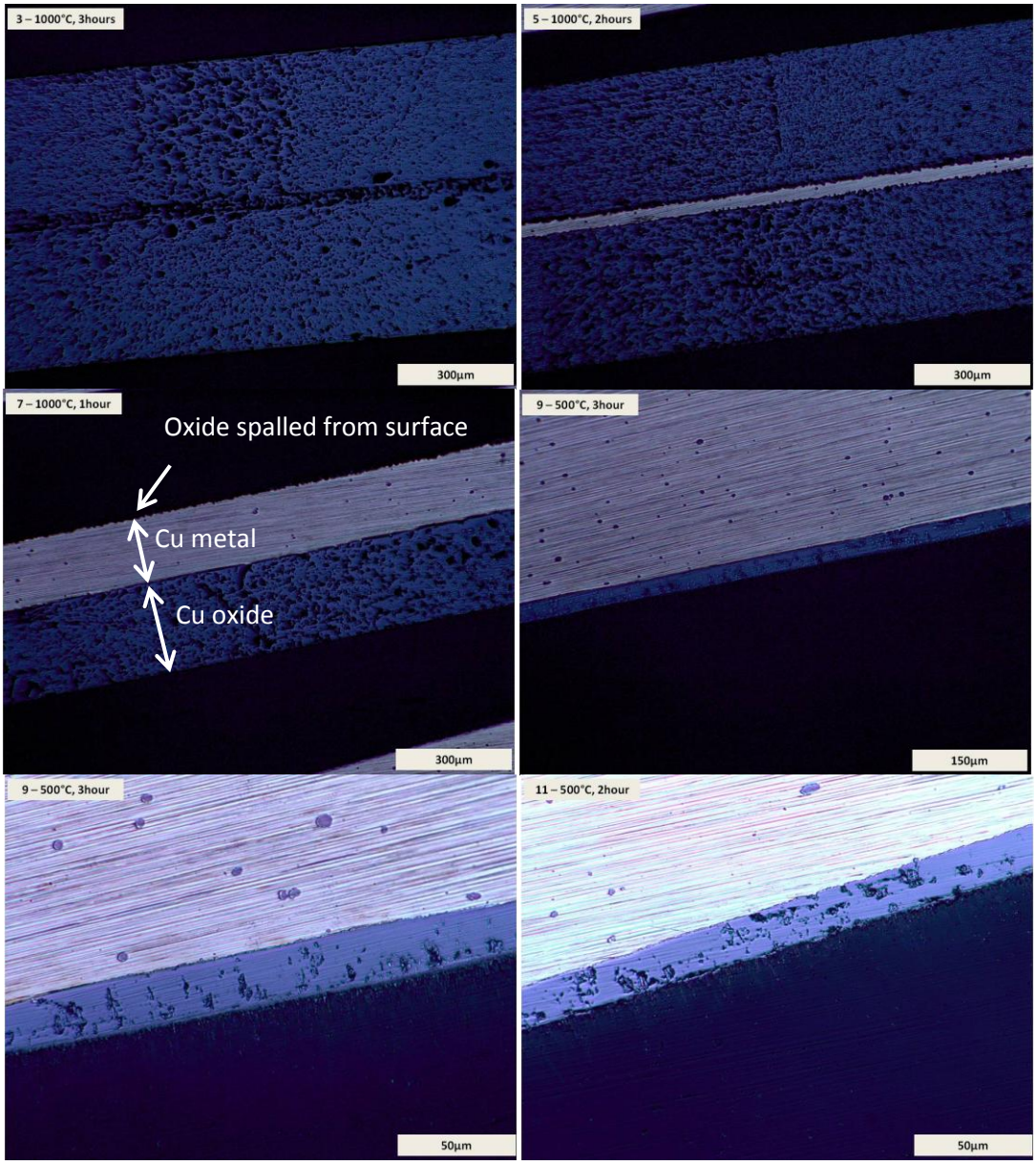

Figure 64: Optical microscopy images of samples 3, 5, 7, 9 and 11 after cross-sectioning and polishing.

Figure 64 shows representative cross sections of samples oxidised at 1000° and 500°C for 1, 2 and 3 hours. For these temperatures it is clear that the oxidation time has a significant impact on the thickness of oxide produced with longer times giving a thicker layer. Callister [113] states that for high temperature oxidation of copper, the oxide growth rate follows a parabolic law and is controlled by ionic diffusion of oxygen through the oxide:

$w^2 = k_1 t + k_2$ where w = weight gain per unit area, t = time and k_1 and k_2 are constants (dependent on the temperature and the partial pressure of O_2).

For the samples oxidised at 1000°C and 500°C the values of k_1 and k_2 can be calculated by referring to samples 2 and 7 (Table 18), with w values of 2.69x10^{-2} g/cm^2 and 1.65x10^{-2} g/cm^2 and t values of 10800s and 3600s. The equations can then be solved simultaneously:

$$2: 7.2361 \times 10^{-4} = 10800 \times k_1 + k_2$$

$$7: 2.7225 \times 10^{-4} = 3600 \times k_1 + k_2$$

$$7\ (x3): 8.1675 \times 10^{-4} = 10800k_1 + 3k_2$$

Subtracting 2 from 7 gives:

$$7(x3)\text{-}2: 9.314 \times 10^{-5} = 2k_2 \rightarrow\ k_2 = 4.657 \times 10^{-5}\ \text{g/cm}^2$$

Putting this value back into the equation for sample 2 gives:

$$2:\ 7.2361 \times 10^{-4} = 10800 \times k_1 + 4.657 \times 10^{-5} \rightarrow k_1 = 6.269 \times 10^{-8}\ \text{g/cm}^2\text{.s}$$

To check that this value is correct, one can use it to calculate the weight gain per unit area for the samples oxidised at 1000°C for 2 hours:

$$w^2 = 7200 \times 6.269 \times 10^{-8} + 4.657 \times 10^{-5}$$

$$w = 2.231 \times 10^{-2}\ \text{g/cm}^2$$

This value is close to that of the measured values of 2.3x10^{-2} g/cm^2 and 2.41x10^{-2} g/cm^2. The error here could be due to the errors associated with the measurement of the surface areas of the samples. The measurement was taken using calipers with an accuracy of ±0.05mm, but the calculation of surface area assumed that the samples were perfectly rectangular. As the samples were cut by hand this is quite unlikely, and could explain the discrepancy seen in the predicted mass gain here.

Repeating this process for samples 9 and 13, oxidised at 500°C for 3hours and 1 hour respectively, gives k_1 and k_2 values of 2.115x10^{-10} g/cm^2.s and 6.498x10^{-7} g/cm^2. These then give a predicted w value for a 2 hour oxidation at 500°C of 1.474x10^{-3} g/cm^2, in agreement with the measured values (samples 11 and 12).

For low temperature oxidations, e.g. Cu to Cu_2O at 140°C, the oxidation of Cu follows a logarithmic law:

$$w = k_1 \log(k_2 t + k_3)$$

Due to the weight gain being so small for the samples oxidised at 140°C, i.e. only just measurable with the resolution of the to the micro-balance used here, it was thought that there was little point in computing the k_1, k_2 and k_3 constant values, as the errors associated with them would be very large. Also the above equation would be more sensitive to any of the assumptions used to calculate the starting surface areas of the samples.

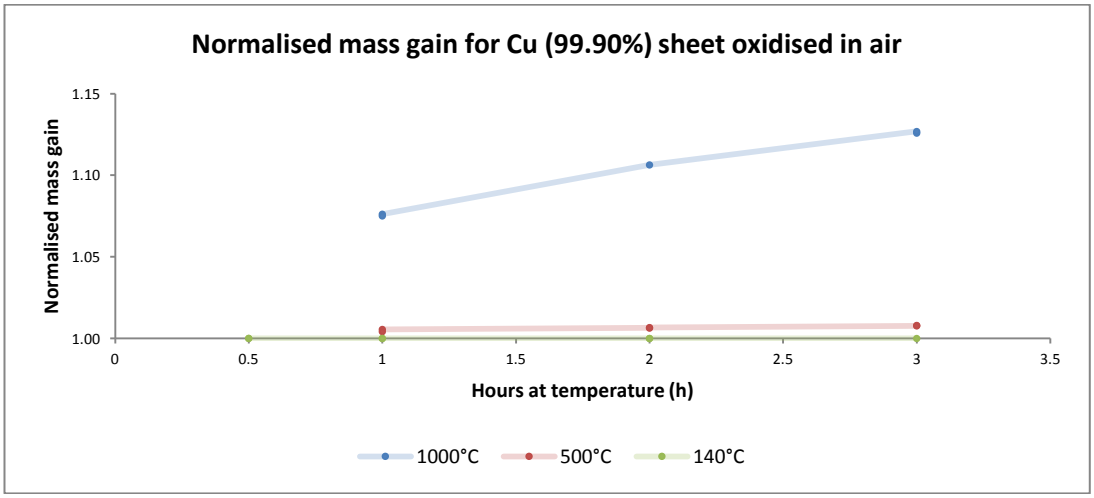

Figure 65: Mass gain for Cu samples oxidised in air at 1000°C, 500°C and 140°C.

Figure 65 shows the normalized mass increase for the oxidised samples. The mass change is greatest for the samples oxidised at 1000°C. From the few data points recorded here it seems that the oxidation could be following a parabolic rate law, as expected from the literature review. The oxidations performed at 500°C also appear to be following the same

law but with a much lower growth rate. This is to be expected as diffusion of oxygen through the growing oxide would be much lower at 500°C than at 1000°C. For the low temperature oxidation at 140°C it is harder to determine which oxidation regime is being followed as the mass increase is only just within the resolution of the scales used to weigh the samples. The mass increases shown in Table 18 (samples 15 – 22) for this temperature also yield slightly unexpected results. It appears as if the biggest mass increase is seen in the samples oxidised for only 30 minutes, whereas the smallest mass change was seen in those samples oxidised for 3 hours. This result is counter-intuitive as one would expect a longer time at temperature to allow more oxygen through the barrier layer to form more oxide. It is possible that with the impurity content of the substrates used (around 0.01% by weight), impurity material near to the surface is more volatile at these temperatures and so degasses from the substrate reducing the mass. The manufacturer's data sheet for the copper used for these experiments shows that impurities can include bismuth and lead, both with relatively low melting points. This could therefore be the cause of the anomalous results seen here, but without performing a highly sensitive chemical analysis it is impossible to be certain that this is the mechanism behind the mass loss.

The bottom two images in Figure 64 (samples 9 and 11) show another interesting feature not seen in the other oxidised samples shown here, i.e. CuO nanowires protruding around 50µm from the oxide surface. Several mechanisms have been proposed in recent years to explain the growth of CuO nanowires via thermal oxidation. As CuO was also known to be a p-type oxide, it was thought that these structures may provide a suitable surface on which to grow n-type layers via ALD for the construction of PV devices.

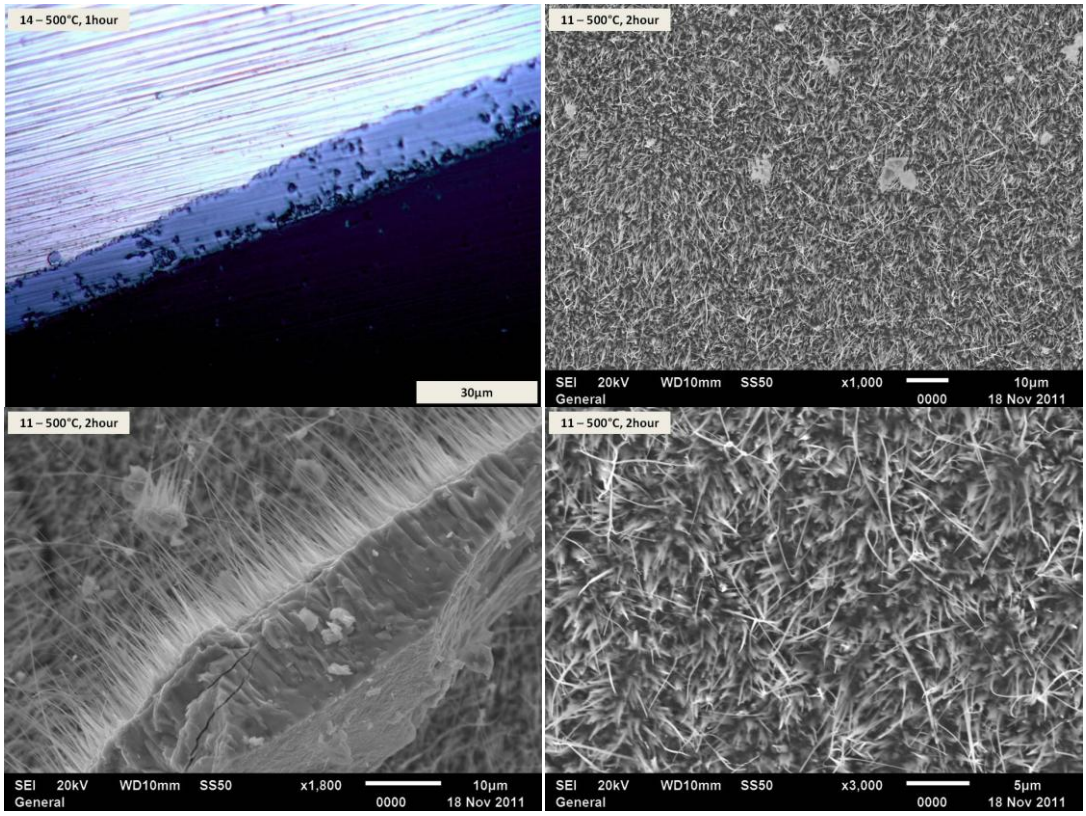

Figure 66: Optical and SEM images of samples 14 and 11 showing cross-section and nanostructured surface morphology.

Figure 66 shows a cross section of sample 14, again showing nanowire growth. Also present in the figure are SEM micrographs of sample 11. The top right image shows the uniformity of the nanowires across the upper surface of the sample. The bottom left image shows a section of the oxide on its side. From this image it can be ascertained that the nanowires tapper from a wide base at the upper surface of the oxide to a thin point at their tips, that the nanowire length varies across the sample surface and that the wires show a degree of flexibility not normally associated with brittle CuO. An estimate of the nanowire lengths, as measured from the SEM images, puts them between 10µm and 50µm long.

Quenching:

The Pilling-Bedworth ratios for the different copper oxides on copper can be calculated as follows:

$$PBR = \frac{V_{oxide}}{V_{metal}} = \frac{M_{oxide}\,\rho_{metal}}{n\,M_{metal}\,\rho_{oxide}}$$ where n = number of metal atoms per oxide molecule.

For CuO on Cu :

$$PBR = \frac{79.55 \times 8.94}{1 \times 63.55 \times 6.31} = 1.77$$

For Cu_2O on Cu:

$$PBR = \frac{143.09 \times 8.94}{2 \times 63.55 \times 6.00} = 1.67$$

These values indicate that the oxides formed take up a larger volume than the Cu substrate and that they must be under compressive stress when they form if this volume mismatch is anisotropic. The general rules for PBR are that PBR < 1 has a smaller volume than the substrate from which it was grown meaning it is likely to form a porous or cracked oxide, PBRs > 2 indicate a highly compressed oxide with a high probability of oxide spallation and 1 < PBR < 2 will usually form a protective barrier layer. As the values calculated here show, the PBRs for both oxides are approaching the upper limit of the volume ratio before spallation occurs.

Cu, CuO and Cu_2O have coefficients of thermal expansion (α) of 18.6x10^{-6}/°C, 9.3x10^{-6}/°C, and 4.3x10^{-6}/°C respectively. As the oxides are forming at high temperature it is assumed that they grow strain-free, due to the high diffusivity and mobility of the atomic species present. Once the heat treatment is complete, the strain is introduced into the layers as the samples cool. If the cooling rate is too high, then as the temperature decreases the strain at the interfaces between layers will build up until it outpaces the ability of the crystallites within the material to rearrange themselves to accommodate this strain. This ability, i.e. the mobility of the atoms via thermal diffusion, also decreases with temperature, increasing the likelihood of spallation occurring as the material approaches room temperature. As it stands for the Cu and oxides grown at 500°C in air, the Cu would contract the most during cooling, followed by the CuO and then the Cu_2O. As the Cu_2O layer is sandwiched between

the Cu substrate and the CuO surface it was thought that by increasing the cooling rate it might be possible to control the delamination of the surface CuO leaving the layer of Cu_2O on top of the Cu substrate. This would be advantageous in the construction of PV devices as the band gap of Cu_2O (2.17eV) is more suited to the absorption of the visible spectrum photons than that of CuO (1.2eV). During some of the earlier thermal oxidation runs, it had been noted that if a sample was taken out of the reactor before it had reached room temperature, then a small proportion of the surface oxide would spall exposing the Cu_2O underneath.

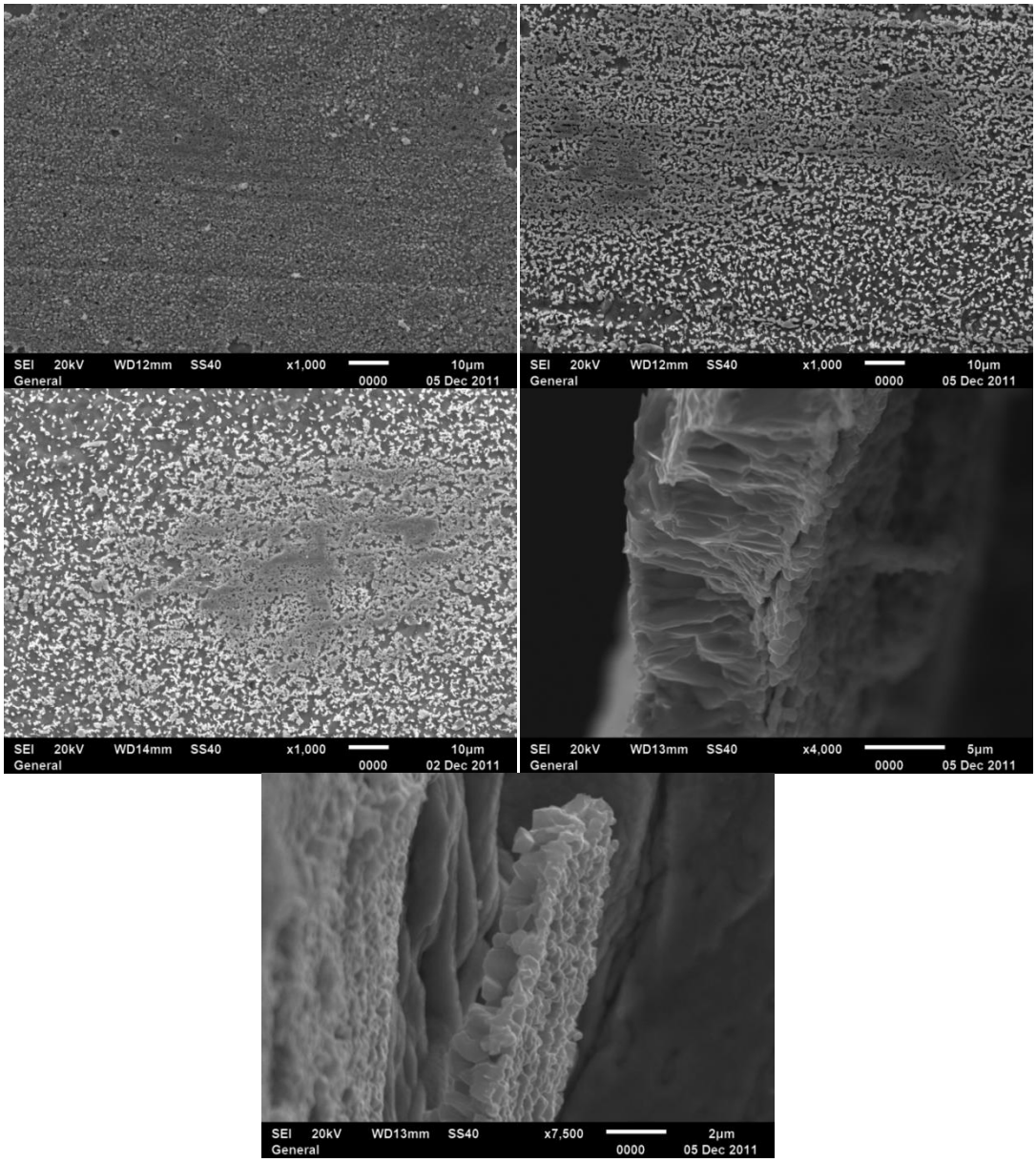

Figure 67: SEM images of quench test samples (all samples oxidised for 2 hours in air at 500°C). Top left: Quenched in air x1000. Top right: hot water (~90°C) quenched x1000. Middle left: Cold water quenched x1000. Middle right: Close up of partly spalled oxide from air quenched sample. Bottom: Partially spalled oxide from hot water quenched sample.

Figure 67 shows SEM images of the samples following a 500°C air anneal and quenching in different media. The first three images show the upper surfaces of the samples quenched in air, hot water and cold water, respectively. The upper surface of each of the samples is comprised of what appears to be cubic Cu_2O (the two oxides can be differentiated by the grain morphology, with Cu_2O showing smaller grains and a more obvious polycrystalline structure and CuO showing a more columnar and thicker oxide), indicating that the quenching has worked to some degree and the CuO layer has been removed. Of the

quenching media used, the cold water (middle left image) was predicted to have the most significant effect on the surface as it had the largest ability to absorb heat from the sample. The air quench (first image, top left) was predicted to have the least effect. It can be seen in the images presented here that the CuO has been removed from each of the samples. Unfortunately, each sample also shows that the Cu_2O layer has also lost material as a result of the quenching process. Visual examination of the SEM images shows that the air quenched sample has the most retained surface oxide followed by the hot water quenched sample and finally the cold water quenched sample. In each of the samples, the retained oxide appears porous, and the uniformity also appears to vary across the sample surface, with the most significant variation seen in the cold water quenched sample. It is unclear from the result here whether the lower areas exposed by the quench are Cu metal or a further layer of oxide. If they are exposed Cu metal then the use of this technique to create the substrate for a Cu/Cu_2O/n-type/TCO photovoltaic cell is flawed, as it would be highly likely that any deposited n-type material will be able to contact directly to the Cu substrate, providing an easier path for current to flow and also allow it to bypass the Cu_2O. Another factor visible from the first two images is that the rolling process has had a noticeable effect on the morphology of the Cu_2O. Since the samples were not vacuum annealed/stress relieved/recrystallised prior to the experiments, this could be due to high density, oriented dislocations within the metal, the effects of grain boundaries (which would show anisotropy from the rolling process) on the oxide growth or the effects of elongated precipitates from any impurities within the copper.

The final two images in Figure 67 show partially delaminated oxide found at the edges of the sample after quenching. The middle right image shows a ~5µm thick layer of dense oxide, thought to be retained CuO with a thin layer of a more porous oxide underneath (the Cu substrate is located just off to the right of the image). This is thought to be the Cu_2O layer. In the bottom image another delaminated oxide layer is shown, this time around 1µm

thick. Here the CuO has been removed leaving just the Cu_2O layer. It can be seen that this layer looks as though it is comprised of two different grain morphologies, with larger grains growing at the Cu surface and switching to a finer grain structure at the interface between the Cu_2O and the CuO. This could be a result of the quenching process, where the larger contraction of the CuO (c.f. the Cu_2O) has caused a high stress at the interface as the sample was quenched creating a high density of crystal defects which could pile up at impurity sites, eventually merging with nearby defects to create new grain boundaries. However, if the cooling rate of all layers was uniform during the quench, since the biggest contraction would be found in the Cu substrate, one would expect this effect to be reversed compared to the image shown here, with the smaller grains located at the Cu/Cu_2O interface. This process cannot be ruled out here as the actual cooling rates of each of the layers is currently unknown. It may well be that the thermal shock imparted into the Cu substrate is significantly lower than that experienced by the outer oxide layers.

5.3.2 Conclusion

Thermal growth of Cu oxides on Cu sheet was performed at several different temperatures and durations in a normal air environment. Samples grown at 500°C and 1000°C were found to follow a parabolic oxidation rate as predicted by the literature. Samples grown at 140°C were thought to be following a logarithmic growth rate. This was not conclusively proven due to the low mass gain of the samples. SEM analysis showed that at the higher two temperatures, the upper surface of the oxide was made from dense CuO with a less dense, nanocube layer of Cu_2O between it and the Cu substrate. Quenching from high temperatures to remove the CuO was partially successful, but with the parameters tried here portions of the underlying Cu_2O was also removed, limiting the usefulness of this technique for the construction of PV devices. It is possible that a higher temperature quench (above 100°C) using a medium such as hot oil may address this issue. For several of

the samples grown at 500°C, the upper surface of the oxide was found to consist of long CuO nanowires.

5.4 Effect of Initial Strain on Thermally Grown CuO Nanowires

The results from the previous set of experiments, i.e. the unintended growth of high density CuO nanowires on the surface of samples oxidised at 500°C warranted further investigation. If this growth could be controlled then these surfaces could be used as part of a p-n device, given the p-type nature of both Cu oxides.

CuO NWs were grown by thermally oxidising Cu sheet in standard atmospheric conditions at 500°C for 150 minutes. Samples were prepared with a range of positive and negative surface strains which altered the nucleation rate of CuO NWs. Tensile strains were found to enhance the nucleation rate of NWs while compressive strains suppressed their nucleation. This could be explained using the growth mechanism proposed by Mema *et al.*, i.e. a combination of both the strain induced growth and grain boundary diffusion mechanisms. Other proposed growth mechanisms such as VLS and VS growth were ruled out.

Sample Preparation:

High purity Cu sheet (99.9975%) was cut into strips measuring approximately 0.5x10x70mm. The Cu strips were vacuum annealed at 500°C for several hours to relieve any stresses within the material. After cooling to room temperature under vacuum to prevent any unwanted oxidation reactions the samples were removed from the furnace and bent around different diameter metal bars to form spirals. The spirals were left for several minutes and then straightened out again before being flattened by hand in a vice (between two Cu sheets to limit contamination from the vice jaws).

This bending process was used to introduce a varying amount of crystalline defects along the length of each sample. For the end of each sample in contact with the metal bars during

the bending process the level of deformation was the greatest as the radius of curvature was at its smallest. The other end, i.e. the last region to be formed into the spiral shape, had the largest radius of curvature and so would be less deformed. The upper surface of the samples (i.e. the part not in direct contact with the metal bar) firstly experienced tensile stresses as it was rolled into the spiral shape and then underwent compression as it was re-straightened out. The lower surface experienced compression followed by tension.

Additional samples were prepared via a different route to separate the combined surface strain effects of the compression/tension and tension/compression that would have occurred during the preparation sequence outlined above. For these samples Cu strips were cut from the as received sheet and tightly rolled around a 3.14mm diameter bar. They were then vacuum annealed overnight at 500°C to stress relieve and recrystallise the microstructure whilst in a coiled up state. Once cooled under vacuum, the samples were unrolled and flattened in a vice between two copper plates. One of the samples was then oxidised following the oxidation treatment outlined below and the other was tested on both the upper and lower surfaces using a Vickers microhardness tester.

Hardness Testing:

Once straightened, the samples were hardness profiled along their length using a Vickers micro-hardness tester with a 1kg load indented for 10 seconds. This was used as a measure of the amount of dislocations and crystal defects present within the samples. Having all received the same processing treatment (all samples were cut from the same piece of Cu sheet) as well as the same stress-relief vacuum anneal, it was found that the grain sizes of each sample were the same. All variation in hardness could then be attributed to the induced bending deformation and the number of dislocations present within the material.

Thermal Oxidation:

Oxidation of the deformed samples was carried out at 500°C in a normal air atmosphere. The samples were placed directly into the furnace once it reached the required temperature. Each sample was annealed for 150 minutes and then furnace cooled. Cooling was carried out at a rate of around 1°C/min to attempt to reduce damaging stresses in the surface oxides which could cause spallation.

Grain Size Analysis.

Two strips of Cu, one vacuum annealed and the other vacuum annealed and deformed to ±12% surface strain were mounted in epoxy and polished to a 1µm finish. The samples were etched using a mixture of 2:1 distilled water and (70%) HNO_3 for 30 seconds at room temperature. Following the acid dip the samples were rinsed in distilled water and acetone then air dried. Images were taken from across the exposed surface of each sample at 400x magnification using differential interference contrast optics to enhance any height differences and allow for easier identification of the Cu grain boundaries. 10 lines of a known length were drawn on to each of the images and the number of intersected Cu grains was recorded. Dividing this number by the line length allowed the average grain diameter to be determined for each image.

SEM Imaging:

SEM imaging was carried out using a JEOL JSM-6610 thermionic emission electron microscope with a 10kV beam, 13mm working distance and spot size of 50.

5.4.1 Results and Discussion

Several growth mechanisms have been proposed by different research groups to describe the thermal growth of CuO NWs on Cu; Vapour-Liquid-Solid growth (VLS), Vapour-Solid growth (VS), Short-circuit Cu_2O/CuO grain boundary diffusion and Stress-induced growth.

Vapour-Liquid-Solid and Vapour-Solid growth: For many materials one dimensional nanostructures and nanostructured surfaces can be produced via a chemical vapour deposition (CVD) mechanism. At a high enough temperature and low enough atmospheric pressure gaseous species, either produced as vapour from the substrate or introduced into the reaction chamber from a separate source, saturate the surface of the substrate forming nano-scale liquid droplets. These solidify from the base up, raising the remainder of the liquid up from the surface on top of a growing column of crystalline material. Simultaneously more vapour is deposited as liquid keeping the now raised droplets at a uniform diameter. If sufficient precursor gases are present in the atmosphere then the structures continue to grow yielding a dense forest of uniform, crystalline nanowires. For self-catalytic growth this mechanism is characterised by the presence of a solidified metallic droplet at the tip of each NW[165]. VS growth occurs by a similar CVD mechanism but without the requirement of the liquid phase. Precursor species in the atmosphere crystallise directly on to inhomogeneities at the surface generating nanostructures[166]. The protrusions arising from these inhomogeneities serve as sites for further deposition of crystalline material, growing out from the surface.

In the case of CuO NW growth, VLS and VS mechanisms have recently been ruled out. Both mechanisms require a relatively high vapour pressure of precursor species (in this case Cu atoms). At the temperatures that NWs are seen to grow (~300 - 700°C) the vapour pressures of pure Cu are in the region of ~10^{-9} Torr[155,157]. This would yield far too few Cu atoms in the atmosphere above the surface to account for the NW growth rates observed.

Additionally, due to the CVD element of the growth mechanism, were either of these mechanisms correct, deposition of Cu and/or it's oxides would occur on all surfaces within the oxidation environment; this has not been observed[167,168,169]. Since the melting points of the two oxides are known to be higher than that of Cu (Cu - 1080°C [170], Cu_2O - 1230°C [171] and CuO - 1336°C [172]) it can reasonably be inferred that these materials have lower vapour pressures within the oxidation temperature range and are not therefore the source of any significant Cu vapour.

Short-Circuit grain boundary diffusion: Within the temperature range that the atmospheric oxidation of Cu to CuO occurs (160-1040°C) the growth of the oxides is controlled by two different diffusion mechanisms. In ambient atmospheric conditions NWs have been shown to grow between ~300-~700°C [96,155,157]. For temperatures above ~700°C the conversion of Cu to Cu_2O/Cu_2O to CuO is rate controlled by bulk lattice diffusion. Below this temperature diffusion of atoms within grains is reduced; grain boundary and lattice defect diffusion become the dominant mechanisms for mass transport[96,173]. Both mechanisms result in parabolic rate laws for the growth of the Cu oxides but can be differentiated by a change in the oxidation rate constants seen within the different temperature ranges. Several variants of this growth mechanism have been proposed:

In the first variant NWs grow at the interface between the Cu_2O and CuO layers. Mass transport occurs by the egress of Cu ions from the metal substrate along the Cu_2O grain boundaries where they react with incoming O ions at the Cu_2O/CuO interface to form NWs[155]. NWs would protrude from the surface at CuO grain boundaries.

The second variation on the growth mechanism is that NWs grow from the surface of CuO grains at the CuO/atmosphere interface. Cu ions travel along the grain boundaries of both the Cu_2O and CuO layers where they surface diffuse towards the centre of the upper surface grains and are deposited at the edge of stepped atomic planes. On any grains

where two crystallographic planes meet at the surface, this interface would have a higher available free energy, allowing the deposition and reaction of the Cu atoms. Species deposited on either side would lattice match to the adjacent planes producing the characteristic bi-crystal structure. Once the NWs are nucleated, Cu atoms continue to surface diffuse up the side walls of the NW where they deposit at the stepped edges of the still-present bi-crystal structure on the tip[99,167].

Several HRTEM studies have showed that many of the observed NWs show a bi-crystal structure with a (11-2)(00-1) twin boundary running up the centre of the NWs[96, 99,155,174]. This internal grain boundary could allow increased movement of Cu atoms which are delivered for the reaction with oxygen depositing more CuO at the NW tip. Also there has been some indication in SEM images following long oxidations (more than 2 hours) that NWs originate from the interface between the Cu_2O and CuO layers[155].

However, in other work, evidence for a Cu-rich core was not found at within the twin boundary[167]. It has also been shown in short-duration oxidation experiments that the bi-crystal NWs originate near the centre of the upper surface of individual CuO grains. The bi-crystal structure seen in many NWs would then result from the nucleation and merger of single crystal NWs growing on each exposed surface facet of the CuO grains[167]. The proposed explanation for the earlier results that showed the CuO NW nucleation point at the Cu_2O/CuO boundary is that a proportion of the Cu atoms that arrive up from the CuO grain boundaries are directly incorporated into the CuO layer which continues to thicken. For long oxidation times this additional oxide covers the NW bases. As the thickness of the upper CuO layer remains roughly constant due to the continuing oxidation of CuO $\leftrightarrow$ Cu_2O, the base of the NW recedes into the bulk oxide, eventually reaching the CuO/Cu_2O interface[167].

Stress Induced growth: Nanowires grown on the upper oxide surface are the result of a stress relaxation process. This is caused by lattice strain at interfaces of the different oxide's crystal structures, differences in the molar volumes of the oxides and metal substrate, differences in the densities of the materials and/or differences in the thermal expansion properties of the oxides and metal. Strain fields built up in the upper most CuO layer act as nucleation points for the growth of new crystals (i.e. NWs) which then releases the strain in the layer[155]. Strain fields in the underlying layers could also provide additional energy to facilitate mass transport and enhance the delivery rate of Cu ions towards the oxidation surface.

Controlling parameters for CuO NW growth:

The morphology of thermally grown CuO NWs has been shown to be dependent on several factors, most importantly growth temperature, growth duration and oxygen partial pressure. Gonçalves *et al.* found that between temperatures of 400 - 700°C NWs could be grown on the CuO surface. The diameter of the NW bases was found to correlate linearly with temperature and an empirical relationship was proposed by the group:

$d \cong (17T/30) - (590/3)$ where d = NW diameter (nm) and T = temperature (°C).

The length of the NWs showed a parabolic growth law, similar to those of the bulk oxide layers, indicating that the rate limiting step was mass transport by diffusion. In this case the length of the NWs was found to be proportional to the square root of the oxidation time: $l^2 = kt$ where l = NW length (m), k = rate constant (m^2/min) and t = oxidation time (mins). For growth at 400 and 700°C values for k were 1.7×10^{-14} m^2/min and 7.3×10^{-12} m^2/min respectively[157]. Other research groups have reported similar observations for the NW growth window[96,155,175], NW diameter-temperature dependence[96,174] and NW length-time relationship[96,175].

Various groups have also reported a relationship between the oxidation temperature and the number density of the resultant NWs. Growth temperatures near to the upper limit of the growth window show a lower number of NWs/unit area than for lower temperatures[174]. Recent work by Mema *et al.* and Yuan *et al.* has also suggested a link between the stresses/strains within the different layers of the $Cu/Cu_2O/CuO$ structure before and during the oxidation process. By using thin sheets of Cu bent to a constant radius of curvature before the oxidation, Mema *et al.* were able to introduce both tensile and compressive stresses into the opposite surfaces of the Cu sheet. They found that the tensile stresses enhanced the nucleation rate of NW structures giving around 5 times as many NWs per unit surface area compared to unstressed Cu sheet. The compressive stresses had no effect on the NW density. The report showed that this could be the result of a modification to the Cu_2O and CuO bulk oxide layers whereby the increase in tensile stress causes a high nucleation rate for Cu_2O grains. This gave a higher number of smaller grains with an increased number of grain boundaries. Since the grain structure of the CuO layer is governed by the microstructure of the layer it is grown from, this also leads to smaller, more numerous CuO grains. These results illustrate that the growth of the NWs is actually governed by a combination of both the Stress-Induced and Short-Circuit diffusion mechanisms outlined above.

Using a more severe bending process to introduce tensile and compressive strains in the initial Cu sample, the aim of this paper was to continue the investigation into the effects of tensile and compressive stresses on the density of CuO NWs.

Theoretical Calculations:

The radius of curvature for each spiral sample at a distance x from the end with the highest level of deformation could be estimated using the following equation:

$$r_c(x) = \frac{d}{2} + \frac{xt}{\pi d}$$

where r_c = radius of curvature (mm) of the inner surface, d = diameter of bar that the sample had been wrapped around (mm), x = distance from most deformed end of the sample (mm) and t = thickness of the sample (mm).

To calculate the theoretical strain at the upper and lower surfaces of the sample it was assumed that there was a neutral axis running through the centre of copper samples where the strain field was equal to zero. To start with, the surface strain for a circular Cu sample (constant radius of curvature) tightly wrapped around a bar of diameter d was derived. The circumference of the bar and thus the circumference of the inner surface of the ring was:

$$C_{inner} = \pi d$$

The length of the neutral axis for the Cu ring, located at the rings centre would be:

$$C_{neutral} = 2\pi\left(\frac{d}{2} + \frac{t}{2}\right) = \pi(d + t)$$

And similarly the length of the outer surface (under tension) would be:

$$C_{outer} = 2\pi\left(\frac{d}{2} + t\right) = \pi(d + 2t)$$

Assuming that the strain at the midpoint of the ring was zero, i.e. $\varepsilon_{neutral} = 0$, the strain at the upper and lower surface could be deduced:

$$\varepsilon_{outer} = \frac{\Delta l}{l} = \frac{\pi(d + 2t) - \pi(d + t)}{\pi(d + t)} = \frac{\pi d + 2\pi t - \pi d - \pi t}{\pi d + \pi t} = \frac{t}{d + t}$$

$$\varepsilon_{inner} = \frac{\Delta l}{l} = \frac{\pi d - \pi(d + t)}{\pi(d + t)} = \frac{\pi d - \pi d - \pi t}{\pi d + \pi t} = -\frac{t}{d + t}$$

In the above equations $d = 2r_c$, where the radius of curvature (r_c) is constant at any distance x from the most tightly curled end of the sample. To modify these equations so that they apply to the samples wound up as spirals the radius of curvature at the middle of the sample, located at the neutral axis, was modified to:

$$r_c(x) = \frac{d}{2} + \frac{xt}{\pi d} + \frac{t}{2}$$

This method was quite simplistic in that it did not account for the increase in x that would be expected over a number of rotations when converting from a circular equation to a spiral one, but as this increase was negligible over the distances considered the additional terms required could be ignored.

Replacing the diameter in the ε_{inner} and ε_{outer} equations with the term for the variable radius of curvature gave:

$$\varepsilon_{outer}(x) = \frac{t}{2t\left(\frac{x}{\pi d} + 1\right) + d}$$

And $\varepsilon_{inner}(x) = -\varepsilon_{outer}(x)$

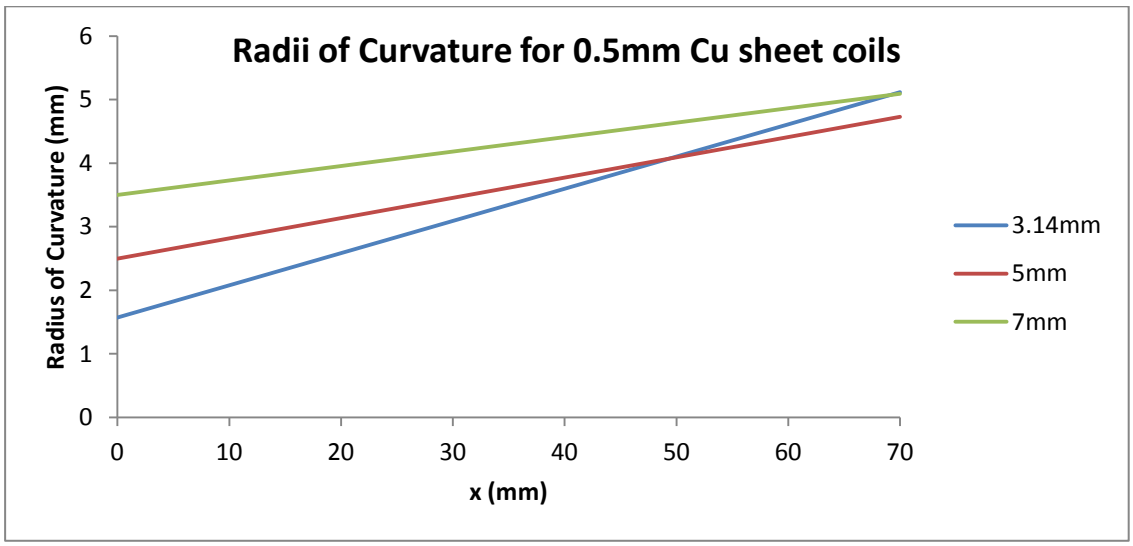

Figure 68: Graph showing the calculated radii of curvature for three 0.5mm thick Cu sheet samples coiled around bars of different diameters.

Figure 68 shows the results of the calculation of radius of curvature for the samples used in these experiments. As expected, the r_c value increases in a linear manner for each sample along its length. These values were used to calculate the theoretical surface strain on the upper surface of each sample (Figure 69).

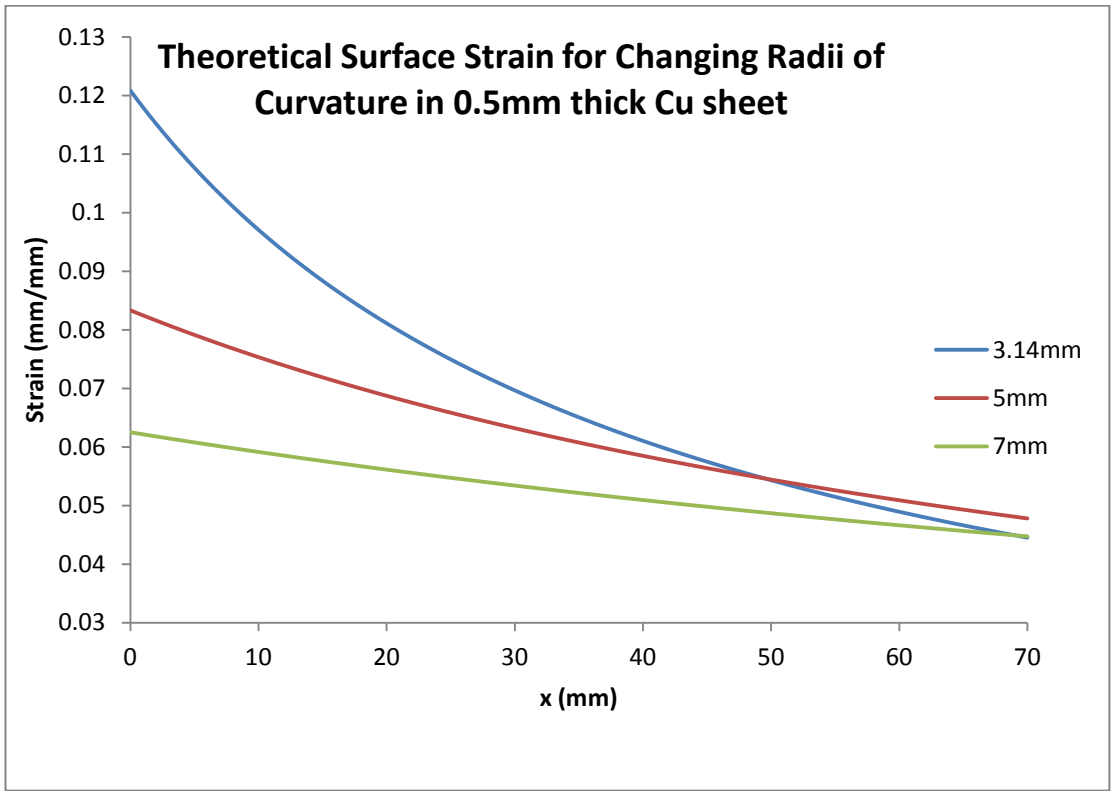

Figure 69: Variation in calculated surface strain along the length of three 0.5mm thick Cu sheet samples with different initial radii of curvature.

It can be seen that the surface strain decreases along the sample length as the value of r_c increases. The sample wrapped around the smallest diameter bar shows the greatest surface strain which quickly tails off as the distance from the coil to the centre of the bar gets progressively bigger. This sample also shows the largest variation in surface strain (from ~12% to ~4%). For the other samples the variation in surface strain as well as the maximum surface strain is significantly smaller, approximately 8.5% to 5% for the 5mm sample and 6.5% to 4.5% for the 7mm sample.

As stated earlier, the tensile strain on the "upper" surface was expected to be mirrored by an equal magnitude compressive strain on the lower surface of the sample. This was under

the assumption that the neutral axis, where the two strains cancel each other out, would be located midway through the thickness of the sheet, i.e. 0.25mm from either the upper and lower surfaces.

Once rolled into the coils, very little spring-back occurred and the Cu sheet remained tightly rolled up. This indicated that the stresses accompanying the strains achieved were of a sufficient magnitude to exceed the yield strength of the copper metal.

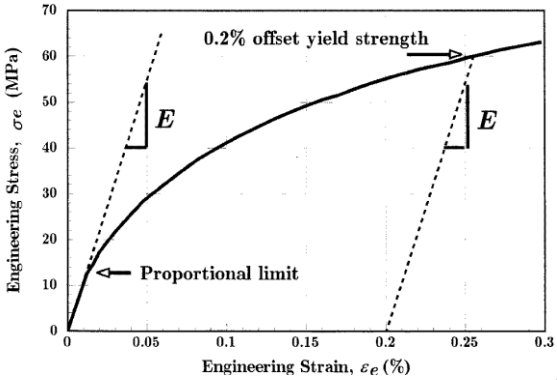

Figure 70: Stress-strain curve for annealed polycrystalline Cu[176].

Figure 70 shows part of the stress-strain curve for annealed polycrystalline Cu. From this graph it can be seen that the stresses associated with the maximum strain undergone by each sample were approximately ±45MPa for the 12% strained sample, ±35MPa for the 8.5% strained sample and ±30MPa for the 6.5% strained sample.

Grain Size Analysis:

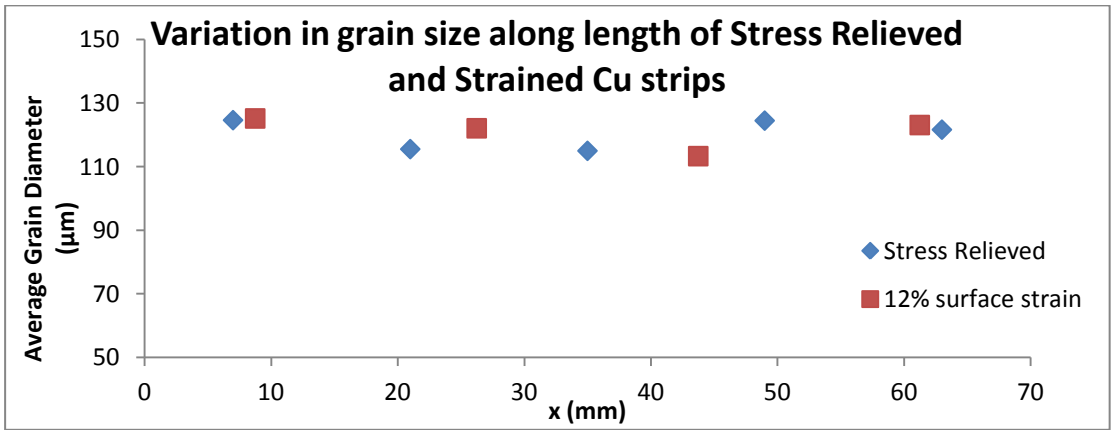

Figure 71: Graph showing the average grain sizes of annealed and deformed (1.67mm radius of curvature) Cu sheet. Average grain diameter remains constant at 120µm ±10µm after deformation.

Figure 71 shows the results of the grain size analysis for two samples; one vacuum annealed (i.e. stress relieved and recrystallised) and the other vacuum annealed/coiled /uncoiled/flattened. For the strained sample, if the deformation process was to have any effect on the grain size, one would expect that higher levels of deformation would lead to a decrease in grain size: this would show itself on the graph as an increasing average grain diameter for increasing values of x with a minimum at $x = 0$. As can be seen in Figure 71 this was not the case as the grain size remained uniform across the sample at 120µm ±10µm. This was also the same value as seen in the un-deformed sample indicating that no change in grain size has occurred due to the coiling/uncoiling procedure.

Hardness Testing:

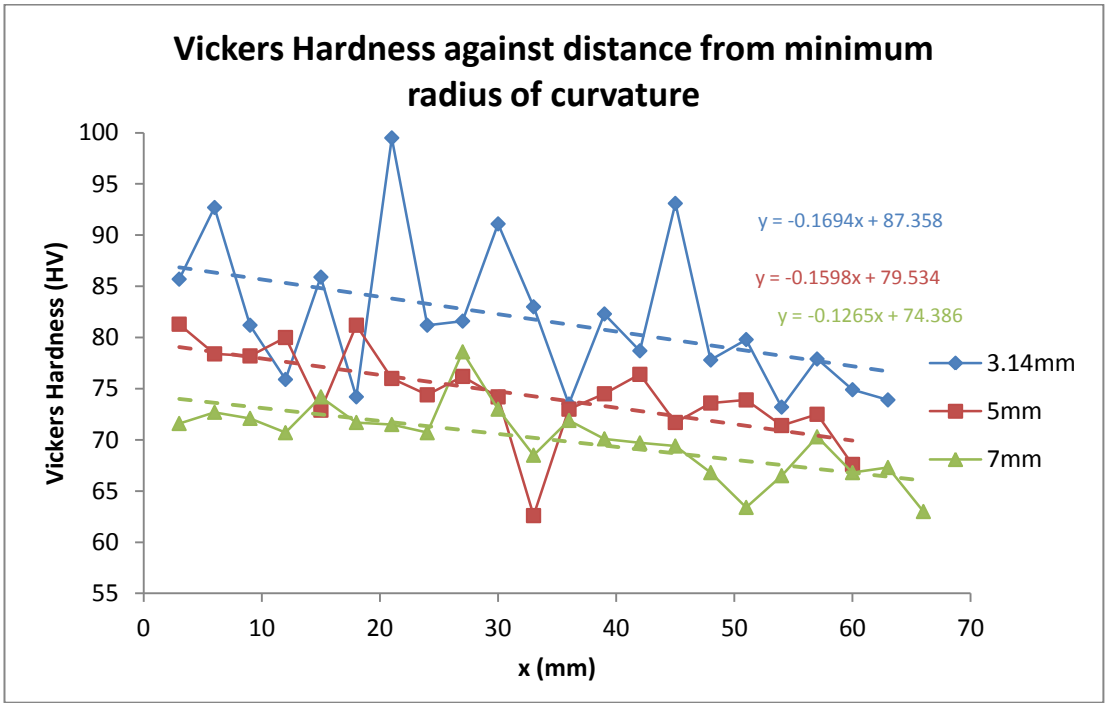

Figure 72: Change in Vickers Hardness along the length of three annealed, coiled, uncoiled and flattened Cu sheet samples.

Figure 72 shows the hardness values along the length of three samples having undergone different levels of deformation. These samples were stress relieved in a vacuum furnace at 500°C for several hours then coiled around bars of different diameters, uncoiled and flattened. As expected, the sample that received the highest amount of deformation (~12%

surface strain from the theoretical calculations) work-hardened the most. It was also noticed that the data points for this sample also showed the largest amount of error, >±15HV. For the other two samples the hardness was found to decrease with increasing initial radii of curvature (at x=0). The associated error was also reduced relative to the increasing initial radii of curvature, with the 5mm sample having an error of around ±15HV and the 7mm sample having an error of around ±10HV. The deviation from the line of best fit when the hardness was measured along the samples was thought to have originated from the process used to induce curvature in the samples. As the samples were manually coiled, it proved difficult to introduce a truly uniform bending along the samples. As such, the samples could be thought of as being comprised of short, straight (or less deformed) sections joined by more severely deformed sections. Because the samples were coiled about themselves, however, the average hardness along their length did follow the line of best fit. Ideally the samples would be mechanically coiled which would decrease the noise seen in the hardness graphs.

These samples were comprised of high purity Cu (99.9975%) and the grain size of the samples was found to remain constant at around 120µm diameter regardless of the level of deformation (Figure 71). Because of this it was postulated that the variation in hardness seen along the length and between the samples was entirely due to the number of dislocations present. Grain size effects could be ruled out and hardening effects of any dislocation pinning entities such as substitutional impurities and precipitates could be treated as negligible due to the high purity of the samples. The hardness of pure polycrystalline Cu ranges from approximately 30HV to 100HV. It can be assumed that at the lower end of this scale high purity Cu was relatively free from dislocations and other strength effecting entities and that at the higher end of the scale the number of dislocations was approaching a maximum level. It follows that at the most deformed ends of the samples surface Cu grains would have a higher number of surface terminated

dislocations. At the oxidation temperatures used, where the dominant diffusion processes are via grain boundaries and dislocations as opposed to bulk diffusion, this would serve to enhance the nucleation and growth rates of the Cu oxides, creating finer grained oxide layers above the substrate.

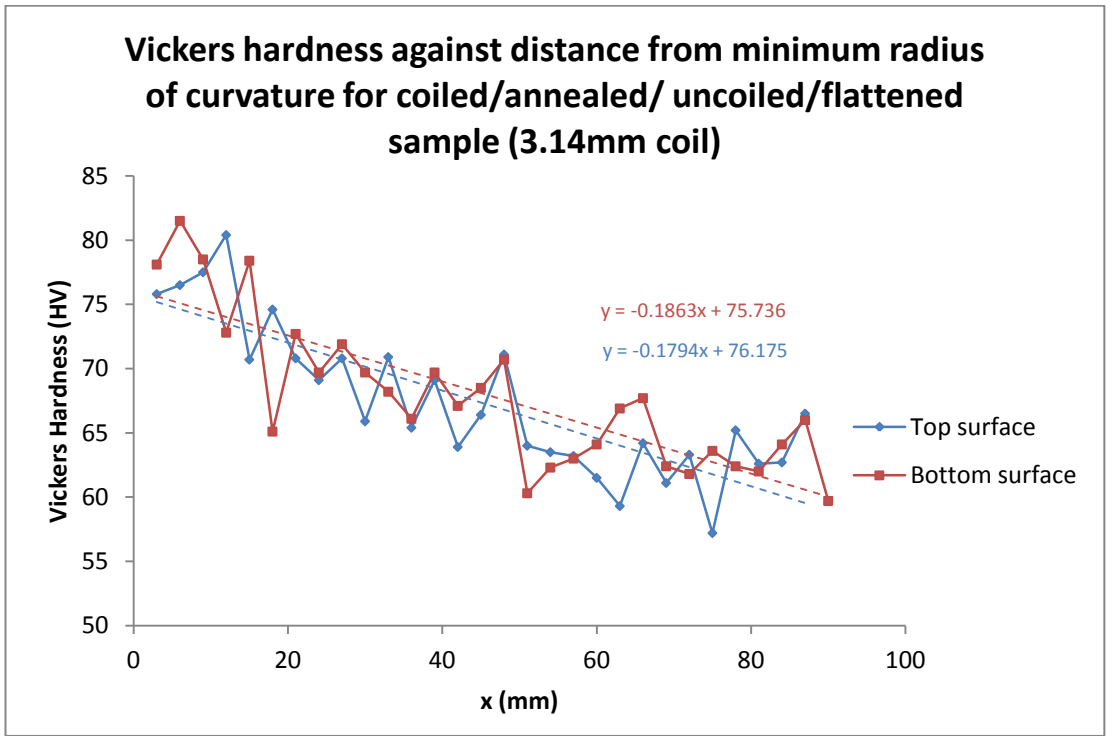

Figure 73: Vickers Hardness against distance from minimum radius of curvature for sample coiled around a 3.14mm bar, annealed, uncoiled and flattened. Top and bottom surfaces (compression and tension, respectively) show similar hardness values implying that the theoretical assumption used regarding the location of the neutral strain axis is correct.

Figure 73 shows the Vickers hardness measurements taken from the top and bottom surfaces of a sample that had been coiled around a 3.14mm bar, vacuum annealed, uncoiled and flattened. Compared to the 3.14mm sample shown in Figure 72, this graph showed a lower overall hardness (by around 10HV) and a similar hardness gradient (around -0.17 to -0.18 HV/mm) along its length. The difference seen in the magnitude of the HV values was attributed to the differences in sample preparation; the first samples were annealed/coiled/uncoiled before measurement, effectively introducing both tensile and compressive stresses in both the upper and lower surfaces. The sample shown in Figure 73 was coiled/annealed/uncoiled before measurements were taken. The fact that the first

sample was significantly harder than the second sample showed that when coiling and uncoiling the first sample the introduction of an opposing stress field was in fact additive to the overall hardness and that the newly introduced dislocations did not significantly annihilate any existing dislocations already present in the Cu sheet.

Figure 74: Photograph of sample surface (compression) after annealing while coiled, flattening then oxidising in an ambient atmosphere at 500°C for 150 minutes. The end in the left of the image has undergone the most deformation. Visual inspection shows a less reflective surface at the less deformed end indicating a higher density of nanowires.

Figure 75: Reverse surface (tension) of same sample as shown in . Visual inspection shows a small area of low reflectivity (from around 1-3cm along from the left hand edge).

Figure 74 and Figure 75 show images of the Cu strip (coiled/ annealed/ uncoiled/ flattened/ oxidised) following oxidation at 500°C in a standard air atmosphere for 150 minutes. It can be seen from these images that there has been significant flaking of the upper oxide layer on both sides of the sample although the effect is more apparent on the compression side. This was due to the differing rates of contraction of the various layers in the sample during cooling after the oxidation. The Cu substrate, with a linear coefficient of expansion of 16.6×10^{-6} K^{-1} would have contracted most during cooling leading to a significant compressive strain in the oxide layers above. Directly above the Cu substrate, the Cu_2O would have contracted much less with a coefficient of thermal expansion of ~4×10^{-6} K^{-1}. The upper CuO layer, with a coefficient of thermal expansion around 8×10^{-6} K^{-1} would also contract more than the Cu_2O layer. Overall this contraction would result in high stresses at the Cu/Cu_2O interface, with the Cu in tension and the Cu_2O in compression. At the Cu_2O/CuO interface the Cu_2O would again be under compression whilst the CuO would be in tension. Due to the drop to room temperature of 475K the CuO layer would contract by ~

$3.8x10^{-3}$ m/m, the Cu_2O by ~ $1.9x10^{-3}$ m/m and the Cu by ~ $7.89x10^{-3}$ m/m. For a sample with no internal stresses prior to oxidation this would result in the middle Cu_2O layer being compressed by the Cu substrate (ε ~ ± $6x10^{-3}$ on either side of the Cu_2O/Cu interface) and the CuO surface oxide (ε ~ ± $2x10^{-3}$ on either side of the Cu_2O/CuO interface). This effect could account for the hill and valley surface morphology seen by several groups[157,177] by providing the necessary energy to deform the upper layers of oxide whilst the samples are cooling, i.e. at temperatures high enough for diffusion to still be occurring. The compressive stress field running through the Cu_2O layer (~3 times lower at the Cu_2O/CuO interface than at the Cu/Cu_2O interface) may also provide additional energy towards atomic diffusion as atomic species would tend to migrate from the highest compressive stress towards the lowest. As the sample temperature approached RT diffusion would be significantly reduced and the remaining thermal contraction would create further stresses that could then go on to buckle the Cu_2O layer and cause the spallation seen.

SEM Imaging:

Due to the large area of the samples in conjunction with the high stress mismatch between the thermally grown oxide layers, the oxides on the sample surface were not uniform when viewed from one side to the other. In some cases this manifested itself as areas where the upper surface oxide (planar CuO or planar CuO with CuO NWs) had flaked away exposing the polycrystalline Cu_2O interface layer. This occurred significantly more for the compressed surface than the tensile surface. In other cases CuO NWs were seen, but with large variation in density and morphology across the surface. To minimise any bias in the measurement of the NW density, images were taken along a line running down the centre of the samples at 3mm intervals. No x-y deviation from the line was permitted resulting in several images where the upper CuO and NWs were completely absent. This also accounts for the relatively large spread in the NW densities seen in Figure 76 and Figure 77.

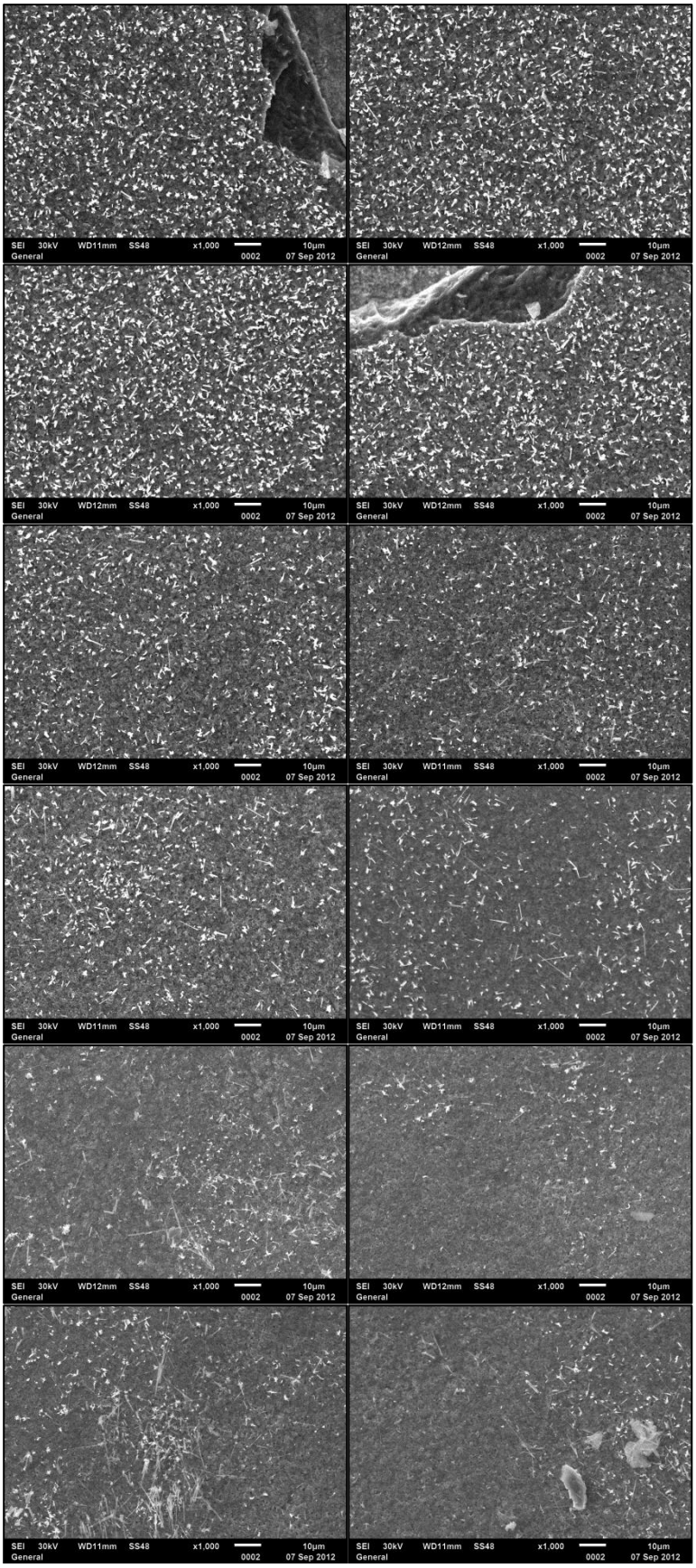

Figure 76: Selection of SEM micrographs taken at regular intervals along the length of the compression side a thermally oxidised Cu sample that was coiled/vacuum annealed/uncoiled/flattened prior to oxidation. Image order goes from top left (low compressive strain) horizontally to bottom right (high compressive strain).

Figure 76 shows a selection of the SEM images taken of the compression side of the Cu sheet. It can be seen that in moving from the upper right image to the lower left (low to high compressive strain) the growth of CuO NWs is suppressed leading to the production of sparse and patchy areas of NW growth. This indicates that the effect of compressive stresses within the substrate prior to oxidation is to decrease the nucleation rate of CuO NWs. This result is different to that seen by Mema *et al.*[99]. In their paper very little difference was seen in the number density of the CuO NWs between the compressive stress and zero-stress samples. This could be explained by the fact that using the strain equation described above, the strains used for their experiments were around 1.2%, around 10 times lower than those used here. In their paper they postulate that the growth of NWs is facilitated by pre-existing tensile stresses. These reduce the lattice mis-match strain associated with the oxidation of Cu (3.61Å) to Cu_2O (4.26Å) by effectively increasing the size of the Cu unit cell. This then gives a lower nucleation barrier for the growth of oxide islands and promotes the formation of a finer grained Cu_2O (and by implication, CuO) layer. It would seem reasonable then to state that the converse could also be true, i.e. that pre-existing compressive stresses reduce the apparent dimensions of the Cu unit cell, increasing the oxidation lattice mis-match and increasing the grain size of the Cu_2O and CuO layers. A lower number of grain boundaries then reduces grain boundary diffusion and limits the number of NWs formed.

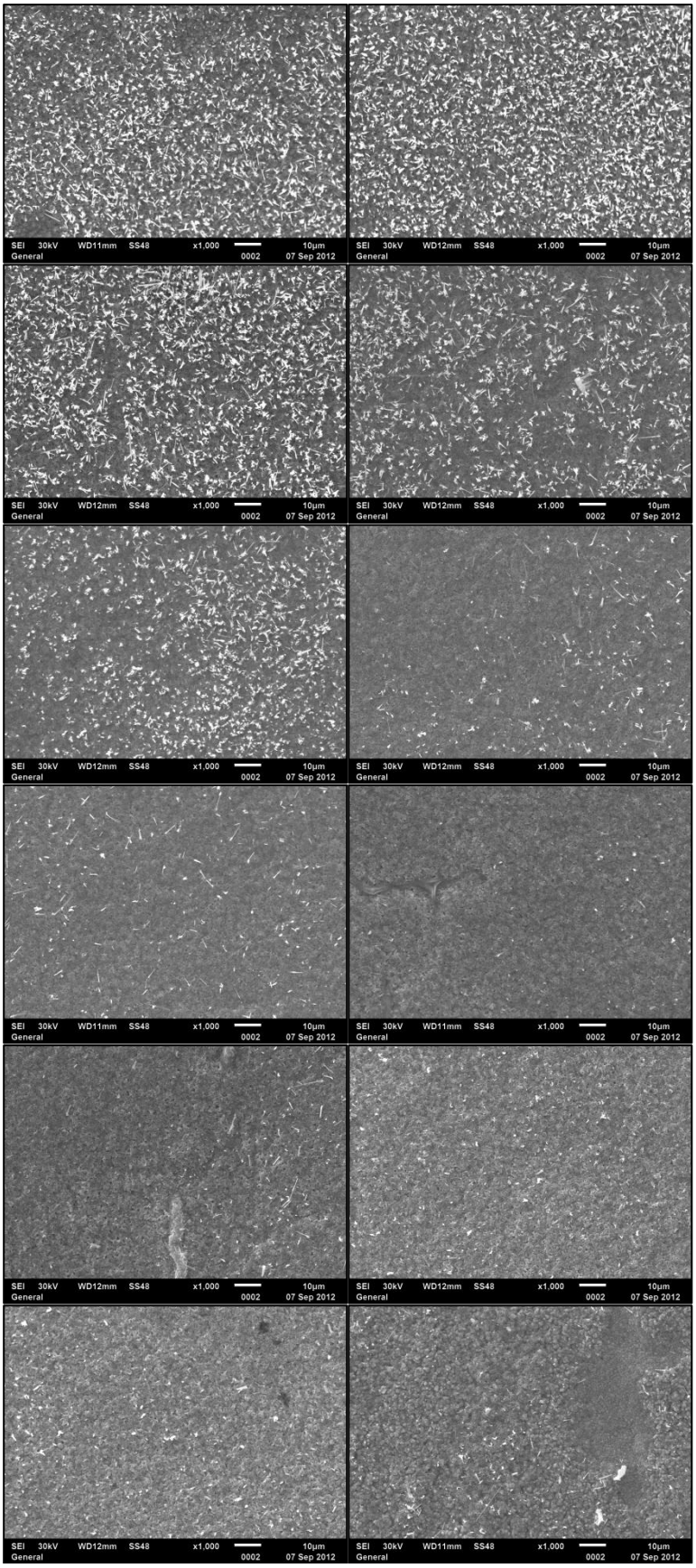

Figure 77: Selection of SEM micrographs taken at regular intervals along the length of the tension side a thermally oxidised Cu sample that was coiled/vacuum annealed/uncoiled/flattened prior to oxidation. Image order goes from top left (high tensile strain) horizontally to bottom right (low tensile strain).

Figure 77 shows the reverse side of the same sample, with the upper left image corresponding to high tensile strain and the lower right to lower tensile strain. These images are in agreement with the relationship proposed by Mema *et al.* in that the parts of the sample under high strain show a higher number of NWs per unit area than the parts under low strain. Another point that should be noted is that even in the low strain tensile areas (Figure 77), and the high strain compressed areas (Figure 76) NW formation was not completely suppressed. This would be expected if the Mema *et al.* mechanism was correct as grain boundary diffusion would still occur to some degree in large grained samples, allowing the delivery of Cu ions to the surface of the CuO grains were they could surface diffuse and nucleate new growth at the stepped interfaces of different atomic planes at the CuO grain/atmosphere boundary.

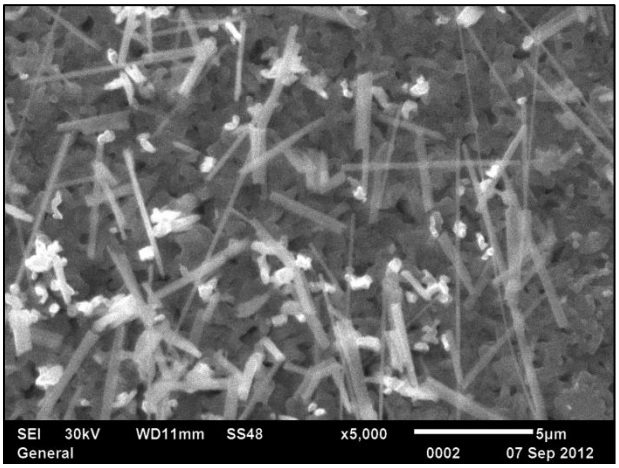

Figure 78: CuO NWs grown on compressed side of Cu sheet.

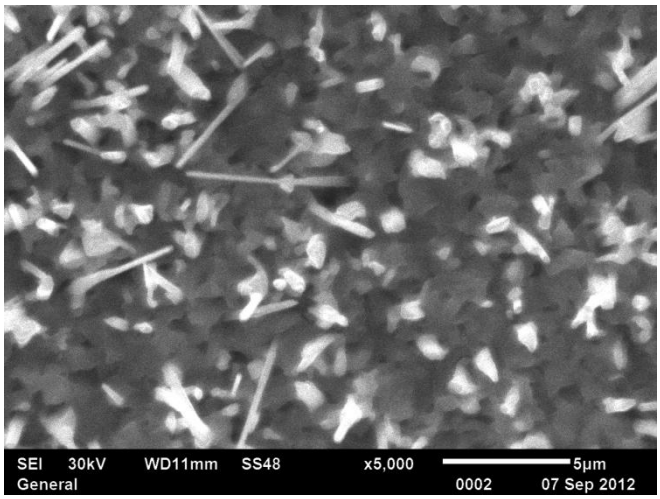

Figure 79: CuO NWs grown on tensile side of Cu sheet.

Analysis of the SEM images showed that there were at least two distinct NW morphologies present across the samples (Figure 78 and Figure 79). For the low NW density areas, the majority of the NWs had low aspect ratios (~5-10) and NW base diameters of approximately 200-500nm. The second NW type seen had much higher aspect ratios (~50-100); these NWs were noticeably thinner than the first type with base diameters around 100-200nm. It could also be seen in these images that where the intersection of the NWs with the bulk surface was visible NWs appeared to grow from the centre of the CuO grains and not from the grain boundaries, again adding weight to the growth mechanism proposed by Mema *et al.*.

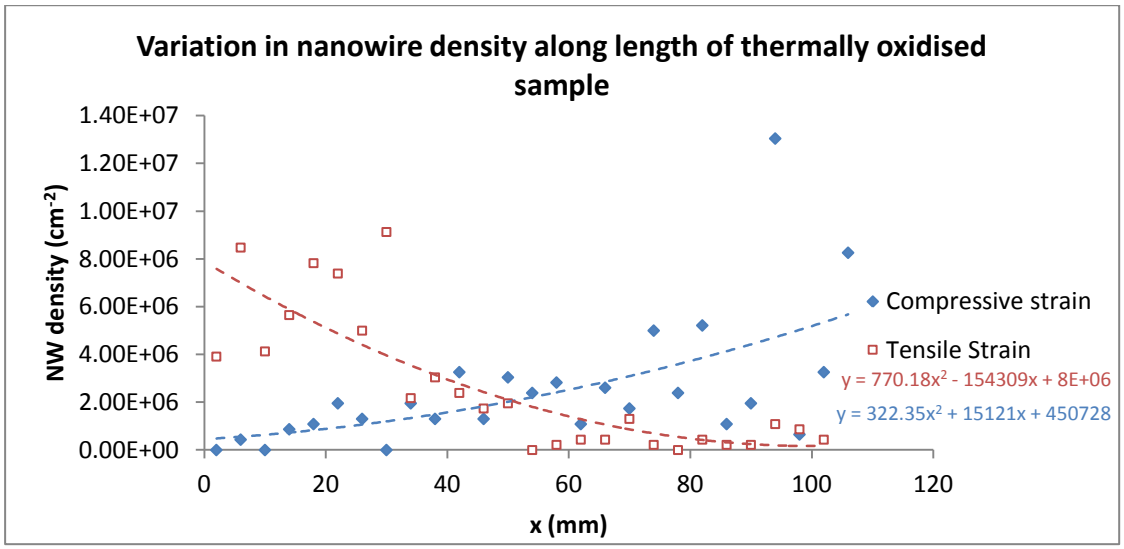

Figure 80: Graph showing the change in nanowire density along the length of both sides of a thermally oxidised Cu sample that was coiled/vacuum annealed/uncoiled/flattened prior to oxidation.

Figure 80 shows the analysis of the SEM images taken on either side of the Cu sample. At x=0 the surfaces had undergone the most deformation. Although the data spread is quite large for both the tension and compression surfaces a clear trend can be observed. Regarding the tension side, a decrease in the amount of stress within the sample resulted in fewer NWs being nucleated. The converse was seen in the compression side, with a decrease in the amount of stress promoting the growth of NWs. The parabolic lines of best fit shown in the graph were included to illustrate the effects seen and should only be treated as very approximate. It was possible that they were both underestimates due to the inclusion of data points in which the upper oxides (and any NWs) were not present. From

comparison of the data spread for the tension and compression sides it also seemed as though the compression side had suffered more spallation during cooling than the tension side.

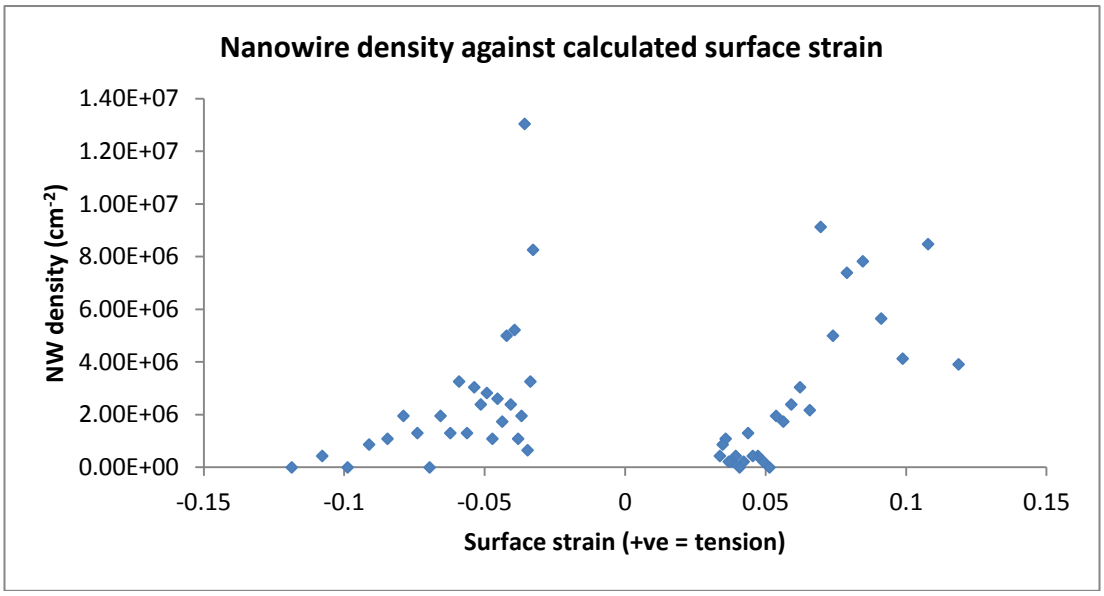

Figure 81: Graph showing nanowire density against calculated surface strain from either side of a coiled/vacuum annealed/uncoiled/flattened sample.

Using the strain equation outlined above, Figure 81 shows the data for NW density against surface strain for both sides of the oxidised sample. As expected, the same trends can be observed with an increase in tensile strain promoting the growth of NWs and an increase in compressive strain suppressing their growth.

5.4.2 Conclusions

CuO NWs were grown by thermally oxidising Cu sheet in a standard atmosphere at 500°C for 150 minutes. Samples were prepared with a range of positive and negative surface strains which altered the nucleation rate of CuO NWs. Tensile strains were found to enhance the nucleation rate of NWs while compressive strains suppressed their nucleation. This could be explained using the growth mechanism proposed by Mema *et al.*, i.e. a combination of both the strain induced growth and grain boundary diffusion mechanisms. Other proposed growth mechanisms such as VLS and VS growth were ruled out.

5.5 Growth of CuO Nanowires Through an ALD Al_2O_3 Barrier Layer

A significant problem often encountered when growing CuO NWs on Cu sheet by thermal methods is the mechanical stability of the oxide layers. Due to the high interfacial stresses generated by the mismatch in coefficients of thermal expansion of each of the layers and the temperature change from ~500°C to room temperature, significant oxide spallation can occur leaving a non-uniform surface. Attempts to create electronically functional devices from these substrates may be hindered by the inclusion of high levels of defects and short-circuit diffusion paths as non-adjacent layers are allowed to come into electrical contact with each other. This study looks at the effect of the mechanical stability of thermally grown CuO NWs after the introduction of a mediating thin barrier oxide layer.

Different thicknesses of Aluminium Oxide were deposited via ALD onto prepared Cu metal substrates (strained and cleaned) prior to thermal oxidation. SEM and XPS were used to assess the resultant structures. It was found that for Al_2O_3 thicknesses between ~4 and 20nm the CuO Nanowire density could be reduced while leaving the length and diameters of the NWs unchanged. Above ~20nm Al_2O_3 the growth of CuO was severely hindered resulting in patchy island type growth. The mechanical stability of the layered structures was also found to increase with the addition of the ALD barrier layer.

6 Cu samples measuring 15x15x0.3mm were cut from highly tensioned strips of Cu sheet (~14% strain). Native oxide and other impurities were removed by rinsing in 30% HNO_3 (~10s) followed by distilled water, acetone and isopropanol rinses. Samples were dried in room temperature flowing air. A Cambridge Savannah ALD reactor was used to deposit different thicknesses of Al_2O_3 onto the upper surfaces of the Cu sheet. Pieces of Si wafer placed close to the Cu tabs were also included in the reactor to allow measurement of the deposition thickness via ellipsometry.

ALD deposition of Al_2O_3 was carried out using TMA and H_2O co-reactants in alternating pulses with 5sccm of Ar as the carrier gas and purge medium. Each cycle of ALD consisted of 0.02s TMA/2s purge/0.01s H_2O/2s purge. Deposition was conducted with a substrate temperature of 150°C, the lowest point in the growth window for Al_2O_3 from TMA and H_2O, to minimise oxidation of the Cu while in the reactor chamber. The number of ALD cycles used for each sample is shown in Table 19.

Table 19: Number of ALD cycles used for each sample

Sample No.	Aimed for Deposition Thickness (nm)	No. of ALD cycles @ ~0.1nm/cycle
CuBL1	0	0
CuBL2	5	50
CuBL3	10	100
CuBL4	15	150
CuBL5	20	200
CuBL6	30	300

Following ALD, the samples were placed inside a standard atmosphere box furnace at 500°C for 1 hour. Samples were cooled to room temperature at 0.2°C/minute before being removed from the furnace. X-ray Diffraction (XRD), Scanning Electron Microscopy (SEM) and X-ray Photoelectron Spectroscopy (XPS) measurements were taken of each sample to determine the effect of any changes brought about by the different Al_2O_3 barrier layer thicknesses.

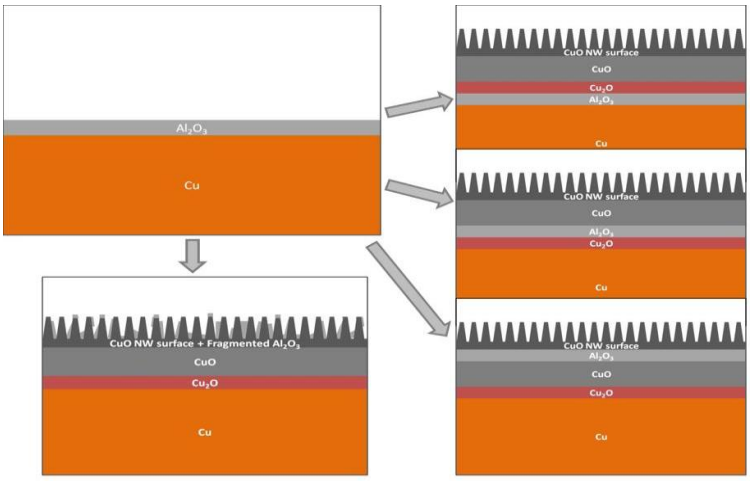

Figure 82: Possible locations of ALD Al_2O_3 layer after oxidation.

Figure 82 shows four possible scenarios for the location of the Al_2O_3 layer after the thermal oxidation and cooling of the samples (layer thicknesses not shown to scale). The top left image shows the sample surface after cleaning and ALD of Al_2O_3. Top and middle right show the Al_2O_3 layer in what was thought to be its most likely location, acting as a strain mediator at either the Cu/Cu_2O interface or the Cu_2O/CuO interface. The bottom right image shows the Al_2O_3 at the CuO NW/CuO interface. This was thought to be a fairly unlikely situation, as the Al_2O_3 layer would probably hinder O^{2-} diffusion, limiting the formation of the higher oxygen content oxide underneath. Instead the CuO layer would be much thinner (or non-existent) and the lower oxygen ratio oxide (Cu_2O) would be thickened accordingly. The final likely scenario (shown bottom left) was that O^{2-} diffusion would progress unhindered, forming both oxide layers and the CuO NWs underneath the Al_2O_3 layer. If this were the case, the change in surface area due to the production of the NWs, coupled with the adhesion of the Al_2O_3 layer to the growing oxide would result in the breakup of the barrier oxide layer, fragments of which would remain at the surface.

5.5.1 Results and Discussion

Table 20: Al_2O_3 film deposition parameters (measured from Si wafer pieces adjacent to Cu samples)

Sample No.	Al_2O_3 film thickness (nm)	No of Cycles	Growth Rate (nm/cycle)
CuBL1	0	0	0
CuBL2	3.82	50	0.076
CuBL3	8.04	100	0.080
CuBL4	12.2	150	0.081
CuBL5	15.4	200	0.077
CuBL6	22.9	300	0.076

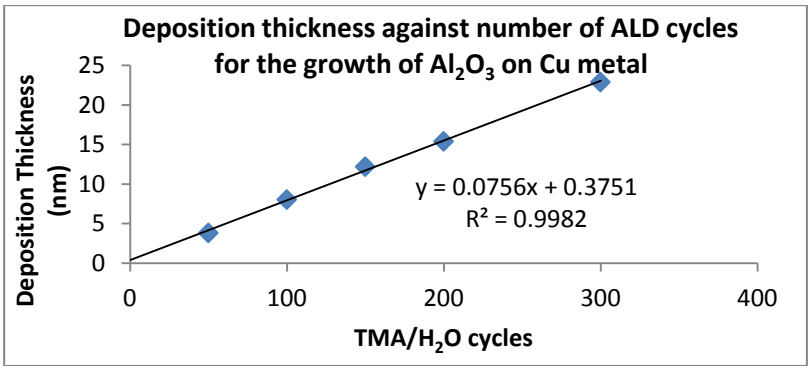

Figure 83: ALD growth curve showing linear response of oxide thickness for increasing ALD cycles.

Initial observations following the deposition of varying thicknesses of Al_2O_3 and the thermal oxidation treatment indicated that the barrier layer coating of ALD Al_2O_3 could be used to minimise spallation of the CuO NW surface and possibly control the length/spacing of the resultant NWs. Table 20 and Figure 83 showed the variation in Al_2O_3 thickness on Si wafer pieces for different numbers of TMA/H_2O cycles. It was seen that the thickness increased in a linear manner with a growth rate of around 0.76Å/cycle. Literature values for the growth rate of ALD Al_2O_3 quote values of between 0.97 and 1.3Å/cycle between temperatures of 77°C and 177°C [187, 188, 189], although these values are extremely process dependant. The results seen in this set of experiments showed a lower growth rate. If nucleation of the initial alumina layers was the cause of this low growth rate then one would expect that the line of best fit shown in the graph would intercept the y-axis at some negative value. As it is, the intercept is at 0.38nm which is close enough to 0nm to rule out this effect. The low growth rate seen could be caused by incomplete coating during each ALD cycle. If, for example, one TMA/H_2O cycle results in 70% coverage, then each subsequent cycle would first fill in the remaining gaps from the previous cycle and then produce patchy growth of the next layer. This could be caused by either a combination of low mobility of surface species coupled with too low exposures of precursor gases or by high desorption levels of precursors which would mean they could leave the surface before being exposed to the co-reactant. It should also be noted that the growth rate shown here is for TMA/H_2O on Si; It is possible that this growth rate does not necessarily apply to the growth of Al_2O_3 on the Cu pieces. Ellipsometry measurements of the Cu samples failed to return any results due to difficulties encountered focussing the device on the substrates due to the high reflectivity. Another factor to consider is that the ALD growth temperature of 150°C is at the lower end of the saturative growth window (typically quoted as 150°C to 300°C). This temperature was chosen to limit the formation of CuO on the Cu substrate when exposed to oxygen from the H_2O precursor.

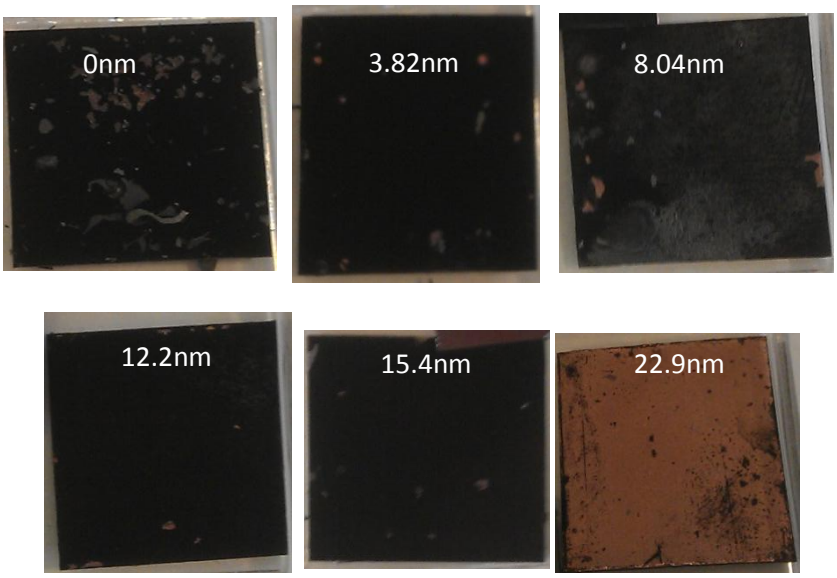

Figure 84: Images of samples surfaces after ALD of varying thicknesses of Al_2O_3 and 1hour thermal oxidation in air at 500°C.

Figure 84 shows images of each sample after ALD of Al_2O_3 and thermal oxidation. The spallation of the CuO NW and surface oxide appeared to be reduced by the addition of the Al_2O_3 barrier layer. The control sample, with 0nm of Al_2O_3, showed the highest level of spallation indicating that the strain mismatch between the substrate/oxide layers was at its greatest compared with the other samples. The next four samples showed similar levels of spallation to each other, all retaining large proportions of the grown oxide. The final sample showed very little growth of the CuO oxide when observed with the naked eye. Because of the lack of spalled material around the sample when it was being removed from the furnace, the absence of readily visible NW and planar oxide growth was attributed to the inhibition of ionic movement; Both ingress of O^{2-} ion and egress of Cu^{2+} ions could have been stopped or significantly reduced by the barrier layer Al_2O_3.

There are several mechanisms that could account for the increase in retained Cu oxide for higher thicknesses of Al_2O_3. The first is that the Al_2O_3 layer acts as a strain mediator between different layers of the growing oxide during the thermal oxidation and following cooling cycle. The coefficient of thermal expansion for Alumina is ~8.0µm/mK [(181)] compared to ~16.5µm/mK for Cu [(182)], ~4.3µm/mK for Cu_2O [(183)] and ~9.3µm/mK for CuO

[193]. Based solely on these values, the most beneficial positions for the Al_2O_3 layer would be at either the Cu/Cu_2O interface or the Cu_2O/CuO interface. Due to the comparatively low expansion/contraction of the Cu_2O layer, either of these interfaces were thought to be the most likely position for the initiation of any spallation. From previous experiments, particularly from previous SEM images taken of spalled samples, it seemed as though the spallation initiates originally from within the Cu_2O layer or at the Cu_2O/CuO interface as retained Cu_2O could be seen on nearly all of the samples where spallation had taken place (its presence was indicated by a characteristic red colour and a distinctive cubic-grained microstructure when viewed under SEM). Although the expansion/contraction mismatch is more significant for the Cu/Cu_2O interface (difference of 12.2µm/mK compared to 5.0µm/mK for the Cu_2O/CuO interface), it was thought that the fact that the spallation occurred for the lower mismatch could be partially explained by the differences in ductility of the metal substrate and the oxides.

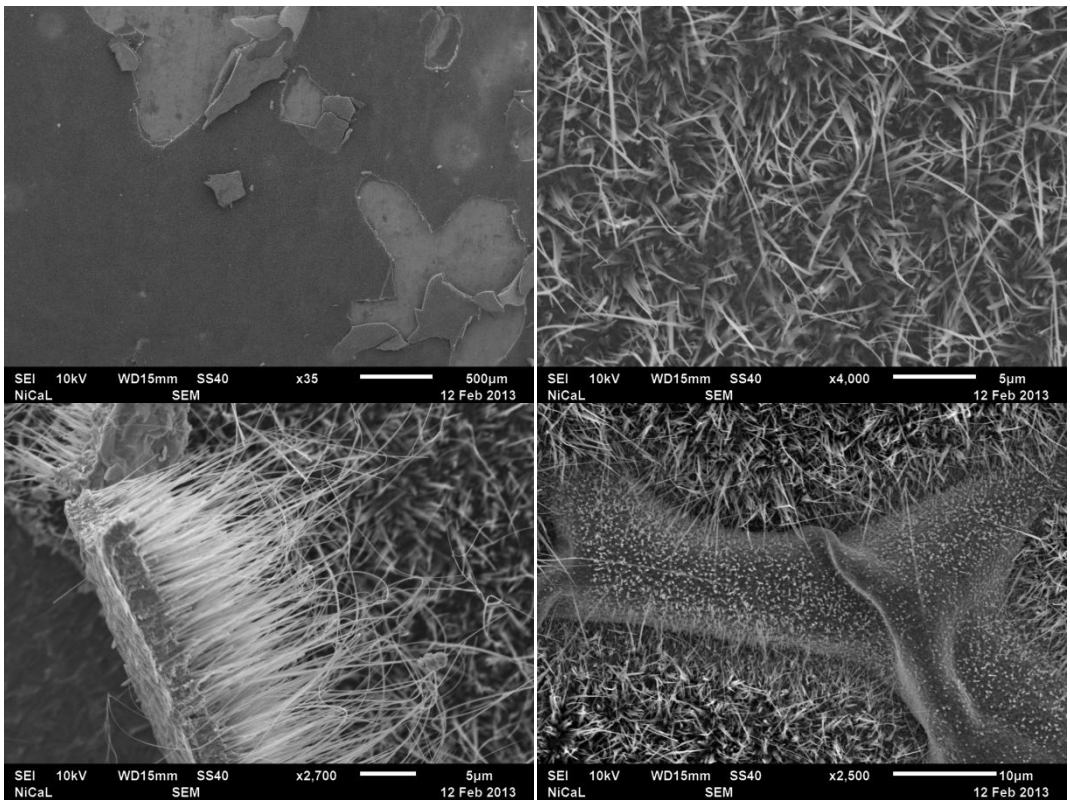

Figure 85: SEM micrographs of sample CuBL1 (no Al_2O_3) after oxidation.

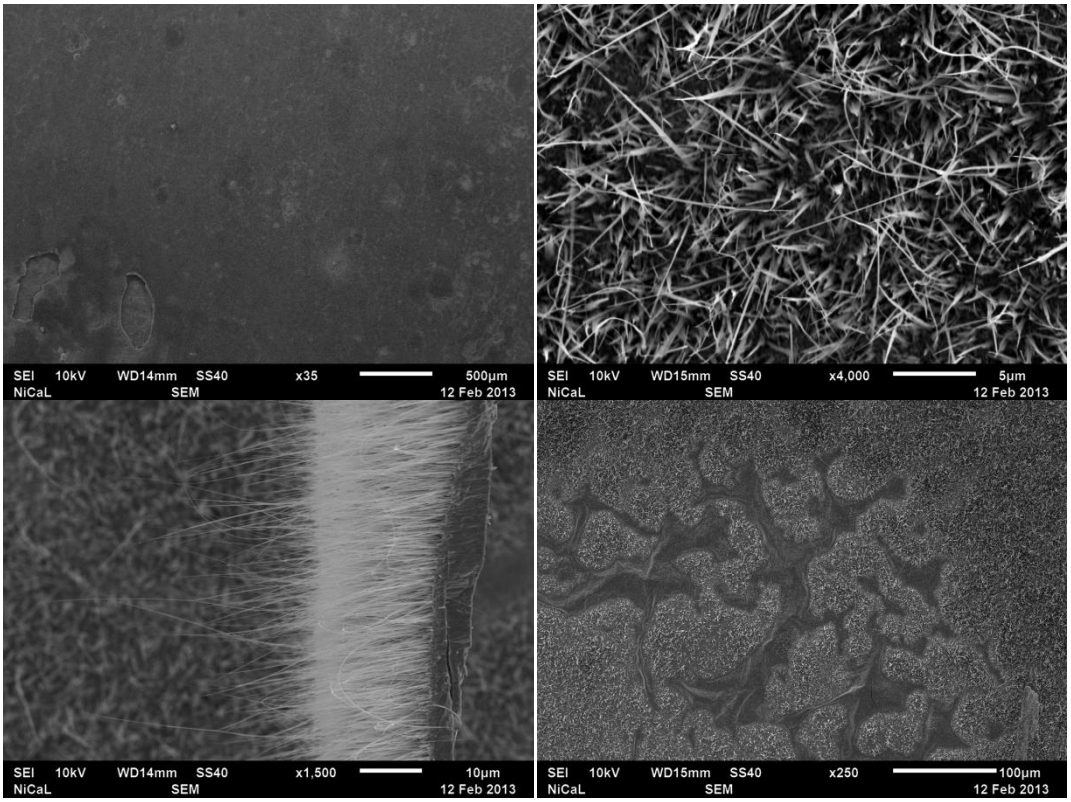

Figure 86: SEM micrographs of sample CuBL2 (3.82nm Al_2O_3) after oxidation.

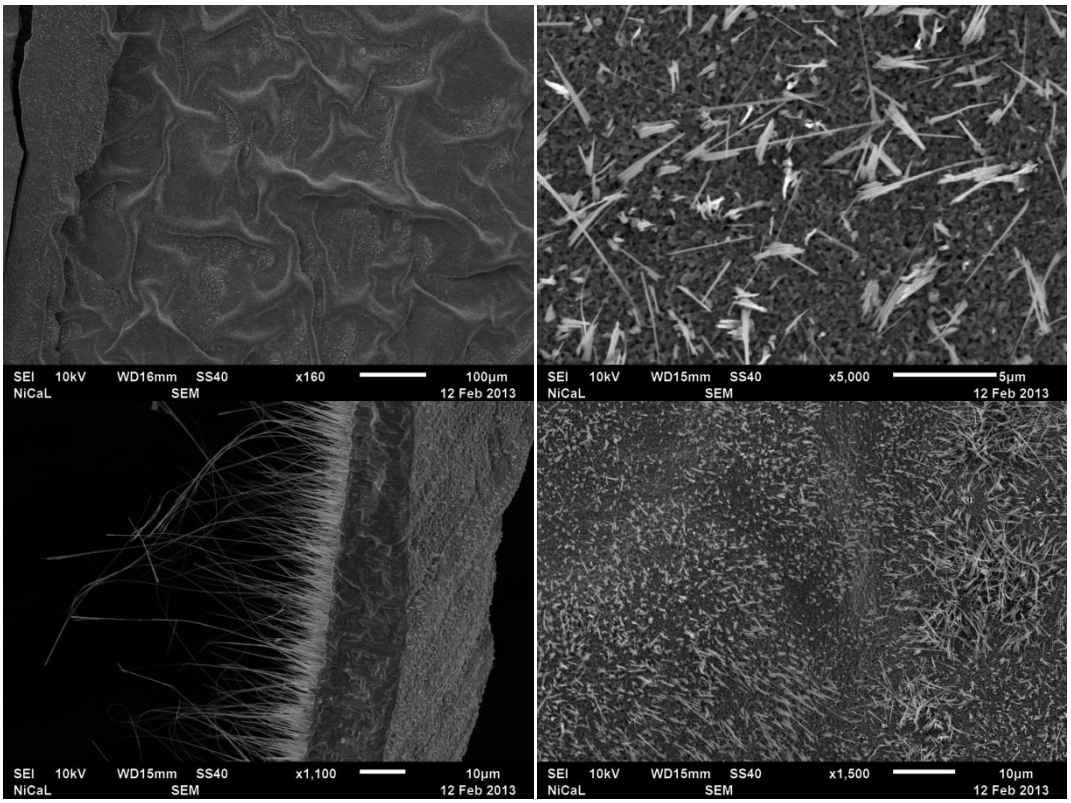

Figure 87: SEM micrographs of sample CuBL3 (8.04nm Al_2O_3) after oxidation

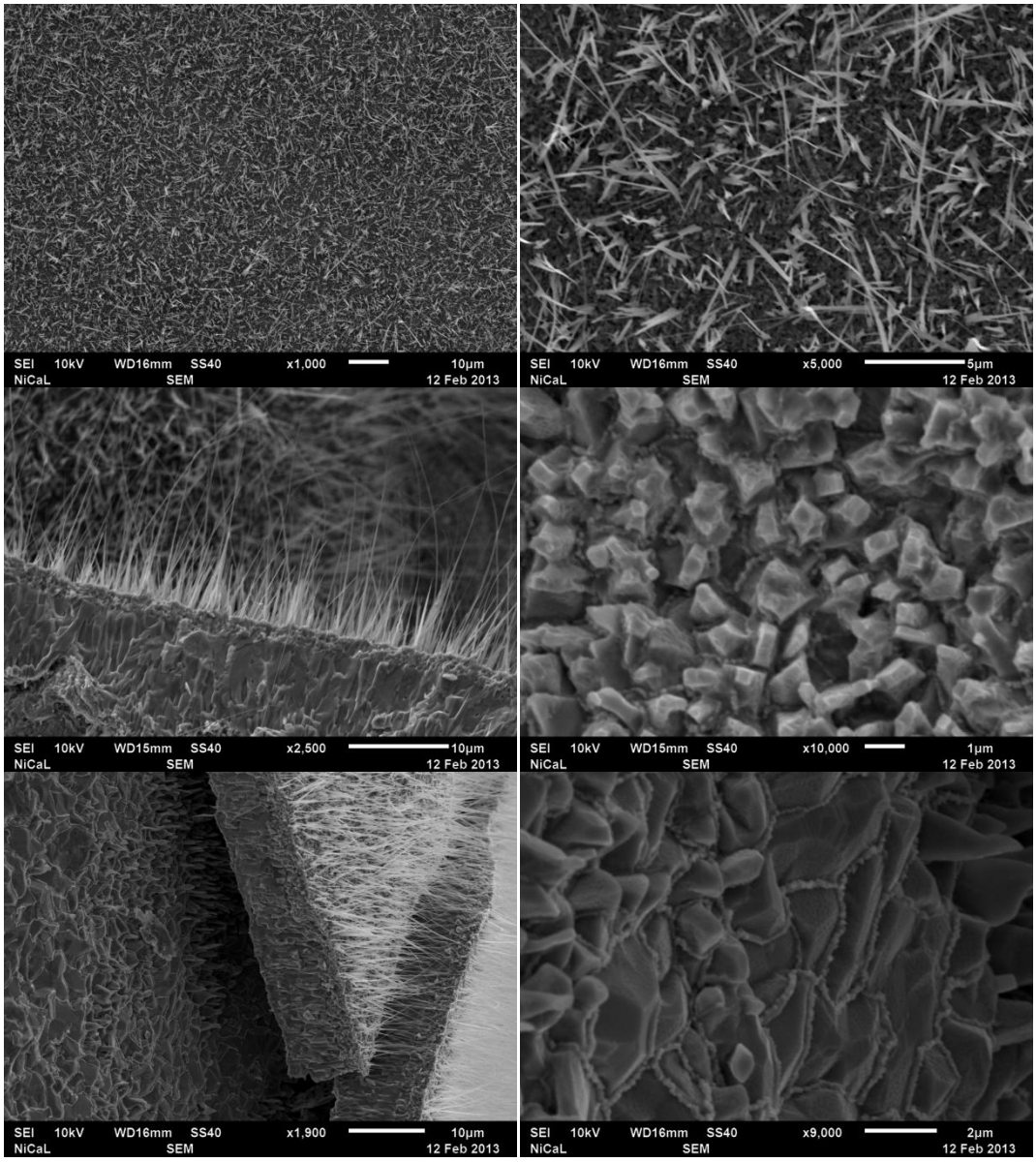

Figure 88: SEM micrographs of sample CuBL4 (12.2nm Al_2O_3) after oxidation.

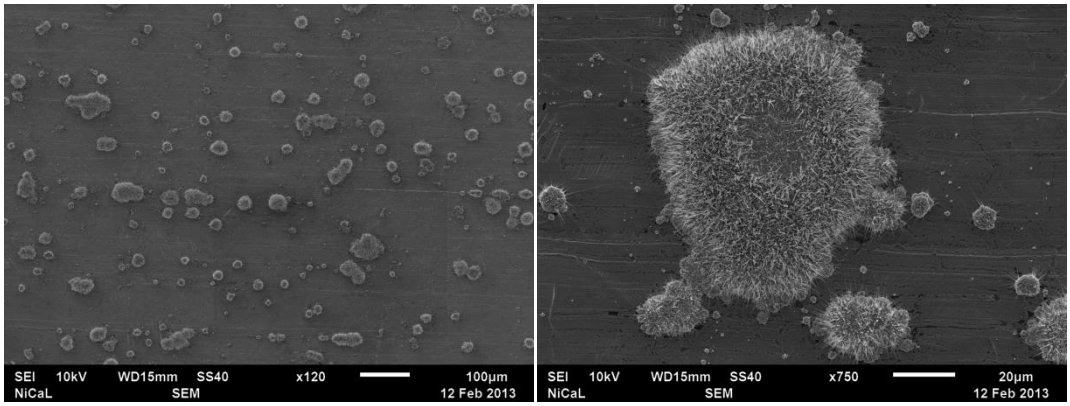

Figure 89: SEM micrographs of sample CuBL6 (22.9nm Al_2O_3) after oxidation.

Figure 85 to Figure 89 show SEM micrographs at various magnifications of each of the sample surfaces. The first images in each of these figures show low magnification images of each surface to illustrate the extent of surface damage to each sample, either from the oxidation process or mechanical damage imparted during handling. The 2nd image in each set shows higher magnification views of undamaged areas for each sample. These show the resultant NW density after ALD and the oxidation treatment. The NW density for the first two samples (0nm Al_2O_3 and 3.82nm Al_2O_3) appear to be roughly the same. For thicknesses of 8.04nm and above the NW density drops off significantly producing only a few NWs per μm^2. The NW lengths and diameters seem unchanged by the presence of the Al_2O_3 barrier layer. Because the growth of the NWs is driven by the amount of tensile strain in the underlying Cu layer, as well as GB diffusion of Cu ions through the intermediate oxide layers[99], this effect was expected due to inhibited diffusion of the Cu ions to the oxidation front. Another point of note is that in several of the samples where the top layers of oxide have spalled away, the exposed layer (thought to be Cu_2O) shows a wrinkled appearance. This presumably was caused by the relatively large contraction of the Cu metal as it was cooled from 500°C to RT. Interestingly, these features are often seen on the upper CuO layer when no barrier layer is included (Figure 85, bottom right image) where they can affect the nucleation and growth of the NW structure[177].

The barrier layer Al_2O_3 may be changing the adhesive properties between the layers of oxide and the substrate; if, for example, the barrier layer is sited between the Cu and the Cu_2O layer then it could have a lower adhesive strength to either layer, compared to the original Cu/Cu_2O interface, allowing the Cu_2O layer to detach and become convoluted during the thermal contraction. With the adhesive strength between the Cu_2O/CuO layer unchanged, the CuO layer remains relatively unaffected by the large contraction of the Cu substrate. This convolution and detachment of the Cu_2O layer may also account for the

reduced NW density seen. When areas of the Cu_2O detach from the CuO layer, diffusion pathways could sever, locally preventing delivery of Cu ions to the surface.

In the last three images in Figure 88 another interesting feature was seen at the Cu_2O/CuO interface that is not normally present without the inclusion of the Al_2O_3 layer. The cube-like Cu_2O grains appear to be surrounded by a much finer grained material which outlines each Cu_2O grain boundary. From the way it is related to the Cu_2O grain boundaries it seems reasonable to suggest that this is either the Cu ions arrested the point of oxidation after GB diffusing to the Cu_2O/CuO interface driven by the strains in the underlying layers or part of the Al_2O_3 barrier layer pushed up into the Cu_2O layer by the same strain-based mechanism. It was thought that the second scenario was more likely as this feature had not been witnessed previously in any other samples oxidised without the barrier layer.

The final SEM images (Figure 89) shows the 22.9nm Al_2O_3 sample surface after oxidation. Clearly the barrier layer had significantly reduced Cu diffusion as only very small islands of CuO had formed, up to 10's of μm across. Each island shows NW growth. Presumably thicker layers of barrier layer would serve to further reduce the number of viable diffusion paths, reducing the appearance of the NWs and islands.

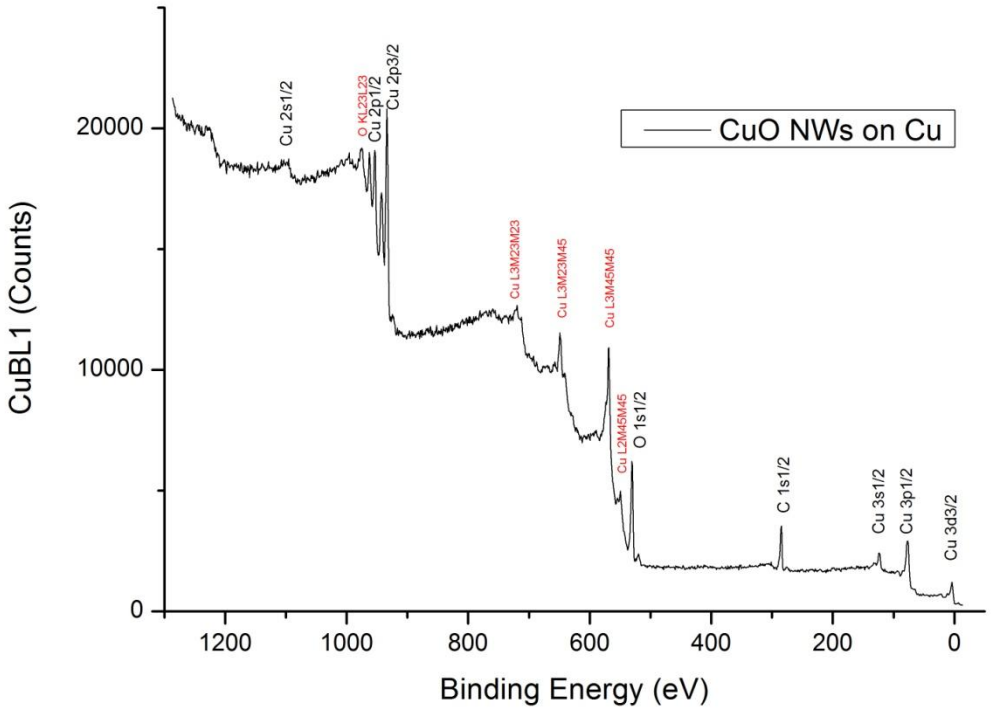

Figure 90: XPS spectra for sample CuBL1 (no Al_2O_3).

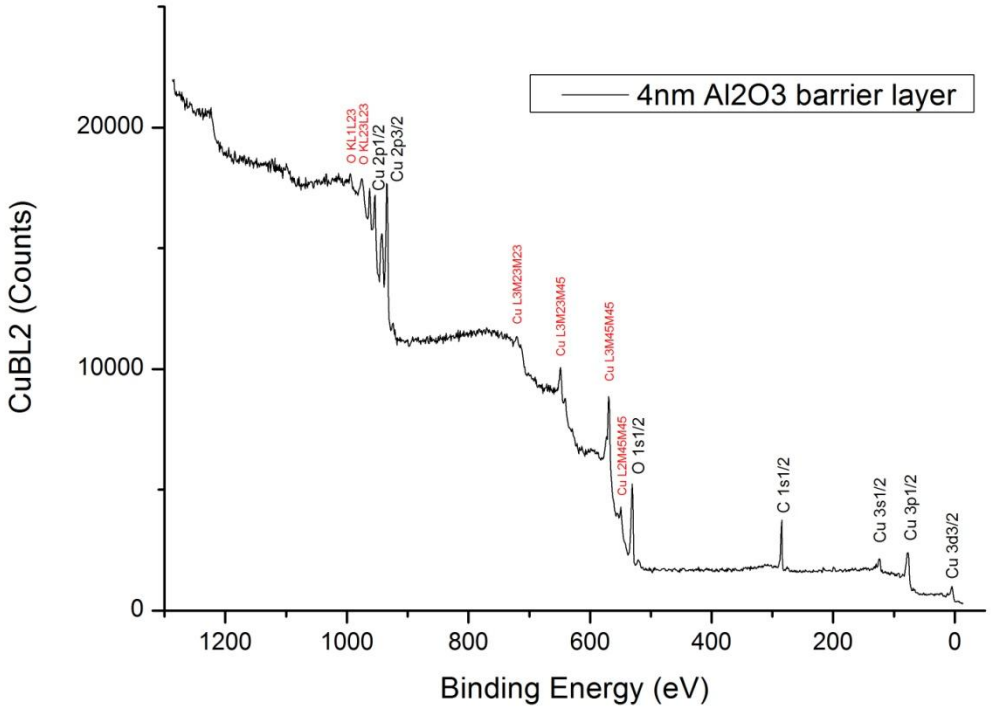

Figure 91: XPS spectra for sample CuBL2 (3.82nm Al_2O_3).

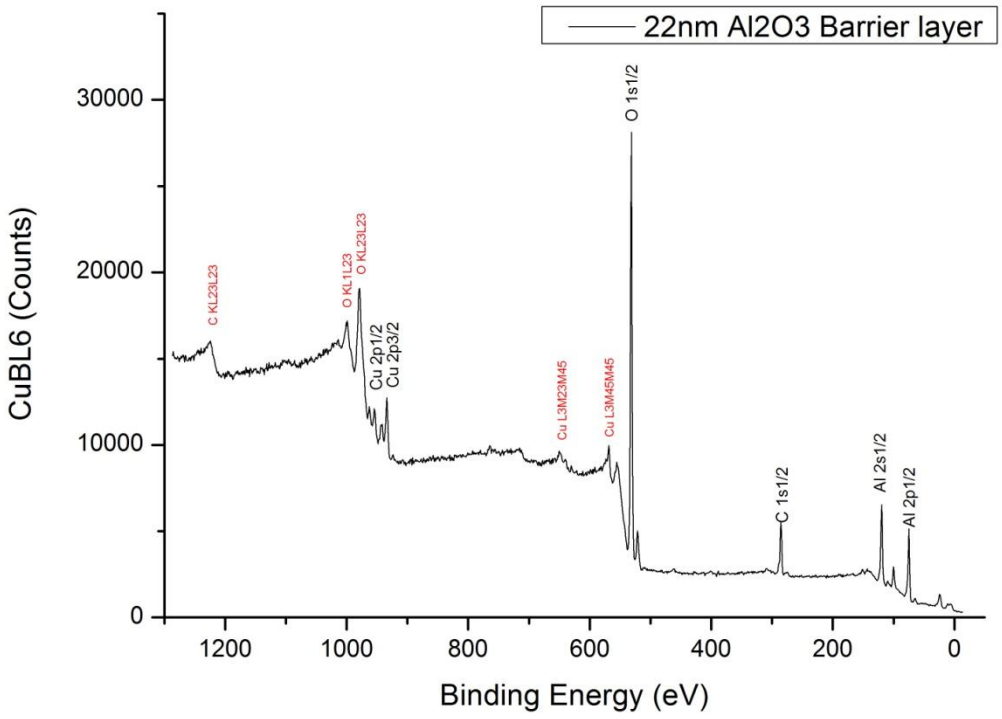

Figure 92: XPS spectra for sample CuBL6 (22.9nm Al_2O_3).

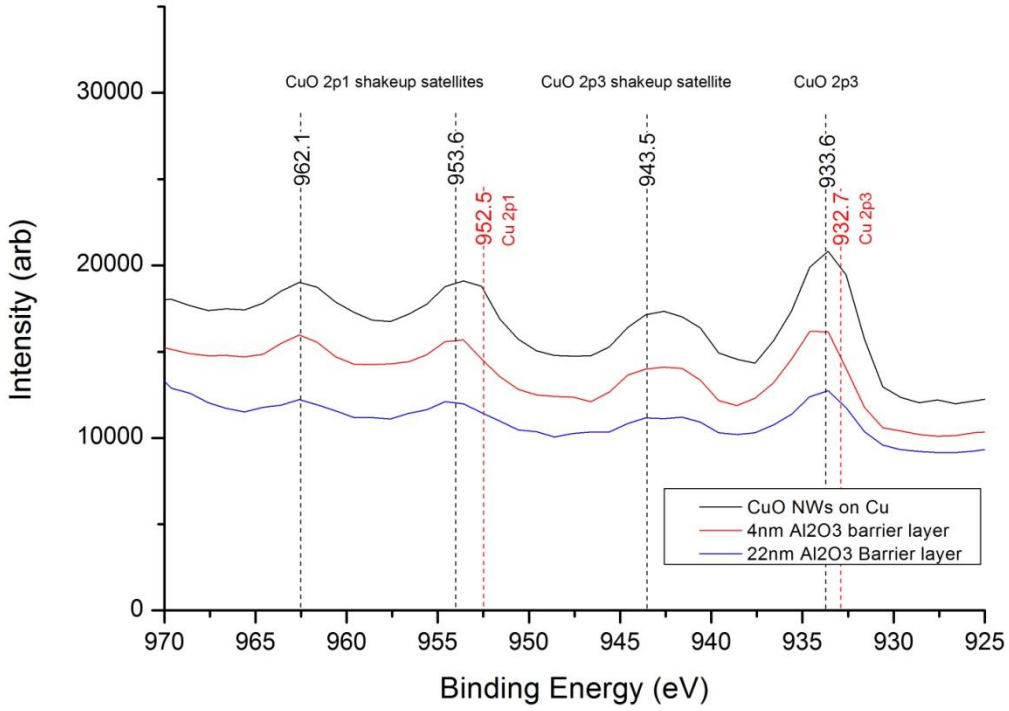

Figure 93: XPS spectra for sample CuBL1, 2 and 6 showing characteristic CuO satellite peaks.

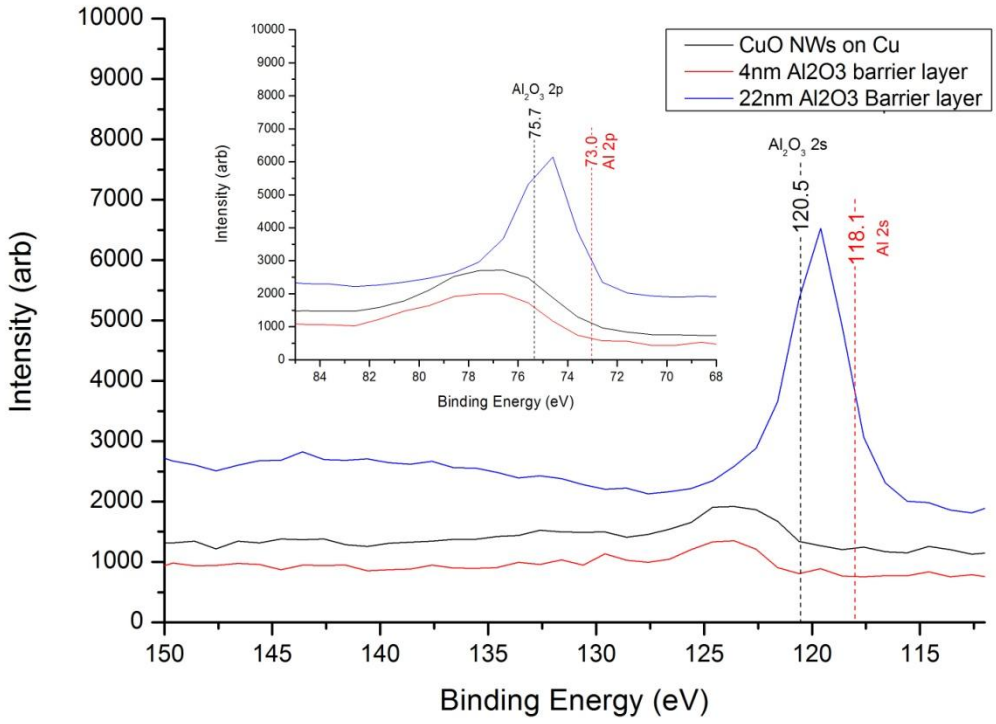

Figure 94: XPS spectra for sample CuBL1, 2 and 6 showing Al 2s peaks (inset: Al 2p peaks).

Figure 90 to Figure 94 show XPS spectra for several of the samples. These were taken to ascertain whether the Al_2O_3 layer had remained at the sample/air interface following the oxidation treatment or if the Cu oxides had grown through barrier layer. Figure 90 shows the scan for the normally grown material. The scan shows all of the expected Cu and O XPS peaks as well as several auger signals for Cu. No peaks are visible corresponding to Al or it's oxides. Figure 91 shows the XPS scan for the sample with 3.82nm Al_2O_3. Very little difference can be seen between this and the previous scan indicating that none of the deposited Al_2O_3 is present on the sample surface. Figure 92 shows the XPS scan for the sample with the thickest layer of Al_2O_3. This differs significantly from the previous two scans. The peaks associated with Cu are still apparent, but this time additional peaks exist corresponding to Al. Also, the peaks for O are much stronger than in the other scans. This tells us that the Al or Al_2O_3 is present on the surface of the sample. The presence of the Cu

peaks reflect the fact that some oxide has managed to grow through the barrier layer but has failed to cover the entire surface.

Closer examination of some of the satellite peaks for CuO (Figure 93) on each of the scanned samples show a good agreement with those of the oxide and not Cu metal. The only possible exception is for the CuO 2p3 shakeup peak at 943.5eV which appears to be centred at a slightly lower energy than expected. Scans shown in the literature[184] show this satellite as a sharp peak at 943.5eV with a plateau tail stretching to around 940eV. The rounded hump seen here is most likely because of the low resolution used for the scan, where a higher resolution scan would differentiate the two parts of the expected peak. In this figure it is clear that each of the samples scanned have CuO present at the surface.

Figure 94 shows each of the scanned samples at energies where one would expect to find Al or Al_2O_3 peaks. For samples without the Al_2O_3 ALD or with 4nm of the barrier layer, no indication of either the metal or oxide peaks can be seen. For the sample with 22nm of barrier layer oxide both peaks are visible although each is slightly shifted to lower eV values. Again, this could be because of the low resolution used for the scans. This figure shows that the Al species are only present at the surface for the 22nm sample and rules out the layer profile shown in the bottom left of Figure 82.

5.5.2 Conclusion

Al_2O_3 deposited by atomic layer deposition can be used as an interfacial layer to increase the mechanical stability of CuO NWs grown thermally on strained Cu sheet below thicknesses of 22nm. Increasing the thickness of this layer up to 22nm could possibly be used to reduce the density of CuO NWs. From observations of the XPS profile and SEM images of cleaved oxide it appeared that the barrier layer remained at the Cu/Cu_2O or Cu_2O/CuO interface after oxidation.

5.6 Growth of High Surface Area Cu_2O Nanostructures

Problems were anticipated with the use of CuO nanowires as one of the functional layers in p-n heterojunction devices. Work by other groups had shown that the conductivity, hole mobility and hole diffusion length could be very low in CuO, resulting in poor performance of devices made using this material. Cu_2O however, showed much more promise as an electronically functional layer, with electronic properties more suited to p-n devices. Ideally, a substrate of CuO nanowires could be used as a starting point for the reduction of the oxide to Cu_2O, whilst retaining the form of the nanowires.

CuO nanowires were grown via a simple air annealing method on Cu substrates. The CuO nanowires were then reduced to Cu_2O by a controlled vacuum anneal at 940°C, forming a high porosity, high aspect ratio surface in preparation for ALD of n-type oxides to produce a photovoltaic device. The produced surface structures were characterised by XRD, SEM and Raman spectroscopy.

Cu coupons, cut from Cu sheet (99.90%), were first stress relieved. This was done by placing the samples in a vacuum furnace at room temperature, evacuating the furnace to remove any gaseous species that could react with the Cu surface, and heating the furnace up to 500°C at 1°C/minute. The samples were then left at temperature overnight. Once stress relieved, the furnace was then cooled at 1°C/minute. Once the furnace temperature was below 50°C, the system was vented and the samples removed from the furnace.

The samples were then placed inside a second furnace utilising a normal air atmosphere (partial pressure of O_2 around 0.21atm) which had previously been heated to 500°C. After 3 hours the heating for the furnace was switched off, allowing the furnace and the samples to slow cool to room temperature. This process produced a highly strained multi-layered oxide structure at the sample surface (CuO/Cu_2O) which promoted the nucleation and growth of long CuO NWs at the Cu_2O/atmosphere interface. Visually speaking, the samples changed

from a reflective coppery appearance to a matt black, highly unreflective appearance. SEM and XRD were used to confirm the presence of CuO and CuO NWs.

For the final thermal treatment, the samples were placed back inside the vacuum furnace at room temperature and the furnace was evacuated. The furnace was slowly heated to 940°C at around 1°C/minute and held at temperature for 6 hours. The furnace was then cooled at 1°C/minute back to room temperature and vented. SEM and XRD were used to characterise the change in surface structure.

5.6.1 Results and Discussion

Once the vacuum anneal had been completed and the furnace temperature was below 50°, the samples were removed and examined using SEM. It was noted that the sample surfaces had changed from matte black surface to matte red, indicating that the annealing process had completed as expected and that the CuO nanowires had been at least partially reduced to Cu_2O.

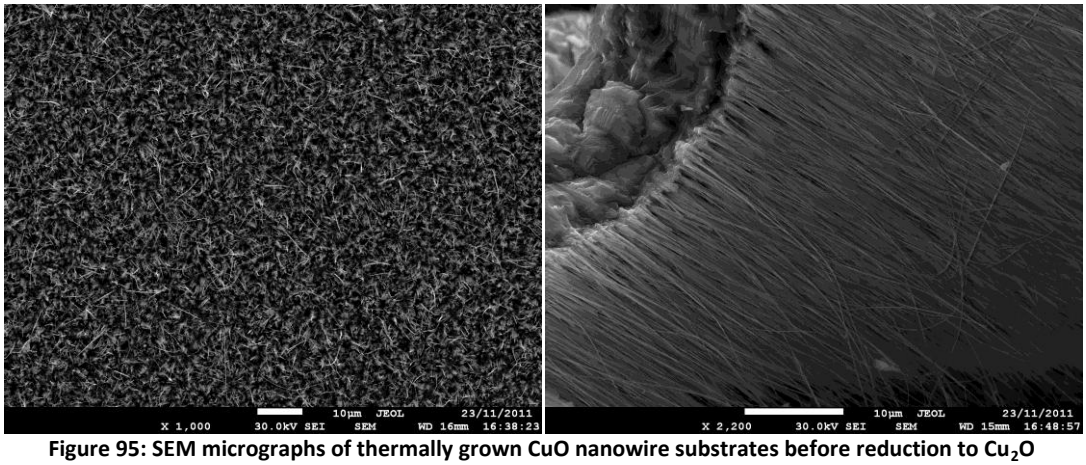

Figure 95: SEM micrographs of thermally grown CuO nanowire substrates before reduction to Cu_2O

Figure 95 shows SEM micrographs taken of the sample before the reduction anneal. In the left image it can be seen that the upper surface consisted of a high density of tightly packed CuO nanostructures with a high uniformity. The image on the right shows an SEM micrograph of a broken section of oxide near to the sample's edge. From this image it is apparent that the nanowires were greater than 50µm in length, very tightly packed at their

bases and showed a slight tapering from base to tip. Also visible is the high flexibility of the wires. Many of them can be seen to be bending from their original vertical (wrt. the CuO substrate) positions. This flexibility was also noted when the micrographs were taken as individual nanowires would move around under the influence of the electron beam.

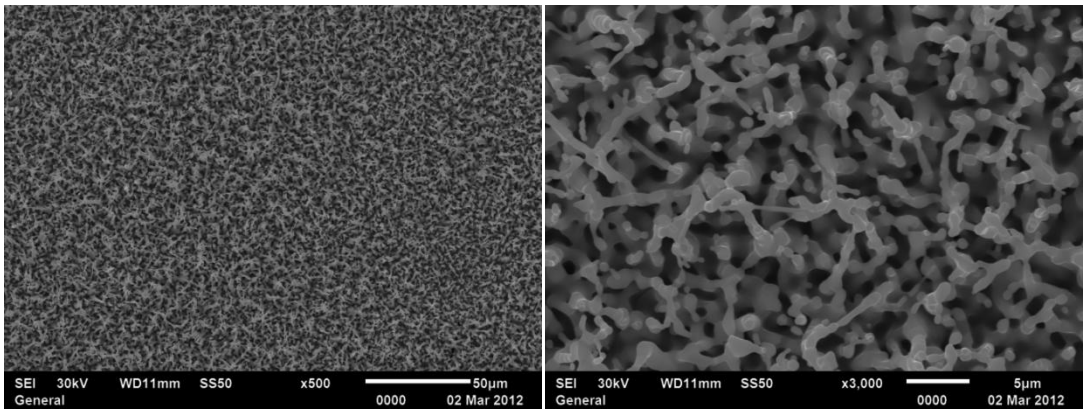

Figure 96: SEM micrographs of the Cu_2O nanostructures produced following a vacuum anneal at 940°C.

Figure 96 shows two SEM micrographs taken of the sample after the vacuum anneal. The first image, at 500x magnification, shows that the uniformity across the surface has remained. It is apparent that the morphology of the oxide has changed and has become much less spikey. The second image, at 3000x magnification, shows that this is the case. The original nanowires comprising the surface structure seem to have clumped together during the anneal, merging into an open, high porosity morphology with individual components thicker than the original nanowires from which they formed.

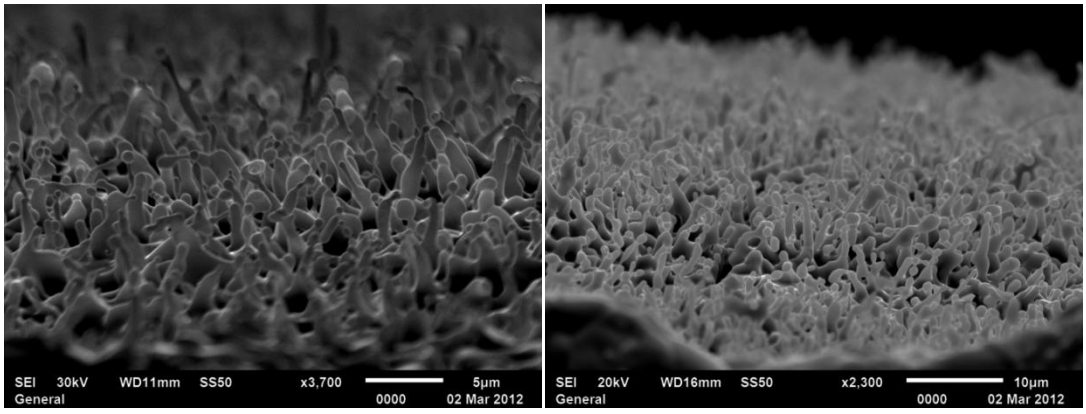

Figure 97: SEM micrographs of reduced nanostructures viewed from the side.

Figure 97 shows the same sample when viewed from the side using SEM. From these images it can be seen that the Cu_2O pillars formed by the reduction of the nanowire structures are around 1µm in width and reach between 5µm and 10µm above the surface. This is a significant change from the original structure where the individual nanostructures were over 50µm long and in the region of a few hundred nanometres in width. One would expect this reduction in density and associated increase in porosity as the CuO structures were expected to lose significant mass in the form of oxygen ions lost to the reactor environment. For the complete conversion of CuO to Cu_2O the following chemical reaction was proposed:

$$4CuO \rightarrow 2Cu_2O + O_2$$

In terms of mass lost, this reaction would give around $\frac{16}{4\times79.55} = 5\%$ of the original surface oxide mass lost as O_2.

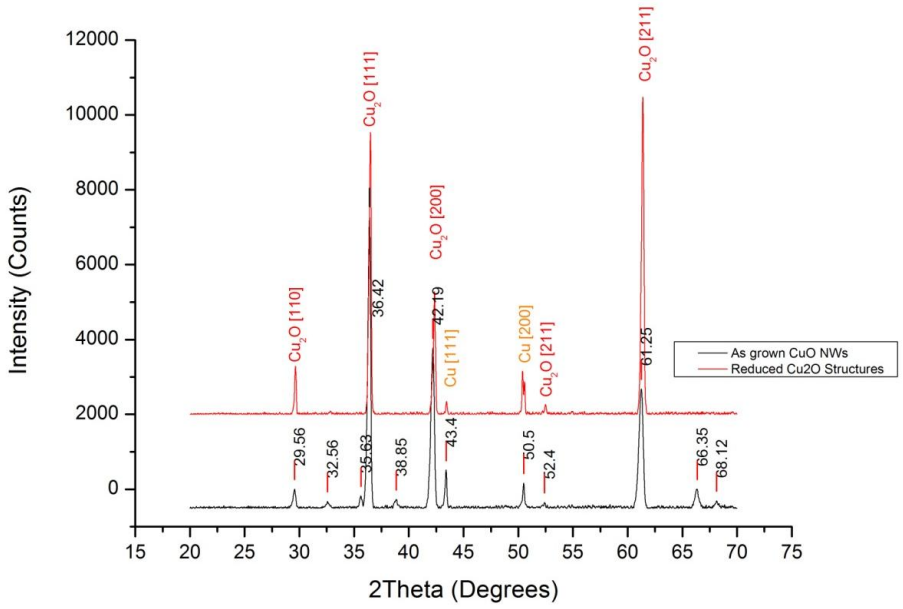

Figure 98: XRD spectra for nanowire sample after oxidation (black line) and after vacuum reduction (red line).

Figure 98 shows XRD Spectra for the nanostructured samples before (black line) and after (red line) vacuum annealing. The structure of the CuO NW samples was known from previous studies and the available literature to consist of CuO NWs at the surface, a thin

layer of bulk CuO beneath, a thicker layer of bulk Cu_2O underneath that and the Cu metal substrate. Because of the relative thinness of the layers, it was assumed that the X-ray beam would be able to penetrate all the way down to the substrate and provide information on each of the individual layers. The as grown CuO NWs show XRD peaks associated with Cu and Cu_2O as well as several unidentified smaller peaks. No clear peaks are visible corresponding to CuO, but this was to be expected for several reasons; the relative thinness of the CuO NWs and CuO bulk layer compared to the thicker Cu_2O could cause overlapping peaks from the two materials to merge. Also the three peaks that should be seen for CuO ([111], [200] and [220]) lie within 0.2 2θ degrees of the Cu_2O peaks with the same indices. Because of this it is problematic to separate the contribution of the two materials.

In the as grown scan (black line) multiple peaks are visible. At 29.56, 36.42, 42.19, 52.40 and 61.25 2θ degrees peaks are seen that correspond to Cu_2O. The relative intensities indicate that there was no preferential growth along any particular axis during the oxidation treatment. The two peaks at 42.40 and 50.50 2θ degrees correspond to those of the Cu substrate, and again show no preferential orientation. The remaining small peaks at 32.59, 35.63, 38.85, 66.35 and 68.12 remain unidentified but could be due to additional reactive species present in the atmosphere during oxidation such as Cl, P, C, etc. forming complex oxides with the Cu and O.

In the XRD scan after the vacuum reduction annealing step these additional peaks have been eliminated, hinting that they were probably confined to the exposed surface of the sample and hence were easily driven off at the low pressures and high temperatures used for the experiment. Several other changes are visible in comparison with the as grown CuO NW sample. The relative intensities of the Cu[111] and Cu[200] peaks have switched following the vacuum anneal. As the samples were above 900°C for several hours, and each

started with a relatively high defect density (imparted from the initial tensile strain on the samples) it was expected that the Cu substrate would recrystallise during the process. This appears to have happened with highly preferential growth of the [200] direction, at least in the upper few microns of the substrate where the X-ray beam was able to penetrate. This could either be caused by growth nucleated from the remaining defects in the metal layer or from lattice matching to the Cu_2O layer above. A similar effect was also noted for the Cu_2O peaks; the [220] peak at 61.38 2θ degrees is much stronger than expected indicating that this is a highly favoured growth direction.

The increase in the porosity of the surface as well as the probable change from CuO to Cu_2O, mean that this treatment could be applicable for use in the production of a high surface area Cu_2O based PV device. The higher porosity of the samples after annealing lends itself well to subsequent ALD processes and may also be advantageous for increased light adsorption. To achieve conformal coating with ALD on high aspect ratio structures the precursor exposures (Pa.s) required can be high, necessitating high reactor pressures or very long cycle durations. With the lower surface structure aspect ratios seen as a result of these experiments, the minimum precursor exposure values should be much reduced.

5.6.2 Conclusion

High temperature vacuum reduction annealing of CuO nanowire surfaces has been shown to produce Cu_2O nanostructured surfaces. These Cu/Cu_2O substrates could then be used in conjunction with ALD of n-type and TCO materials for the production of Cu_2O based photovoltaic devices. Further work and experimentation is required to determine the factors that govern the final morphology of the substrates as well as addition work to examine the quality Cu/Cu_2O interface.

5.7 ALD of TiO_2 on to Anodised Cu_2O Nanostructured Surfaces

Experimental work was carried out on Cu_2O nanostructured surfaces. These substrates showed a lower aspect ratio than the AAO substrates used in previous depositions, allowing shorter run times and a lower precursor exposure. Cu_2O was chosen for its inherent p-type nature and in conjunction with TiO_2 it was thought that these materials could form a nanostructured p-n junction which could then be utilised for future photoelectric devices.

Atomic layer deposition was used to deposit n-type TiO_2 onto p-type nanostructured Cu_2O substrates. It was found that, in comparison with the Si reference wafers used, the quantity of TiO_2 deposited was not conclusively measurable by either mass gain or XRD. This indicated that there could be a problem with the nucleation of TiO_2 material on the cubic Cu_2O surfaces.

Cu/Cu_2O substrates were produced via anodisation of Cu sheet in aqueous KOH and NH_4F electrolyte. TiO_2 was deposited onto the substrates using a Picosun ALD reactor with titanium isopropoxide (TiP) and H_2O reactants. As the substrate surfaces were nanostructured, with estimated aspect ratios of between 10 and 50, it was thought that conformal deposition would increase the mass of the samples by a measurable amount. By comparing the weight gain against ellipsometry measurements of the deposited oxide thickness on a planar Si substrate, it would be possible to use this data to calculate the actual aspect ratio of the substrate and the volume of the deposited oxide.

The TiP bubbler was kept at 110°C and the H_2O was kept at room temperature. The reactor chamber was held at 225°C for the deposition. As the substrates were fairly high aspect ratio it was decided to perform a high exposure growth run to ensure that the precursor gases were given sufficient time to reach every surface. This was achieved by using multiple pulses of each precursor, effectively introducing a much larger volume of each reactant into the chamber than would normally be used for a planar deposition.

One cycle of the run consisted of:

Table 21: 1 cycle for the deposition of TiO_2 onto Cu/Cu_2O substrates

Step Number	Precursor	Ar flow (sccm)	Pulse (s)	Purge (s)	
1	TiP	50	0.1	0.5	X 79
2	TiP	50	0.1	180	X 1
3	H_2O	25	0.1	0.5	X 79
4	H_2O	25	0.1	180	X 1

The total number of cycles used in the deposition onto sample Cu1 and Cu3 was 500. For Cu2 this was reduced to 300 cycles. The number of pulses of each precursor was also reduced from 80 to 50 and the purge time increased to 190 seconds.

Ellipsometry and XRD were used to assess the success of the run.

5.7.1 Results and Discussion

The results from measuring the change in mass of the sample during ALD were inconclusive. For a high surface area sample, one would expect a relatively high increase in mass during deposition assuming a conformal coating had been achieved. As a simple example, if one had a 10mm radius circular sample with a structured surface consisting of circular features averaging 1µm deep, 1µm wide and 1µm apart (i.e. an aspect ratio equal to 1) then values for the area of the upper surface area could be in the region of $10^{-3}m^2$. With a 50nm deposition of TiO_2 (density = $4.23g/cm^3$) this would give a mass change of roughly $10^{-4}g$, above the noise level of the micro-balance used in this experiment. The surface values used for this example are likely to be an underestimate as the anodised Cu surface was thought to have a much higher aspect ratio, and hence a higher surface area.

Table 22: Mass change and Ellipsometry Results for ALD of TiO_2 on to anodised Cu samples

Sample	Pre-deposition mass (g)	Post-deposition mass (g)	Mass change (g)	Thickness on Si wafer (nm)
Cu1	0.03852	0.03849	- 0.00003	58.6
Cu2	0.06397	0.06408	+ 0.00011	17.2
Cu3	0.07060	0.07063	+ 0.00003	46.9

As can be seen in Table 22 the sample masses did not increase as much as expected, with the possible exception of sample Cu2. The results from the ellipsometer also disagree with mass gain values as the thinnest TiO_2 film thickness corresponds to the greatest mass increase seen. From previous experiments on silicon wafers it was estimated that the ALD process would deposit around 50nm of TiO_2. There are several possible explanations for the discrepancies seen between these two sets of results. The Cu oxide substrate is likely to have a different affinity for the precursor molecules compared to the Si wafer substrates used for the ellipsometry measurements. Because of this, the growth rate of TiO_2 may be higher on the silicon than on the Cu oxide which would decrease the amount of weight gain seen on the Cu sheet samples. It is also possible that there could be different phases of oxide across the Cu samples surface, each of which could have their own nucleation and growth rates for TiO_2 via ALD. By the same reasoning, the different crystalline faces of the Cu oxide(s) could also be associated with different rates of nucleation and growth.

Another possible reason for the lack of weight gain is that the sample could be degassing due to the low pressure and elevated temperatures within the reactor. This was thought to be possible due to the use of an aqueous based technique to create the structured surface, which may have left some volatile residue in the sample.

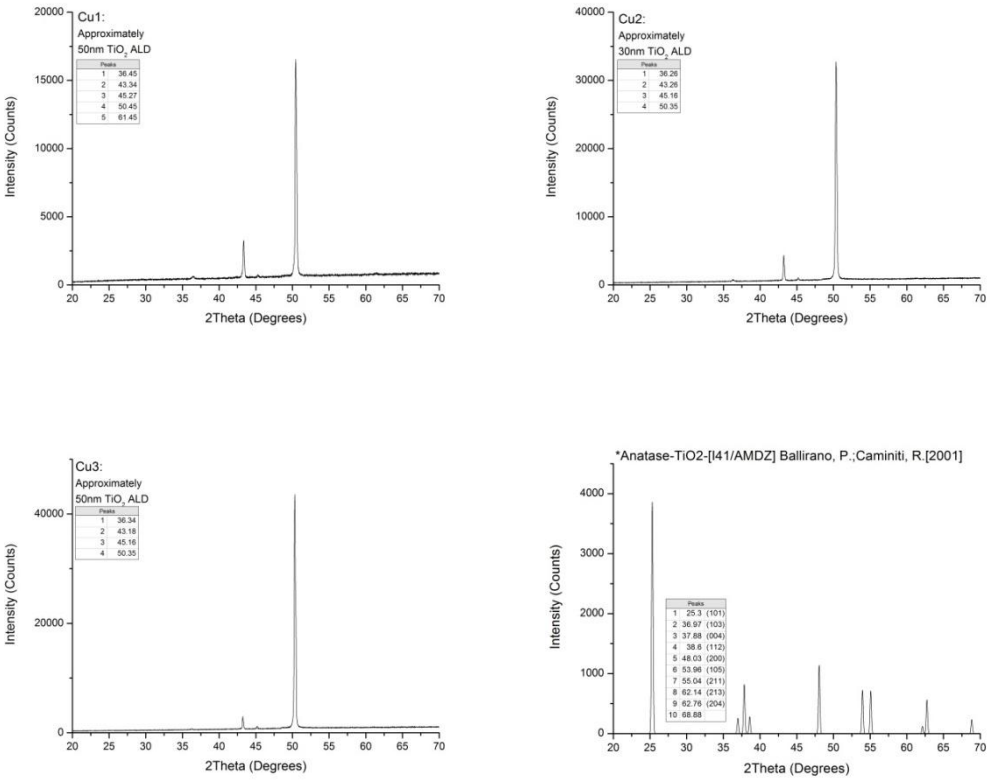

Figure 99: XRD scans of samples Cu1, Cu2 and Cu3 after TiO_2 ALD and the reference TiO_2 anatase file.

In each of the XRD scans for the three samples (Figure 99), the two prominent peaks at 43.3° and 50.4° come from the (111) and (200) planes of the Cu substrate. Two of the remaining peaks at 36.3°, 61.5° are probably from the structured oxide surface, corresponding to the (111) and (220) planes of Cu_2O, although slightly shifted (±0.1°) from the reference patterns. One would also expect to see the (200) peak for Cu_2O as has a higher intensity than that of the (220); these factors could be an indication that the Cu_2O grown during the anodisation has incorporated some strain into the oxide and that it may be showing preferential orientation. Of the oxide XRD reference patterns examined so far, the peak seen at 45.2° is closest to that of the (210) plane of the rutile TiO_2 phase. However, the peak is over 1° out from that of the reference pattern (located at 44.1°). Either the deposited TiO_2 is extremely strained by epitaxial growth on the Cu_2O or this peak is from something else, maybe some low level impurity precipitates within the Cu substrate or absorbates/deposits from the anodisation process. Since the non-Cu peaks are so much

lower in strength than the Cu peaks it is possible that further peaks are present which could be revealed by a slower XRD run and would give further indication of the nature of the oxide layers. As it stands, these scans are inconclusive in determining whether the TiO_2 ALD run was successful or not.

5.7.2 Conclusion

ALD of TiO_2 was carried out on Si wafers and anodised Cu/Cu_2O samples. XRD and Ellipsometry were used to assess the deposition. Additional peaks were seen in the XRD results for the samples after ALD but due to the thinness of the deposited film the analysis was inconclusive as to whether TiO_2 had successfully been deposited.

5.8 ALD onto Planar and Nanostructured Surface Conclusions

Experiments into the growth of nanostructured surfaces from aluminium and copper metals were carried out using a variety of different techniques.

For high purity copper metal, electropolishing was investigated as a means to produce a uniform, oxide free surface. Samples were polished in 70% H_3PO_4/30% distilled H_2O at voltages of 1.5V, 2.0V and 2.5V. The results from these experiments were less conclusive than those for electropolishing Al metal, as nearly all treatments resulted in a rougher surface than that found by mechanical polishing. However, the best results were found to be for samples polished at 2.0V. Another avenue explored in regards to Cu metal preparation was methods to remove native oxides formed from over-exposure to air or from handling of the material without gloves. The best method of removing native oxide was found to be a 10 second dip in a solution of 20vol% HNO_3 and 80vol% H_2O at room temperature. Following the acid dip, samples were rinsed in distilled water, isopropanol and then air dried.

Growth of nanostructured surfaces on the two aforementioned material systems was conducted using a range of oxide growth techniques. Porous aluminium oxide was grown via anodisation in 0.5M oxalic acid at 50V. Under these conditions the oxide was found to grow at a rate of 5.7μm/h. It was also found that the average domain size of the hexagonally ordered pores grew at a rate of 34nm/h as the strain fields of neighbouring domains interacted with each other.

For Cu metal, anodisation in an electrolytic solution of KOH and NH_4F was found to produce nanostructured Cu_2O at the sample surfaces. Problems were experienced with the experimental setup however resulting in the production of low aspect ratio nanometer scale cubes instead of the high aspect ratio leaf-like structures seen by other groups. This

was attributed to stagnation of the electrolyte in the vicinity of the anodised surface, with the local increase in pH to neutral levels causing the formation of the cube structures seen.

Thermal oxidation of Cu metal was carried out at a range of temperatures in a normal air environment to determine the morphology and growth rate of the oxide layers. Samples grown at 500°C and 1000°C were found to follow a parabolic oxidation rate law as predicted by the literature. Samples grown at 140°C were thought to follow a logarithmic growth rate law. It was found that the grown oxide consisted of a thick surface layer of CuO followed by a much thinner layer of Cu_2O between the upper oxide and the metal substrate. For samples oxidised at 500°C it was observed that long CuO nanowires had grown from the upper oxide layer. Additionally, quenching tests in different media were used to determine whether the upper layer of oxide could be removed to leave a uniform Cu_2O surface. The quenching media used (air, cold water and near boiling water) resulted in the spallation of the CuO layer but also resulted in significant loss of the Cu_2O intermediate layer.

In another set of Cu oxide growth experiments, Al_2O_3 was deposited onto a cleaned Cu metal surface before oxidation using ALD of TMA and water. This was to see whether diffusion of the Cu ions would occur through the alumina barrier layer and if so, whether this layer could act as a strain mediator and limit the spallation of the oxides that had occurred with most of the previously grown samples. It was found that increasing thicknesses of the barrier layer, up to 22nm, suppressed the formation of the CuO nanowires, and that at 22nm thickness the barrier oxide became near impermeable to the Cu ions, arresting oxide growth in all but a few locations. XPS results also indicated that for the thinner barrier layers the alumina was situated at either the Cu/Cu_2O or the Cu_2O/CuO interface.

Tests were also carried out into vacuum annealing of CuO nanowire structures. At furnace temperatures of 940°C it was found that excess oxygen was driven out of the samples leaving a porous high aspect ratio structure of Cu_2O on the Cu substrate, different to any seen during the literature review.

Further experiments were carried out into the growth mechanism behind the formation of the CuO nanowires. As it had been noticed that the nanowires failed to grow on stress-relieved (annealed) Cu metal it was hypothesised that the strain left over from the rolling process had played an important role in their growth. Samples were prepared with a range of tensile and compressive strains and oxidised in air at 500°C. It was found that tensile strains in the Cu metal increased the nucleation rate of the nanowires whilst increasing compressive strains suppressed their growth. This was attributed to the growth mechanism proposed by Mema et al., i.e. a combination of stress induced and grain boundary diffusion growth mechanisms.

Enhanced exposure ALD experiments were carried out for the deposition of n-type material onto AAO templates and Cu_2O nanostructured surfaces. For deposition into the high aspect ratio AAO templates, it was found that preferential deposition occurred at the upper and lower surfaces and at the ends of the pores. Increasing the residence time of the reactive molecules was found to reduce this effect although it was not reduced completely. To achieve near perfect conformal deposition the exposure models reviewed showed that the growth times required could be prohibitively long.

Further experimental work was carried out using a stop-valve mechanism on the ALD reactor to increase the residence time (and hence the exposure) of precursors within the reactor chamber. Compared to the previous set of experiments, more uniform deposition within the pores was found to take place. However, in all samples tested the deposition of material still showed preferential growth at the surfaces of the substrate. It was concluded

that even higher exposures and purge times would be necessary to conformally coat the inner walls of the pores.

Atomic Layer Deposition was used to coat porous anodised aluminium oxide templates with TiO_2 and to assess the conformality of the process in coating high aspect ratio substrates with the salient dimensions (i.e. the pore diameter) lower than the mean free path length of the precursor molecules at the pressures and temperatures used. For the deposition parameters tested, it was found by mass gain and EDX that partial deposition within the pore occurred, but that the amount of coating within the pores was significantly less than that at the template surfaces.

TiO_2 was deposited onto Cu_2O nanostructures grown from Cu sheet anodised in KOH and NH_4F. Results for the deposition were inconclusive as only one sample showed any significant mass gain. This could have been due to several factors, e.g. a retardation of the nucleation and growth of TiO_2 on Cu_2O compared to that seen on the Si reference wafers or possibly mass lost by the substrates due to degassing at the temperatures and pressures used for the deposition. The latter explanation was thought to be less likely as XRD of the substrates following the deposition did not show conclusive evidence of TiO_2 deposition.

The conformal and non-line of sight deposition of material onto nanostructured substrates via ALD was anticipated to cause problems with the construction of functional devices due to the increased likelihood of short circuits. In an attempt to limit this effect, several mechanical masking substrate holders were designed to fit inside a Cambridge Savannah ALD reactor (See Appendix 2). One of these designs was fabricated and tested using Al-doped ZnO (a transparent conductive oxide). It was found by electrical conductivity measurements that the masking effect worked, isolating the substrate edges from the deposition. The device geometry was also found to interfere somewhat with the ALD process, causing preferential deposition at the boundaries of the masked area, probably

due to incomplete removal of the precursor gases from the recesses and undercuts of the device during the ALD purge step. This would have caused CVD-like growth in these areas. Further design work and modification of the device would be required, or alternatively modification of the deposition process (increased purge times) to combat this issue.

6 Photovoltaic testing and TCO synthesis

6.1 PV Testing of Anodised Cu substrates Coated with TiO_2 via ALD

99.90% HDHC Cu sheet, thickness 0.45mm, was cut in to squares approximately 2cm to a side. Several samples were vacuum annealed to relieve any stresses in the metal due to the sheet rolling process. A selection of samples was electropolished while others were mechanically polished or used with no surface smoothing process. Samples were then anodised in either aqueous electrolyte or propylene glycol containing NH_4F and KOH and varying the concentration of active species as well as the duration of the anodisations. N-type ALD using either TiO_2 or ZnO oxides was then carried out followed by ALD of TCO material forming multilayered samples consisting of Cu/Cu_2O/n-type(TiO_2/ZnO)/TCO. Some samples were subjected to heat treatment (oxidation in air at 500°C) between layering steps to see if the quality of the oxides could be improved. Representative samples were tested throughout the fabrication processes using SEM, XRD and Raman spectroscopy.

Once devices had been fabricated photovoltaic testing was carried out using standard fluorescent lighting conditions and a Keithley multimeter in two probe mode. The voltage across the sample was driven from -0.5V to 0.5V in 50 equal steps. This simple testing would enable functioning devices to be selected for further photovoltaic tests using an AM1 or AM2 light source (AM1 is the spectrum and power of light from the sun that falls on the equatorial band of the earth at midday, i.e the full solar spectrum when passed through one atmosphere perpendicular to the Earth's surface. AM2 is the same spectrum passed through two atmospheres.).

Additional experiments were conducted to test two methods of removing the deposited oxides from selected areas of the device surfaces to allow electronic isolation of the individual layers. The upper surface of one device was mechanically scored using a steel tip

and another device was dipped into conc. HCl to dissolve the ZnO/GZO (Gallium doped ZnO). In this way both of the electrical contacts could be made from the top surface of the devices facilitating an easy photovoltaic test setup. SEM imaging was used to see the effects on the surface of each of the tests.

Table 23: Process parameters for Cu based solar devices

Sample number	Heat treat-ment	Electro-polishing	Anodisation	Heat treat-ment	n-type ALD	Heat treat-ment	TCO ALD
Cu001	Vacuum - 550°C – 1 hour	2V – 420s – 70% H_3PO_4 + 30% H_2O	0.15M KOH + 0.1M NH_4F + H_2O – 6V – 300s		TiO_2 – Picosun reactor – 500 cycles – 50nm		
Cu002	Vacuum - 550°C – 1 hour	1.5V – 420s – 70% H_3PO_4 + 30% H_2O	0.15M KOH + 0.1M NH_4F + Propylene glycol – 30V – 300s	Air - 500°C – 30mins	TiO_2 – Picosun reactor – 500 cycles – 50nm	Air - 500°C – 30mins	
Cu003	Vacuum - 550°C – 1 hour		0.15M KOH + 0.1M NH_4F + Propylene glycol – 30V – 1200s		TiO_2 – Picosun reactor – 500 cycles – 50nm		
Cu004	Vacuum - 550°C – 1 hour		0.15M KOH + 0.1M NH_4F + H_2O – 6V – 300s	Air - 500°C – 30mins			
Cu005	Vacuum - 550°C – 1 hour	2V – 420s – 70% H_3PO_4 + 30% H_2O					
Cu006	Vacuum - 550°C – 1 hour		0.15M KOH + 0.1M NH_4F + H_2O – 6V – 420s		ZnO + GZO (20:1) – Cambridge – 3360 cycles – 500nm		
Cu007			0.15M KOH + 0.1M NH_4F + H_2O – 6V – 420s		ZnO – Cambridge – 500 cycles – 50nm		GZO – Cambridge – 3360 cycles – 450nm
Cu008			0.15M KOH + 0.1M NH_4F + H_2O – 6V – 420s				
Cu009			0.15M KOH + 0.1M NH_4F + H_2O – 6V – 420s		ZnO – Cambridge – 500 cycles – 50nm		GZO – Cambridge – 3360 cycles – 450nm
Cu010			0.15M KOH + 0.1M NH_4F + H_2O – 6V – 300s				
Cu011			0.15M KOH + 0.1M NH_4F + H_2O – 6V – 420s		ZnO – Cambridge – 500 cycles – 50nm		GZO – Cambridge – 3360 cycles – 450nm
Cu012					ZnO – Cambridge – 500 cycles – 50nm		GZO – Cambridge – 3360 cycles – 450nm
Cu014-1	Vacuum - 500°C – 3 hours		0.1M KOH + 0.1M NH_4F + H_2O – 6V – 600s		Picosun – Al_2O_3 – 7.5nm – TiO_2 – 50nm – 575 cycles		GZO (20:1) – Cambridge – 3360 cycles – 450nm
Cu014-2	Vacuum - 500°C – 3 hours		0.1M KOH + 0.1M NH_4F + H_2O – 6V – 1200s		Picosun – Al_2O_3 – 7.5nm – TiO_2 – 50nm – 575 cycles		GZO (20:1) – Cambridge – 3360 cycles – 450nm
Cu014-3	Vacuum - 500°C – 3 hours		0.1M KOH + 0.1M NH_4F + H_2O – 6V – 300s		Picosun – Al_2O_3 – 7.5nm – TiO_2 – 50nm – 575 cycles		
Cu015-1	Vacuum - 500°C – 3 hours		0.15M KOH + 0.1M NH_4F + H_2O – 6V – 300s		Picosun – Al_2O_3 – 7.5nm – TiO_2 – 50nm – 575 cycles		
Cu015-2	Vacuum - 500°C – 3 hours		0.15M KOH + 0.1M NH_4F + H_2O – 6V – 600s		Picosun – Al_2O_3 – 7.5nm – TiO_2 – 50nm – 575 cycles		GZO (20:1) – Cambridge – 3360 cycles – 450nm
Cu015-3	Vacuum - 500°C – 3 hours		0.15M KOH + 0.1M NH_4F + H_2O – 6V – 1200s		Picosun – Al_2O_3 – 7.5nm – TiO_2 – 50nm – 575 cycles		GZO (20:1) – Cambridge – 3360 cycles – 450nm
Cu016-1	Vacuum - 500°C – 3		0.2M KOH + 0.1M NH_4F + H_2O – 6V – 300s		ZnO – Cambridge – 50nm – 500 cycles		GZO (20:1) – Cambridge – 3360

	hours						cycles – 450nm
Cu016-2	Vacuum - 500°C – 3 hours		0.2M KOH + 0.1M NH_4F + H_2O – 6V – 600s		ZnO – Cambridge – 50nm – 500 cycles		GZO (20:1) – Cambridge – 3360 cycles – 450nm
Cu016-3	Vacuum - 500°C – 3 hours		0.2M KOH + 0.1M NH_4F + H_2O – 6V – 1200s		ZnO – Cambridge – 50nm – 500 cycles		GZO (20:1) – Cambridge – 3360 cycles – 450nm

6.1.1 Results and Discussion

Electropolishing of the cut Cu samples (Cu001, Cu002, Cu005) was conducted in a solution of 70% H_3PO_4 and 30% H_2O for 420s at 1.5V and 2V with a carbon rod as the cathode. After the electropolishing, visual examination of the surface showed that the polishing had not succeeded and had significantly increased the surface roughness of each of the samples. It was decided that further experimental work should be carried out at a later date to investigate this process fully.

From the previous anodisation experiments following the work of Allam *et al*. [101] it was decided that further experimentation was required to explore the anodisation process as the leaf-like structure found by the M.I.T. group had not yet been successfully replicated. Previous attempts to reproduce the structure had all resulted in island growth of the porous oxide leaving bare Cu in certain areas. The anodisation voltage, duration and electrolyte composition were varied to determine their effect on the resultant oxide morphology. The parameters selected for variation were anodisation duration and electrolyte composition. The anodisation of samples using the propylene glycol based electrolyte appeared to have been unsuccessful in producing the porous Cu_2O structure from visual examination of the samples after anodisation. Little difference was seen between the samples anodised in water for different durations, indicating that the process could be quickly reaching a steady state at the start of the anodisation, with dissolution of the surface oxide matching the growth of new oxide from the substrate.

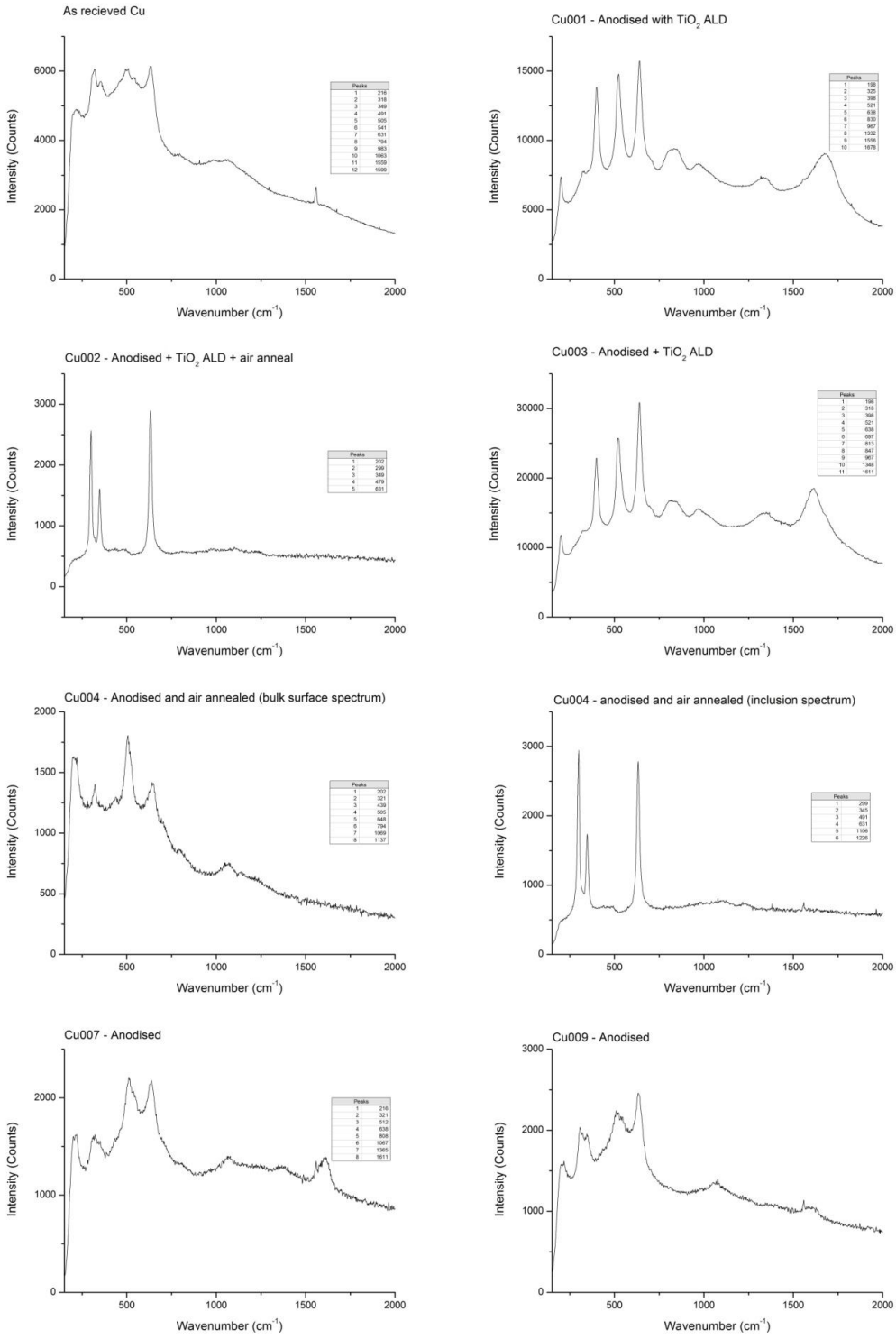

Figure 100: Raman Spectra for as received Cu and samples Cu001 (Anodised/TiO_2 ALD), Cu002 (Anodised/TiO_2 ALD/Air anneal), Cu003 (Anodised/TiO_2 ALD), Cu004 (Anodised/Air anneal), Cu007 (Anodised) and Cu009 (Anodised).

The Raman spectra for several samples can be seen in Figure 100. For the first graph, the as received Cu sample, it is clear that the Raman modes are much weaker compared to the background noise than the in the other samples. This is to be expected as the Cu metal

substrate should have no Raman signal of its own, due to the presence of delocalized electrons. The signal that can be seen must be from a thin surface oxide or due to precipitates within the material. Work by Debbichi et al. provides experimental and computational values for the Raman modes of CuO and Cu_3O_4 [185]. For CuO, modes occur at 147, 161, 302, 321, 349, 478, 533, 587 and 635 wavenumbers. For Cu_3O_4 the modes are found at 318, 510, 541 and 651 wavenumbers. Along with the values for Cu_2O at 109, 154, 218, 308, 436, 515, 635, 665 and 820 wavenumbers [62], these can be used to identify the presence of each of the Cu oxides. In the as received spectrum peaks are found corresponding to each of the Cu oxides indicating their presence at the surface. Samples Cu002 and Cu004 both show similar profiles with the peak locations corresponding with those of CuO, to within a few wavenumbers. This indicates that the air annealing process has formed CuO on the samples. The last two Raman spectra (Cu007 and Cu009) show the peaks for the samples after anodisation. The location of the peaks points to the oxide being formed from both Cu_2O and Cu_3O_4. The spectra shown for samples Cu001 and Cu003 after ALD of TiO_2 show significant differences from the other spectra, with the three major peaks around 318, 398 and 521 wavenumbers showing the presence of TiO_2 anatase [186]. This shows that, although hard to distinguish in the XRD data (Figure 105), the TiO_2 ALD process was successful in depositing on to the anodised Cu surface. Again referring to the spectra for Cu002, it appears as if the annealing process has removed any deposited TiO_2.

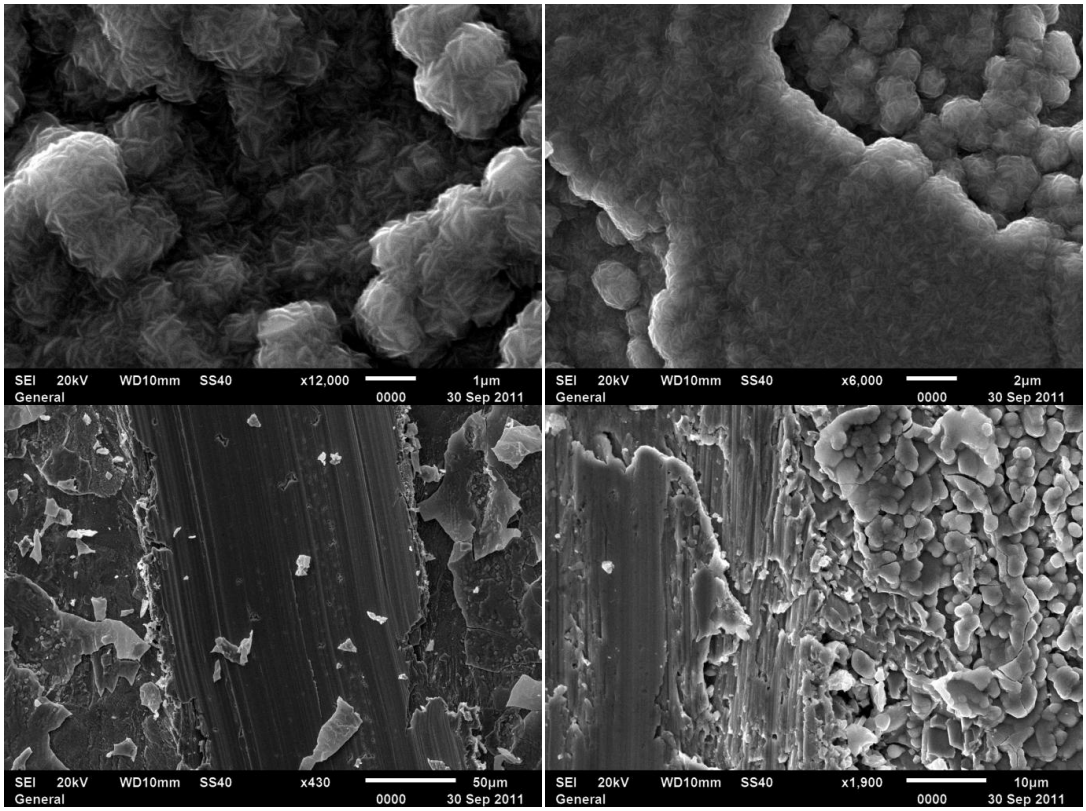

Figure 101: SEM images of sample Cu009 after anodisation and ZnO/GZO ALD. Top two images show representative examples of surface. Bottom images show effect of mechanical scoring as a way to electronically isolate surface areas to reduce the chance of short circuit. Scoring has failed in this regard as the oxide has been crushed into rather than scratched away from the Cu substrate.

Figure 101 shows the surface of sample Cu009 after anodisation and ALD of ZnO/GZO imaged using SEM. The upper surface of the sample shows what looks to be a polycrystalline conformal coating of the n-type and TCO material. From this image it would appear that the ALD process had been successful in depositing a conformal coating onto the nanostructured Cu_2O surface.

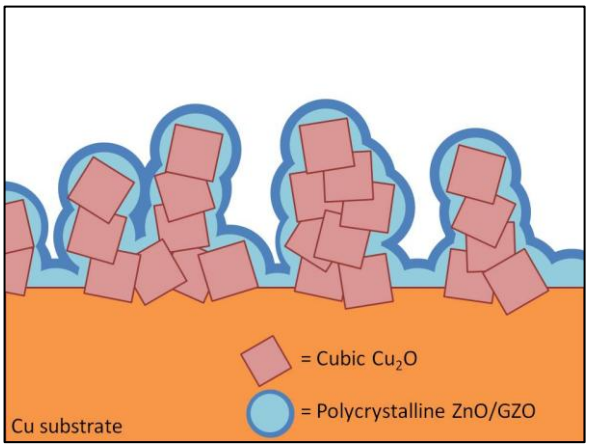

Figure 102: Representation of the expected cross section of the PV devices after anodisation of Cu and ALD of ZnO/GZO (not to scale).

Figure 102 shows a schematic diagram of how the device structure was thought to appear in cross-section based upon the SEM images from earlier experiments and the SEM images in Figure 101, Figure 103 and Figure 104. The bottom two images in Figure 101 show the effect of mechanical scoring on the film using a sharp steel tip. This was done in to attempt to electronically isolate sections of the surface to enable both contacts used for the PV curve testing to be applied from the top. It is apparent from these images that instead of removing a portion of the deposited oxides as was intended, they have been crushed into the Cu surface. Electrical contact between the crushed areas and the as deposited oxides still remains.

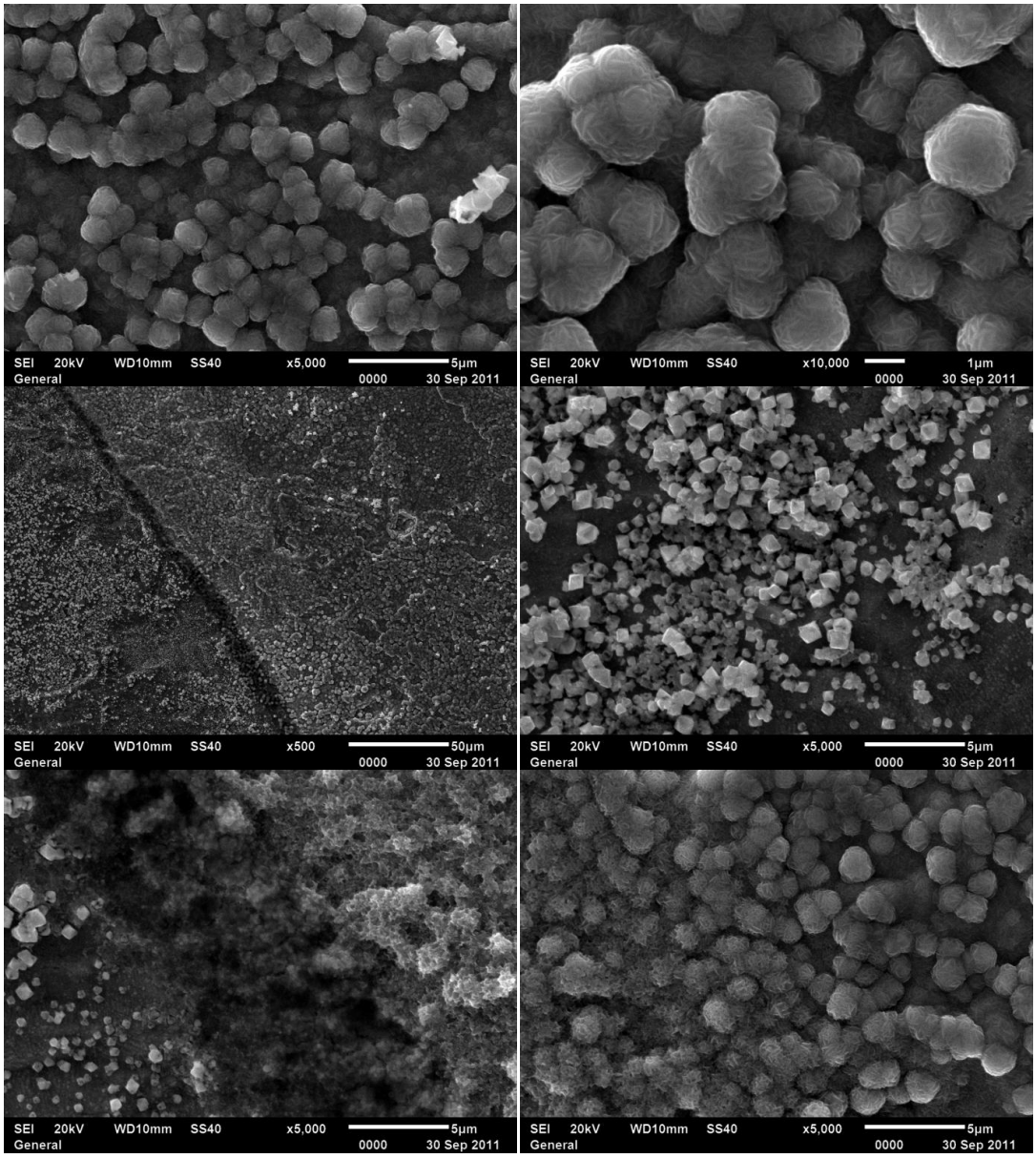

Figure 103: SEM images showing sample Cu011 after anodisation and ZnO/GZO ALD. Top two images show representative sample surface. Middle left image shows effect of HCl acid dip as a method of electronically isolating selected areas of the surface. The dark line running from top left to bottom middle corresponds to the surface of the acid during the dip treatment, oxide to the left of the line was fully submerged, oxide to the right remained in normal atmosphere. Middle right image shows close up of HCl submerged surface; all ZnO and GZO has been removed from the Cu/Cu_2O substrate. Bottom left shows area of sample exposed to HCl surface. The meniscus of the HCl solution has clearly had a significant effect on the sample, removing material back into the Cu substrate. Bottom right image shows area of sample just above the HCl dip line, some effect of chemical attack on the GZO TCO can be seen towards the left of the image, which shows a much more jagged surface compared to the un-attacked area on the right of the image. This was thought to be caused by the high partial pressure of HCl vapour just above the acid surface.

Figure 103 shows several SEM images of sample Cu011. Again, the polycrystalline ZnO/GZO ALD coating can be seen and appears to have formed the same topographical structure as in the earlier samples. This sample was also used to test another method of electronically isolating selected areas of the sample surface, this time using a concentrated HCl acid dip to

dissolve the GZO and ZnO layers. The middle left image shows the effect of this dip at 500x magnification. Four distinct areas can be identified: on the left of the image the cubic Cu_2O can be seen. This is also shown in the middle right SEM image at higher magnification. This cubic form of Cu_2O is similar to that which was found by Singh et al. when anodising Cu foil in H_2O [103]. It is clear from this image that the HCl has successfully removed the ZnO and GZO whilst leaving the Cu_2O intact. The second area is the dark line, approximately 5μm wide, running from the top to the bottom of the image. This corresponds to the location of the HCl meniscus when the dipping process was carried out. This area is deeply recessed into the sample surface (also shown in the bottom left image at higher magnification) indicating that the reactivity at the HCl meniscus is higher than that of the bulk acid. The third area, to the right of the dark line, corresponds to just above the HCl surface during the dip. It can be seen in the bottom two images that in this area the TCO has been slightly attacked during the process and has taken on a more faceted and rough appearance. This area is approximately 50μm in width. The last distinct area is at the right of the image and shows the same surface features as the majority of the surface.

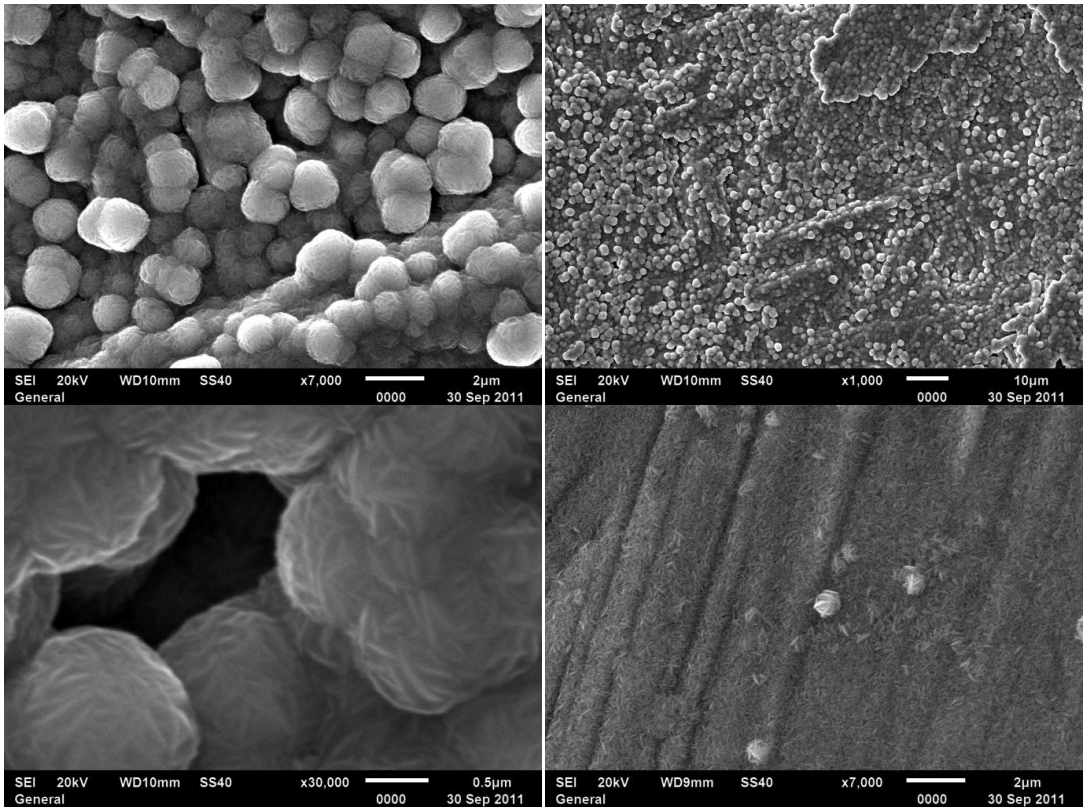

Figure 104: SEM images Cu015-3 after ZnO/GZO ALD. Bottom right image shows ALD of ZnO and GZO onto planar Cu.

The final set of SEM images (Figure 104) show the surface of sample Cu015-3 after anodisation and ALD of ZnO/GZO. As with the previous SEM images the ALD process has successfully deposited a conformal coating over the Cu_2O substructure, forming the same ~1-2µm polycrystalline spherical shapes. For all of the samples shown here, this is roughly the size that would be expected given that the Cu_2O cubes forming the underlying substrate had edge lengths of around 100nm; an additional conformal layer of 500nm on each side, with the highest deposition rate at the centres of each cubic face, would yield near-spherical structures with a diameter of 500nm + 100nm + 500nm = 1.1µm. The bottom right image of this set shows the edge of the sample where it had been masked from the anodisation process, inhibiting the formation of Cu_2O. During the ALD process this area was unmasked. The image shows the same polycrystalline ZnO/GZO oxides, but instead of forming spheres around the Cu_2O cubes, it has deposited in a simple planar form.

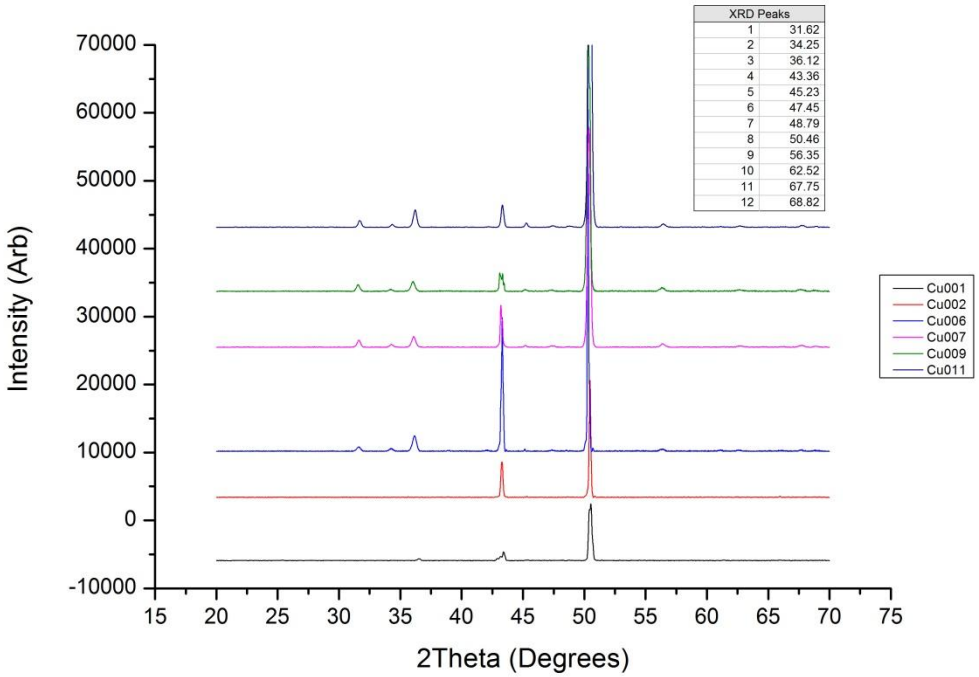

Figure 105: XRD results for samples Cu001 (Anodised), Cu002 (Anodised), Cu006, Cu007, Cu009 and Cu011 (Anodised/ALD – approximately 500nm ZnO/GZO).

Figure 105 shows the XRD spectra for selected devices at various points throughout their fabrication. Each of the graphs shows two major peaks at 43.3° and 50.4° corresponding to the (111) and (200) planes of cubic Cu [(159)]. The lower two lines correspond to samples Cu001 and Cu002 after anodisation. The red line for Cu002 only shows the Cu peaks. The electrolyte used in the anodisation of this sample was 0.15M KOH, 0.1M NH_4F and propylene glycol. This test was done to see what effect changing the composition of the electrolyte would have, as experiments performed by Allam et al. [(101)] using ethylene glycol as the major electrolyte component had produced an interesting nanostructured copper oxide different to that produced by anodisation in an aqueous electrolyte. Visual examination of the surface showed little change after the anodisation. Subsequent optical microscopy showed small isolated islands of grown material. The reason for the lack of additional peaks on the XRD scan is therefore that the oxide islands were probably too thin and too widely spaced to be picked up with the hour-long scan performed here. Cu001, anodised in the aqueous electrolyte, shows one additional peak at around 36.1°. This could

be evidence of either the (111) cuprite peak at 36.4°, the (111) tenorite peak at 36.6° or the (004) peak in paramelaconite at 36.3° [160,161,162]. Although the (004) of paramelaconite is the closest of the peaks to the literature value, it was thought that this peak corresponded to the cuprite (111) as this plane is the most intense peak in Cu_2O. After the anodisation the sample had taken on a red hue, further backing up this hypothesis.

The remaining samples to undergo XRD scanning were samples Cu006, Cu007, Cu009 and Cu011. Each of these had been anodised to produce a structured Cu_2O surface and then used as a substrate for ALD of ZnO/GZO. Each of these samples showed the same XRD profiles containing the both Cu peaks, the (111) of Cu_2O and several additional peaks. The additional peaks were located at 31.6°, 34.3°, 45.2°, 47.5°, 48.8°, 56.5°, 62.5°, 67.8° and 68.8°. These show a high correspondence to the zincite P63MC peaks [187]. From the reference file it seems that there are a couple of peaks missing from this scan, i.e. those located at 36.3° and 66.5°. The major (101) peak at 36.3° is located very close to the Cu_2O (100), and as can be seen by comparing the scans of Cu001 to Cu006 – Cu011 the peak at this location has increased in intensity. The zincite peak at 66.5° has the lowest intensity of the expected peaks and could therefore be present, but difficult to detect without running a much longer scan.

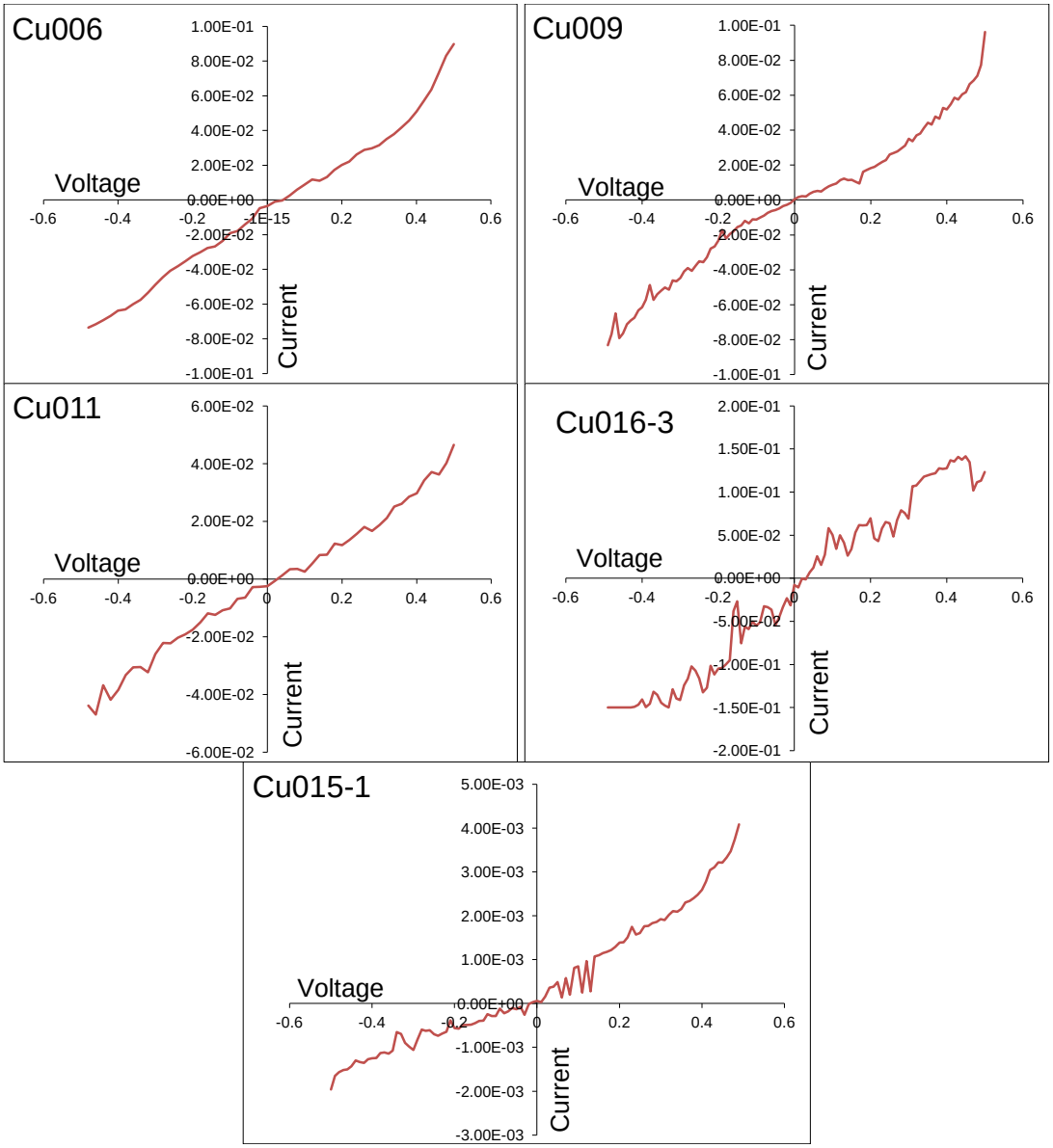

Figure 106: Initial photovoltaic test results for illuminated samples Cu006, Cu009, Cu011, Cu016-3 ($Cu/Cu_2O/ZnO/GZO$) and Cu015-1 ($Cu/Cu_2O/TiO_2$). Currents at 0V bias (Short Circuit Currents) are -3.6mA, 0.44mA, -2.9mA, -7.9mA and 60.5µA respectively. For Cu006, Cu011 and Cu016-3 the Voltages at 0A current (Open Circuit Voltages) are approximately 40mV.

Figure 106 shows the initial photovoltaic curves (illuminated) for several samples. All samples were tested for photodiode characteristics (Cu001 to Cu016-3) but most showed only an ohmic response with a linear response to the changing voltage and resistances between 1 and 15Ω. This was attributed to problems with the contacts between the source meter and the sample surfaces. Due to the possible temperature sensitivity of the fabricated devices sputtered gold contacts were not used as it was known that the substrate temperature can rise significantly under sputtering conditions. As such, contact

was made directly between the tungsten-carbide probe tips and the sample surface. For those PV curves showing an ohmic response it was thought that the probe tips had pierced the upper layers of the devices, making direct contact with the Cu substrate beneath. This also had a significant negative effect on the reproducibility of the results.

Although several of the PV curves shown in Figure 106 show slight short circuit currents being produced at 0V bias (between -2.9mA and -7.9mA), the noise level associated with the readings is of a similar magnitude (roughly speaking, greater than ±10mA). Because of this it is difficult to say whether the produced current is a real effect or not.

Each of the curves shown in Figure 106 show roughly the same trend, i.e. two different resistances as the driven voltage sweeps from forward to reverse bias. Above +0.4V the devices display a marked decrease in resistance (with the exception of Cu016-3). This indicates that there is a limited amount of p-n junction behavior occurring, and that when the sweeping voltage reaches +0.4V charge carriers begin to cross the junction lowering the resistance and providing an easier path for current to flow along. The ohmic response present below +0.4V shows that there could be significant leakage associated with each of the devices. The fourth and fifth SEM images in Figure 103 provide a sign of what may have been causing this effect. In these images it appears as if the Cu_2O nanostructures have large areas between them which could be exposed Cu substrate. If this is the case, as is consistent with the previous set of experiments (where the anodisation produced a patchy Cu_2O covering), then when ALD of the n-type and TCO materials was carried out, a secondary interface between the n-type material (ZnO or TiO_2) and the Cu substrate would be formed. Any photo-generated carriers within the n-type layer (both materials have band gaps of around 3eV or 315nm) would then rapidly undergo recombination as there would be no mechanism present to separate the electron-hole pairs. The effect this would have

on the devices would be to act as a simple ohmic resistor, as was seen in the voltage sweeps in Figure 106.

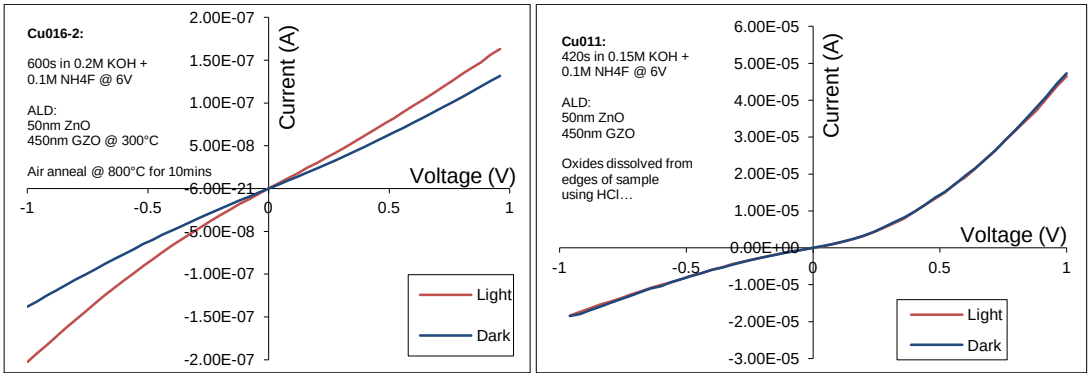

Figure 107: PV curves for samples Cu011 and Cu016-2 under fluorescent illumination and dark conditions.

Figure 107 shows illuminated and dark PV curves for samples Cu011 and Cu016-2. The curve for Cu016-2 shows a marked difference in the resistance of the device under different illumination conditions. Since the short circuit current for this device is effectively 0A the indication is that the p-n junction between the Cu_2O and the ZnO is not functioning as expected. Either photo-generated charge carriers are not being produced close enough to the junction or they are being produced but the recombination time is very short, meaning that they would be mutually annihilated before being separated by the junction. The former point is unlikely because it can clearly be seen that under different illumination conditions the resistance of the device changes, showing that additional carriers are being produced within the active layers or that the mobility is increasing. In both the illuminated and dark curves, a slight change in resistance can be seen at around -0.5V and also possibly at around 0.5V, although this change is much less pronounced. As with the earlier tests, each of these graphs show a semi-ohmic response to the sweeping voltage. The implication of this is that as before, interfaces could have been formed between the Cu substrate and the n-type active layer providing an easier path for conduction.

6.1.2 Conclusion

Several techniques and processing routes were tried during the experiments conducted here. For several of them, such as the electropolishing, Cu anodisation and electrical isolation of the active layers via mechanical scoring and acid etching failed to produce conclusive results. Further experimentation should be carried out to address the issues highlighted with these techniques.

Raman and XRD analysis of the samples at various points through the construction of the devices showed that Cu_2O had been grown by the anodisation procedure and that the deposition of TiO_2 had been successful. The geometry of the upper surfaces of the devices was also examined using SEM and was found to exhibit a spherical, polycrystalline layers of TiO_2 on nanocubes of Cu_2O.

Photovoltaic measurements using IV sweeps from -0.5V to +0.5V indicated that ohmic contact had been made between the n-type layer and the Cu substrate, bypassing the Cu_2O layer and negating the effect of the p-n junction. The small photocurrent produced in three of the devices was of the same magnitude as the background noise level, meaning it was difficult to determine whether the devices were functioning. A change in the slope of the IV curves between +0.4V and +0.5V was taken to indicate that the p-n junction was working to some degree at high forward bias, and overcoming the localized ohmic contacts.

6.2 ALD of Ga-doped ZnO TCO substrates for CdTe - based photovoltaics

Atomic layer deposition of gallium doped zinc oxide films was investigated as a method of fabricating transparent conducting oxide substrates for cadmium telluride based photovoltaic cells. The growth parameters and properties of gallium-doped ZnO were established for a range of dopant concentrations. 1 at% gallium-doped films exhibited the lowest electrical sheet resistances and were selected as substrates to deposit $Cd_{1-x}Zn_xS$ / CdTe photovoltaic cells. The average current density - voltage characteristics of 16 cells under AM1.5 illumination yielded a conversion efficiency of 10.8% and a fill-factor of 65%.

Transparent conducting oxides (TCO) are exploited to make the "front" electrical contact to thin film photovoltaic (PV) solar cells, serving two functions, firstly to transmit the solar radiation to the underlying cell. Secondly the TCO conducts the photocurrent to the external circuit. The integral nature of the TCO means that it plays a significant role in determining the overall efficiency of thin film solar cells. Consequently to achieve high efficiency cells, the TCO transmission of solar radiation must be maximized at the same time ensuring very low electrical resistance. Bosio et al. [188] have made a comprehensive review of the TCOs used for CdTe PV cells. Materials such as fluorine-doped SnO_2 (FTO), indium tin oxide (ITO) and increasingly doped ZnO are being developed for this purpose. Previously, ZnO based TCO films have been deposited by a diverse range of physical vapour deposition techniques including: sputtering, pulsed laser deposition, molecular beam epitaxy and ion plating. Chemical vapour deposition (CVD) processes have been demonstrated for TCO's via metalorganic CVD and more recently atomic layer deposition (ALD). The latter has been adopted by industry for the deposition of metal oxides [189], because it has a number of advantages over other deposition techniques. These include the potential for large area growth, good film uniformity, and low pin - hole densities [190]. ALD

is a process that uses alternating pulses of chemical precursor, which are chemisorbed onto the substrate and relies upon surface reactions to eliminate by-products and to build up the desired thin film material. The reactor is purged with an inert gas between the precursor pulses to suppress unwanted gas phase or pre-reactions and with appropriate adjustment of the experimental conditions, the process proceeds via saturative steps. The ALD growth of Ga-doping of ZnO (ZnO:Ga) has been investigated previously by Saito et al. [191]. Diethylzinc (DEZn), H_2O and triethylgallium (TEGa) were used as the Zn, O and Ga precursors, respectively. To achieve the gallium-doping, the TEGa was simultaneously introduced with DEZn and the flow rates of the zinc and gallium precursors were varied by varying the bubbler temperature. Ga-doping was performed under Zn-rich growth conditions and electron concentrations of the order of 10^{20} cm^{-3} were reported. We have recently reported the growth of ZnO:Ga achieved by combining series of deposition cycles using DEZn and TEGa [192]. In contrast to the method used by Saito et al, this approach controls the doping via the control of the DEZn : TEGa cycle ratio. This study examines the effect of the growth parameters on the electrical and optical properties of gallium doped ZnO TCO films using the method developed in reference 192. ALD ZnO:Ga is shown to provide an effective TCO for CdTe-based solar cells.

Atomic layer deposition:

The atomic layer deposition experiments were performed in a Cambridge Nanotech Savannah 100 system, which comprises of a 100 mm diameter heater controllable between 25 and 400ºC. The liquid diethylzinc and triethylgallium (TEGa) sources were delivered into the process chamber from independently heated bubbler sources. The precursor delivery was achieved via vapour draw. The precursor delivery module and delivery lines from the module to the process chamber are heated. Precursors are delivered into the chamber by

fast ALD valves with a minimum opening time of 10 ms. Details of the ALD parameters employed are shown in Table 24.

Table 24: ALD growth parameters

Substrate Temperature	100-350°C
Pressure	200 mTorr
Argon flow	5 std cm^3min^{-1}
Pulse Sequences (precursor/purge/water/purge)	
DEZn	0.02/2/0.01/2 s
TEGa	0.1/2/0.01/2 s

MOCVD of the $Cd_{1-x}Zn_xS$/CdTe cells:

The $Cd_{1-x}Zn_xS$ / CdTe device structure was grown using the atmospheric pressure MOCVD process described previously [193]. This entailed in situ doping of the 2 µm thick CdTe layer with 1 x 10^{18} cm^{-3} of As from trisdimethlyaminoarsenic (tDMAAs) with a termination of high concentration of As (>1×10^{19} cm^{-3}) to improve ohmic properties at the back contact [194]. A $CdCl_2$ layer was deposited and annealed in situ in the MOCVD reactor, as described by Barrioz et al. [195], and therefore no etching of the surface was required prior to evaporating the 16 0.25 cm^2 gold back contacts.

Physical Characterisation:

Electron microscopy was performed using a JEOL 2100F in bright field illumination mode. Energy dispersive x-ray analysis of the samples were made using a JEOL 2000FX equipped with EDAX Genesis 4000 X-Ray system to measure the composition. Electrical resistivity measurements were made with a four-point probe system comprising a Lucas Signatone Corp SP4 Four Point Probe Head and a Keithley Series 2400 Sourcemeter®. Film thickesses were estimated using a Rudolph Auto EL IV ellipsometer measuring silicon 100 n-type wafer samples placed alongside the glass specimens. Hall Effect measurements to obtain carrier concentration and mobility were made on bespoke equipment using the Van der Pauw sample configuration, Keithley Series 2400 Sourcemeter®, and a 0.3T magnetic field.

Laboratory PV cell devices were tested on 5×5 cm^2 TCO substrates. The $Cd_{1-x}Zn_xS$ & CdTe layers were removed from the edges of the device to reveal the TCO and an In/Ga eutectic was applied to the TCO to enhance the front contact. The photovoltaic I–V device measurements were carried out using an Abet Technologies Ltd. AM1.5 solar simulator. A Fraunhofer amorphous silicon reference cell was used for calibration before cell measurements.

6.2.1 Results and Discussion

Dopant incorporation:

To deposit the Ga-doped ZnO films with varying dopant concentrations, samples were prepared using different ratios of DEZn : TEGa ALD cycles. The ZnO:Ga films are deposited using x cycles of ZnO steps, via exposure of the surface to successive steps of DEZn and then water vapour. Intermittent pump purge steps are used to prevent gas-phase pre-reaction, which ensures the surface reaction. After the x ZnO cycles, a single Ga-O cycle is deposited, via exposure of the surface to TEGa and then water vapour. The whole process is repeated until the required film thickness is achieved. The TEGa precursor exhibited good vapor draw transport at room temperature using an ALD-valve opening time of between 0.2 to 0.3 seconds. TEGa does not form a deposit with water vapour at a substrate temperature ≤ 250°C. In the presence of the growing OH-terminated ALD ZnO film, the TEGa reaction with water is catalysed, promoting gallium incorporation. The deposition of gallium-doped ZnO was achieved using varying combinations of ZnO and gallium oxide deposition cycles. Figure 108 shows the atomic percentage of gallium dopant content quantified using the Ga K and Zn K lines in the energy dispersive X-ray spectrum of films deposited on holey carbon films. The proportion of dopant incorporated within the films is approximately proportional to the fraction of dopant ALD cycles (TEG /(TEGa + DEZn)) used in the growth process as

anticipated. For a cycle ratio TEGa : DEZn of 1:5, or TEG /(TEGa + DEZn)) = 16.7%, the measured gallium is 2.9 at%.

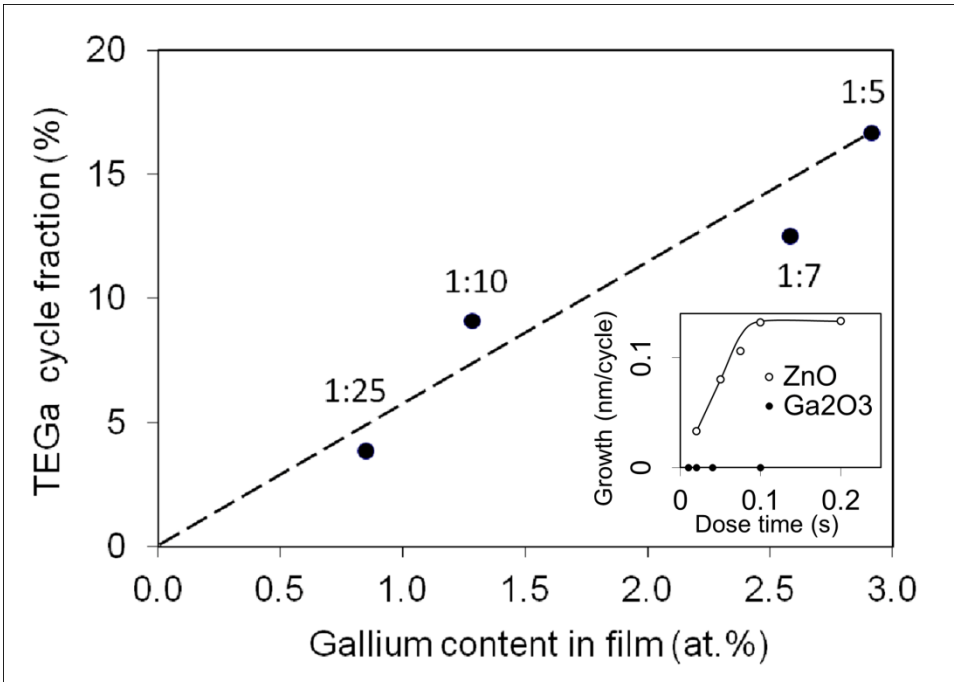

Figure 108: Gallium content in film measured by energy dispersive X-ray analysis versus percentage Ga/(Ga+Zn) ALD cycle fraction at 250˚C.

The typical microstructure of the ZnO:Ga thin films is illustrated in Figure 109 which shows bright field transmission electron micrographs of a 1 at% doped ZnO:Ga film deposited at 250°C. The ZnO:Ga film consists of crystallites of the order of a few nanometers in diameter. At 500k times magnification, the lattice fringing within the individual crystallites can be seen. The films have a random crystalline orientation and showed no segregation of gallium-related phases over the composition range examined here.

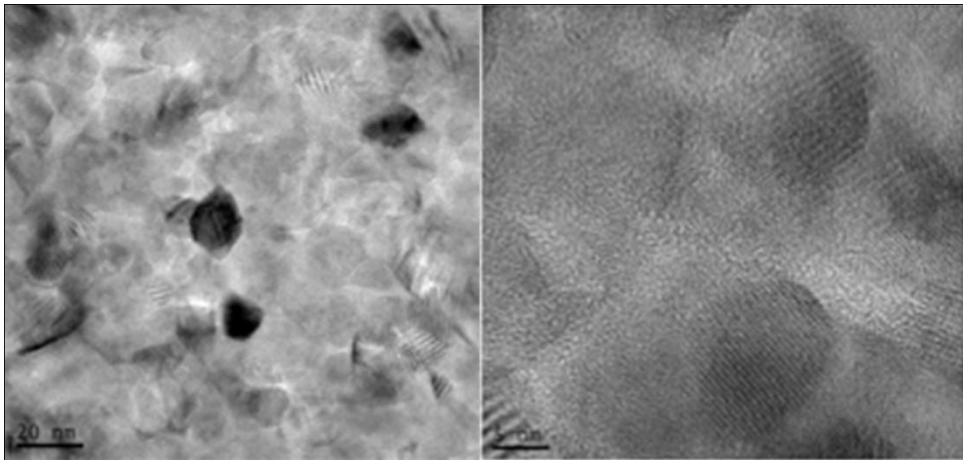

Figure 109: Transmission electron micrograph, plan view bright field images of ZnO:Ga film using TEGa : DEZn cycle ratio of 1:20 at 300˚C.

Figure 110 shows X-ray diffraction data of the (100), (002) and (101) reflections recorded from 50nm thick films grown with varying TEGa ; DEZn cycle ratios. For the 1:90 ratio, the intensities of ZnO-related diffraction features has a near random polycrystalline proportion, however as the gallium content is increased (e.g. to 1:5) texturing of the film growth occurs in favour of the <002> c-axis growth direction.

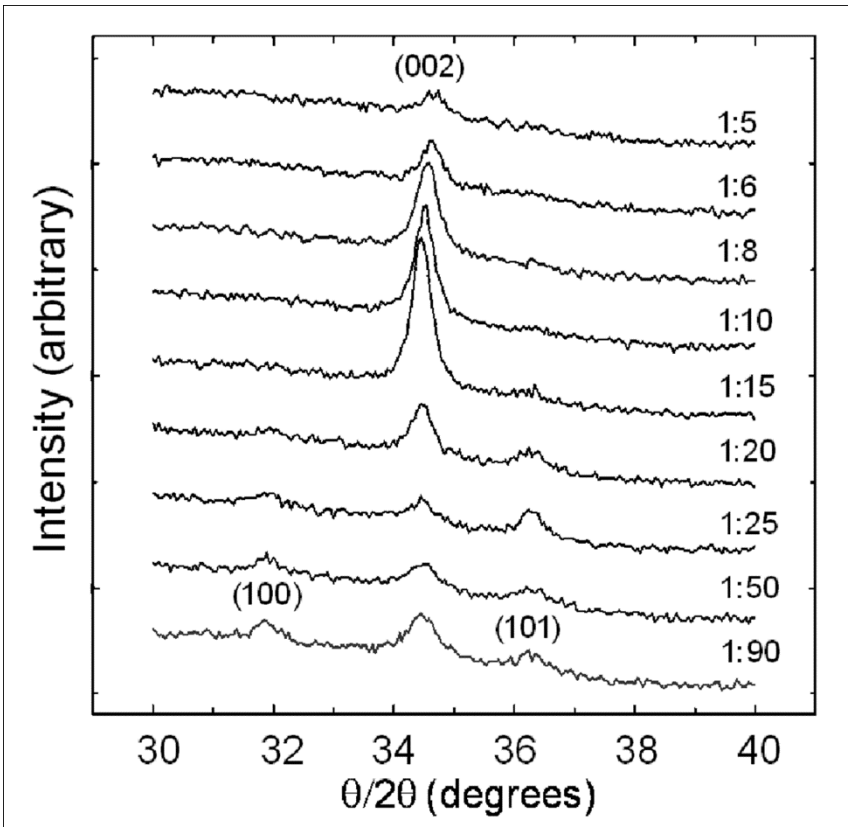

Figure 110: X-ray diffraction spectra of ZnO:Ga films grown using varying ratios of TEGa : DEZn cycles.

Electrical Properties:

The electrical sheet resistance of approximately 50nm thick ZnO:Ga layers with varying gallium contents, deposited at 250°C was measured. The sheet resistance was found to be a minimum at 4 - 6% TEGa cycles (0.5 – 1 at%) as shown in Figure 111. Above this value, the sheet resistance rises monotonically and becomes more resistive than the undoped ZnO. Hall Effect measurements were made on the films to measure the electrical charge carrier concentration and mobility.

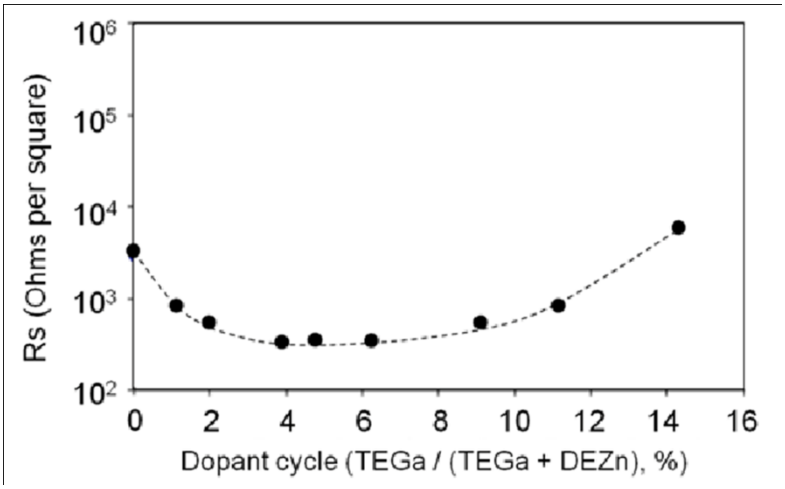

Figure 111: Variation of sheet resistance of ZnO:Ga films as a function of percentage dopant cycles (TEGa / (TEGa + DEZn).

Figure 112 shows the corresponding variation in the carrier mobility and carrier concentration. All of the films exhibited n-type conductivity. As the Ga level is increased from zero to approximately 2 at%, the carrier concentration rises to a maximum of 5.0 x $10^{20}cm^{-3}$ before reducing as further amounts of Ga is incorporated. The maximum carrier concentration coincides with a carrier mobility of 7 cm^2 / V.s. The reduction in carrier concentration at higher doping levels has also been observed in CVD Ga-doped ZnO films [196]. It was proposed that at high gallium concentrations, the free electron density decreases because an increasing number of dopant atoms form some kind of neutral point defects, which do not contribute free electrons.

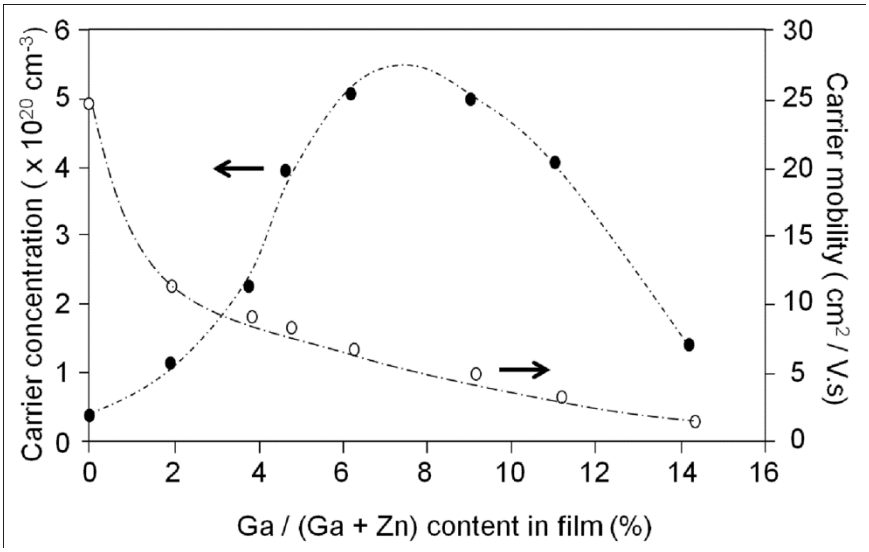

Figure 112: Carrier concentration and mobilities of varying doping levels in ZnO:Ga films measured by the Hall effect.

The optical properties of the ZnO:Ga films were assessed by UV-Vis spectrophotometry. Figure 113 shows a typical transmission spectra for a ZnO:Ga film. In the visible region, the spectrum is overlaid with Fabry-Perot type oscillations due to the thickness of these films, which are 500 – 550nm. The peak transmissions of the films, is approximately 80% in the visible spectrum. The inset shows threshold for transmission of doped films with carrier concentrations in the range 6.9 – 9.4 x 10^{20} cm^{-3}. The threshold shifts to lower wavelengths as the carrier concentration increases, which can be explained in terms of the Burnstein-Moss effect [197,198], because the gallium-induced carriers occupying states just above the bottom of the ZnO conduction band. This has the effect of pushing the absorption edge to higher energies. The same effect has been observed in gallium-doped ZnO deposited by pulsed laser deposition [199].

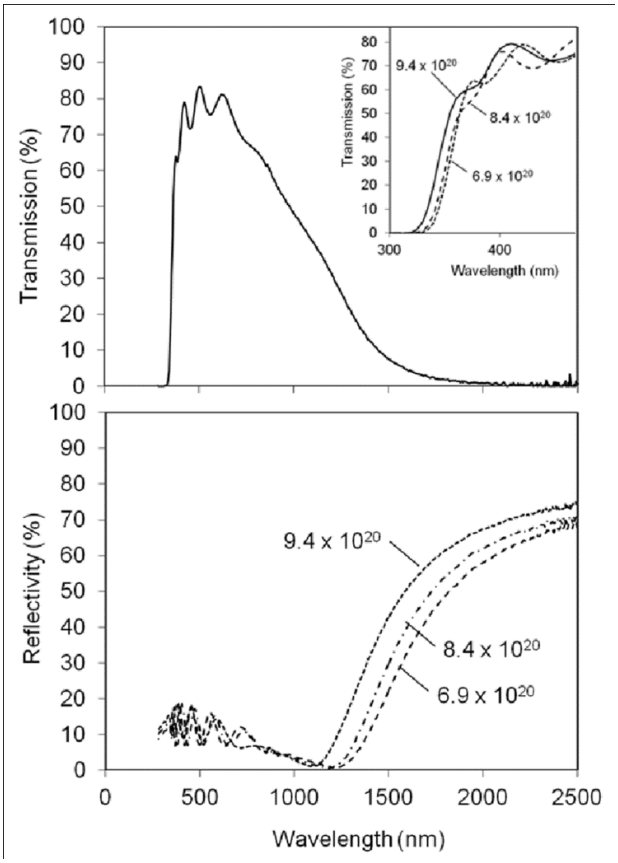

Figure 113: UV-Visible-IR transmission (upper) of ZnO:Ga films deposited on glass. The inset shows the influence of carrier concentration on the band edge. Reflectivity (lower) shows the effect of carrier concentration on the IR cut-off.

Cell Characteristics:

The baseline MOCVD process [193] typically used to produce $Cd_{1-x}Zn_xS$ / CdTe devices on ITO/aluminosilicate substrates, with sheet resistance 5-11 (Ohms per square), was transferred to the devices fabricated in this study using 430nm thick ZnO:Ga films (5.3 Ohms per square, 230 μΩ.cm) on sodalime glass and compared to devices on NSG TEC C15 substrates. Table 25 shows mean I-V results for cells (0.25 cm^2 in area) produced on ZnO:Ga / glass and NSG TEC C15 substrates.

Table 25: Average of device parameters illuminated under AM1.5. Efficiency (η), short circuit current density (J_{sc}), open circuit voltage (V_{oc}), series resistance (R_s) and shunt resistance (R_{sh}).

I-V parameter	ZnO:Ga	NSG TEC C15
η (%)	10.8	10.9
J_{sc} (mA cm^{-2})	23.9	25.8
V_{oc} (mV)	690	727
FF (%)	65.0	57.9
Rs (Ω/□)	3.2	2.6
R_{sh} (Ω.cm^2)	743	588

Mean efficiencies of both device types are comparable, but significant variation occurs in short current density (J_{sc}), open circuit voltage (V_{oc}) and fill-factor (FF). The devices produced on ZnO:Ga / glass suffered from some blistering effects which were notable immediately after the samples were removed from the MOCVD growth chamber. This was not observed for the devices grown on NSG TEC C15. The low V_{oc} in the CdTe device on ZnO:Ga may be attributed to the lateral inhomogenity across the device associated with the blistering. This also resulted in a reduction of J_{sc} and an increase in series resistance (R_s). The low sheet resistance of the ZnO:Ga would be expected to have the opposite effect on R_s where lateral conduction in the TCO is superior to NSG TEC C15.

However, FF and shunt resistance (R_{sh}) are improved for the ZnO:Ga device in comparison to the device on NSG TEC C15. Optimisation of the surface preparation of the ZnO:Ga before device deposition to improve nucleation is expected to make significant increase in PV performance. Overall, ZnO:Ga shows huge promise for use as a TCO in thin film CdTe PV devices.

6.2.2 Conclusion

Atomic layer deposition was used to deposit thin films of gallium-doped zinc oxide. The doping was controlled, by varying the ratio of deposition cycles for ZnO and gallium oxide. In the range 250 – 350°C substrate temperature, gallium could be incorporated at concentrations up to approximately 3 atomic % without apparent segregation at the temperatures investigated. At 1 at% gallium doping the maximum carrier concentration of $5.0 \times 10^{20} cm^{-3}$ at a deposition temperature of 250°C coincides with a carrier mobility of approximately 7 cm^2 / V.s. UV-Visible spectrophotometry shows that the gallium doping shifts the transmission edge of the ZnO:Ga films via a Burnstein-Moss mechanism. $Cd_{1-x}Zn_xS$ / CdTe photovoltaic cells deposited on ZnO:Ga / glass substrates yielded a quantum efficiency of 10.8% and a fill-factor of 65% under AM1.5 illumination. With removal of the observed blistering effect device performance will improve significantly.

6.3 Photovoltaic testing and TCO Conclusions

Cu_2O nanostructured surfaces were synthesised by anodisation Cu metal sheet in electrolytic solutions of aqueous KOH and NH_4F. The resultant structures were then used as substrates for the growth of n-type TiO_2 or ZnO by atomic layer deposition. Finally Ga-doped ZnO was deposited using atomic layer deposition to form the transparent top contact. Several devices were imaged using SEM to assess the deposition and to examine the effects of mechanical scoring and HCl acid dips as methods to electronically isolate the active layers from the Cu substrate. IV characterisation tests were carried out to assess the quality of the pn-junctions. All samples tested showed leaky, slightly rectifying characteristics with only a few samples showing any difference in electrical response under dark and illuminated conditions. Several possible reasons for the results were proposed including the IV equipment probe tips piercing the surfaces and bypassing of the active layers of the devices, and possible short circuits of the ALD layers making direct contact to the Cu metal back contact. However, in several of the devices, the change in resistance seen at around +0.4V was taken to be an indication that the devices had at least partially formed the desired pn-junction.

Ga-doped ZnO transparent conductive oxides were prepared with a range of Ga concentrations for use as front contacts in CdSe and CdTe photovoltaic devices. Sheet resistance measurements showed that the films doped with 1at% Ga (corresponding to a doping ratio of 4-6% TEGa cycles) had the highest conductivity and were then used as substrates for the deposition of $Cd_{1-x}Zn_xS$ / CdTe. Photovoltaic testing under AM1.5 illumination on 16 devices produced with these materials yielded a conversion efficiency of 10.8% and a fill-factor of 65%.

7 Future Work

This project explored methods of utilising high interface area pn-junction devices to enhance photo-generated current in PV devices. Although a fully functioning high surface area PV device was not realised during this work, several steps along the envisioned processing route were addressed. To reach the intended milestones of the project and to be able to produce a working photovoltaic device, further research and experimentation would be required. For an AAO based device, the focus of this further research would concentrate primarily on methods to achieve fully conformal coatings within the scaffold material using ALD. This could be done by either increasing the precursor exposure, or by increasing the partial pressure of the precursor to near atmospheric levels, both of which would decrease the MFP of precursor molecules and increase the number of surface-precursor collisions. Further research could also be aimed at increasing the porosity of the AAO templates to their maximum value of around 0.9. This would facilitate the ALD process and allow for a higher proportion of active material within the device. Another issue that would need to be addressed is that of making reliable ohmic contacts to the front and back of the devices and to maximise the amount of current harvested from the devices by the selection of optimal ratios of p-type, n-type and TCO material.

Further work could also be conducted on the use of CuO and Cu_2O nanostructures in photovoltaic devices. Several steps would need to be addressed to realise reliable CuO and Cu_2O based devices. One of the main issues encountered in the proceeding work was how to achieve electronic isolation of the active layers and to reduce the possibility of short-circuits. Techniques developed for the processing of integrated circuits could be applicable to this work, such as the use of UV masks, resists and developers. This would require several experiments testing the compatibility of the multitude of IC techniques with the materials used in this system. The CuO nanowires produced for this project also deserve

further attention, possible focussed on methods to protect the thermally grown oxide NWs from spallation (experiments into further control of the cooling of the material after oxidation, as well as experiments into controlling the thermal expansion mismatch between the NWs and the substrate.).

The Cu_2O nanostructures grown by the reduction of CuO NWs should be investigated to a higher degree. Possible lines of enquiry would address whether the oxide layers fully reduce to Cu_2O, methods for removing the remaining Cu metal after growth to allow ohmic contacts to be applied and deposition of n-type and TCO materials followed by IV PV testing.

8 References

1. 2.626 Fundamentals of Photovoltaics, Fall 2008 [Internet]: Massachusetts Institute of Technology: MIT OpenCourseWare; c2008 [cited 2013 04 Aug]. Available from: http://ocw.mit.edu.

2. The International Energy Agency. 2012 key world energy statistics. France: The International Energy Agency; 2012.

3. Friedman AL, Brittain D, Menon L. Roles of pH and acid type in the anodica growth of porous alumina. The Journal of Chemical Physics 2007;127:154717.

4. Ding GQ, Yang R, Ding JN, Yuan NY, Yuan YZ. Fabrication of porous anodic alumina with ultrasmall nanopores. Nanoscale Research Letters 2010;5:1257-63.

5. Sulka GD, Brzózka A, Zaraska L, Jaskuła M. Through-hole membranes of nanoporous alumina formed by anodizing in oxalic acid and their applications in fabrication of nanowire arrays. Electrochim Acta 2010 05/30;55(14):4368-76.

6. Masuda H, Yada K, Osaka A. Self-ordering of cell configuration of anodic porous alumina with large-size pores in phosphoric acid solution. Japanese Journal of Applied Physics Part 2-Letters & Express Letters 1998;37(11):L1340-2.

7. Garcia-Vergara SJ, Skeldon P, Thompson GE, Habazaki H. Stress generated porosity in anodic alumina formed in sulphuric acid electrolyte. Corros Sci 2007 10;49(10):3772-82.

8. Zaraska L, Sulka GD, Szeremeta J, Jaskuła M. Porous anodic alumina formed by anodization of aluminum alloy (AA1050) and high purity aluminum. Electrochim Acta 2010 05/30;55(14):4377-86.

9. Lee W, Ran J, Gösele U, Nielsch K. Fast fabrication of long-range ordered porous alumina membranes by hard anodisation. Nat Mater 2006;5:741-7.

10. Edwards JD, Keller F. Formation of anodic coatings on aluminum. Trans Electrochem Soc 1941;79(1).

11. Keller F, Hunter MS, Robinson DL. Structural features of oxide coatings, on aluminium. J Electrochem Soc 1953;100:411-9.

12. Nasirpouri F, Abdollahzadeh M, Almasi MJ, Parvini-Ahmadi N. A comparison between self-ordering of nanopores in aluminium oxide films achieved by two- and three-step anodic oxidation. Current Applied Physics 2009 01;9(1).

13. Nai-Qin Z, Xiao-Xue J, Chun-Sheng S, Jia-Jun L, Zhi-Guo Z, Xi-Wen D. Effects of anodizing conditions on anodic alumina structure. J Mater Sci 2007 06;42(11):3878-82.

14. Gu QD, Yang R, Jian ND, Yuan NY, Yuan YZ. Fabrication of porous anodic alumina with ultrasmall nanopores. Nanoscale Research Letters 2010 08;5(8):1257-63.

15. Jessensky O, Muller F, Gosele U. Self-organized formation of hexagonal pore arrays in anodic alumina. Appl Phys Lett 1998;72(10):1173-5.

16. Akolkar R, Wang Y, Kuo H. Kinetics of the electrolytic coloring process on anodized aluminum. J Appl Electrochem 2007 02;37(2):291-6.

17. Curioni M, Koroleva EV, Skeldon P, Thompson GE. Flow modulated ionic migration during porous oxide growth on aluminium. Electrochim Acta 2010;55(23):7044-9.

18. Day ME, Delfino M, Salimian S. Low energy ion etching of aluminum oxide films and native aluminum oxide. J Appl Phys 1992 12;72(11):5467.

19. Thompson GE. Porous anodic alumina: Fabrication, characterization and applications. Thin Solid Films 1997;297(1-2):192-201.

20. Danielewski M. Corrosion: Fundamentals, testing, and protection, kinetics of gaseous corrosion processes, 2003, ASM handbook, vol 13A, 97-105. In: ; 2003. .

21. Houser JE, Hebert KR. The role of viscous flow of oxide in the growth of self-ordered porous anodic alumina films. Nature Materials 2009 05;8(5):415-20.

22. Su ZX, Zhou WZ. Formation mechanism of porous anodic aluminium and titanium oxides. Adv Mater 2008;20(19):3663,+.

23. Kopp O, Lelonek M, Knoll M. Influence of surface morphology on oxide growth in porous alumina. Electrochim Acta 2009 11/01;54(26):6594-7.

24. Perez I, Robertson E, Banerjee P, Henn-Lecordier L, Son SJ, Lee SB, Rubloff GW. TEM-based metrology for HfO2 layers and nanotubes formed in anodic aluminum oxide nanopore structures. SMALL 2008;4(8):1223-32.

25. Mei YF, Siu GG, Fu RKY, Chen P, Wu XL, Hung TF, Chu PK, Yang Y. Formation mechanism of alumina nanotubes and nanowires from highly ordered porous anodic alumina template. J Appl Phys 2005 2;97(3):034305.

26. Wang X, Li C, Ma L, Cao H, Zhang B. Fabrication of alumina nanowires from porous alumina membranes by etching in phosphoric acid solution. Surface Review & Letters 2009 02;16(1):73-8.

27. Metzger RM, Konovalov VV, Sun M, Xu T, Zangari G, Xu B, Benakli M, Doyle WD. Magnetic nanowires in hexagonally ordered pores of alumina. IEEE Trans Magn 2000 Jan2000;36(1):30-5.

28. Lazarowich RJ, Taborek P, Yoo B-, Myung NV. Fabrication of porous alumina on quartz crystal microbalances. J Appl Phys 2007 05/15;101(10):104909.

29. Ali G, Ahmad M, Akhter JI, Maqbool M, Cho SO. Novel structure formation at the bottom surface of porous anodic alumina fabricated by single step anodization process. Micron 2010 08;41(6):560-4.

30. Kheng Tan L, Knoll W, Gao H, Zong Y. Atomic layer deposition of TiO_2 to bond free-standing nanoporous alumina templates to gold-coated substrates as planar optical waveguide sensors. The Journal of Physical Chemistry - Part C 2008 10/16;112(45):17576.

31. Li AP, Muller F, Birner A, Nielsch K, Gosele U. Hexagonal pore arrays with a 50-420 nm interpore distance formed by self-organization in anodic alumina. J Appl Phys 1998;84(11):6023-6.

32. Masuda H. Highly ordered nanohole arrays in anodic porous alumina. In: R. B. Wehrspohn, editor. Ordered porous nanostructures and applications. New York: Springer-Verlag GmbH; 2005. .

33. Masuda H, Fukuda K. Ordered metal nanohole arrays made by a two-step replication of honeycomb structures of anodic alumina. Science 1995 06/09;268(5216):1466-8.

34. Nielsch K, Choi J, Schwirn K, Wehrspohn RB, Gosele U. Self-ordering regimes of porous alumina: The 10% porosity rule. Nano Letters 2002;2(7):677-80.

35. Beck G, Petrikowski K. Influence of the microstructure of the aluminum substrate on the regularity of the nanopore arrangement in an alumina layer formed by anodic oxidation. Surf Coat Technol 2008 07/30;202(21):5084-91.

36. Li F, Zhang L, Metzger RM. On the growth of highly ordered pores in anodised aluminium oxide. Chemistry of Materials 1998;10:2470-80.

37. Masuda H, Satoh M. Fabrication of gold nanodot array using anodic porous alumina as an evaporation mask. Jpn J Appl Phys 1996;35:L126-9.

38. Yuan JH, He FY, Sun DC, Xia XH. A simple method for preparation of through-hole porous anodic alumina membrane. Chemistry of Materials 2004;16(10):1841-4.

39. Masuda H, Asoh H, Watanabe M, Nishio K, Nakao M, Tamamura T. Square and triangular nanohole array architectures in anodic alumina. Adv Mater 2001;13(3):189-92.

40. Pitzschel K, Moreno JMM, Escrig J, Albrecht O, Nielsch K, Bachmann J. Controlled introduction of diameter modulations in arrayed magnetic iron oxide nanotubes. ACS NANO 2009;3(11):3463-8.

41. Salerno M, Patra N, Losso R, Cingolani R. Increased growth rate of anodic porous alumina by use of ionic liquid as electrolyte additive. Mater Lett 2009 08/31;63(21):1826-9.

42. Lee W, Schwirn K, Steinhart M, Pippel E, Scholz R, Gösele U. Structural engineering of nanoporous anodic aluminium oxide by pulse anodization of aluminium. Nature Nanotechnology 2008 04;3(4):234-9.

43. Losic D, Lillo M, Losic D. Porous alumina with shaped pore geometries and complex pore architectures fabricated by cyclic anodization. Small 2009;5(12):1392-7.

44. Rasband WS. ImageJ [computer program]. Version 1.44i. U. S. National Institutes of Health, Bethesda, Maryland, USA: 1997. .

45. Matefi-Tempfli S, Matefi-Tempfli M, Piraux L. Characterization of nanopores ordering in anodic alumina. Thin Solid Films 2008 04/30;516(12):3735-40.

46. Tsuchiya H, Schmuki P. Self-organized high aspect ratio porous hafnium oxide prepared by electrochemical anodization. Electrochemistry Communications 2005 1;7(1):49-52.

47. Tsuchiya H, Berger S, Macak JM, Ghicov A, Schmuki P. Self-organized porous and tubular oxide layers on TiAl alloys. Electrochemistry Communications 2007 9;9(9):2397-402.

48. Sieber I, Hildebrand H, Friedrich A, Schmuki P. Formation of self-organized niobium porous oxide on niobium. Electrochemistry Communications 2005 1;7(1):97-100.

49. Tsuchiya H, Macak JM, Sieber I, Taveira L, Ghicov A, Sirotna K, Schmuki P. Self-organized porous WO3 formed in NaF electrolytes. Electrochemistry Communications 2005 3;7(3):295-8.

50. Yablonovitch E. Inhibited spontaneous emission in solid-state physics and electronics. Phy Rev Lett 1987;58(20):2059-62.

51. Wu HY, Zhao Y, Jiao QZ. Nanotube arrays of Zn/Co/Fe composite oxides assembled in porous anodic alumina and their magnetic properties. J all Com 2009(487):591-4.

52. Han N, Deng P, Chen J, Chai L, Gao H, Chen Y. Electrophoretic deposition of metal oxide films aimed for gas sensors application: The role of anodic aluminum oxide (AAO)/Al composite structure. Sensors & Actuators B: Chemical 2010 01/29;144(1):267-73.

53. Bennett SP, Menon L, Heiman D. Magnetic properties of GaMnAs nanodot arrays fabricated using porous alumina templates. J Appl Phys 2008 07/15;104(2):024309.

54. Hong C, Tang TT, Hung CY, Pan RP, Fang W. Liquid crystal alignment in nanoporous anodic aluminum oxide layer for LCD panel applications. Nanotechnology 2010;21(28).

55. White RL, New RMH, Pease RFW. Patterned media: A viable route to 50 Gbit/in^2 and up for magnetic recording? IEEE Trans Magn 1997;33(1):990-5.

56. Huang CH, Li EJ, Chang WJ, Wang NF, Hung CI, Houng MP. Charge trapping behavior of SiO2-anodic Al_2O_3-SiO_2 gate dielectrics for nonvolatile memory applications. Solid State Electronics 2009 03;53(3):279-84.

57. Zhao QA, Wen GH, Liu ZG, Fan YB, Zou GT, Li L, Zheng RK, Ringer SP, Mao HK. Synthesis of dense, single-crystalline CrO2 nanowire arrays using AAO template-assisted chemical vapor deposition. Nanotechnology 2011;22(12).

58. Bao X, Li F, Metzger RM. Synthesis and magnetic properties of electrodeposited metal particles on anodic alumite film. J Appl Phys 1996 04/15;79(8):4866.

59. Pellin MJ, Stair PC, Xiong G, Elam JW, Birrell J, Curtiss L, George SM, Han CY, Iton L, Kung H, et al. Mesoporous catalytic membranes: Synthetic control of pore size and wall composition. Catalysis Letters 2005 06;102(3):127-30.

60. Tacchini I, Terrado E, Anson A, Martinez MT. Anatase nanotubes synthesized by a template method and their application as a green photocatalyst. J Mater Sci 2011;46(7):2097-104.

61. Ito T, Yamaguchi H, Okabe K, Masumi T. Single-crystal growth and characterization of Cu_2O and CuO. Journal of Materials Science 1998(33):3555-66.

62. Solache-Carranco H, Juarez-Diaz G, Esparza-Garcia A, Briseno-Garcia M, Galvan-Arellano M, Martinez-Juarez J, Romero-Paredes G, Pena-Sierra R. Photoluminescence and X-ray diffraction studies on Cu2O. Journal of Luminescence 2009(129):1483-7.

63. Park JH, Natesan K. Oxidation of copper and electronic transport in copper oxides. Oxidation of Metals 1993;39(5/6):411-35.

64. Raebiger H, Lany S, Zunger A. Origins of the p-type nature and cation deficiency in Cu_2O and related materials. Physical Review B 2007(76).

65. Li Z, Liu J, Wang D, Gao Y, Shen J. $Cu_2O/Cu/TiO_2$ nanotube ohmic heterojunction arrays with enhanced photocatalytic hydrogen production activity. International Journal of Hydrogen Energy 2011;37(8):6431-7.

66. Zhu LH, Zhang JY, Chen ZY, Liu KL, Gao H. Effect of Cu_2O morphology on photocatalytic hydrogen generation and chemical stability of TiO_2/Cu_2O composite. Journal Of Nanoscience And Nanotechnology 2013;13(7):5104-8.

67. Liu H, Wang J, Fan XM, Zhang FZ, Liu HR, Dai J, Xiang FM. Synthesis of Cu_2O/T-ZnOw nanocompound and characterization of its photocatalytic activity and stability property under UV irradiation. Materials Science and Engineering B-Advanced Functional Solid-State Materials 2013;178(2):158-66.

68. Xiong ZZ, Zheng MJ, Liu SD, Ma L, Shen WZ. Silicon nanowire array/Cu_2O crystalline core-shell nanosystem for solar-driven photocatalytic water splitting. Nanotechnology 2013;24(26).

69. Liu MM, Liu R, Chen W. Graphene wrapped Cu_2O nanocubes: Non-enzymatic electrochemical sensors for the detection of glucose and hydrogen peroxide with enhanced stability. Biosensors & Bioelectronics 2013;45:206-12.

70. Jiang T, Xie T, Yang W, Fan H, Wang D. Photoinduced charge transfer process in p-Cu2O/n-Cu2O homojunction film and its photoelectric gas-sensing properties. Journal of Colloid and Interface Science 2013;405:242-8.

71. Lv P, Zheng W, Lin L, Peng F, Huang Z, Lai F. I-V characteristics of ZnO/Cu_2O thin film n-i-p heterojunction. Physica B 2011;406:1253-7.

72. Gupta N, Singh R, Wu F, Narayan J, McMillen C, Alapatt GF, Poole KF, Hwu S, Sulejmanovic D, Young M, et al. Deposition and characterization of nanostructured Cu2O thin-film for potential photovoltaic applications. Journal of Materials Research 2013;28(13):1740-6.

73. Nam D, Cho I, Lee J, Cho E, Sohn J. Active layer thickness effects on the structural and electrical properties of p-type Cu_2O thin-film transistors. Journal of Vacuum Science & Technology: Part B 2012;30(6):060605-1,060605-5.

74. PV Education.org - Absorption coefficient [Internet] [cited 2013 Dec/07]. Available from: http://pveducation.org/pvcdrom/pn-junction/absorption-coefficient.

75. Malerba C, Biccari F, Mittiga A, Leonor AR, D'Incau M, Scardi P. Absorption coefficient of bulk and thin film cu 2O. Solar Energy Mater Solar Cells 2011 / 10 / 01 /;95(10):2848-54.

76. Muñoz-Rojas D, Jordan M, Yeoh C, Marin AT, Kursumovic A, Dunlop LA, Iza DC, MacManus Driscoll JL, Chen A, Wang H. Growth of ~5 $cm^2V^{-1}s^{-1}$ mobility, p-type copper(I) oxide (Cu_2O) films by fast atmospheric atomic layer deposition (AALD) at 225°C and below. AIP Advances 2012 / 01 / 01 /;2(4).

77. Jiang TF, Xie TF, Chen LP, Fu ZW, Wang DJ. Carrier concentration-dependent electron transfer in Cu_2O/ZnO nanorod arrays and their photocatalytic performance. Nanoscale 2013;5(7):2938-44.

78. Bhattacharyya SR, Reppin D, Sanguino P, Ayouchi R, Polity A, Schwarz R, Hofmann D, Meyer BK. Photoconductivity study of sputter-deposited Cu_2O films. Acta Physica Polonica A 2011;120(6):A11-4.

79. Dimitriadis CA, Papadimitriou L, Economou NA. Resistivity dependence of the minority carrier diffusion length in in single crystals of Cu_2O. J Mater Sci Lett 1983 / 11 / 01 /;2(11):691-3.

80. Sculfort JL, Guyomard D, Herlem M. Photoelectrochemical characterization of the p-Cu_2O-non aqueous electrolyte junction. Electrochim Acta 1984;29:459-65.

81. Sung SY, Kim SY, Jo KM, Lee JH, Kim JJ, Kim SG, Chai KH, Pearton SJ, Norton DP, Heo YW. Fabrication of p-channel thin-film transistors using CuO active layers deposited at low temperature. Appl Phys Lett 2010;97(22).

82. Lee SS, Bai H, Liu Z, Sun DD. Optimization and an insightful properties-activity study of electrospun TiO_2/CuO composite nanofibers for efficient photocatalytic H_2 generation. Applied Catalysis B: Environmental 2013 / 08 / 01 /;140-141:68-81.

83. Gao F, Liu X, Zhang J, Song M, Li N. Photovoltaic properties of the p-CuO/n-si heterojunction prepared through reactive magnetron sputtering. Journal of Applied Physics 2012;111:084507.

84. Nagaraju G, Hwan Ko Y, Su Yu J. Facile synthesis of ZnO/CuO nanostructures on cellulose paper and their p-n junction properties. Mater Lett 2014 / 01 / 01 /;116:64-7.

85. Dimopoulos T, Peic A, Mullner P, Neuschitzer M, Resel R, Abermann S, Postl M, List EJW, Yakunin S, Heiss W, et al. Photovoltaic properties of thin film heterojunctions with cupric oxide absorber. Journal of Renewable and Sustainable Energy 2013;5:011205.

86. Samarasekara P, Kumara NTRN, Yapa NUS. Sputtered copper oxide (CuO) thin films for gas sensor devices. Journal of Physics: Condensed Matter 2006;18:2417-20.

87. Shao P, Deng S, Chen J, Chen J, Xu N. Study of field emission, electrical transport, and their correlation of individual single CuO nanowires. J Appl Phys 2011 01/15;109(2):023710.

88. Zhan RZ, Chen J, Deng SZ, Xu NS. Fabrication of gated CuO nanowire field emitter arrays for application in field emission display. Journal of Vacuum Science & Technology: Part B 2010;28(3):558-61.

89. Ji H, Miao X, Wang L, Qian B, Yang G. Microwave-assisted hydrothermal synthesis of sphere-like C/CuO and CuO nanocrystals and improved performance as anode materials for lithium-ion batteries. Powder Technol 2013 6;241(0):43-8.

90. Karunakaran C, Manikandan G, Gomathisankar P. Microwave, sonochemical and combustion synthesized CuO nanostructures and their electrical and bactericidal properties. J Alloys Compounds 2013;580:570-7.

91. Gopalakrishna D, Vijayalakshmi K, Ravidhas C. Effect of annealing on the properties of nanostructured CuO thin films for enhanced ethanol sensitivity. Ceram Int 2013 / 09 / 01 /;39(7):7685-91.

92. Jundale DM, Joshi PB, Sen S, Patil VB. Nanocrystalline CuO thin films: Synthesis, microstructural and optoelectronic properties. Journal of Materials Science - Materials in Electronics 2013(8):1492.

93. Tahir D, Tougaard S. Electronic and optical properties of Cu, CuO and Cu_2O studied by electron spectroscopy. Journal of Physics Condensed Matter 2012 / 05 / 02 /;24(17).

94. Izaki M. Effects of annealing on optical and electrical characteristics of p-type semiconductor copper (II) oxide electrodeposits. Thin Solid Films 2012;520:2434-7.

95. Copper Development Association. Equilibrium diagrams - CDA publication no 94. ; 1992.

96. Xu CH, Woo CH, Shi SQ. Formation of CuO nanowires on cu foil. Chemical Physical Letters 2004(399):62-66.

97. Adegboyega GA. An investigation of copper oxide films for photovoltaic applications. Solar & Wind Technology 1985;2(3/4):191-4.

98. Hansen BJ, Lu G, Chen J. Short-circuit diffusion of long bi-crystal CuO nanowires. Journal of Nanomaterials 2008(Special Issue 1):1-45.

99. Mema R, Yuan L, Du Q, Wang Y, Zhou G. Effect of surface stresses on CuO nanowire growth in the thermal oxidation of copper. Chemical Physical Letters 2011(512):87-91.

100. Hansen BJ, Lu G, Chen J. Direct oxidation growth of CuO nanowires from copper-containing substrates. Journal of Nanomaterials 2008(Special Issue 1):1-7.

101. Allam NK, Grimes CA. Electrochemical fabrication of complex copper oxide nanoarchitectures via copper anodization in aqueous and non-aqueous electrolytes. Mat Lett 2011;65(12):1949-55.

102. Caballero-Briones F, Palacios-Padros A, Calzadilla O, Sanz F. Evidence and analysis of parallel growth mechanisms in Cu2O films prepared by cu anodization. Electrochim Acta 2010;55(14):4353-8.

103. Singh DP, Neti NR, Sinha ASK, Srivastava ON. Growth of different nanostructures of Cu_2O (nanothreads, nanowires, and nanocubes) by simple electrolysis based oxidation of copper. J Phys Chem C 2007;111:1638-45.

104. Suntola T. Atomic layer epitaxy. Mater Sci Rep 1989;4(5):261-312.

105. Kim H, Lee HBR, Maeng WJ. Applications of atomic layer deposition to nanofabrication and emerging nanodevices. Thin Solid Films 2009 02/27;517(8):2563-80.

106. Global Market for Atomic Layer Deposition to Be Worth $978 Million In 2014 [Internet]: BCC Research; c2010 [cited 2014 . Available from: http://bccresearch.wordpress.com/2010/02/04/global-market-for-atomic-layer-deposition-to-be-worth-978-million-in-2014/.

107. Gordon RG, Hausmann D, Kim E, Shepard J. A kinetic model for step coverage by atomic layer deposition in narrow holes or trenches. Chemical Vapor Deposition 2003;9(2):73-8.

108. Rose M, Bartha JW. Method to determine the sticking coefficient of precursor molecules in atomic layer deposition. Appl Surf Sci 2009;255(13-14):6620-3.

109. Elam JW, Routkevitch D, Mardilovich PP, George SM. Conformal coating on ultrahigh-aspect-ratio nanopores of anodic alumina by atomic layer deposition. CHEMISTRY OF MATERIALS 2003;15(18):3507-17.

110. Pakkala A, Putkonen M. Atomic layer deposition. In: K. Seshan, editor. Handbook of deposition techniques for film and coatings. 3rd Edition ed. United States: Elsevier Inc.; 2009 .

111. Tynell T, Yamauchi H, Karppinen M, Okazaki R, Terasaki I. Electron doping of ALD-grown ZnO thin films through al and P substitutions. J Mater Sci 2013 / 04 / 01 /;48(7):2806-11.

112. Weinreich W, Wilde L, Muller J, Sundqvist J, Erben E, Heitmann J, Lemberger M, Bauer AJ. Structural properties of as deposited and annealed ZrO2 influenced by atomic layer deposition, substrate, and doping. Journal of Vacuum Science & Technology A 2013;31(1).

113. Callister WDJ. Materials science and engineering an introduction. 5th Edition ed. USA: John Wiley & Sons; 2000. .

114. Zeghbroeck BV. Principles of semiconductor devices; 2011 .

115. Abdu Y, Musa AO. Copper (I) oxide (Cu_2O) based solar cells - A review. Bayero Journal of Pure and Applied Sciences 2009;2(2):8-12.

116. Anopore Inorganic Membranes. Whatman [Internet]: General Laboratory Supply; c2014 [cited 2014 09/01/2014]. Available from: http://www.gogenlab.com/products/anopore(r)-inorganic-membranes-whatman.

117. Rahimi MH, Tabaian SH, Marashi SPH, Amiri M, Dalaly MM, Saramad S, Ramazani A, Zolfaghari A. The effect of aluminum electropolishing on nano-pores arrangement in anodic alumina membranes. International Journal of Modern Physics B: Condensed Matter Physics; Statistical Physics; Applied Physics 2008 07/30;22(18):3267-77.

118. Solache-Carranco H, Juárez-Díaz G, Esparza-García A, Briseño-García M, Galván-Arellano M, Martínez-Juárez J, Romero-Paredes G, Peña-Sierra R. Photoluminescence and X-ray diffraction studies on Cu_2O. J Lumin 2009 12;129(12):1483-7.

119. Chopra KL, Major S, Pandya DK. Transparent conductors - A status review. Thin Solid Films 1983;102:1-46.

120. Liu H, Avrutin V, Izyumskaya N, Ozgur U, MorKoc H. Transparent conducting oxides for electrode applications in light emitting and absorbing devices. Superlattices and Microstructures 2010;48:458-84.

121. Exarhos GJ, Zhou XD. Discovery-based design of transparent conducting oxide films. Thin Solid Films 2007;515:7025-52.

122. Zhou YW, Liu X, Wu FY, Zhang CK, Zhang XY. The characteristics of $Cd_xSn_{1-x}O$ films prepared by RF magnetron sputtering from powder targets. Surface and Coatings Technology 2013 / 08 / 15 /;228:S150-4.

123. Faÿ S, Steinhauser J, Oliveira N, Vallat-Sauvain E, Ballif C. Opto-electronic properties of rough LP-CVD ZnO:B for use as TCO in thin-film silicon solar cells. Thin Solid Films 2007 / 10 / 15 /;515(24):8558-61.

124. Song D-, Shin K-, Kim Y-, Choi Y-, Choi I-, Han J-. Low temperature synthesis of al doped ZnO thin films by facing target sputtering. Surface and Coatings Technology 2013 / 08 / 15 /;228:S101-6.

125. Wong LM, Chiam SY, Pan JS, Wang SJ, Chim WK. Highly conductive and transparent aluminum-doped zinc oxide thin films deposited on polyethylene terephthalate substrates by pulsed laser deposition. Thin Solid Films 2013 / 10 / 31 /;545:285-90.

126. Zhang MY, Nian Q, Cheng GJ. Room temperature deposition of alumina-doped zinc oxide on flexible substrates by direct pulsed laser recrystallization. Appl Phys Lett 2012;100(15).

127. Lee S, Cheon D, Kim WJ, Ham MH, Lee W. Ga-doped ZnO films deposited with varying sputtering powers and substrate temperatures by pulsed DC magnetron sputtering and their property improvement potentials. Appl Surf Sci 2012;258(17):6537-44.

128. Ahn KJ, Park JH, Shin BK, Lee W, Yeom GY, Myoung JM. Effect of sputtering power on the properties of ZnO:Ga transparent conductive oxide films deposited by pulsed DC magnetron sputtering with a rotating cylindrical target. Appl Surf Sci 2013;271:216-22.

129. Ynineb F, Hafdallah A, Aida MS, Attaf N, Bougdira J, Rinnert H, Rahmane S. Influence of sn content on properties of ZnO:SnO_2 thin films deposited by ultrasonic spray pyrolysis. Materials Science in Semiconductor Processing 2013 / 01 / 01 /;16(6):2021-7.

130. Seo YJ, Sung CH, Anwar MS, Heo SN, Kim GW, Koo BH, Kil GS, Park DW. Structure and properties of transparent conductive sb 2O 5-doped SnO_2 thin films fabricated by using pulsed laser deposition. Journal of the Korean Physical Society 2012 / 05 / 01 /;60(10):1543-7.

131. Braga A, Baratto C, Sberveglieri G, Bontempi E, Colombi P. Transparent front contact optimization in dye sensitized solar cells: Use of cadmium stannate and titanium oxide by sputtering. Thin Solid Films 2013 / 01 / 01 /.

132. Chen XL, Geng XH, Xue JM, Li LN. Two-step growth of ZnO films with high conductivity and high roughness. Journal of Crystal Growth 2007(1):77.

133. Bhachu DS, Waugh MR, Zeissler K, Branford WR, Parkin IP. Textured fluorine-doped tin dioxide films formed by chemical vapour deposition. Chemistry-A European Journal 2011;17(41):11613-21.

134. Beena D, Vinodkumar R, Navas I, Ganesan V, Yamuna A, Pillai V. Transparent conducting indium molybdenum oxide films by pulsed laser ablation. J Alloys Compounds 2012; 539: 63-8.

135. Hu P, Li B, Feng L, Wu J, Jiang H, Yang H, Xiao X. Effects of the substrate temperature on the properties of CdTe thin films deposited by pulsed laser deposition. Surf Coat Technol 2012 12;213:84-9.

136. Aklilu M, Tai Y. Self-assembled monolayers assisted thin film growth of aluminum doped zinc oxide by spray pyrolysis method. Appl Surf Sci 2013 / 01 / 01 /.

137. Goetzberger A, Hoffmann VU. Photovoltaic solar energy generation. Germany: Springer-Verlag GmbH; 2005. .

138. El Chaar L, Lamont LA, El Zein N. Review of photovoltaic technologies. Renewable and Sustainable Energy Reviews 2011;15:2 165-75.

139. Krüger T. On the origin of the staebler-wronski effect. J Appl Phys 2006 03/15;99(6):063509.

140. Wei HM, Gong HB, Chen L, Zi M, Cao BQ. Photovoltaic efficiency enhancement of Cu_2O solar cells achieved by controlling homojunction orientation and surface microstructure. The Journal of Physical Chemistry - Part C 2012;116:10510-5.

141. Nishi Y, Miyata T, Nomoto J, Minami T. Influence of Cu_2O surface treatment on the photovoltaic properties of al-doped ZnO/Cu_2O solar cells. Thin Solid Films 2012; 520(10): 3819-22.

142. Minami T, Nishi Y, Miyata T, Nomoto J. High-efficiency oxide solar cells with ZnO/Cu_2O heterojunction fabricated on thermally oxidized Cu_2O sheets. Applied Physics Express 2011;4:062301-3.

143. Aarik J, Aidla A, Uustare T, Ritala M, Leskelä M. Titanium isopropoxide as a precursor for atomic layer deposition: Characterization of titanium dioxide growth process. Appl Surf Sci 2000 7/2;161(3-4):385-95.

144. Cao G, Liu D. Template-based synthesis of nanorod, nanowire, and nanotube arrays. Adv Colloid Interface Sci 2008 01/15;136(1-2):45-64.

145. Zhao Q, Wen G, Liu Z, Yuan J, Li D, Zou G, Zheng R, Ringer SP, Mao H. High-density, vertically aligned crystalline CrO_2 nanorod arrays derived from chemical vapor deposition assisted by AAO templates. Chemical Communications: Chem Comm 2009 07/14;2009(26):3949-51.

146. Morant C, Márquez F, Campo T, Sanz JM, Elizalde E. Niobium and hafnium grown on porous membranes. Thin Solid Films 2010 09/30;518(23):6799-803.

147. Peng X-, Zhang X, Yu L, Zhou LI. Preparation And Photoluminescence Properties of $NdVo_4$ Nanotubes In AAO Template. Modern Physics Letters B 2009 08/30;23(22):2647.

148. Lee J, Ju HK, Lee JK, Kim HS, Lee J. Atomic layer deposition of TiO_2 nanotubes and its improved electrostatic capacitance. Electrochemistry Communications 2010 02;12(2):210.

149. Foong TRB, Shen Y, Hu X, Sellinger A. Template-directed liquid ALD growth of TiO_2 nanotube arrays: Properties and potential in photovoltaic devices. Advanced Functional Materials 2010 05/10;20(9):1390.

150. ASTM International. ASTM E112 - 10 standard test methods for determining average grain size. ; 2010.

151. Li S, Zhang G, Guo D, Yu L, Zhang W. Anodization fabrication of highly ordered TiO_2 nanotubes. Journal of Physical Chemistry C 2009 / 07 / 23 /;113(29):12759-65.

152. Babonneau F, Doeuff S, Leaustic A, Sanchez C, Cartier C, Verdaguer M. XANES and EXAFS study of titanium alkoxides. Inorg Chem 1988;27(18):3166-72.

153. Whatman Anodisc Filter Membranes [Internet]; c2014 [cited 2014 01/09]. Available from: http://www.fishersci.com/ecomm/servlet/fsproductdetail_10652_600468__-1_0.

154. Pettit FS. Surface engineering of copper and copper alloys. In: Surface engineering, vol 5, ASM handbook. ASM International; 1994. .

155. Hansen BJ, Chan HL, Lu JA, Lu GH, Chen JH. Short-circuit diffusion growth of long bi-crystal CuO nanowires. Chemical Physics Letters 2011;504(1-3):41-5.

156. Musa AO, Akomolafe T, Carter MJ. Production of cuprous oxide, a solar cell material, by thermal oxidation and study of its physical and electrical properties. Sol En Mater & Sol Cells 1998(51):305-16.

157. Gonçalves AMB, Campos LC, Ferlauto AS, Lacerda RG. On the growth and electrical characterization of CuO nanowires by thermal oxidation. J Appl Phys 2009 08;106(3):034303-8.

158. Allam NK, Grimes CA. Effect of cathode material on the morphology and photoelectrochemical properties of vertically oriented TiO_2 nanotube arrays. Solar Energy Mater Solar Cells 2008;92(11):1468-75.

159. Swanson T. Cubic cu XRD. U.S.: Natl. Bur. Stand.; 1953. Report nr 539, I.

160. Swanson T. Cu2O (cuprite) XRD. U.S.: Natl. Bur. Stand.; 1953. Report nr 539, II.

161. Schmahl NG, Eikerling GF. Tenorite (CuO) XRD. Z. Phys. Chem. Neue Folge. (Wiesbaden); 1968. Report nr 62.

162. Frondel C. Paramelaconite XRD. U.S.: Am. Mineral.; 1941. Report nr 26, 664.

163. Robinson P. Properties of wrought coppers and copper alloys, properties and selection: Nonferrous alloys and special-purpose materials. In: ASM handbook, vol 2. ASM International; 1990. .

164. Danielewski M. Introduction to fundamentals of corrosion in gases, Corrosion: Fundamentals, testing, and protection. In: ASM handbook, vol. 13A. ASM International; 2003. .

165. Her Y, Chiang C, Jean S, Huang S. Self-catalytic growth of hierarchical In_2O_3 nanostructures on SnO_2 nanowires and their CO sensing properties. CrystEngComm 2012;14(4):1296-300.

166. Hsu Y, Lu S. Vapor-solid growth of sn nanowires: Growth mechanism and superconductivity. J Phys Chem B 2005 03/01; 2012/09;109(10):4398-403.

167. Yuan L, Wang Y, Mema R, Zhou G. Driving force and growth mechanism for spontaneous oxide nanowire formation during thermal oxidation of metals. Acta Materialia 2011;59(6):2491-500.

168. Kaur M, Muthe KP, Despande SK, Choudhury S, Singh JB, Verma N, Gupta SK, Yakhmi JV. Growth and branching of CuO nanowires by thermal oxidation of copper. Journal of Crystal Growth 2006(289):670-5.

169. Wang Y, Shen R, Jin X, Zhu P, Ye Y, Hu Y. Formation of CuO nanowires by thermal annealing copper film deposited on Ti/Si substrate. Appl Surf Sci 2011;258:201-6.

170. ASM International. Metals handbook. In: J. R. Davis, editor. ASM desk editions. ASM International; 2000. .

171. Sigma-Aldrich. Copper (I) oxide MSDS. Sigma-Aldrich; 2012.

172. Sigma-Aldrich. Copper (II) oxide MSDS. Sigma-Aldrich; 2012.

173. Zhu Y, Mimura K, Lim J, Isshiki M, Jiang Q. Brief review of oxidation kinetics of copper at 350 °Cto 1050 °C. Metallurgical and Materials Transactions A 2006;37A:1231-7.

174. Steinhauer S, Brunet E, Maier T, G.C. Mutinati, Köck A, W.-D. Schubert, Edtmaier C, Gspan C, Grogger W. Synthesis of high-aspect-ratio CuO nanowires for conductometric gas sensing. Procedia Engineering 2011;25:1477-80.

175. Chen JT, Zhang F, Wang J, Zhang GA, Miao BB, Fan XY, Yan D, Yan PX. CuO nanowires synthesized by thermal oxidation route. J Alloys Compounds 2008;454:268-73.

176. Roylance D. Stress-strain curves. 2001.

177. Chen JT, Zhang F, Wang J, Zhang GA, Miao BB, Fan XY, Yan D, Yan PX. CuO nanowires synthesized by thermal oxidation route. Journal of Alloys and Compounds 2008(454):268-73.

178. Elam JW, George SM. Growth of ZnO/Al_2O_3 alloy films using atomic layer deposition techniques. Chemistry of Materials 2003;15(4):1020-8.

179. Ferguson JD, Weimer AW, George SM. Atomic layer deposition of Al_2O_3 films on polyethylene particles. Chemistry of Materials 2004;16(26):5602-9.

180. Oh B, Kim J, Han J, Seo D, Jang HS, Choi H, Baek S, Kim JH, Heo G, Kim T, et al. Transparent conductive ZnO:Al films grown by atomic layer deposition for si-wire-based solar cells. Current Applied Physics 2012;12:273-9.

181. ASM International. Engineering tables: Ceramics and glasses. In: ASM desk editions: Engineered materials handbook. ; 2002. .

182. ASM International. Properties of pure metals: Cu. In: ASM handbook. 2nd Edition ed. ; 2002. .

183. ASM International. Gaseous corrosion mechanisms: Stresses in scales. In: 2nd Edition ed. ; 2005.

184. Adem E. VG scientific XPS handbook. VG Scientific; 1991. .

185. Debbichi L, de Lucas, M. C. M., Pierson JF, Kruger P. Vibrational properties of CuO and Cu_4O_3 from first-principles calculations, and raman and infrared spectroscopy. Journal of Physical Chemistry C 2012 05/10;116(18):10232-7.

186. Hardcastle FD, Ishihara H, Sharma R, Biris AS. Photoelectroactivity and raman spectroscopy of anodized titania (TiO_2) photoactive water-splitting catalysts as a

function of oxygen-annealing temperature. Journal of Materials Chemistry 2011;21(17):6337-45.

187. Yvon K, Jeitschko W, Parthe E. ZnO (zincite) P63MC XRD pattern. Journal of Applied Crystallography 1977;10(73).

188. Bosio A, Romeo N, Mazzamuto S, Canevari V. Polycrystalline CdTe thin films for photovoltaic applications. Progress In Crystal Growth And Characterization Of Materials 2006;52(4):247-79.

189. Jones AC, Chalker PR. Some recent developments in the chemical vapour deposition of electroceramic oxides. Journal Of Physics D-Applied Physics 2003;36(6):R80-95.

190. Ritala M, Leskelä M, Dekker J-, Mutsaers C, Soininen PJ, Skarp J. Perfectly conformal TiN and Al2O3 films deposited by atomic layer deposition. Chemical Vapor Deposition 1999 / 01 / 01 /;5(1):7-9.

191. Saito K, Hiratsuka Y, Omata A, Makino H, Kishimoto S, Yamamoto T, Horiuchi N, Hirayama H. Atomic layer deposition and characterization of ga-doped ZnO thin films. Superlattices and Microstructures 2007;42(-):172-5.

192. Materials research society symposium proceedings, 1315; 2012; ; 2012. .

193. Irvine SJC, Barrioz V, Lamb D, Jones EW, Rowlands-Jones R. MOCVD of thin film photovoltaic solar cells-next-generation production technology? J Cryst Growth 2008 / 11 / 15 /;310(23):5198-203.

194. Materials research society symposium proceedings 1012; 2007; 2007.

195. Barrioz V, Irvine SJC, Jones EW, Rowlands RL, Lamb DA. In situ deposition of cadmium chloride films using MOCVD for CdTe solar cells. Thin Solid Films 2007 / 05 / 31 /;515(15):5808-13.

196. Hu J, Gordon RG. Atmospheric pressure chemical vapor deposition of gallium doped zinc oxide thin films from diethyl zinc, water, and triethyl gallium. J Appl Phys 1992 12;72(11):5381.

197. Burstein E. Anomalous optical absorption limit in InSb [4]. Physical Review 1954 / 01 / 01 /;93(3):632-3.

198. Moss T. Optical properties of semiconductors. New York: Academic Press; 1961. .

199. Sans JA, Segura A, Sánchez-Royo JF, Barber V, Hernández-Fenollosa MA, Marí B. Correlation between optical and transport properties of ga-doped ZnO thin films prepared by pulsed laser deposition. Superlattices and Microstructures 2006;39(-):282-90.

200. ASM International. General information and data: Engineering tables - ceramics and glasses. In: ASM engineered materials handbook. 2nd Edition ed. ; 2002 .

201. Farm E, Kemell M, Ritala M, Leskela M. Selective-area atomic layer deposition using poly(methyl methacrylate) films as mask layers. Journal of Physical Chemistry C 2008(112):15791-5.

202. Farm E, Kemell M, Ritala M, Leskela M. Selective-area atomic layer deposition with microcontact printed self-assembled octadecyltrichlorosilane monolayers as mask layers. Thin Solid Films 2008;517(2):972-5

9 Appendix 1. Geometric factors, surface areas and predicted mass gains

9.1 Geometric model of AAO structures

A set of equations was devised to allow various parameters to be calculated using the mass gain of the samples after ALD onto nanostructured surfaces.

9.1.1 Porosity and Number of Pores

The pore arrangement for a perfectly ordered AAO template can be seen in Figure 114.

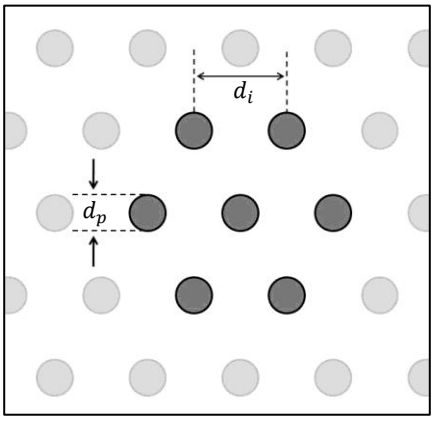

Figure 114: Pore arrangement for a perfectly ordered AAO template

Following on from the anodisation of an Al sample a regular hexagonal porous structure is produced with the interpore spacing, pore diameter and pore density controlled by the voltage and electrolyte used. The thickness of the oxide, and hence the depth of the pores, is controlled by the duration of the anodisation.

The cross sectional area of each pore is defined by the equation:

$$A_{pore} = \pi \left(\frac{d_p}{2}\right)^2$$

For a circular AAO template, the area of the sample upper surface (excluding pores) is:

$$A_{template} = \pi R^2$$

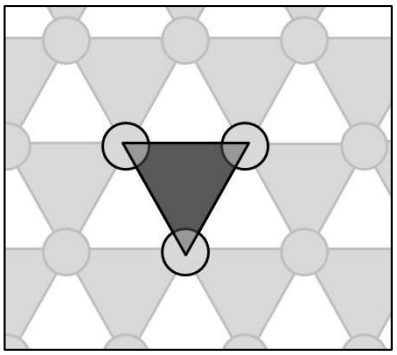

Figure 115: Diagram used to calculate the total number of pores

The shaded triangle shown in Figure 115 has an area of:

$$A_{triangle} = \frac{1}{2} \times base \times height = \frac{1}{2} d_i d_i \sin 60 = \frac{\sqrt{3}}{4} {d_i}^2$$

This area includes the area of 3 x 1/6 pores. Therefore 1 pore is contained in an area of $\frac{\sqrt{3}}{2} {d_i}^2$. From this the number of pores in the total surface area can be derived by dividing the total upper surface area by the area associated with one pore:

$$n = (\pi R^2) \Big/ \left(\frac{\sqrt{3}}{2} {d_i}^2 \right) = \frac{2\pi R^2}{\sqrt{3} {d_i}^2}$$

Porosity is defined as the ratio of apparent volume to the volume of voids, in this case pores. Since for an ideal template the voids all extend perpendicularly down from the surface, the porosity can be calculated from a consideration of the respective areas of a thin slice of the template parallel to the template surface.

$$\alpha = \frac{area\ of\ pores}{apparent\ area} = \left[n\pi \left(\frac{d_p}{2} \right)^2 \right] \Big/ (\pi R^2)$$

$$\alpha = \frac{\left(\frac{2\pi R^2}{\sqrt{3} {d_i}^2} \right) \pi \left(\frac{d_p}{2} \right)^2}{\pi R^2} = \frac{2\pi R^2 \pi {d_p}^2}{4\sqrt{3} {d_i}^2 \pi R^2} = \frac{\pi}{2\sqrt{3}} \left(\frac{d_p}{d_i} \right)^2$$

9.1.2 Porosity of AAO Templates Derived from Mass Measurements

Commercial through-hole AAO templates with an average pore diameter of 100nm, template diameter of 1.2cm and thickness of 60µm were purchased from Whatman. Having undergone a single anodisation cycle the template geometry was less than ideal, with very few hexagonally coordinated pores resulting in a wide distribution of interpore distances.

A solid amorphous Al_2O_3 disc with the same thickness and diameter as the purchased templates would have a mass of 0.03154g assuming an alumina density of 3.96g/cm^3 [200]. The average mass of the AAO templates was found to be 0.01247g. The average porosity could then be found:

$$\alpha = \frac{mass\ of\ porous\ template}{mass\ of\ solid\ template} = \frac{0.01247}{0.03154} = 0.395$$

Rearranging the porosity equation to make d_i the subject gives:

$$d_i = \sqrt{\frac{\pi {d_p}^2}{2\sqrt{3}\alpha}}$$

This gives the average interpore distance for the 100nm pore diameter templates as 152nm.

9.1.3 AAO Template Surface Areas

ALD requires that there are a high enough number of precursor molecules to completely saturate a surface. For high aspect ratio structures some consideration of the surface area is necessary as it can be high enough to dictate the amount of precursor gas required to achieve a conformal coating.

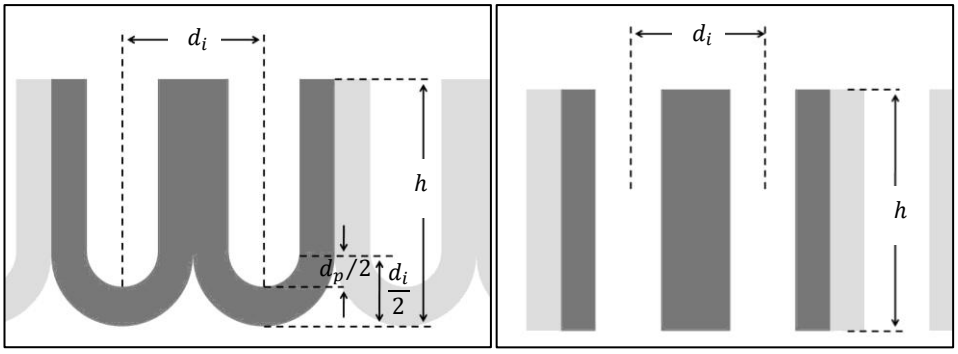

Figure 116: Left - Notation for closed AAO templates, Right - Notation for through-hole AAO

For closed templates (Figure 116) the area of the template upper surface is:

$$A_{upper} = \pi R^2 - n\pi\left(\frac{d_p}{2}\right)^2 = \pi R^2\left(1 - \frac{\pi}{2\sqrt{3}}\left(\frac{d_p}{d_i}\right)^2\right) = \pi R^2(1-\alpha)$$

The area of the lower surface can be approximated as:

$$A_{lower} = \pi R^2$$

The combined surface area of the cylindrical pores is:

$$A_{pores} = n\pi d_p\left(h - \frac{d_i}{2}\right) = \frac{\pi^2 d_p R^2}{\sqrt{3}d_i}\left(\frac{2h}{d_i} - 1\right)$$

The surface area of the hemispherical pore bases is:

$$A_{hemispheres} = 2n\pi\left(\frac{d_p}{2}\right)^2 = \frac{\pi^2 R^2 {d_p}^2}{\sqrt{3}{d_i}^2}$$

The total surface area on which ALD will occur is:

$$A_{total} = A_{upper} + A_{lower} + A_{pores} + A_{hemispheres}$$

Using typical values, i.e. d_p = 100nm, d_i = 152nm, R = 6.5cm, h = 60µm and α = 0.395 the above equations give the following values:

$$A_{upper} = 8.063 \times 10^{-5}\text{m}^2$$

$$A_{lower} = 1.327 \times 10^{-4}\text{m}^2$$

$$A_{pores} = 0.125\ \text{m}^2$$

$$A_{hemisphere} = 1.042 \times 10^{-4}\text{m}^2$$

From the above results it is clear that the pore surface area is the dominant term for high aspect ratio templates, i.e. when $h \gg d_i$ and d_p. Therefore, for the calculation of surface area the upper and lowers surfaces as well as the hemisphere terms can be counted as negligible.

For through-hole templates the same treatment can be applied:

$$A_{upper} = A_{lower} = \pi R^2(1-\alpha)$$

$$A_{pores} = \frac{2\pi^2 d_p h R^2}{\sqrt{3}{d_i}^2}$$

The total surface area on which ALD will occur is:

$$A_{total} = 2A_{upper} + A_{pores}$$

Using the same standard values as before, these equations give:

$$2A_{upper} = 1.606 \times 10^{-4}\text{m}^2$$

$$A_{pores} = 0.125\ \text{m}^2$$

Again, the surface area of the pores is the dominant term. For the surface area equations for closed and through-hole templates, a good approximation of the surface area can therefore be found by using the equation:

$$A_{pores} = \frac{2\pi^2 d_p h R^2}{\sqrt{3}{d_i}^2}.$$

9.1.4 Mass Gain During ALD and Estimation of Coating Depth

For a given thickness and density of deposited material the increase in mass can be estimated for a complete conformal coating. Using a similar technique to that above, the mass increase can be calculated for depositions where $t \leq d_p/2$:

$$M_{total} = M_{upper} + M_{lower} + M_{torii} + M_{pores} + M_{hemispheres}$$

$$M_{total} = \left[\rho t\left(\pi R^2 - n\pi\frac{{d_p}^2}{4}\right)\right] + [\rho t\pi R^2] + \left[\frac{1}{2}\rho n\pi^2 d_p t^2\right] + \left[\rho n\pi h\left(d_p t - t^2\right)\right] + \left[\frac{2}{3}\rho n\pi\left(\left(\frac{d_p}{2}\right)^3 - \left(\frac{d_p - 2t}{2}\right)^3\right)\right]$$

Using the same values as previously, also including a deposition thickness of t = 20nm and a density of 4.23g/cm^3 gives:

$$M_{upper} = 6.821 \times 10^{-6}\text{g}$$

$$M_{lower} = 1.123 \times 10^{-5}\text{g}$$

$$M_{tori} = 5.539 \times 10^{-6}\text{g}$$

$$M_{pores} = 8.463 \times 10^{-3}\text{g}$$

$$M_{hemispheres} = 5.759 \times 10^{-6}\text{g}$$

As with before, the mass increase associated with the pores is the dominant term, accounting for over 99% of the mass gain. A reasonable estimate for the mass gain can therefore be calculated from:

$$M = \rho n\pi h\left(d_p t - t^2\right)$$

The depth of coating in the pores can be estimated after a successful ALD process, on the proviso that the following assumptions have been satisfied:

- True ALD has occurred in the template, with no PVD or CVD component.
- Deposition into the pores is diffusion limited, i.e. the sticking coefficient of precursor molecules is much greater than the hopping coefficient.
- Partial coating of the pores results in preferential deposition at the pore openings, filling them in from the surface inwards.
- Coating occurs equally at both upper and lower surfaces and equally at both ends of the pores.
- No loss of template material occurs during ALD process, such as water vapour, dissolved acid molecules etc.

For through-hole templates, calculation of the maximum mass increase for a given thickness of deposition compared to the measured mass increase gives the depth percentage from each surface:

$$\%Ingress = \frac{M_{measured}}{M_{max}} \times 50$$

$$Penetration\ depth = \frac{M_{measured} h}{2M_{max}} = \frac{M_{measured}}{2\rho n\pi\left(d_p t - t^2\right)}$$

9.1.5 Estimation of Exposure Required for Conformal Coating

Gordon *et al.* proposed the following equations to find the minimum exposure required to achieve a conformal coating in a single ALD cycle[(107)].

For a planar surface;

$$Pt = S\sqrt{2\pi mkT}$$

where P = partial pressure of precursor near the surface (Pa), t = time (s), S = saturation dose (m^{-2}), m = molecular mass (kg), k = Boltzmann's constant ($1.38 \times 10^{-23} JK^{-1}$) and T = temperature (K).

The molecular mass of $Ti(O^iPr)_4$ is 283.9g/mol [143] or 4.7144×10^{-25}kg/molecule

For deposition of TiO_2 using $Ti(O^iPr)_4$ and H_2O at 225°C this gives:

$$\frac{Pt}{S} = \sqrt{2\pi \times (4.7144 \times 10^{-25}) \times 1.38 \times 10^{-23} \times (225 + 273)} = 1.4268 \times 10^{-22} \text{ N.s}$$

Presuming a value of S based on the diameter of a $Ti(O^iPr)_4$ (0.6Å [152]), and presuming a spherical packing constant of 0.7405 gives:

$$S = \frac{1}{\pi(0.3 \times 10^{-10})^2} \times 0.7405 = 2.6190 \times 10^{20} \text{m}^{-2}$$

This gives the required exposure to coat a planar surface as:

$Pt = 2.6190 \times 10^{20} \times 1.4268 \times 10^{-22} = 3.737 \times 10^{-2}$Pa.s or 2.8028×10^{-4} torr.s. This gives the required exposure as 0.28mtorr for 1 second or 1torr for 0.28ms.

For a high aspect ratio structure;

$$Pt = S\sqrt{2\pi mkT}\left(1 + \frac{19a}{4} + \frac{3a^2}{2}\right)$$

where a = the aspect ratio = h/d_p. For the 100nm and 200nm pore diameter templates used, the aspect ratios are 600 and 300 respectively. For the former, this gives a minimum exposure of 20.286×10^3 Pa.s (152.2torr.s). For the latter a minimum exposure of 5.098×10^3Pa.s (38.2torr.s) is required.

The equation for minimum exposure per cycle required to achieve a conformal coating proposed by Elam *et al.* is[109]:

$$Pt = 2.3 \times 10^{-7}\sqrt{amu}\,\tau\left(\frac{l}{d_p}\right)^2$$

Where Pt has units of torr.s, amu is in amu and τ has units of 10^{15}cm^{-2}.

Converting to S.I. units gives:

$$Pt = 7.524 \times 10^{-11}\sqrt{m}\, S\left(\frac{h}{d_p}\right)^2$$

Using the same estimated values as previously gives:

$$Pt = (7.524 \times 10^{-11}) \times \sqrt{4.7144 \times 10^{-25}} \times (2.6190 \times 10^{20}) \times \left(\frac{60\times10^{-6}}{100\times10^{-9}}\right)^2 = 4871\text{Pa.s}$$

(36.53 torr.s) for the 100nm pores and 9.13torr.s for the 200nm pores.

These estimates are within roughly the same order of magnitude as the previous equations and suggest that high partial pressures of precursor gases are required to obtain a conformal coating if cycle times are to be kept reasonably short. Usual reactor exposures are roughly 0.1torr.s or less, more than a factor of 10 lower than that required for HAR depositions.

9.2 Through-hole AAO Pn-junction surface area model: design 1

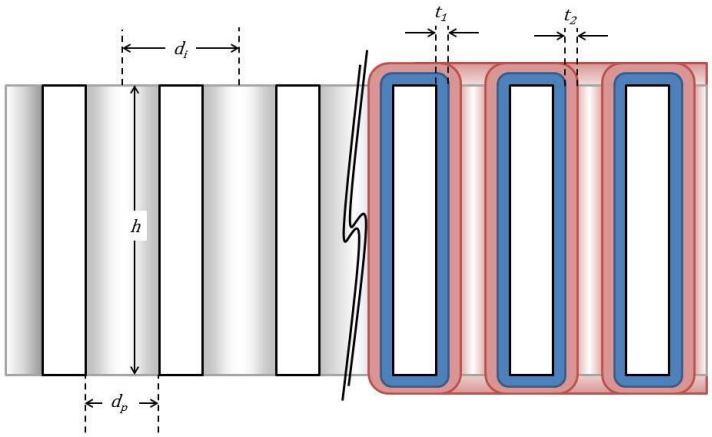

Figure 117: Deposition of n and p-type semiconductor materials onto through-hole AAO

In this model, ALD of p and n type materials onto perfectly regular hexagonally arranged pores in AAO is considered (Figure 117).

The surface area of the structure on the left has already been shown to approximate:

$$A_{total} = 2A_{upper} + A_{pores}$$

Which can be rearranged to:

$$A_{total} = \pi R^2 \left(2 + \frac{\pi d_p}{\sqrt{3}{d_i}^2}\left[2h - d_p\right]\right)$$

Since πR^2 is the apparent upper or lower surface area, the surface area per unit apparent area (A_{unit}) is:

$$A_{unit} = 2 + \frac{\pi d_p}{\sqrt{3}{d_i}^2}\left[2h - d_p\right]$$

If a conformal coating of an n type material with a thickness of t_1 is applied to the template, the available surface area will change. d_p becomes $d_p - 2t_1$, d_i remains unchanged and h becomes $h + 2t_1$, assuming a right angled edge at the upper and lower surfaces.

By applying the same methodology as used for the determination of the AAO surface area the new surface area can be calculated:

$$A_{total_n} = 2A_{upper_n} + A_{pores_n}$$

The number of pores is:

$$n = \frac{2\pi R^2}{\sqrt{3}{d_i}^2}$$

The new surface areas within the pores and at the upper and lower surfaces are:

$$A_{pores_n} = n\pi\left(d_p - 2t_1\right)(h + 2t_1)$$

$$A_{upper_n} = \pi R^2 - n\pi\left(\frac{d_p - 2t_1}{2}\right)^2$$

Combining and rearranging these equations gives:

$$A_{total_n} = \pi R^2 \left(\frac{2\pi}{\sqrt{3}{d_i}^2} \left[d_p h - 2t_1 h - 2{t_1}^2 - \frac{{d_p}^2}{2} \right] \right)$$

$$A_{unit_n} = \frac{2\pi}{\sqrt{3}{d_i}^2} \left(d_p h - 2t_1 h - 2{t_1}^2 - \frac{{d_p}^2}{2} \right)$$

Conformal deposition of a p-type material on top of this n-type layer would give a pn-junction with an interface area = A_{unit_n} (m/m).

9.3 Through-hole AAO Pn-junction surface area model: design 2

In the second design, the surface area of the template available for deposition should be changed to allow for the fact that the pore length is shorter and that deposition of the p and n-type materials would not take place on both sides of the device. Prior the sputtering or evaporation of the back contact, the deposition area of the template would be:

$$A_{total} = 2A_{upper} + A_{pores}$$

After the sputtering of the back contact this would reduce to:

$$A_{total} = 2A_{upper} + A_{pores} - A_{sputtered}$$

where

$$A_{sputtered} = A_{upper} + n\pi d_p s_d - n\pi \left(\frac{d_p}{2} \right)^2$$

and s_d is the sputtering depth. Therefore:

$$A_{total} = A_{upper} + A_{pores} - \frac{2\pi^2 R^2 d_p s_d}{\sqrt{3} d_i^2} + n\pi \left(\frac{d_p}{2} \right)^2$$

Due to the geometry of this model,

$$A_{upper} + n\pi\left(\frac{d_p}{2}\right)^2 = \pi R^2.$$

Therefore:

$$A_{total} = \pi R^2\left(1 + \frac{2\pi d_p}{\sqrt{3}d_i^2}[h - 2s_d]\right)$$

After deposition of n-type material with a thickness = t, the available surface for the pn-junction becomes:

$$A_{total_n} = \pi R^2 + A_{pores_n} \text{ where } A_{pores_n} = 2n\pi\left(\frac{d_p - 2t}{2}\right)(h - s_d)$$

$$A_{total_n} = \pi R^2\left(1 + \frac{2\pi}{\sqrt{3}d_i^2}[d_p - 2t][h - s_d]\right)$$

9.4 Geometric model of CuO nanowires

9.4.1 Surface Area and Volume

By considering the geometry of thermally grown CuO NW samples, important substrate parameters such as surface area and surface area per unit mass could be roughly estimated. This was done using a method similar to that used for the calculation of the AAO substrate parameters. Several assumptions were made to allow the calculations to proceed; NWs arranged in a close packed uniform hexagonal lattice and equally spaced, NW base and tip diameters were circular in cross section and uniform, all NWs were the same length exhibited conical frusta geometry. These approximations are all somewhat oversimplifications and probably overestimate the number and surface area of the NW substrates.

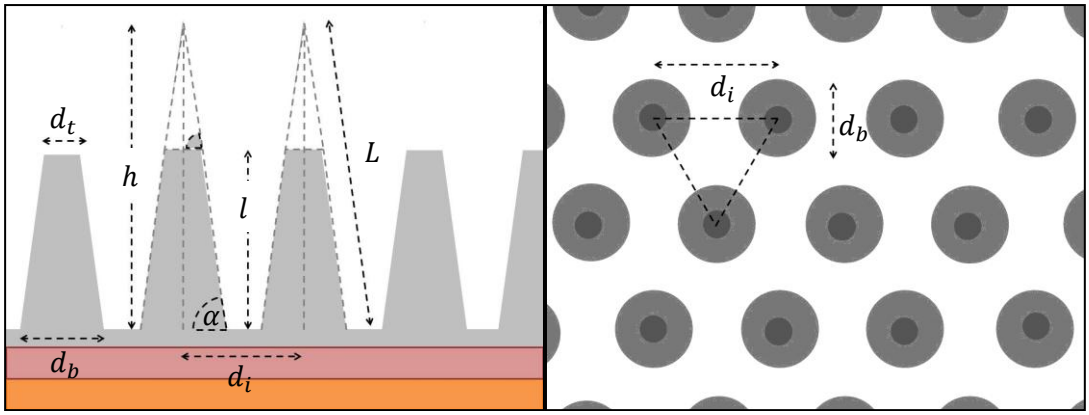

Figure 118: Schematic of Conical NW surface and associated calculation parameters

Because the CuO templates produced were to be used in conjunction with ALD of n-type semiconductor materials, it was important to determine the minimum distance between the NWs at the NW/planar CuO interface. If this distance was found to be of the same scale or smaller than the MFP of the largest of the ALD precursor molecules then any ALD process would have to be modified to increase the precursor exposure (Pa.s) and ensure a conformal coating. The average gap between the NW bases could be calculated from:

$$d_g = d_i - d_b$$

The total number of NWs on the surface could be found using either of the following equations, depending on the shape of the substrate:

Rectangular surface ($x \times y$): $N = \frac{xy}{{d_i}^2 \sin 60^\circ} = \frac{2xy}{\sqrt{3}{d_i}^2}$

Circular surface (radius = r): $N = \frac{\pi r^2}{{d_i}^2 \sin 60^\circ} = \frac{2\pi r^2}{\sqrt{3}{d_i}^2}$

The number density, i.e. the number of nanowires per unit area, could be determined from:

$$n = \frac{2 \times 10^{-4}}{\sqrt{3}{d_i}^2}$$

The total surface area of the sample was split up into three components; the area at the tip of each NW, the surface area of the conical section for each NW and the area at the planar

CuO layer associated with each NW. The sum of these gave the total surface area associated with each NW; this value multiplied by the number of NWs gave the total surface area.

$$A = N(A_b + A_w + A_t)$$

The tip area for each NW was:

$$A_t = \pi\left(\frac{d_t}{2}\right)^2$$

The area associated with the base was:

$$A_b = {d_i}^2 \sin 60° - \pi\left(\frac{d_b}{2}\right)^2 = \frac{\sqrt{3}}{2}{d_i}^2 - \pi\left(\frac{d_b}{2}\right)^2$$

For the remaining term, the surface area of a cone could be found from the equation $A = \pi\left(\frac{d_b}{2}\right)L$, where L was the length of the cone edge wall from base to tip. In the diagram above (Figure 118), each NW was represented by a cone shape with it's top section removed. To find the edge length of the full cone (L) the angle between the NW base and the substrate (α) was calculated:

$$\alpha = \tan^{-1}\left(\frac{2l}{d_b - d_t}\right)$$

From this angle, h and L can be deduced:

$$h = \frac{d_b}{2}\tan(\alpha) \text{ and } L = \sqrt{\left(\frac{d_b}{2}\right)^2 + h^2}$$

The surface area of a cone with height h and base diameter d_b can be calculated from the equation:

$$A_{w(t)} = \pi \frac{d_b}{2} L$$

Since this cone tapers up to a sharp point, the area of the top section ($A_{w(i)}$) should be removed to properly reflect the geometry shown in Figure 118:

$$A_{w(i)} = \pi \frac{d_t}{2} \sqrt{\left(\frac{d_t}{2}\right)^2 + (h-l)^2}$$

$$A_w = A_{w(t)} - A_{w(i)} = \frac{\pi}{2}\left(d_b \sqrt{\left(\frac{d_b}{2}\right)^2 + h^2} - d_t \sqrt{\left(\frac{d_t}{2}\right)^2 + (h-l)^2} \right)$$

$$A_w = \frac{\pi}{2}\left(d_b \sqrt{\left(\frac{d_b}{2}\right)^2 + \left(\frac{d_b l}{d_b - d_t}\right)^2} - d_t \sqrt{\left(\frac{d_t}{2}\right)^2 + \left(\frac{d_b l}{d_b - d_t} - l\right)^2} \right)$$

Combining the equations for A_w, A_b and A_t gives the surface area for a circular sample:

$$A = N(A_b + A_w + A_t)$$

$$A = \frac{2\pi r^2}{\sqrt{3} {d_i}^2}\left(\frac{\sqrt{3}}{2} {d_i}^2 - \pi \left(\frac{d_b}{2}\right)^2 + \frac{\pi}{2}\left(d_b \sqrt{\left(\frac{d_b}{2}\right)^2 + \left(\frac{d_b l}{d_b - d_t}\right)^2} - d_t \sqrt{\left(\frac{d_t}{2}\right)^2 + \left(\frac{d_b l}{d_b - d_t} - l\right)^2} \right) + \pi \left(\frac{d_t}{2}\right)^2 \right)$$

Using typical values, i.e. r = 0.5cm, d_i = 2µm, d_b = 500nm, d_t = 50nm and l = 50µm, the above equation gives a surface area of ~1x10^{-3}m^2 for a 1cm diameter surface. For comparison, a sample with the same diameter but without nanowires would have a surface area of around 2x10^{-5}m^2, around 50 times smaller.

10 Appendix 2. ALD Masking Device Design

The manufacture of multi-layered thin-film devices, such as photovoltaic modules, optoelectronic devices, semiconductor circuits, etc. requires care to be taken to ensure that depositions of thin-film material occur where intended, and that only layers designed to be in contact are in contact with each other to avoid problems such as short-circuits etc.. For this purpose it is common practice to use one of a variety of masks. For line-of-sight depositions, such as sputtering, MBE, CVD, PVD, masks can be used that shade the areas to be protected from the deposition. Within certain tolerances it is acceptable for the masks used to have only partial or no contact with the deposition surface, as the shadow cast by the mask inhibits deposition, limiting it to only the un-shadowed areas.

Atomic layer deposition (ALD) is a conformal deposition process in which shadowing will not work. The sequential nature of the technique causes all surfaces that come into contact with the precursor gases to be coated in the deposition material. Masks for ALD processes require complete contact with the substrate in order to prevent the precursor gases reaching areas where deposition is not wanted. For substrates with structured surfaces this can present a significant problem as the mask applied may not completely fill the structure, leaving areas where precursor reactants will be able to migrate underneath.

One method which has been demonstrated to work for planar surfaces is the use of a selective PMMA masking layer. Farm et al. spin coated thin layers of PMMA onto surfaces followed by UV lithography to selectively cure the polymer. After rinsing off the uncured PMMA, ALD of Ir, Pt, Ru, Al_2O_3 and TiO_2 was attempted and the resulting depositions characterised. For the deposition of Ir, Pt, Ru and TiO_2, the PMMA surfaces were found to passivate, limiting growth to the exposed surfaces. For Al_2O_3 growth was found to occur

across the entire upper surface of the sample but not through the PMMA layer. The masks could then be lifted off leaving the surface patterned as required [201]. The major drawbacks of the technique are the initial investment in a vacuum spin coater and UV lithography equipment, as well as the fact that the PMMA would probably not conformally coat a high aspect ratio structured surface.

Another method for masking samples during ALD is by micro-printing or selective adsorption of Self Assembled Monolayers (SAMs) [202]. This technique utilises specific compounds that will form a spontaneous adsorbed monolayer of material across the sample. The monolayer then repels one or both of the ALD precursors, inhibiting the ALD reaction at these sites. The drawback of this technique is that SAMs have to be chosen for each set of ALD precursors, as a SAM that prevents one ALD material may not prevent others. Compared to the technique mentioned above this method does have the capability to conformally coat high aspect ratio surfaces to a limited degree, although this will be restricted by factors such as how well the monolayer material is able to infiltrate the porous structure.

Several mechanical ALD masking devices were designed in Pro-Engineer Wildfire to enable the deposition of ALD material in specific areas of planar surfaces whilst leaving other areas uncoated. One design was manufactured and tested using ALD of aluminium doped zinc oxide (AZO). This material was chosen so that the effectiveness of the mask could be tested using simple conductivity measurements. It was found that deposition was limited to the exposed area of the substrate, as intended, but that the deposition that did occur showed certain CVD-like characteristics, i.e. enhanced deposition rate away from the centre of the mask. This was attributed to incomplete removal of the unreacted precursors from the recesses of the masking device.

To begin with high temperature Kapton tape was used as a mask. The tape itself could withstand the expected range of deposition temperatures (100°C - 300°C) but the tape adhesive was found to degas significantly, interfering with the deposition and causing uneven and non-conformal coating, severely limiting its usefulness. Another difficulty encountered with this method was that the tape was only available in certain sizes. Because of this masks had to be created using several pieces, cut to size and overlaying one another. Where one piece of tape was laid over another, gaps were inevitably present allowing precursors to deposit material underneath and also exposing the tape's adhesive to the reactor environment. Because of these factors, an alternative masking technique was sought. Designs for a suitable ALD mask had to fit several criteria:

- Withstand temperatures up to 300°C
- No out gassing while at high temperature and low pressure
- Maximum diameter ~150mm
- Maximum depth ~8mm
- Able to protect areas of sample from deposition, i.e. atmospherically isolated from reactor environment
- Low production cost

The following preliminary designs were proposed:

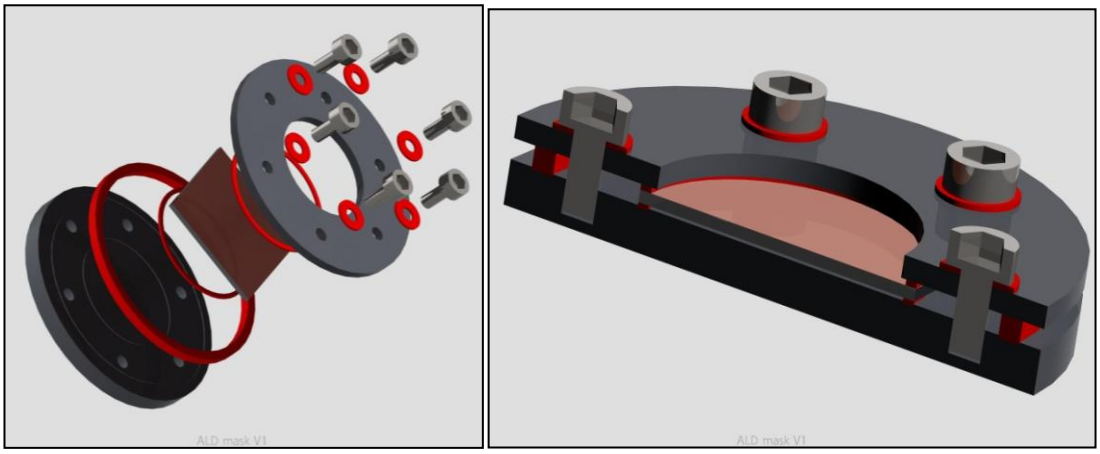

Figure 119: ALD Mask design version 1

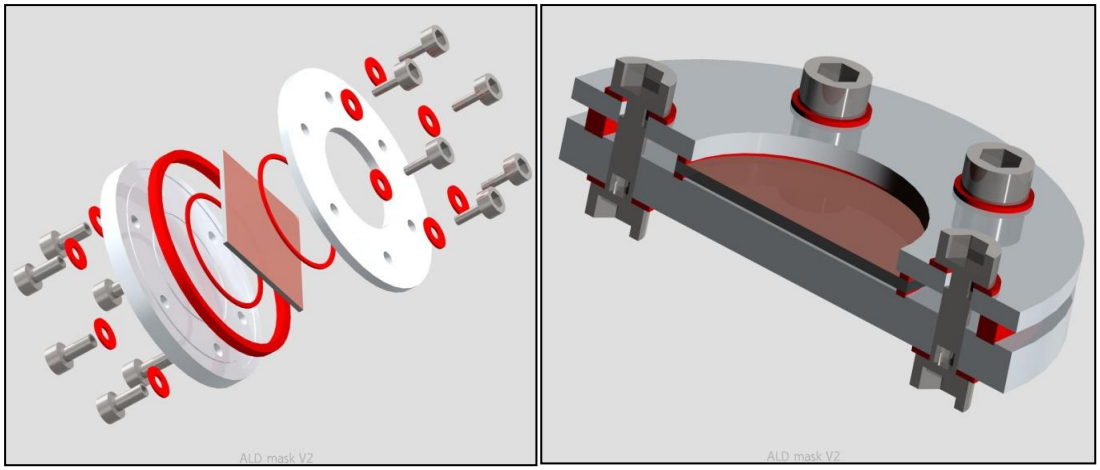

Figure 120: ALD Mask design version 2

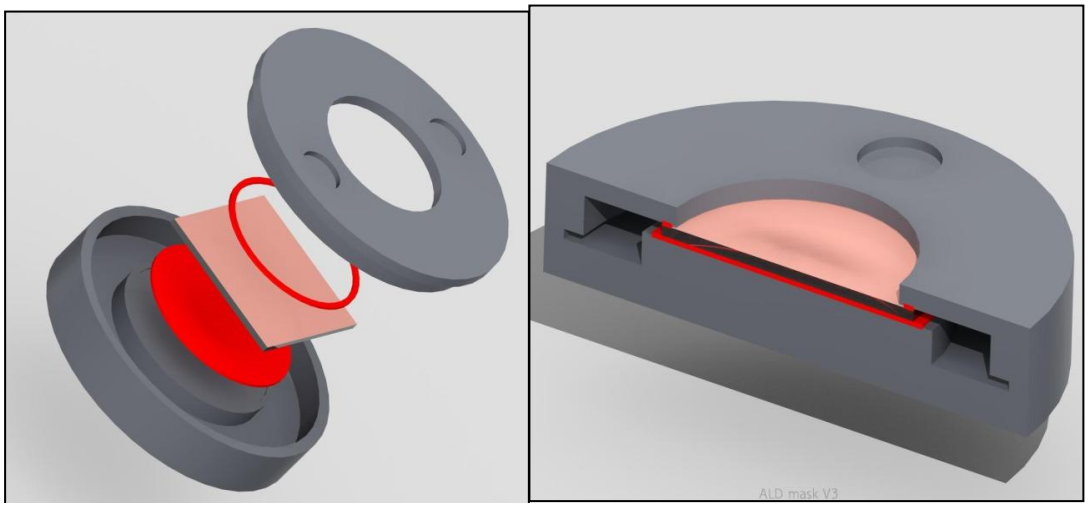

Figure 121: ALD mask design version 3

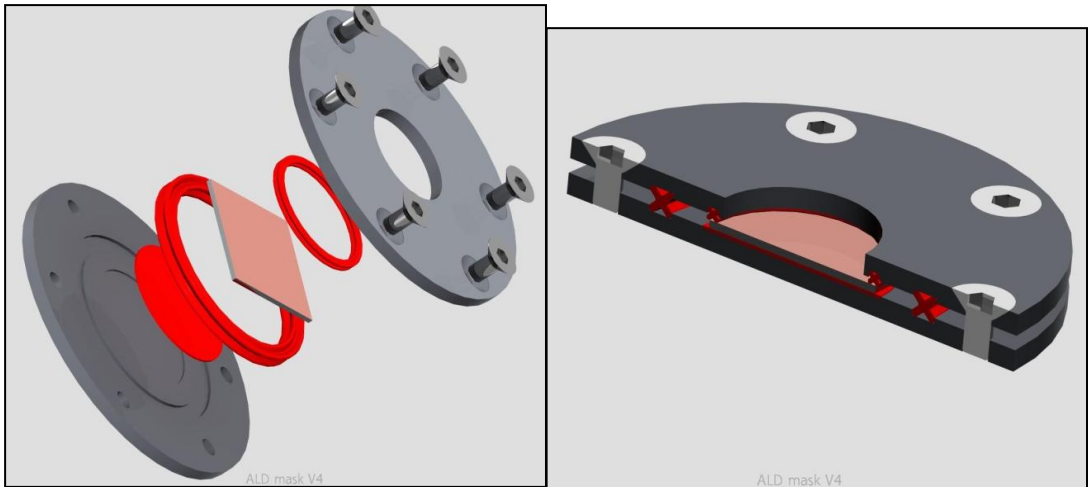

Figure 122: ALD mask design version 4

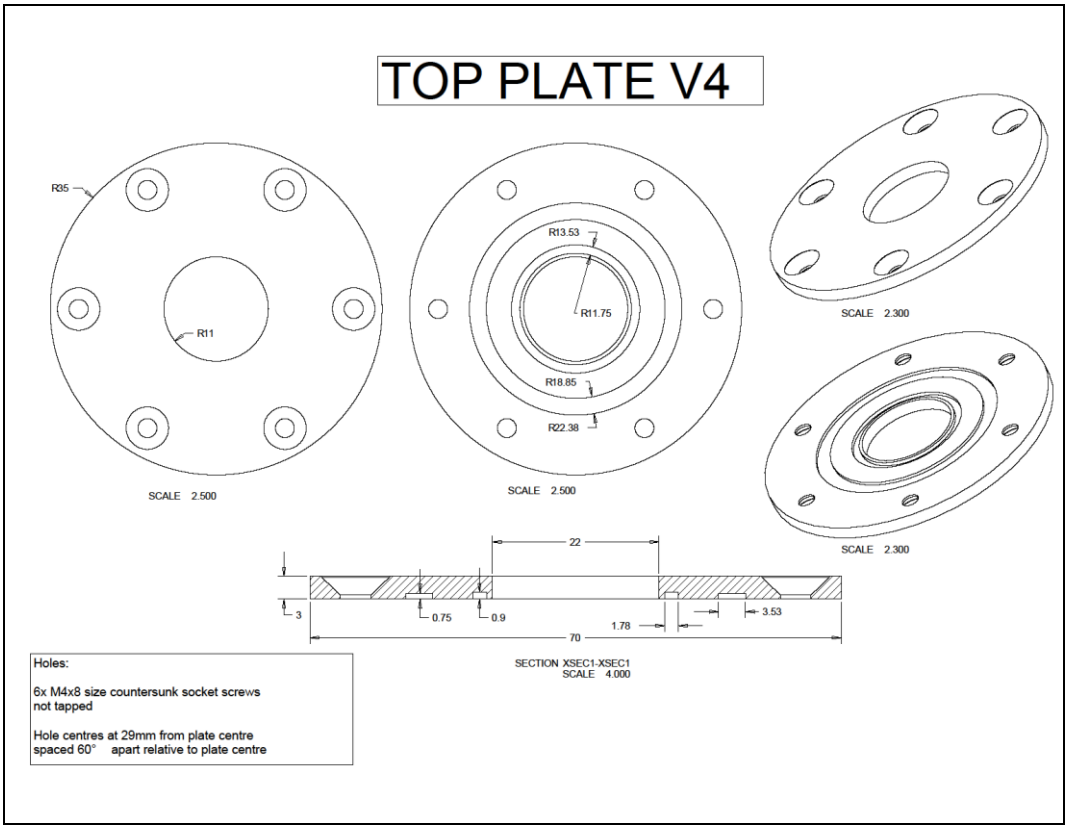

Figure 123: Design drawing for ALD mask top plate V4 (dimensions in mm)

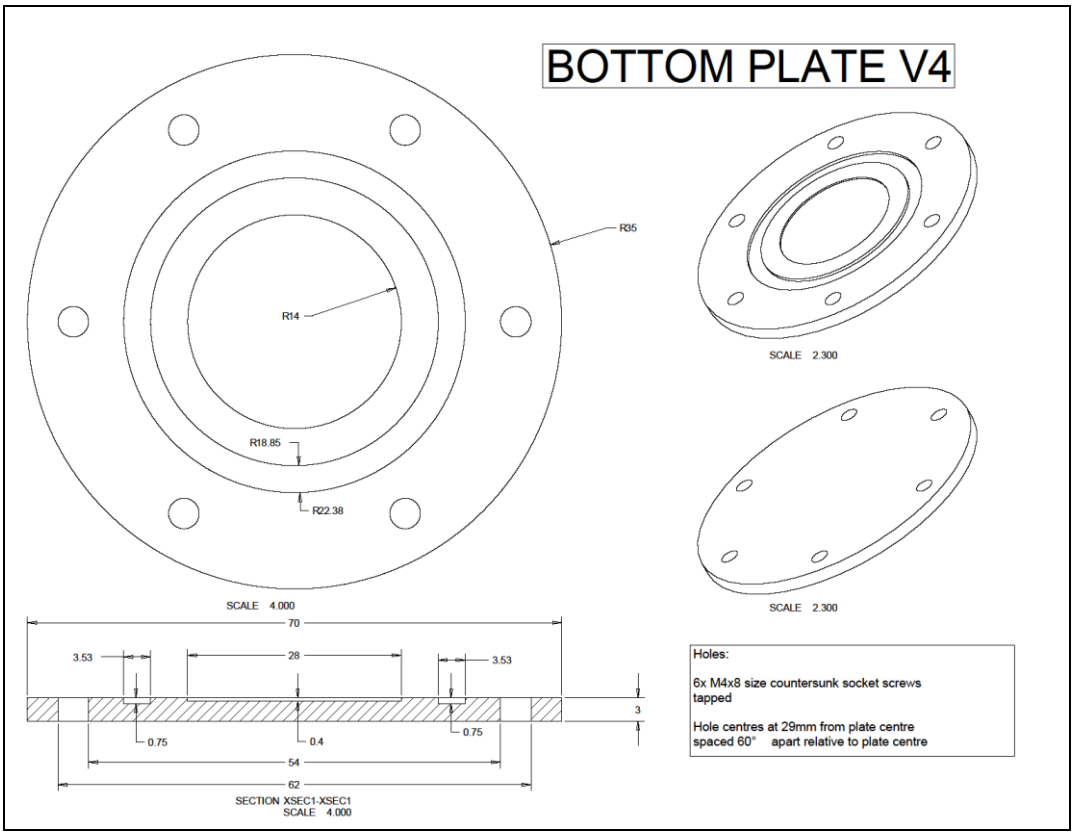

Figure 124: Design drawing for ALD mask bottom plate V4 (dimensions in mm)

The first and second versions of the design were rejected mainly because in their fully assembled state the devices were over 8mm thick, i.e. taller than the Cambridge nanotech savannah reactor chamber space. Other reasons for rejecting the designs were that they each required many high temperature o-rings which along with adding expense would also introduce more possible points of failure. The fourth design was chosen as it required the least number of parts and would fit inside the savannah ALD reactor. Additionally, the large outer o-ring was reduced in size so that the screws would fit on the outside of the enclosed space. This would benefit the design as it would reduce the volume of the enclosed area and hence the amount of trapped atmospheric gases (as the samples and masking device were to be assembled at RTP) limiting the chance of the device degassing whilst being heated under vacuum. Stainless steel was chosen as the top and bottom plate material because of its reasonable temperature resistance, ease of machining and relative inertness within an ALD reactor chamber. The o-rings and rubber pad were chosen to be made from Viton rubber, rated to withstand prolonged exposure to temperatures >200°C. X-section o-rings were chosen over the standard circular section rings as the x shape would allow them to be compressed more enabling better contact with the substrate material. This allows a higher degree of variation in the sample thickness. Additionally, the x shape provides two points of contact with the top and bottom plates, effectively behaving as two vacuum seals. Any trapped gases would then have to breach both legs of the x shape in order to escape into the reactor environment.

1mm thick glass slides were cut into squares measuring 25mm along each edge. After cleaning with distilled water and propanol the masking device was assembled containing the glass slide. Aluminium doped Zinc Oxide (AZO) was chosen for the deposition as its high conduction would indicate whether or not the device had worked as intended, via simple measurements of the conductivity across the sample surface.

Three precursors were used for the deposition; Trimethyl Aluminium (TMA), Diethyl Zinc (DEZ) and H_2O. The temperature of the ALD valves above each bubbler was held constant at 80°C throughout the deposition process. The reactor bed and outer heater were held at 250°C and 150°C respectively. Argon gas was flowed through the reactor at 5sccm, acting as an inert carrier gas as well as the purge gas.

Ten cycles of TMA (0.02s) and H_2O (0.01s) were used to deposit a thin layer of Al_2O_3, with 1 second purges between each pulse. This was done to prepare the surface for the growth of the transparent conductive oxide (AZO) as Al_2O_3 is known to be a good surface on which to grow ALD layers.

For the deposition of AZO, one cycle consisted of the following:

- 0.02s DEZ/1s purge/0.01s H_2O/1s purge x 32
- 0.02s TMA/1s purge/0.01s H_2O/1s purge x 1

For the entire deposition, 100 cycles were used. Once the run had completed the reactor was allowed to cool to below 100°C before the mask and sample were removed. After cooling to RT, the sample was removed from the mask and the resistance across various points of the surface tested using a two-probe multimeter.

10.1 Results and Discussion

Once removed from the mask the sample showed a disc of slightly yellowed material in the centre. The edges of the disc corresponded with the inner edge of the small x-section o-ring. The deposited material showed a variation in thickness across the disc with the centre thinner than the edges and the side nearest the reactor exhaust thicker than the side nearer to the precursor inlet (Figure 125). This variation in thickness was thought to be caused partly by the short purge times used (1s purges were used due to time constraints, for normal deposition of high conductivity AZO 4s purges are normally used) and partly by

turbulence as the precursor gases interacted with the vertical edges of the masking device. This variation in thickness could be minimised by machining a chamfer on the upper mask plate. Little can be done to remove the overhanging lip just above the sample however as it is necessary to secure the smaller x-section o-ring.

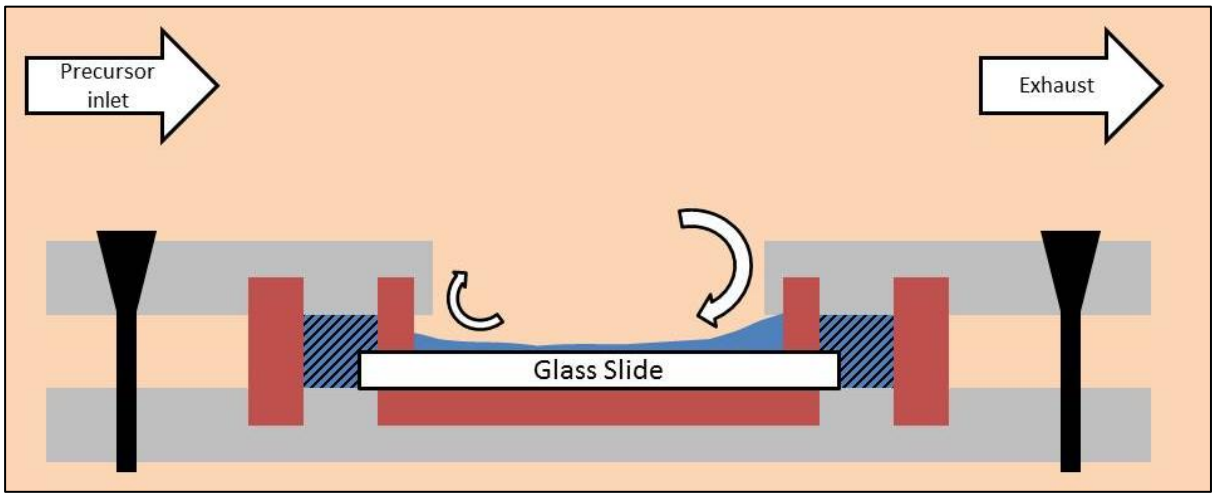

Figure 125: Schematic diagram of the deposition of Al doped ZnO TCO (blue) showing the variation in thickness (not to scale) across the sample surface. Hatching shows volume within mask at normal atmospheric pressure, isolated from reactor environment.

The resistance when measured from corner to corner was above the range of the multimeter (>500MΩ), as would be expected for glass with no surface coating. Measured from the corner to the centre the result was the same.

Measurements of the central disc gave a resistance of 44Ω with the probe tips close together (~1mm separation) and ~100Ω when measured at opposite points on the disc circumference. Since the conductivity of the thin-film AZO disc was found to be fairly high, this indicated that there was no significant electrical connection between the deposited area and any of the masked areas.

10.2 Conclusion

The masking device was found to have worked to a degree, being able to restrict the ingress of ALD precursors and leave the edges of the samples free from deposition without degassing during the run or significantly inhibiting ALD growth.

The variation in deposition thickness can be reduced by using longer purge times, reducing any CVD-like atmospheric reactions, and by machining a chamfer between the upper surface of the top plate and the edge of the inner circle. Further design modifications and deposition tests would be required to prove the validity of this masking technique. The increase of purge times to remove unreacted precursor from the recesses of the device might also limit the usefulness of this technique for future depositions.